



**Fermilab**

FERMILAB-THESIS-2002-18

**A Measurement of Bottom Quark–Antiquark Azimuthal Production  
Correlations in Proton-Antiproton Collisions at  $\sqrt{s} = 1.8$  TeV**

BY

Anthony Allen Affolder

B.A. (University of Chicago, Illinois) 1996

M.A. (University of California, Berkeley) 2002

A dissertation submitted in partial satisfaction of  
the requirements for the degree of  
Doctor of Philosophy  
in  
Physics  
in the  
GRADUATE DIVISION  
of the  
UNIVERSITY OF CALIFORNIA, BERKELEY

Committee in charge:

Professor Marjorie D. Shapiro, Chair

Professor Robert Jacobsen

Professor Stephen Derenzo

Fall 2002

The dissertation of Anthony Allen Affolder is approved:

---

Chair

Date

---

Date

---

Date

University of California, Berkeley

Fall 2002

A Measurement of Bottom Quark–Antiquark Azimuthal Production  
Correlations in Proton-Antiproton Collisions at  $\sqrt{s} = 1.8$  TeV

Copyright 2002

by

Anthony Allen Affolder

This work was supported by the Director, Office of Energy Research, Office of High Energy and Nuclear Physics, Division of High Energy Physics, of the U.S. Department of Energy under contract DE-AC03-76SF00098.

The United States Department of Energy has the right to use this thesis for any purpose whatsoever including the right to reproduce all or any part thereof.

## Abstract

A Measurement of Bottom Quark–Antiquark Azimuthal Production

Correlations in Proton-Antiproton Collisions at  $\sqrt{s} = 1.8$  TeV

by

Anthony Allen Affolder

Doctor of Philosophy in Physics

University of California, Berkeley

Professor Marjorie D. Shapiro, Chair

I report on a measurement of  $b\bar{b}$  azimuthal angular correlations in  $p\bar{p}$  collisions at  $\sqrt{s}=1.8$  TeV using an integrated luminosity of  $86.5 \pm 3.5 \text{ pb}^{-1}$ . The event topology used in this measurement is  $b \rightarrow J/\psi X; \bar{b} \rightarrow \ell X'$  where  $\ell$  can be an electron or muon identified with soft lepton algorithms. The  $b\bar{b}$  purity as a function of  $\Delta\phi^{J/\psi\ell}$  is determined by fitting the decay length of the  $J/\psi$  and the impact parameter of the soft lepton simultaneously. The fraction of  $b\bar{b}$  pairs measured in the same azimuthal hemisphere ( $f_{\text{toward}}$ ) is  $19.2^{+6.5}_{-5.9} {}^{+0.5}_{-0.6}\%$  and  $34.5^{+9.2}_{-8.2} {}^{+8.0}_{-3.1}\%$  for the electron and muon samples, respectively. The first uncertainty is the error returned from the log-likelihood fit, and the second uncertainty is due to the systematic uncertainties in the impact parameter- $c\tau$  shapes of the signal and backgrounds. The measurements, corrected to bottom quark kinematics, are consistent with both leading-log [40] and next-to-leading order [24] QCD predictions. This result is the first measurement of  $b\bar{b}$  production correlations at a hadron collider with no mass or explicit angular requirements on the  $b\bar{b}$  pair.

---

Chair

Date

# Contents

<b>1</b>	<b>Introduction</b>	<b>1</b>
1.1	Standard Model . . . . .	1
1.1.1	Strong interaction (QCD) . . . . .	3
1.1.2	Electroweak interaction . . . . .	4
1.1.3	Neutral bottom meson mass difference and CP violation . . . . .	5
1.2	Theory of Bottom Quark Production at $p\bar{p}$ Colliders . . . . .	6
1.3	Past Experimental Single Differential Bottom Cross Section Measurements at $p\bar{p}$ Colliders . . . . .	10
1.4	Theoretical Motivation for $b\bar{b}$ Angular Production Correlation Measurements	11
1.5	Past Experimental $b\bar{b}$ Angular Production Correlation Measurements Measurements at $p\bar{p}$ Colliders . . . . .	14
1.6	Motivation and Overview of this Analysis . . . . .	16
<b>2</b>	<b>Theoretical Overview</b>	<b>22</b>
2.1	Factorization Theorem . . . . .	22
2.2	Parton Distribution Functions . . . . .	24
2.3	NLO Parton Cross Section . . . . .	25
2.4	Fragmentation . . . . .	27
2.4.1	Independent and string fragmentation models . . . . .	27
2.4.2	Fragmentation functions . . . . .	29
2.5	$k_T$ Smearing . . . . .	31
<b>3</b>	<b>Experimental Apparatus</b>	<b>33</b>
3.1	The Accelerator Complex . . . . .	33
3.1.1	Proton acceleration . . . . .	34
3.1.2	Anti-proton production . . . . .	35
3.1.3	Collisions . . . . .	36
3.2	The CDF Detector . . . . .	37
3.2.1	Silicon Vertex Detector . . . . .	38
3.2.2	Vertex Tracking Chamber . . . . .	42
3.2.3	Central Tracking Chamber . . . . .	43
3.2.4	Calorimetry . . . . .	45
3.2.5	Central muon detectors . . . . .	47
3.2.6	Luminosity counters (BBC) . . . . .	50
3.2.7	Data acquisition and trigger . . . . .	51

<b>4</b>	<b>Data Set and Event Selection</b>	<b>54</b>
4.1	Run 1B Di-muon Triggers and Data Set . . . . .	54
4.2	$J/\psi \rightarrow \mu^+ \mu^-$ Event Selection . . . . .	55
4.3	CMUP $\mu$ Selection Requirements . . . . .	59
4.4	SLT Electron Selection Criteria . . . . .	60
4.4.1	General selection criteria . . . . .	60
4.4.2	Calorimeter requirements . . . . .	60
4.4.3	CES and CPR requirements . . . . .	62
4.4.4	$dE/dx$ requirements . . . . .	63
4.4.5	Conversion removal . . . . .	64
4.4.6	Results of electron selection . . . . .	65
<b>5</b>	<b>Physics Analysis</b>	<b>68</b>
5.1	Signal and Background Description . . . . .	68
5.1.1	Direct and bottom decay $c\tau$ shapes . . . . .	70
5.1.2	Direct impact parameter shape . . . . .	75
5.1.3	Bottom impact parameter shapes . . . . .	76
5.1.4	Residual conversion background rate ( $R_{conv}$ ) . . . . .	83
5.1.5	Residual conversion impact parameter shape . . . . .	92
5.1.6	Sideband impact parameter- $c\tau$ shape . . . . .	99
5.1.7	$B_c \rightarrow J/\psi \ell^+ X$ . . . . .	102
5.1.8	$b \rightarrow J/\psi \ell_{fake}$ . . . . .	105
5.2	Fit Description . . . . .	115
5.2.1	Data . . . . .	116
5.2.2	$b \rightarrow J/\psi X; \bar{b} \rightarrow \ell X'$ signal . . . . .	117
5.2.3	Unconstrained, uncorrelated backgrounds . . . . .	117
5.2.4	Fake $J/\psi$ backgrounds . . . . .	118
5.2.5	$B_c \rightarrow J/\psi \ell X$ backgrounds . . . . .	119
5.2.6	$b \rightarrow J/\psi \ell_{fake} X$ backgrounds . . . . .	120
5.2.7	Residual conversion background . . . . .	121
5.2.8	$n_{signal}$ sums . . . . .	122
5.2.9	Impact parameter- $c\tau$ shape component . . . . .	123
5.2.10	Bin constraints component . . . . .	124
5.2.11	Global constraints component . . . . .	124
5.2.12	Log-likelihood function . . . . .	125
5.3	Fit Results . . . . .	125
5.4	Systematic Uncertainties . . . . .	127
5.4.1	Sequential charm fraction . . . . .	127
5.4.2	Bottom lifetime . . . . .	132
5.4.3	Bottom fragmentation ratios . . . . .	133
5.4.4	$n_{bconv}/n_{dconv}$ ratio . . . . .	134
5.4.5	Residual conversion impact parameter shape . . . . .	134
5.4.6	Direct impact parameter shape . . . . .	135
5.4.7	Direct and bottom $c\tau$ shape . . . . .	136
5.4.8	$N_{db}$ . . . . .	136
5.4.9	Total systematic uncertainty . . . . .	137
5.5	Final Results . . . . .	137

<b>6</b>	<b>Theory Predictions</b>	<b>139</b>
6.1	Correction to Quark Level . . . . .	139
6.2	Comparison to Next-To-Leading Order Theory . . . . .	145
6.2.1	NLO and PYTHIA $p_T$ and rapidity spectra comparisons . . . . .	150
6.2.2	NLO and PYTHIA $\Delta\phi$ , $p_T^{b\bar{b}}$ , and R spectra comparisons . . . . .	150
6.2.3	NLO and PYTHIA total cross section comparison . . . . .	157
6.3	Comparison to Leading-Log Order Theory (PYTHIA) . . . . .	157
<b>7</b>	<b>Conclusions</b>	<b>161</b>
<b>A</b>	<b><math>dE/dx</math> Fit Description</b>	<b>171</b>
<b>B</b>	<b>Conversion Track Quality Study</b>	<b>173</b>
<b>C</b>	<b><math>B_c \rightarrow J/\psi \ell X</math> and <math>b \rightarrow J/\psi \ell_{\text{fake}X}</math> impact parameter-<math>c\tau</math> fit shape</b>	<b>176</b>
<b>D</b>	<b>Toy Monte Carlos Studies</b>	<b>179</b>

# List of Figures

1.1	Current constraints on the Unitarity Triangle (from ref. [7]). . . . .	6
1.2	Example Feynman diagrams contributing to NLO $b\bar{b}$ production calculations at a $p\bar{p}$ collider. Gluon Radiation is the radiative correction to LO diagram. Interference terms are $\mathcal{O}(\alpha_s^4)$ virtual graphs that interfere with LO terms. . . . .	9
1.3	Bottom production measurements at the $S\bar{p}\bar{p}S$ ( $\sqrt{630}$ GeV) Left: UA1 measurements [10] of b quark integrated cross-section. Right: UA1 $\Delta\phi$ measurement [25] using $\mu - \mu$ . . . . .	12
1.4	Current ( $p_T$ ) cross section measurements of bottom production at the Tevatron. Left: D0 [11] and CDF [12] measurements of b quark integrated cross-section. Right: CDF [14] B meson differential cross-section. . . . .	12
1.5	Current single differential (rapidity) measurements of bottom production at the Tevatron (D0[13]). . . . .	13
1.6	$\Delta\phi$ and $R \equiv \sqrt{\Delta\phi^2 + \Delta y^2}$ plots from ref. [21]. . . . .	14
1.7	Current angular correlation measurements of bottom production at the Tevatron. Top Left: D0 $\Delta\phi$ measurement [26] using $\mu - \mu$ . Top Right: CDF $\Delta\phi$ measurement [28] using $\mu - \mu$ . Bottom Left: CDF $\Delta\phi$ measurement [27] using $\mu + \text{Jet}(\text{JetProb})$ . Bottom Right: CDF $\Delta R$ measurement [29] using $\mu + \text{Jet}(\text{SECVTX})$ . . . . .	17
1.8	Sideband subtracted $\Delta\phi$ distribution between fully reconstructed bottom mesons and soft leptons from ref. [30]. Top: $B^+ \rightarrow J/\psi K^+$ . Bottom: $B^0 \rightarrow J/\psi K^{0*}$ . . . . .	19
2.1	Di-photon system transverse momenta. Left: D0 [47]. Right: CDF [48]. . . . .	32
3.1	The Fermi National Accelerator Complex. . . . .	34
3.2	Schematic of anti-proton production. . . . .	35
3.3	A r-z Quadrant Schematic Cross-section of the Collider Detector at Fermilab. . . . .	39
3.4	Schematic of a SVX' Ladder. . . . .	40
3.5	Schematic of a SVX' barrel. . . . .	41
3.6	Schematic of a VTX module. . . . .	43
3.7	Schematic of a CTC end-plate. . . . .	44
3.8	Schematic of a calorimeter tower. . . . .	45
3.9	Schematic of the central muon coverage. . . . .	48
3.10	End-view schematic of a CMU modules. . . . .	49
3.11	Plot of the number of absorption lengths vs. energy for a normal incidence particle. Thin: CMU only. Thick: CMU and CMP. Red: $K^+$ . Blue: $K^-$ . Black: $\pi^{+/-}$ . . . . .	50



4.1	$\chi^2$ probability of the $J/\psi$ vertex fit. . . . .	57
4.2	Di-muon invariant mass distribution from events passing selection criteria. Top: Linear scale. Bottom: Logarithmic scale. . . . .	58
4.3	Top: The $p_T$ of the CMUP muon candidates. Middle Left: Hadronic energy deposited by the SLT CMUP muon candidates (solid, filled) and by CMUP muons from $J/\psi$ decay. Middle Right: $\chi^2$ of r- $\phi$ stub matching in the CMU for the SLT CMUP muon candidates (solid, filled) and for CMUP muons from $J/\psi$ decay. Bottom Left: $\chi^2$ of r-z stub matching in the CMU for the SLT CMUP muon candidates (solid, filled) and for CMUP muons from $J/\psi$ decay. Bottom Right: $\chi^2$ of r- $\phi$ stub matching in the CMP for the SLT CMUP muon candidates (solid, filled) and for CMUP muons from $J/\psi$ decay. . . . .	61
4.4	Top Left: $p_T$ of the SLT electron candidates. Top Right: $E/p$ of SLT electron candidates (filled,solid) and conversion candidates (dotted). Bottom Left: $E_{strip}/p$ of SLT electron candidates (filled,solid) and conversion candidates (dotted). Bottom Right: $E_{wire}/p$ of SLT electron candidates (filled,solid) and conversion candidates (dotted). . . . .	66
4.5	Distribution of electron selection variables for SLT candidates (solid,filled) and conversion candidates (dotted). Top Left: $\Delta x$ . Top Right: $\Delta z$ . Middle Left: $\chi^2_{wire}$ . Middle Right: $\chi^2_{strip}$ . Bottom Left: $Q_{CPR}$ . Bottom Right: $dE/dx$ . . . . .	67
5.1	Cartoon of $L_{xy}$ measurement in $b \rightarrow J/\psi X$ decays. . . . .	71
5.2	Fit of $J/\psi$ mass sideband data. . . . .	73
5.3	Fit of $J/\psi$ signal region. . . . .	75
5.4	The signed impact parameter distribution for the simulated electron direct production. Top: Logarithmic scale. Bottom: Linear scale. . . . .	77
5.5	The signed impact parameter distribution for the simulated direct muon production. Top:Logarithmic scale. Bottom: Linear scale. . . . .	78
5.6	Top: Combined CES and CPR electron selection efficiency from [84]. Bot- tom: CTC $dE/dX$ selection efficiency. . . . .	80
5.7	The impact parameter of events with electrons passing requirement in the flavor creation Monte Carlo sample. Top: Direct bottom. Bottom: Sequen- tial charm. . . . .	81
5.8	The signed impact parameter distribution for the combined electron bottom Monte Carlo. Top: Logarithmic scale. Bottom: Linear scale. . . . .	82
5.9	The signed impact parameter distribution for the combined muon bottom Monte Carlo. Top: Logarithmic scale. Bottom: Linear scale. . . . .	83
5.10	The signed impact parameter distributions of electron Monte Carlo for the three bottom production mechanisms. Both directly produced and sequen- tial muons are in included the distribution. Top: Logarithmic scale. Bottom: Linear scale. . . . .	84
5.11	Fit of the CTC $dE/dx$ measured of events with the tight conversion selection criteria. Top: SLT conversion candidate. Bottom: Pair candidate. . . . .	87
5.12	Fit of the CTC $dE/dx$ measured for events passing the loosest conversion selection criteria, but not the tight selection criteria. Top: SLT conversion candidate. Bottom: Pair candidate. . . . .	88

5.13	The $p_T$ spectra of the SLT conversion candidates. Top Left: 3rd order power law. Top Right: 3.5 order power law. Bottom Left: 4th order power law. Bottom Right: 5th order power law. . . . .	90
5.14	The $p_T$ spectra of the pair candidates. The Monte Carlo is normalized to the data with $p_T > 0.5$ GeV. Top Left: 3rd order power law. Top Right: 3.5 order power law. Bottom Left: 4th order power law. Bottom Right: 5th order power law. . . . .	91
5.15	Top: Conversion impact parameter distribution. Bottom: Impact parameter distribution of bottom flavor creation Monte Carlo. . . . .	93
5.16	Cartoon of impact parameter signing. With perfect tracking, conversion electrons are always positively signed due to the fact that the photon is massless. Bottom decay electrons have a symmetric impact parameter distribution due to the bottom hadron's mass. . . . .	94
5.17	Top: Signed impact parameter of conversion candidates. Bottom: Conversion radius of candidates. . . . .	95
5.18	Top: Signed impact parameter of conversion candidates versus the conversion radius. . . . .	96
5.19	The signed impact parameter distribution for the conversions with correct SVX assignment in Monte Carlo. Top: Logarithmic scale. Bottom: Linear scale. . . . .	97
5.20	The signed impact parameter distribution for the conversions with less than 3 SVX hits assigned in Monte Carlo. Top: Logarithmic scale. Bottom: Linear scale. . . . .	98
5.21	The signed impact parameter distribution for conversions found in data. Red: Monte Carlo fit using the central value of $f_{conv}^{GoodSVX}$ . Green: Monte Carlo fit increasing $f_{conv}^{GoodSVX}$ by one sigma. Blue: Monte Carlo fit decreasing $f_{conv}^{GoodSVX}$ by one sigma. . . . .	100
5.22	The fit of the muon sample's signed impact parameter and $c\tau$ distributions in the $J/\psi$ mass sideband region. . . . .	101
5.23	Mass of $B^+ \rightarrow J/\psi K^+$ candidates found in the Run 1b $J/\psi$ sample. . . . .	104
5.24	Impact parameter- $c\tau$ contour plots of Monte Carlo $B_c \rightarrow J/\psi e \nu$ events and the fit. Top: Monte Carlo. Bottom: Fit to Monte Carlo. . . . .	105
5.25	Impact parameter- $c\tau$ contour plots of Monte Carlo $B_c \rightarrow J/\psi \mu \nu$ events and the fit. Top: Monte Carlo. Bottom: Fit to Monte Carlo. . . . .	106
5.26	Fake SLT electron probability as a function of $p_T$ from [31]. . . . .	108
5.27	Impact parameter- $c\tau$ contour plots of Monte Carlo $b \rightarrow J/\psi e_{Fake} X$ events and the fit. Top: Monte Carlo. Bottom: Fit to Monte Carlo. . . . .	110
5.28	Decay-in-flight probability as a function of $p_T$ in ref. [31]. . . . .	111
5.29	Impact parameter- $c\tau$ contour plots of Monte Carlo $b \rightarrow J/\psi \mu_{Fake} X$ events and the fit. Top: Monte Carlo. Bottom: Fit to Monte Carlo. . . . .	113
5.30	The fit of the electron sample's signed impact parameter and $c\tau$ distribution for the $J/\psi$ mass sideband. . . . .	126
5.31	Result of the $c\tau$ -impact parameter fit for the electron sample in the toward bin. Top: Data. Bottom: Fit. . . . .	127

5.32	Result of the $c\tau$ -impact parameter fit for the electron sample in the toward bin. Top: Projection onto impact parameter axis. Bottom: Projection onto $c\tau$ axis..	129
5.33	Result of the $c\tau$ -impact parameter fit for the electron sample in the away bin. Top: Data. Bottom: Fit.	129
5.34	Result of the $c\tau$ -impact parameter fit for the electron sample in the away bin. Top: Projection onto impact parameter axis. Bottom: Projection onto $c\tau$ axis..	130
5.35	Result of the $c\tau$ -impact parameter fit for the muon sample in the toward bin. Top: Data. Bottom: Fit.	130
5.36	Result of the $c\tau$ -impact parameter fit for the muon sample in the toward bin. Top: Projection onto impact parameter axis. Bottom: Projection onto $c\tau$ axis..	131
5.37	Result of the $c\tau$ -impact parameter fit for the muon sample in the away bin. Top: Data. Bottom: Fit.	131
5.38	Result of the $c\tau$ -impact parameter fit for the muon sample in the away bin. Top: Projection onto impact parameter axis. Bottom: Projection onto $c\tau$ axis..	132
6.1	$p_T$ of the bottom quarks in events that pass selection in the electron PYTHIA samples. The arrows indicate the 90% acceptance value.	141
6.2	$ y $ of the bottom quarks in events that pass selection in the electron PYTHIA samples. The arrows indicate the 90% acceptance value.	142
6.3	$p_T$ of the bottom quarks in events that pass selection in the muon PYTHIA samples. The arrows indicate the 90% acceptance value.	142
6.4	$ y $ of the bottom quarks in events that pass selection in the muon PYTHIA samples. The arrows indicate the 90% acceptance value.	143
6.5	NLO prediction [24] of $f_{toward}$ using various $k_T$ smearing values. The errors include the statistical and systematic errors on the calculation. The PYTHIA prediction is shown as a reference and only includes statistical errors. The experimental result is shown with the vertical black line. The yellow and red areas indicate the error returned by the fit and the total error including the additional systematics. Top: Electrons. Bottom: Muons	149
6.6	NLO prediction [24] of bottom spectra with electron fiducial requirements in table 6.1. The PYTHIA prediction is shown as a reference. Top Left: MRST99 PDF varying the additional $k_T$ smearing. Top Right: CTEQ5M PDF varying the additional $k_T$ smearing. Bottom Left: MRST99 PDF varying the renormalization scale $\mu$ . Bottom Right: MRST99 PDF varying the bottom quark mass $m_B$ .	151
6.7	NLO prediction [24] of bottom spectra with muon fiducial requirements in table 6.1. The PYTHIA prediction is shown as a reference. Top Left: MRST99 PDF varying the additional $k_T$ smearing. Top Right: CTEQ5M PDF varying the additional $k_T$ smearing. Bottom Left: MRST99 PDF varying the renormalization scale $\mu$ . Bottom Right: MRST99 PDF varying the bottom quark mass $m_B$ .	152

6.8	Comparison of the NLO prediction [24] of bottom spectra with electron fiducial requirements in table 6.1 to the PYTHIA prediction. The distributions are all normalized to the total PYTHIA prediction. The uneven binning occurs in $p_T$ regions where the NLO calculation has large negative terms due to virtual diagrams and collinear subtraction. See section 2.3 for a complete explanation. Top Left: Maximum bottom quark $p_T$ . Top Right: Minimum bottom quark $p_T$ . Bottom Left: Rapidity of bottom quark with maximum bottom quark $p_T$ . Bottom Right: Rapidity of bottom quark with minimum bottom quark $p_T$ . . . . .	153
6.9	Comparison of the NLO prediction [24] of bottom spectra with muon fiducial requirements in table 6.1 to the PYTHIA prediction. The distributions are all normalized to the total PYTHIA prediction. The uneven binning occurs in $p_T$ regions where the NLO calculation has large negative terms due to virtual diagrams and collinear subtraction. See section 2.3 for a complete explanation. Top Left: Maximum bottom quark $p_T$ . Top Right: Minimum bottom quark $p_T$ . Bottom Left: Rapidity of bottom quark with maximum bottom quark $p_T$ . Bottom Right: Rapidity of bottom quark with minimum bottom quark $p_T$ . . . . .	154
6.10	Comparison of the NLO prediction [24] of bottom spectra with electron and muon fiducial requirements in table 6.1 to the PYTHIA prediction. Only the NLO predictions are normalized to the total PYTHIA prediction. The uneven binning occurs in $p_T^{b\bar{b}}$ regions where the NLO calculation has large negative terms due to virtual diagrams and collinear subtraction. See section 2.3 for a complete explanation. Left: $p_T$ of $b\bar{b}$ system, electron requirements. Right: $p_T$ of $b\bar{b}$ system, muon requirements. . . . .	155
6.11	Comparison of the NLO prediction [24] of bottom spectra with electron and muon fiducial requirements in table 6.1 to the PYTHIA prediction. Only NLO distributions are normalized to the total PYTHIA prediction. The individual PYTHIA contributions are expected to have different distributions. The uneven binning occurs in $R$ regions where the NLO calculation has large negative terms due to virtual diagrams and collinear subtraction. See section 2.3 for a complete explanation. Top Left: $\Delta\phi^{b\bar{b}}$ , electron requirements. Top Right: $\Delta\phi^{b\bar{b}}$ , muon requirements. Bottom Left: distance $R$ , electron requirements. Bottom Right: distance $R$ , muon requirements . . . . .	156
B.1	Number of SVX hits. Top Left: SLT electron data. Top Right: Conversion Monte Carlos. Bottom Left: Conversion data with the conversion radius less than 6 cm. Bottom Right: Conversion data with the conversion radius greater than 6 cm. . . . .	174
B.2	SVX fit $\chi^2/DOF$ . Top Left: SLT electron data. Top Right: Conversion Monte Carlos. Bottom Left: Conversion data with the conversion radius less than 6 cm. Bottom Right: Conversion data with the conversion radius greater than 6 cm. . . . .	175
B.3	Number of shared hits. Top Left: SLT electron data. Top Right: Conversion Monte Carlos. Bottom Left: Conversion data with the conversion radius less than 6 cm. Bottom Right: Conversion data with the conversion radius greater than 6 cm. . . . .	175

D.1	<i>The minimum log-likelihood distributions of the toy Monte Carlos Left: Electrons Right: Muons. . . . .</i>	182
D.2	<i>The fit <math>f_{toward}</math> distributions of the toy Monte Carlos Left: Electrons Right: Muons. . . . .</i>	183

# List of Tables

1.1	<i>Fundamental fermions in the Standard Model.</i>	2
1.2	<i>Fundamental bosons in the Standard Model.</i>	2
1.3	<i>Bottom angular correlation measurement quantities for this thesis and previous analyses. Top: Approximate bottom kinematics (<math>p_{T_b}, y_b</math>) of measurement due to selection criteria. Bottom: The fraction of <math>b\bar{b}</math> pairs measured (<math>f_{Toward}^{Exp}</math>) and predicted (<math>f_{Toward}^{Theory}</math>) in the same hemisphere in the azimuthal angle, <math>\Delta\phi &lt; \frac{\pi}{2}</math>. Additional cuts list the requirements which decreases the sensitivity of the measurement on the low <math>\Delta\phi</math> and low R regions. The * indicates that the theory prediction corrected to the requirement, instead of correcting the data for the requirement.</i>	18
4.1	<i><math>p_T</math> requirements on Run 1b di-muon triggers used. CMU/CMX/CMUP indicate which muon subsystems had a stub for the two muons. TWO_CFT indicates that both muon candidates have stubs matched to CFT tracks, while ONE_CFT indicates that only one muon stub is matched to a CFT track.</i>	55
4.2	<i><math>\chi^2</math> matching cuts for muons. Muon candidates with stubs in two chambers must pass both chambers <math>\chi^2</math> matching.</i>	56
5.1	<i>Fit result of <math>J/\psi</math> mass sideband data.</i>	73
5.2	<i>Fit result of signal region of <math>J/\psi</math> data.</i>	76
5.3	<i>Fit results for the direct electron and muon Monte Carlo samples.</i>	77
5.4	<i>Sequential charm fractions predicted by PYTHIA Monte Carlo.</i>	81
5.5	<i>Fit results of bottom impact parameter shape.</i>	82
5.6	<i>Tight and looser sets of cuts used in conversion finding.</i>	86
5.7	<i>Results of the fitting the <math>dE/dx</math> of conversion candidates using the tight and looser sets of cuts. For the looser set of cuts, candidates which pass the tight set of selection requirements are excluded.</i>	87
5.8	<i>The conversion selection requirement efficiency(<math>\epsilon_{cv}(cut)</math>) for the standard (tight) selection requirements assuming a given set of loosened cuts is fully efficient.</i>	88
5.9	<i>Average and RMS of <math>p_T</math> spectra (in GeV) for both the SLT conversion candidate and the pair candidate.</i>	92
5.10	<i><math>\epsilon_{cv}(pt)</math> calculated using the given order of Monte Carlo power law spectra for the <math>\pi^0</math>.</i>	92
5.11	<i>Parameters used in fit to “Good” SVX portion of the conversion impact parameter shape.</i>	97

5.12	Parameters used in fit to “BAD” SVX portion of the conversion impact parameter shape. . . . .	99
5.13	Fit result of addition muon with the $J/\psi$ candidate in the sideband region. . . . .	101
5.14	Fit results and constraints for the electron and muon samples. $n_{signal}$ and $n_{conv}$ are not fit parameters but are functions of fit parameters. . . . .	128
5.15	Fit results of $f_{toward}$ varying $f_{seq}$ in the bottom impact parameter shape by $\pm 1\sigma$ . . . . .	133
5.16	Fit results of $f_{toward}$ varying the bottom lifetimes in the bottom impact parameter shape by $\pm 1\sigma$ . . . . .	133
5.17	Fit results of $f_{toward}$ varying the $\Lambda_b$ fragmentation fraction in $F_b^{d_0}$ shape by $\pm 1\sigma$ . . . . .	134
5.18	Fit results of $f_{toward}$ fixing either $n_{dconv}$ or $n_{bconv}$ to zero. . . . .	134
5.19	Fit results of $f_{toward}$ varying $f_{conv}^{BadSVX}$ in the residual conversion shape by $\pm 1\sigma$ . . . . .	135
5.20	$f_{toward}$ fit values varying the $F_{direct}^{d_0}$ fit values within errors. . . . .	136
5.21	Fit results of $f_{toward}$ varying $f_{back}^{d_0}$ by $\pm 1\sigma$ . . . . .	136
5.22	Summary of the estimated values of the systematic uncertainty for $f_{toward}$ . . . . .	137
6.1	90% acceptance requirements on the bottom quarks decaying to a $J/\psi$ or a lepton predicting by PYTHIA Monte Carlo and a detector simulation. Top: Electron. Bottom: Muon. . . . .	143
6.2	Correction factor between the experimental measurement and the bottom quarks. Top: Electron sample. Bottom: Muon sample. . . . .	144
6.3	NLO prediction [24] of total cross section and $f_{toward}$ using the fiducial requirements from table 6.1 using the CTEQ5M PDF. . . . .	146
6.4	NLO prediction [24] of total cross section and $f_{toward}$ using the fiducial requirements from table 6.1 and the MRST99 PDF. . . . .	147
6.5	Compilation of the corrected data results, the PYTHIA predictions, and the NLO predictions of $f_{toward}$ using the fiducial requirements from table 6.1 for the theory and the correction factor $C_{B \rightarrow b}$ from table 6.2. Top: Electron. Bottom: Muon. . . . .	148
6.6	PYTHIA and NLO predictions of the total cross section and their ratio ( $k$ ) using the fiducial requirements from table 6.1. . . . .	158
6.7	PYTHIA prediction of $f_{toward}$ and the experimental measurement. . . . .	160
D.1	Average inputs into toy Monte Carlo tests of impact parameter- $c\tau$ likelihood. $n_{side}^{signal}$ is the average number of events generated from the sideband template with a $J/\psi$ mass in the signal region. $n_{side}^{sideband}$ is the average number of events generated from the sideband template with a $J/\psi$ mass in the sideband region. . . . .	180
D.2	Toy Monte Carlo Test Fit Results . . . . .	181

# Acknowledgments

Thanks first goes to my thesis advisor, Marjorie Shapiro. From the first time we talked I knew I wanted to work with you. You introduced me to the richness of bottom physics, and supported me through all the problems (mostly self-created) encountered over the last 6 1/2 years. I would thank the LBL group for their friendship and for all the fruitful discussions. I would especially like to thank Jason Nielsen and Aaron Dominguez for all the useful advice and teaching me almost everything I know about fitting.

I would like to thank the conveners of the bottom group (Mike Schmidt, Kevin Pitts, and Marjorie). You paid attention to a lowly Run I measurement during the hectic beginnings of Run II; the creation of the Run I bottom students' meetings was invaluable. The meeting gave constructive advice and created a sense of belonging to a community. I would like to thank all the students who attended these meetings. The CDF bottom group gave of their vast knowledge freely. Among others, Jonathan Lewis, Vaia Papadimitriou, Barry Wicklund, and the  $B_c$  group gave ideas, and more importantly code, which saved me months of time. Petar Maksimovic gets the credit (or blame) for this thesis topic. I would like to thank Rick Field for all the theoretical guidance he has given to all of the final Run I bottom students.

I would like to thank all the people who made my work on Run II detector the rewarding experience it has been. Young-Kee, who turned stretching mylar and moving lead bricks into learning experience about leadership and pride in one's work. The SVX and ISL people at LBL (Maurice, Igor , Bob Ely, and Carl Haber) for teaching the basics of electronics, for patiently answering my multitude of questions, and for giving me such sage advice. Finally, the ISL group at FNAL (David Stuart, Chris Hill, Doug Glenzinski, Auke-Pieter



Colijn, Tim Nelson, Joel Goldstein, and Joe Incandela) for taking in a wayward graduate student and giving me the opportunity to explore the subtleties of silicon systems, from the top down; showing how attention to details leads to a better detector, and ultimately, better physics results.

I would like to thank all my friends in Chicago, for showing me how great a city this is. Special thanks goes to Amy Connolly for telling me to shut up and stop worrying.

Thanks goes to my parents and grandparents for nurturing my interests, even though they made little sense to you most of the time. You gave me all help I asked for, and a swift kick whenever I needed it.

Finally, I would like to thank my wife, Kirsten, for all the love and support given to me during life as a graduate student. You have made the sacrifices that enabled me to pursue this habit of mine. At least, it will almost profitable now.

# Chapter 1

## Introduction

### 1.1 Standard Model

The Standard Model of particle physics is the current theory of the interactions of fundamental particles. The model has been extremely successful; (almost) all experimental measurements are consistent within the model and measurement uncertainties. Within the Standard Model, matter consists of fermions with spin  $\frac{1}{2}\hbar$ . The four forces of nature (strong, weak, electro-magnetic, and gravity) are mediated by integral-spin gauge bosons. For each fundamental particle, an antiparticle exists with opposite quantum numbers, such as electrical charge.

Two types of fundamental fermions exist in the Standard Model, leptons and quarks. There are three generations of leptons, each of which consists of a charged particle (electron, muon, or tau) and a neutral partner (electron, muon, and tau neutrinos). The generations are arranged by a mass hierarchy, whose source is as of yet unknown. Leptons only interact by the electroweak and gravitational forces.

In an analogous manner, three generations of quarks exist. Each generation consists

Leptons			Quarks		
Flavor	Mass (GeV)	Charge	Flavor	Mass(GeV)	Charge
Electron (e)	0.000511	-1	Up (u)	0.003	2/3
$\nu_e$	$\approx 0$	0	Down (d)	0.006	-1/3
Muon ( $\mu$ )	0.106	-1	Charm (c)	1.3	2/3
$\nu_\mu$	$\approx 0$	0	Strange (s)	0.1	-1/3
Tau ( $\tau$ )	1.777	-1	Top (t)	175	2/3
$\nu_\tau$	$\approx 0$	0	Bottom (s)	4.3	-1/3

Table 1.1: *Fundamental fermions in the Standard Model.*

Name	Mass (GeV)	Charge	Force Carried	Particles Effected
Graviton	0	0	Gravitation	All
Photon ( $\gamma$ )	0	0	Electro-magnetic	All charged
$W^+$	80.4	+1	Weak	Quarks and Leptons
$W^-$	80.4	-1	Weak	Quarks and Leptons
$Z^0$	91.2	0	Weak	Quarks and Leptons
gluon ( $g$ )	0	0	Strong	Quarks and Gluons
Higgs ( $H^0$ )	> 114	0		All massive particles

Table 1.2: *Fundamental bosons in the Standard Model.*

of a charge +2/3 quark (up, charm, and top) and charge -1/3 quark (down, strange, and bottom). Quarks carry 'color' as well as charge and therefore can interact via the strong force as well as the electroweak and gravitational forces. Table 1.1 summarize the characteristics of the fundamental fermions in the Standard Model.

Gravity has yet to be incorporated in the Standard Model as a quantized theory. Gravitation is assumed to be mediated by a massless spin  $2\hbar$  particle. The photon is the spin  $1\hbar$  gauge boson which mediates the electro-magnetic force. The weak force is carried by 3 massive spin  $1\hbar$  bosons, the  $W^+$ ,  $W^-$ , and  $Z^0$ . The strong interaction is transmitted by 8 'colored', spin  $1\hbar$  gluons. Finally, the Higgs Boson ( $H^0$ ) is believed to be the source of electroweak symmetry breaking and mass. The Higgs boson has yet to be seen. Table 1.2 summarizes the fundamental bosons in the Standard Model.

### 1.1.1 Strong interaction (QCD)

Quantum Chromodynamics (QCD) [1], the model of the strong interaction within the Standard Model, is a non-Abelian  $SU(3)$  gauge theory. The charge within QCD is 'color'; each quark has 3 possible colors, and gluons, the force carrier in QCD, have 8 different possible colors. As gluons carry color, gluons can self-couple, unlike photons in QED. Self-coupling of gluons leads to two phenomena in QCD: asymptotic freedom and color confinement. Asymptotic freedom refers to the weakening of strong coupling at small distances (high momentum transfer). Quarks are surrounded by 'cloud' with virtual gluons and quarks. Because gluons can split into gluon pairs, the color charge of the cloud is preferentially the color of the quark. Thus as the quark is probed at smaller distances, less of the color charge of the virtual particles is seen, eventually leaving only the bare color charge of the quark. Therefore, the theory has a small coupling at small distance scales.

Color confinement explains the lack of free quarks in nature; only color singlet objects have been seen. The coupling of the strong force gets large at a scale  $\Lambda_{QCD} \approx 300$  MeV.  $\Lambda_{QCD}$  is approximately the scale where QCD is non-perturbative, because the strong coupling constant  $\alpha_s \rightarrow 1$ . As the force between colored objects increases with distance, eventually enough potential energy is present to create a  $q\bar{q}$  pair out of the vacuum. This process continues until the quark hadronizes into a color singlet object. The simplest color singlet is a meson, the pairing of a quark and antiquark of the same color. The next simplest color singlet is a baryon, which is the combination of three quarks or three antiquarks, each with a different color. Color confinement is a non-perturbative process and has as of yet not been rigorously proven within QCD.

### 1.1.2 Electroweak interaction

The standard electroweak model [2], the unification of the electro-magnetic and weak forces, is a renormalizable  $SU(2)_L \times U(1)_Y$  gauge theory. The symmetry is spontaneously broken using the Higgs Mechanism [3], yielding four vector gauge bosons: the massless carrier of the electro-magnetic force, the photon, and three massive gauge bosons ( $W^+$ ,  $W^-$ , and  $Z^0$ ). The model also predicts a scalar boson ( $H^0$ ) which has yet to be observed<sup>1</sup>.

The electroweak force conserves lepton number within the Standard Model, i.e., the electroweak interaction does not transform leptons between families. Lepton number conservation is a consequence of the massless nature of neutrinos. Current measurements by the SNO collaboration [4] yield a significant signal for non-zero mass difference between neutrino flavors. Therefore, lepton flavor conversation is only an approximate symmetry, but the total lepton number is still conserved as far as we know.

The electroweak decay of quarks violates flavor conservation via charged W bosons. In these decays, quarks can also change between generations. This behavior can be explained if the quarks' weak eigenstates are different from their mass eigenstates. Convention dictates that the mixing is only between the down-type quarks where (d, s, b) are the mass eigenstates and (d', s', b') are the weak eigenstates. The mixing between the mass and weak eigenstates is described by the Cabibbo-Kobayashi-Maskawa (CKM) matrix [6] in the Standard Model with three generations.

$$\begin{pmatrix} d' \\ s' \\ b' \end{pmatrix} = \begin{pmatrix} V_{ud} & V_{us} & V_{ub} \\ V_{cd} & V_{cs} & V_{cb} \\ V_{td} & V_{ts} & V_{tb} \end{pmatrix} \begin{pmatrix} d \\ s \\ b \end{pmatrix} \quad (1.1)$$

---

<sup>1</sup>The current limit on the Standard Model of the Higgs Mass from LEP [5] is  $m_{H^0} > 114.4$  GeV

The CKM matrix is a complex, unitarity matrix with three real angles and one complex phase. Within the Standard Model, the complex phase in the CKM matrix is the source of CP violation. The current 90% confidence limits on the magnitude the the CKM matrix elements are [7]:

$$\begin{pmatrix} 0.9741-0.9756 & 0.219-0.226 & 0.0025-0.0048 \\ 0.219-0.226 & 0.9732-0.9748 & 0.038-0.044 \\ 0.004-0.014 & 0.037-0.044 & 0.9990-0.9993 \end{pmatrix} \quad (1.2)$$

### 1.1.3 Neutral bottom meson mass difference and CP violation

CP violation is expected to be large in bottom decays and provides an important test of the Standard Model. Using the unitarity condition on the first and third columns of the CKM matrix, an “Unitarity Triangle” in the complex plane can be constructed. Constraints on the sides and angles of the triangle can be made with measurements of neutral bottom meson ( $B_d, B_s$ ) mass differences and CP violation, among other measurements. Figure 1.1 shows the current constraints on the “Unitarity Triangle”. A triangle which does not close or in which the angles do not sum to  $\pi$  would be inconsistent with the Standard Model and is a sign of new physics.

In order to experimentally measure CP violation and mass differences in the neutral bottom meson systems, one typically needs four ingredients: a sample of bottom mesons which decay to a particular final state, the proper decay length ( $c\tau$ ) of the bottom meson, the production bottom flavor of the meson, and the decay bottom flavor of the meson (for mass difference measurements only).

The production flavor of the bottom meson can be inferred by the flavor of the other bottom quark at production (a technique known as opposite side flavor tagging). Opposite

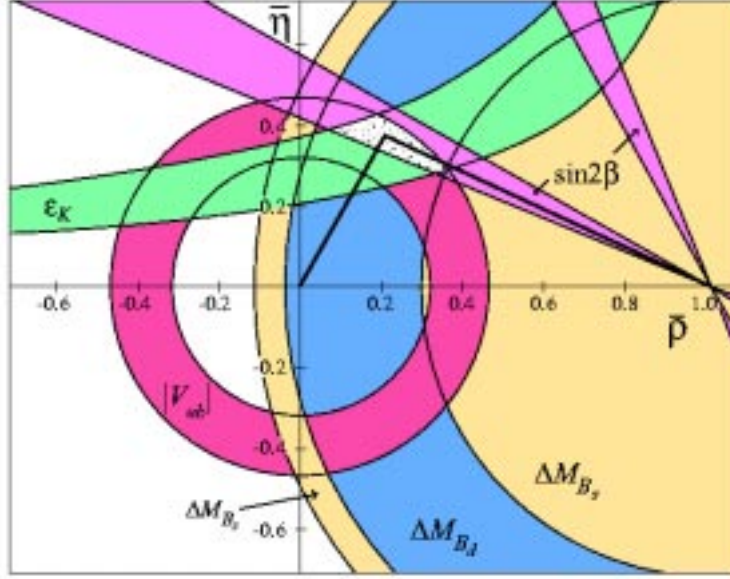


Figure 1.1: *Current constraints on the Unitarity Triangle (from ref. [7]).*

side flavor taggers have looked at the charge of leptons (soft lepton tagging [8]) and kaons (soft kaon tagging [9]), and momentum-weighted charge of jets (jet charge tagging [8]). Development and simulation of these opposite side flavor taggers can be better understood with a measurement of the production correlations between bottom quarks.

## 1.2 Theory of Bottom Quark Production at $p\bar{p}$ Colliders

Bottom quarks are produced at the Tevatron predominately in pairs via the strong interaction. A parton from both a proton and an antiproton hard scatter, producing a bottom quark-antiquark pair. In perturbative QCD, initial states with 2 gluons dominate the production cross section at low-to-moderate momenta ( $< 30$  GeV). Figure 1.2 shows representative Feynman diagrams which contribute to the NLO QCD calculation. The gluon-gluon initial states dominate due to three reasons: the number of gluons at the low momentum fraction pertinent to this analysis ( $0.001 \lesssim x \lesssim 0.1$ ) is much larger than

the number of quarks or antiquarks in the proton; the color factors in the gluon-gluon initial state diagrams is larger than the other diagrams; and the gluon-gluon interaction is  $\hat{t}$  channel, whereas the quark-antiquark interaction is  $\hat{s}$  channel.

Bottom quark production is an interesting test of QCD because decay topologies, first introduced in next-to-leading order calculations, can have cross sections as large as leading order terms at the Tevatron, as shown by the following simple argument. The  $g + g \rightarrow g + g$  cross section is about a factor of a hundred larger than the  $g + g \rightarrow b + \bar{b}$  cross section. As the rate of gluon splitting to bottom quarks ( $g \rightarrow b + \bar{b}$ ) goes as  $\sim \alpha_s$ , a relatively large cross section for such terms is possible. Of course, the cross section is suppressed by the virtuality of the gluon required due to bottom quark's mass. At LHC center-of-mass energies, these terms are predicted to be the dominant bottom production terms.

In leading order(LO) QCD, only  $g + g \rightarrow b + \bar{b}$  and  $q + \bar{q} \rightarrow b + \bar{b}$  processes are included in the calculation and the bottom quarks are always produced back-to-back in the azimuthal angle ( $\Delta\phi^{b\bar{b}} = \pi$ ).

In the next-to-leading order (NLO) calculation, the terms have traditionally grouped into three categories: flavor creation, flavor excitation, and gluon splitting. In perturbation theory, the three categories are not independent, due to interference terms between them. Flavor creation, flavor excitation, and gluon splitting are still useful concepts in describing bottom hadroproduction, as they have minimal overlap in phase space. At NLO, flavor creation consists of the  $2 \rightarrow 2$  processes, in addition to diagrams which add gluon radiation to the  $2 \rightarrow 2$  terms. Flavor excitation includes diagrams in which a initial state gluon splits into a  $b\bar{b}$  pair before interacting with the parton from the other hadron, putting the bottom quarks on-shell. Gluon splitting consists of diagrams where a gluon splits into a  $b\bar{b}$



pair after interacting with the parton from the other hadron. Due to the new three body final states included in NLO calculations ( $b\bar{b}g$ ,  $b\bar{b}q$ , and  $b\bar{b}\bar{q}$ ), the predicted  $\Delta\phi^{b\bar{b}}$  spectra is non-zero over the whole range of possible values, but still peaks back-to-back.

In leading-log (LL) showering Monte Carlos (such as PYTHIA, HERWIG, and ISAJET), the three categories are generated separately and then added together for the prediction. Since interference is not included, the predictions may include some double counting. At the heart of these generators is a leading-order matrix calculation. The incoming and outgoing partons are then allowed to radiate using analytical algorithms that are tuned to experimental measurements. The resulting final partons are hadronized using models described later in section 2.4. The fragmentation and initial and final state radiation algorithms yields a predicted  $\Delta\phi^{b\bar{b}}$  spectra similar to the next-to-leading order calculation.

In this analysis, flavor creation, flavor excitation, and gluon splitting processes within leading-log generators are defined by the number of bottom quarks in the initial and final states of hard scatter process at the heart of the generator. Flavor creation has no bottom quarks in the initial state and two bottom quarks in the final state. Flavor excitation has one bottom quark in the initial and final states. The source of the initial state bottom quark is the evolution of the parton distribution functions (PDF), which are described later. Gluon splitting has no bottom quarks in the initial or final state. The bottom quark pair is created during the final state showering/fragmentation process. In showering Monte Carlos, the relative rates between the three mechanisms are fairly uncertain. The amount of initial state radiation, the fragmentation model, and the PDF all can cause factor of  $\sim 2$  variations in the cross sections for the different mechanisms. Thus, showering Monte Carlos should be tuned to experimental measurements of bottom production, if possible.

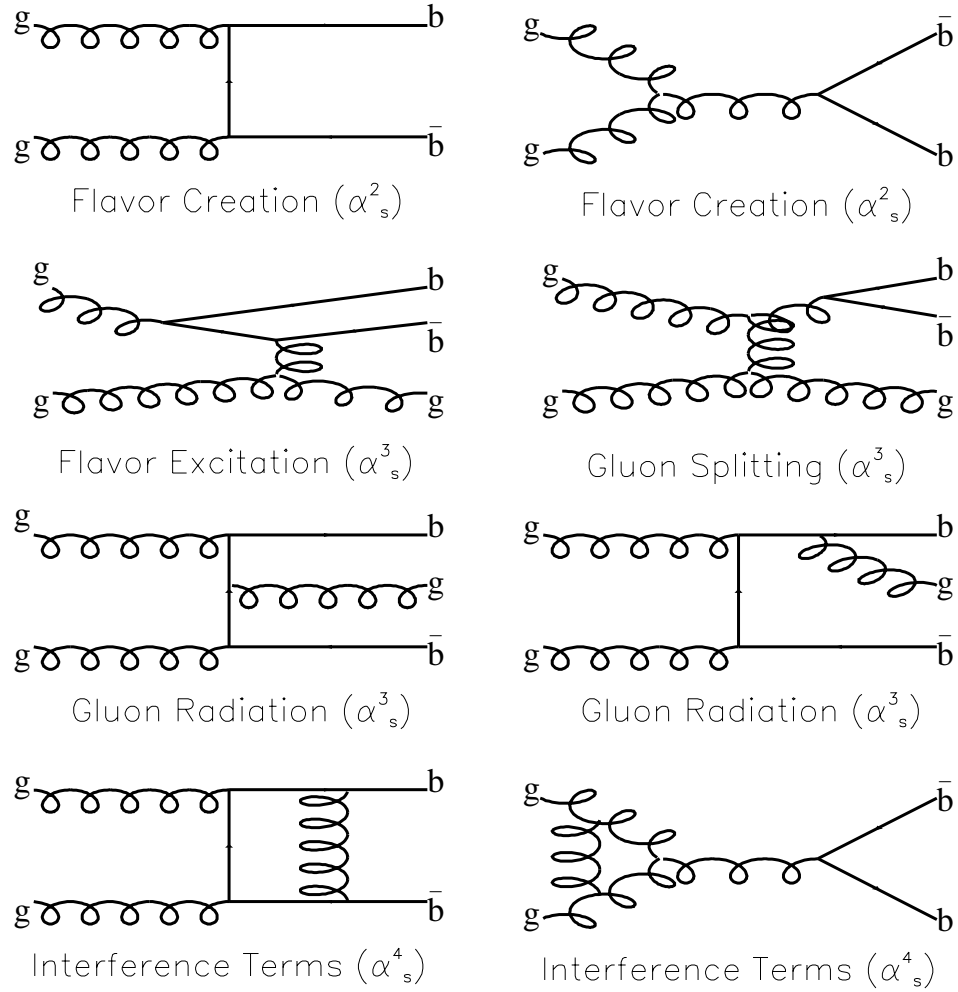


Figure 1.2: Example Feynman diagrams contributing to NLO  $b\bar{b}$  production calculations at a  $p\bar{p}$  collider. Gluon Radiation is the radiative correction to LO diagram. Interference terms are  $\mathcal{O}(\alpha_s^4)$  virtual graphs that interfere with LO terms.

For a more complete description of bottom hadroproduction theory, see chapter 2.

### 1.3 Past Experimental Single Differential Bottom Cross Section Measurements at $p\bar{p}$ Colliders

The first measurements of the bottom production cross sections at a hadron collider were performed by the UA1 collaboration [10]. The analyses used semi-leptonic bottom decays to muons to measure the integrated bottom quark cross section with  $p_T^b > p_T^{min}$  at  $\sqrt{s} = 630$  GeV. As shown in figure 1.3, the analyses showed a slight excess of the measurements relative to the NLO QCD prediction, but were consistent with theory within the systematic uncertainties of the theory prediction.

The bottom cross section was also studied by the D0 [11] and CDF [12] collaborations at the Tevatron with  $\sqrt{s} = 1800$  GeV. Figure 1.4 shows the integrated bottom quark cross section with  $p_T^b > p_T^{min}$ . The measurements used both semi-leptonic bottom decay and bottom decays to  $J/\psi$  mesons. All analyses showed a factor of 2–4 excess in the measured cross section relative to the theory, with a shape consistent with the theory predictions.

In an effort to better understand the excess of events, the D0 collaboration measured the differential bottom cross section as a function of rapidity using semi-leptonic bottom decays to muons with  $2.4 < |y_\mu| < 3.2$  [13]. Again, the NLO predicted shape is consistent with the measured values, but the measured cross section is a factor of 4 larger than the theory prediction.

All of these inclusive bottom quark cross section measurement suffer from similar uncertainties. Due to color confinement, only bottom hadrons are measured in nature. Therefore, the theory prediction has to have a fragmentation function applied to the quark level pre-

diction, or the experimental measurements has to be 'corrected' back to the quark level to remove the fragmentation effects in order to compare the measurements to the QCD prediction. Systematic uncertainties caused by the fragmentation process are described in section 2.4. In addition, uncertainties in the knowledge of the bottom decay kinematics and branching ratios lead to uncertainties in the cross section measurement.

In a complimentary measurement, the CDF collaboration measured the B meson cross section, which is a more directly experimentally measured quantity, using exclusive final states [14]. The use of exclusive final states improves the signal-to-background ratio greatly and removed most of the uncertainty due to decay modeling. The measurement is more sensitive to the bottom fragmentation fractions to given hadron types [15] than the inclusive measurements. The comparison to theory predictions still suffers from the uncertainty in the fragmentation modeling. The measured bottom meson cross section has a  $p_T$  shape consistent with theory, while the total cross section is measured to be a factor of 3 larger than the theory prediction. Recent theoretical papers [16, 17] suggest that the the disagreement between theoretical models and experimental measurements can be reduced by modifications to bottom fragmentation functions, discussed in section 2.4.

## 1.4 Theoretical Motivation for $b\bar{b}$ Angular Production Correlation Measurements

As stated in the previous section, the single differential cross section measurements (in  $p_T$  and rapidity) agree with the predicted shape from NLO QCD, but with a factor of 2–4 larger cross section relative to the theory. The disagreement may indicate the importance of higher order corrections or non-perturbative fragmentation of gluons into bottom quark

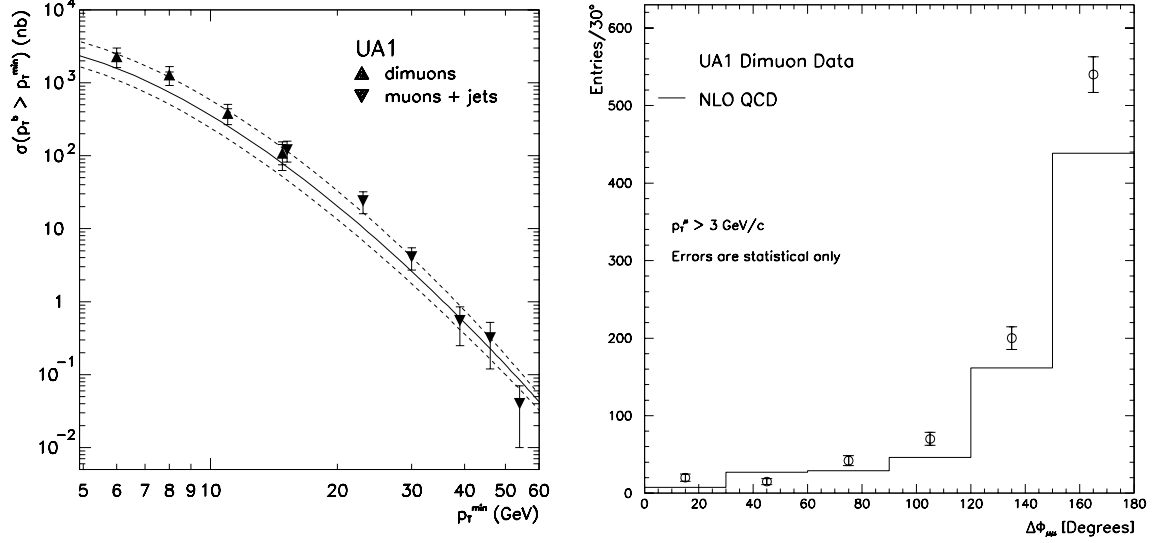


Figure 1.3: *Bottom production measurements at the  $Sp\bar{p}S$  ( $\sqrt{630}$  GeV) Left: UA1 measurements [10] of  $b$  quark integrated cross-section. Right: UA1  $\Delta\phi$  measurement [25] using  $\mu - \mu$ .*

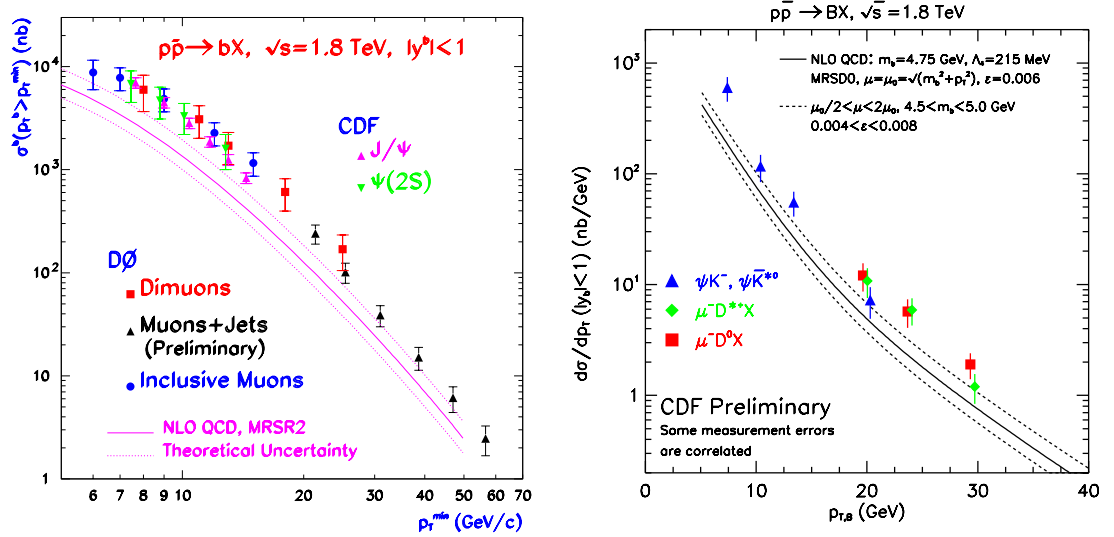


Figure 1.4: *Current ( $p_T$ ) cross section measurements of bottom production at the Tevatron. Left: D0 [11] and CDF [12] measurements of  $b$  quark integrated cross-section. Right: CDF [14]  $B$  meson differential cross-section.*

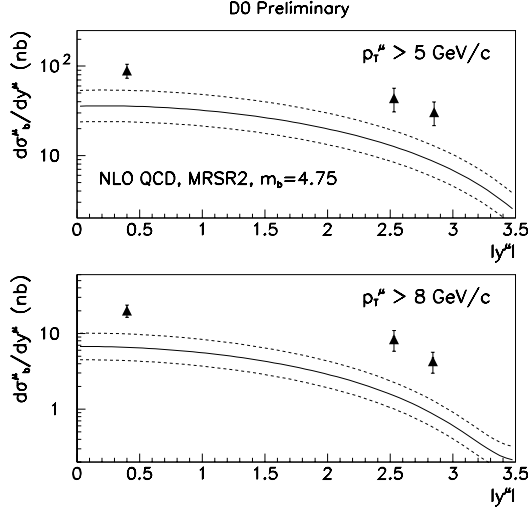


Figure 1.5: *Current single differential (rapidity) measurements of bottom production at the Tevatron (D0[13]).*

pairs [18]. The arguments for non-perturbative fragmentation effects are strengthened by the central values of the gluon splitting rates to bottom quark pairs measured by the LEP experiments and SLD [19], which are higher than the NLO predictions [20]. The errors on both the theory predictions and experimental measurements are large enough to explain the differences between the predictions and measurements.

In order to better understand the bottom quark production mechanisms, it is proposed in ref. [21, 22, 23] to measure correlations between the bottom quarks ( $\Delta p_T$ ,  $\Delta\phi$ ,  $R \equiv \sqrt{(\Delta\phi)^2 + (\Delta y)^2}$ ). Angular correlations are easier to experimentally measure than  $p_T$  correlations, because both bottom decays are not required to be fully reconstructed. In LO QCD, the bottom quarks are produced back-to-back, while the  $2 \rightarrow 3$  terms that first appear in NLO QCD allow the bottom quarks to be produced with any angular relationship [24]. Thus, a low  $\Delta\phi$  or  $R$  measurement ( $< \pi/2$ ) should be able to discern the effects of higher order perturbative or non-perturbative terms in bottom production.

For leading-log showering Monte Carlo, angular correlations are able to distinguish

between flavor creation, flavor excitation, and gluon splitting (fragmentation) terms. Figure 1.6 shows the PYTHIA predictions of  $\Delta\phi$  and  $R$  in ref. [21]. A measurement of low  $\Delta\phi$  and  $R$  will be able to distinguish between the three terms. Such a measurement can be used to tune the relative rates of the three mechanisms, which are relatively uncertain in showering Monte Carlos.

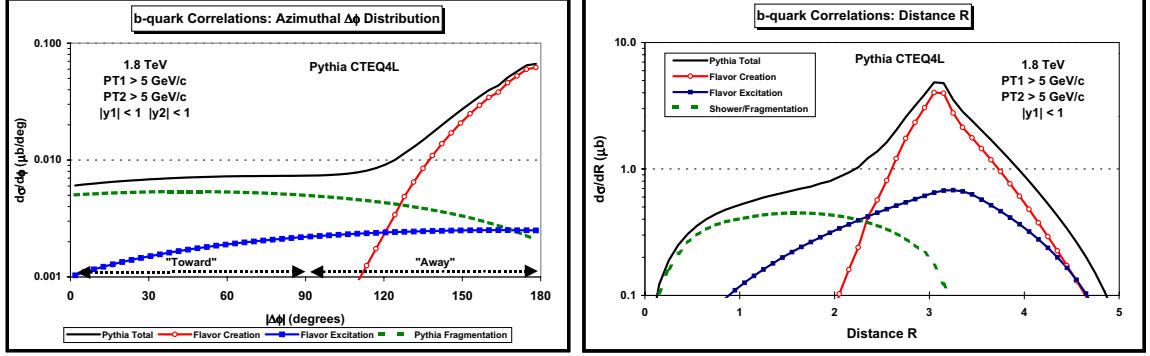


Figure 1.6:  $\Delta\phi$  and  $R \equiv \sqrt{\Delta\phi^2 + \Delta y^2}$  plots from ref. [21].

## 1.5 Past Experimental $b\bar{b}$ Angular Production Correlation

### Measurements Measurements at $p\bar{p}$ Colliders

Motivated by the lack of understanding of the differences between theoretical predictions and experimental measurements of the single differential bottom production cross sections, a series of  $b\bar{b}$  angular correlation measurements were made. The first bottom angular correlations at a hadronic collider was performed by the UA1 collaboration [25] in 1994 at the  $S\bar{p}\bar{p}S$  collider with  $\sqrt{s} = 630$  GeV. The measurements used the di-muon decay signature, in which both bottom quarks decay semi-leptonically. In order to minimize  $J/\psi$ , double sequential decay muons ( $b \rightarrow c\mu X; c \rightarrow \mu X'$ ), and Z muons, a di-muon mass cut of  $4 < M^{\mu\mu} < 35$  GeV was made. This mass cut also minimizes the acceptance of collinear

bottom quark pairs, biasing the  $\Delta\phi^{b\bar{b}}$  distribution measured. The analysis corrected for the varying acceptance versus  $\Delta\phi^{b\bar{b}}$ . The  $\Delta\phi$  shape is consistent with the theoretical prediction, but the prediction is 30 – 40% lower than the measurement. The fraction of the total bottom cross section for non-perturbative gluon fragmentation into  $b\bar{b}$  pairs was measured to be  $\sigma_{nonpert}(\Delta R(b\bar{b} < 1.6)/\sigma_{all}) < 11\%$  @90% c.l..

Similar measurements were carried out at the Tevatron with  $\sqrt{s} = 1800$  GeV. Both the D0 [26] and CDF [27] collaborations performed  $\Delta\phi$  measurements in the di-muon channel in the same manner as UA1. CDF’s measurement required a di-muon mass of  $M^{\mu\mu} > 5$  GeV, whereas D0’s analysis required a di-muon mass of  $6 < M^{\mu\mu} < 35$  GeV. Unlike the UA1 analysis, both D0’s and CDF’s analyses corrected the theory for the  $\Delta\phi$  bias due to the di-muon mass requirement, instead of correcting the data for the acceptance bias. The  $\Delta\phi$  shape in both D0’s and CDF’s analyses are consistent with NLO QCD predictions, but both analyses measured a factor of 2–3 excess in data relative to the theory predictions.

At CDF,  $\Delta\phi^{\mu,b}$  was measured between a muon (presumably from bottom quark decay) and a bottom quark jet identified using a jet probability algorithm (jetprob) [28]. The jet probability algorithm uses the impact parameters of particles in a jet with a cone size  $R=0.4$ ; it calculates the probability of a jet originating from the primary vertex. The jet and the muon was required be a separated by at least 1 in  $\phi$ – $\eta$  space, which again leads to a large non-uniformity in the acceptance versus  $\Delta\phi^{\mu,b}$ . The measurement shows a slight  $\Delta\phi$  shape disagreement and a factor of  $\sim 2$  excess relative to the NLO theory predictions.

Finally, a rapidity correlation measurement was performed by CDF measuring the ratio of a bottom quark being produced with  $2.0 < |y_1| < 2.6$  to  $|y_1| < 0.6$  when the second bottom quark is produced with  $|y_2| < 1.5$  [29]. The first bottom quark was identified with



a semi-leptonic decay to a muon and the second bottom quark was identified by a displaced vertex. The purity of the sample was determined by fitting the transverse momenta of the jet associated with the muon relative to the muon ( $p_{T_{rel}}$ ) and the pseudo decay length of the displaced vertex. The  $\Delta\phi$  between the muon jet and the displaced vertex was required to be greater than  $60^\circ$  in order to remove the contribution from gluon splitting. The ratio measured was consistent with theory.

The results of the measurements are summarized in table 1.3. The approximate  $f_{toward}$ , the fraction of  $b\bar{b}$  pairs produced with  $\Delta\phi^{b\bar{b}} < \pi/2$ , for both the measurements and theory predictions are shown, along with any requirements which yield a non-uniform efficiency versus  $\Delta\phi^{b\bar{b}}$ . The typical theory prediction of  $f_{toward}$  ranges between 16–19% if no  $\Delta\phi$  or  $M^{\mu,\mu}$  are made.

## 1.6 Motivation and Overview of this Analysis

This measurement is optimized to measure the region in phase space least understood in experimental measurements and theoretical predictions: small  $\Delta\phi$  where both bottom quarks point in the same azimuthal direction. As stated above, the previous bottom quark angular production measurements had little sensitivity to this region. The study of opposite side flavor tags using soft leptons (SLT) for the CDF  $\sin 2\beta$  measurement [30] show an unexpected distribution between fully reconstructed bottom decays and the soft leptons. Figure 1.8 shows the sideband  $\Delta\phi$  distribution between  $B^+ \rightarrow J/\psi K^+$  and  $B^0 \rightarrow J/\psi K^{0*}$  candidates, and the soft leptons. Between 30 – 50% of the soft leptons are in the same azimuthal hemisphere, a fraction much larger the expected from leading-log flavor creation Monte Carlo (  $\approx 5\%$  for PYTHIA).

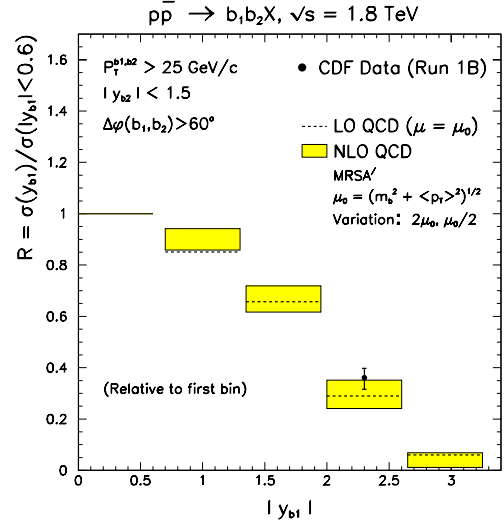
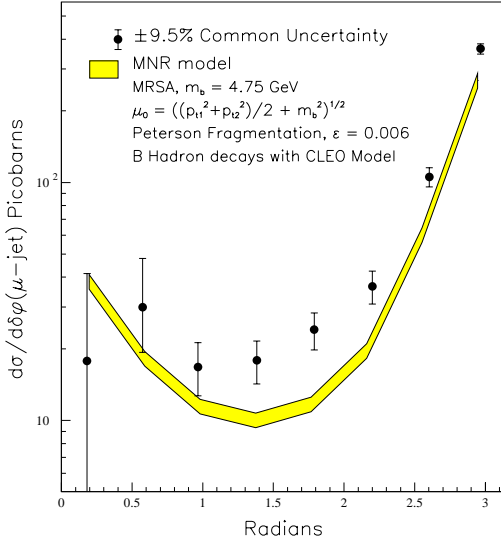
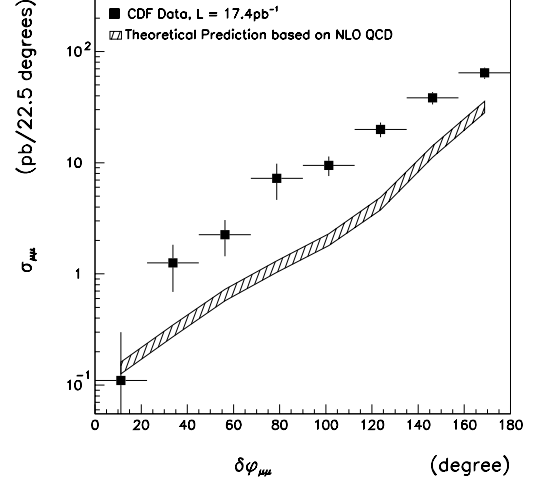
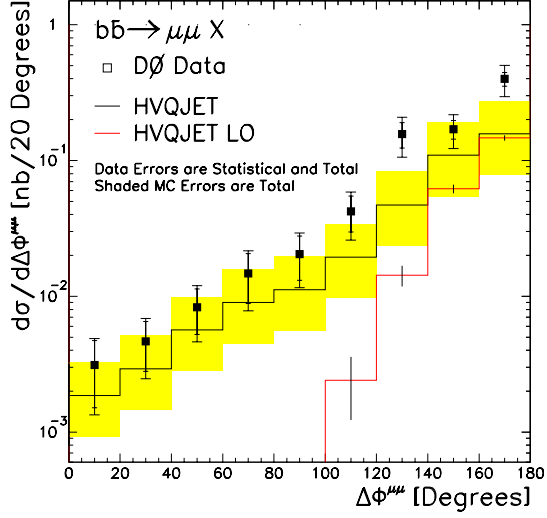


Figure 1.7: Current angular correlation measurements of bottom production at the Tevatron. Top Left:  $D0 \Delta\phi$  measurement [26] using  $\mu - \mu$ . Top Right: CDF  $\Delta\phi$  measurement [28] using  $\mu - \mu$ . Bottom Left: CDF  $\Delta\phi$  measurement [27] using  $\mu + \text{Jet}(\text{JetProb})$ . Bottom Right: CDF  $\Delta R$  measurement [29] using  $\mu + \text{Jet}(\text{SECVTX})$ .

Measurement	$b_{p_T}^1$	$b_{p_T}^2$	$b_y^1$	$b_y^2$
CDF $\Delta\phi^{\mu\mu}$	6.5 GeV	6.5 GeV	0.67	0.67
D0 $\Delta\phi^{\mu\mu}$	8 GeV	8 GeV	1.0	1.0
CDF $\Delta\phi^{\mu,jet}$	15 GeV	20.7 GeV	0.67	1.5
CDF $\Delta R^{\mu,jet}$	25 GeV	25 GeV	0.6	1.5
This Analysis $\Delta\phi^{\mu,J/\psi}$	7.0 GeV	6.0 GeV	0.67	0.61
This Analysis $\Delta\phi^{e,J/\psi}$	6.8 GeV	4.3 GeV	0.67	0.99
UA1 $\Delta\phi^{\mu\mu}$	6.0 GeV	6.0 GeV	2.3	2.3

Measurement	$f_{Toward}^{Exp}$	$f_{Toward}^{Theory}$	Additional Cuts
CDF $\Delta\phi^{\mu\mu}$	7.7%	4.4%	$M^{\mu\mu} > 5 \text{ GeV}^*$
D0 $\Delta\phi^{\mu\mu}$	5.1%	7.0%	$6 < M^{\mu\mu} < 35 \text{ GeV}^*$
CDF $\Delta\phi^{\mu,jet}$	13.4%	18.5%	$\Delta R^{\mu,jet} > 1.0$
CDF $\Delta R^{\mu,jet}$	N/A	18.5%	$\Delta\phi(tags) > 60^\circ$
This Analysis $\Delta\phi^{\mu,J/\psi}$			None
This Analysis $\Delta\phi^{e,J/\psi}$			None
UA1 $\Delta\phi^{\mu\mu}$	18.5%	16.6%	$4 < M^{\mu\mu} < 35 \text{ GeV}$

Table 1.3: Bottom angular correlation measurement quantities for this thesis and previous analyses. Top: Approximate bottom kinematics ( $p_{T_b}, y_b$ ) of measurement due to selection criteria. Bottom: The fraction of  $b\bar{b}$  pairs measured ( $f_{Toward}^{Exp}$ ) and predicted ( $f_{Toward}^{Theory}$ ) in the same hemisphere in the azimuthal angle,  $\Delta\phi < \frac{\pi}{2}$ . Additional cuts list the requirements which decreases the sensitivity of the measurement on the low  $\Delta\phi$  and low  $R$  regions. The \* indicates that the theory prediction corrected to the requirement, instead of correcting the data for the requirement.

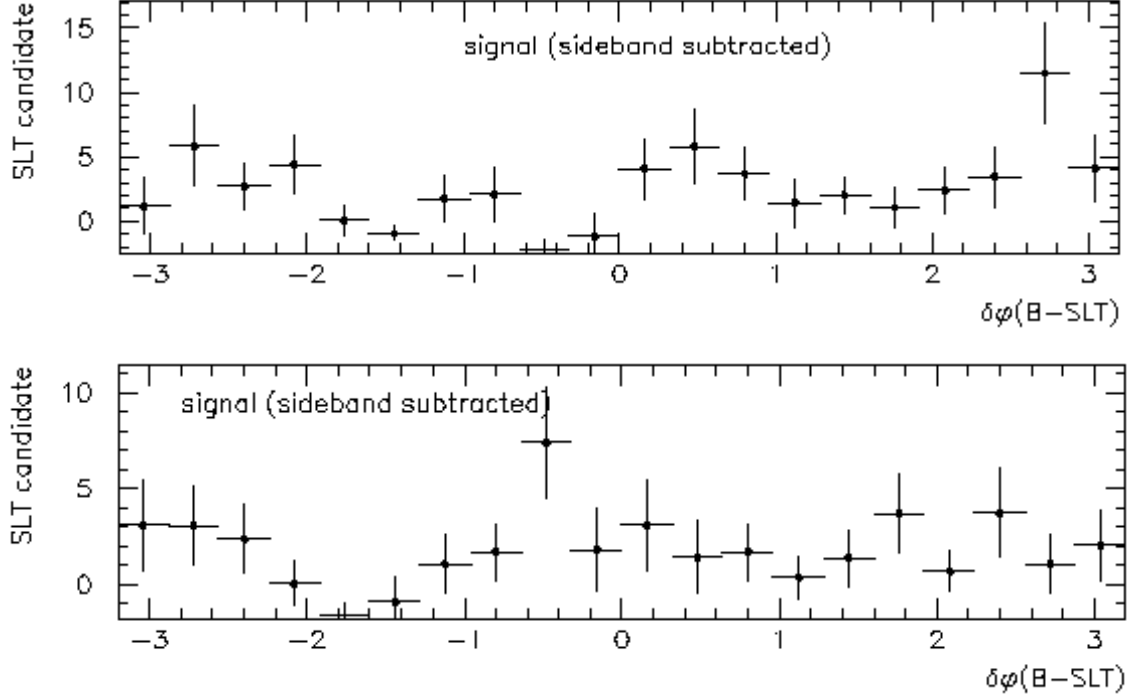


Figure 1.8: Sideband subtracted  $\Delta\phi$  distribution between fully reconstructed bottom mesons and soft leptons from ref. [30]. Top:  $B^+ \rightarrow J/\psi K^+$ . Bottom:  $B^0 \rightarrow J/\psi K^{0*}$ .

This analysis uses the bottom pair decay signature of  $b \rightarrow J/\psi X, \bar{b} \rightarrow \ell^+ X$ .<sup>2</sup> Angular requirements that were necessary in previous di-lepton measurements due to double sequential semi-leptonic decay ( $b \rightarrow c\ell X; c \rightarrow \ell X'$ ) are avoided by the chosen signal.  $B_c$  is the only particle that decays directly into  $J/\psi$  and an additional lepton. The only other source of candidates where the additional lepton and  $J/\psi$  candidates originate from the same displaced decay are hadrons that fake leptons or decay-in-flight of kaons and pions; the number of events from  $B_c$  or from 'fake' leptons can be estimated well by using techniques from ref. [31]. Thus, no angle requirement between the two candidate bottom decay products are necessary, yielding uniform efficiency over the entire  $\Delta\phi^{b\bar{b}}$  range.

Several properties of bottom decay are used to increase and measure the  $b\bar{b}$  purity of the sample. As stated above, the relatively large semi-leptonic signal is used to identify the

<sup>2</sup>Charge conjugate decays are assumed until explicitly disallowed.

non-trigger bottom decay. The long lifetime of the bottom quark is exploited to measure the purity of the sample. The impact parameter of the additional lepton and the pseudo- $c\tau$  of the  $J/\psi$  are fit simultaneously in order to determine the  $b\bar{b}$  fraction of the two  $\Delta\phi$  regions.

The selection criteria used in this analysis has similar bottom momenta and rapidity acceptances to CDF's Run II displaced track(SVT) [32] and  $J/\psi$  triggers, and the addition leptons have momenta very similar to the opposite side taggers planned for Run II (opposite kaon, opposite lepton and jet charge flavor taggers). Therefore, this measurement aids in the development and understanding of flavor taggers for such Run II measurements as  $\sin(2\beta)$  and the  $B_s$  mass difference.

Finally, measuring the fraction of bottom quark pairs produced in the same hemisphere  $f_{toward}$  minimizes systematic uncertainties. As the selection in both the  $\Delta\phi < \pi/2$  and  $\Delta\phi > \pi/2$  regions are the same, the uncertainties in the lepton selection efficiency, tracking efficiency, luminosity, etc. mostly cancel in the fraction measurement.

This thesis has the following organization. Chapter 2 gives a more detailed description of the theoretical prediction of bottom production at the Tevatron. Chapter 3 describes the accelerator complex at Fermilab and the portions of the Collider Detector at Fermilab (CDF) used in this analysis. Chapter 4 describes the  $J/\psi$  data set and the selection criteria for the analysis. In chapter 5, the  $f_{toward}$  fitting procedure is described including the determination of the  $c\tau$  and impact parameter shapes of the various signal and background sources, and estimates of the size of some backgrounds. The results of the fit in both the additional electron and muon samples are presented with an estimate of the systematic uncertainties. In chapter 6, the comparison between the theoretical predictions and the

measurements are shown for both leading-log showering Monte Carlo and NLO QCD theory.

Finally, chapter 7 includes the summary of the results.

## Chapter 2

# Theoretical Overview

In this chapter, a more formal description of the QCD prediction of bottom hadroproduction is given. First, the Factorization Theorem is described. Next, the three components (Parton Distribution Functions (PDF), the NLO parton cross section, and Fragmentation Function) used within the Factorization Theorem are discussed. Finally,  $k_T$  smearing, a modification of the NLO prediction which attempts to model the effects of multiple soft gluon radiation, is presented.

### 2.1 Factorization Theorem

The description of bottom production at hadron colliders using QCD includes two processes which involve the transfer of soft (low) momentum gluons. Within QCD theory, the proton is a complex multi-body object which consists of three valence quarks and a sea of virtual gluons and quark-antiquark pairs. The exchange of soft gluons within the proton prevents a first principles calculation of the internal state of the proton in perturbative QCD. Thus, the partons involved in the hard scatter (high momentum) process

are not well defined in perturbative QCD. Additionally, color confinement requires that the produced bottom quarks be hadronized, which also involves soft interactions that are also not calculable in perturbative QCD.

Fortunately according to the Factorization Theorem [33], the short distance parton scattering which produces the bottom quarks is separable from the long distance parton evolution within the proton and the long distance interactions of the partons within the bottom hadrons. Thus, the hard scatter is calculated by perturbative QCD, while the non-perturbative aspects of bottom hadroproduction are determined empirically from experimental measurements. The distribution of the partons' momentum fraction within the proton and hadronization process of the bottom quarks are assumed to be universal for a given quark species and only dependent on the momentum transfer ( $Q^2$ ) involved in the collision. Thus, these non-perturbative effects can be determined in measurements with less complicated experimental environments and/or theoretically precise predictions (such as  $e + e -$  colliders, fixed target experiments using hadronic targets and leptonic beams, and electroweak boson and high  $p_T$  jet production in hadronic colliders) and then applied to the theoretical prediction of bottom hadroproduction.

Schematically, the cross section to produce bottom hadrons C and D from the fragmentation of bottom antiquark  $\gamma$  and bottom quark  $\delta$  from the hard scatter of partons  $\alpha$  and  $\beta$  inside the proton A and antiproton B respectively is:

$$\sigma(p_A \bar{p}_B \rightarrow B_C \bar{B}_D) = \sum_{\alpha, \beta} f_{\alpha}^A(x_{\alpha}, \mu_F^2) f_{\beta}^B(x_{\beta}, \mu_F^2) \oplus \hat{\sigma}(\alpha\beta \rightarrow \bar{b}_{\gamma} b_{\delta}, \mu_R) \oplus F_{\gamma}(z_{\gamma}, \mu_H^2) F_{\delta}(z_{\delta}, \mu_H^2) \quad (2.1)$$

where:  $\oplus$  denotes a convolution integral,  $\hat{\sigma}$  is the parton cross section,  $f$  is the parton distribution function (PDF), and  $F$  is the fragmentation function. All three components



of the QCD prediction depend on the experimentally determined value of  $\Lambda_{QCD}$  used in the calculation, as the value of  $\Lambda_{QCD}$  sets the value of the QCD coupling strength  $\alpha_s$  at energy scale  $Q$ .

## 2.2 Parton Distribution Functions

Parton distribution functions describe the longitudinal momentum carried by the various partons in the proton.  $f_\alpha^A(x_\alpha, \mu_F)$  is the probability of a parton of flavor  $\alpha$  to have a momenta between  $x_\alpha P_{proton}$  and  $(x_\alpha + \delta x)P_{proton}$  at energy scale  $\mu_F$ . The PDFs change or 'evolve' as a function of the energy scale of the interaction because shorter distances within the proton are probed. As the energy of the probe increases, the effects of the emission of softer gluons from a quark and the splitting of gluons in  $q\bar{q}$  pairs are resolved. Therefore, the PDFs populate lower and lower regions of  $x$  as the factorization scale,  $\mu_F$ , increases. The evolution of the PDFs are determined by a set of equations, first described by Altarelli and Parisi [34], which are calculated in perturbative QCD to the same fixed order as the parton cross section.

As the PDFs are non-perturbative, the functional form of the PDFs are empirical and have to be fit from experimental measurements. As no one experiment is sensitive to all partons over the entire  $x$  region, the PDFs have to be determined by a global fit to wide range of experimental data. Two groups which perform such global analyses are the CTEQ [35] and MRST [36] collaborations. Both groups fit a set of PDFs to following type of experimental measurements:

- Deep Inelastic Scattering(DIS) of muons on nucleonic targets ( $\mu N \rightarrow \mu X$ ) at SLAC, FNAL, and CERN.

- DIS of muon neutrinos on nucleonic targets ( $\nu_\mu N \rightarrow \mu X$ ) at FNAL.
- DIS in electron–proton collisions ( $F_2^p$  and  $F_L$  proton form factors) at HERA.
- DIS of proton on nucleonic targets ( $pN \rightarrow \gamma X$  and  $pN \rightarrow \mu^+ \mu^- X$ ) at FNAL and CERN.
- DIS in proton–antiproton collisions (W asymmetry and  $p\bar{p} \rightarrow jet X$ ) at FNAL.

In this analysis, the CTEQ3L PDF is used in PYTHIA showering Monte Carlos and both the CTEQ5M and MRST99M PDFs are used in the NLO QCD theory prediction.

## 2.3 NLO Parton Cross Section

Unlike the light quark cross sections, the bottom quark cross section can be calculated at fixed order in perturbative QCD reliably as  $p_T^b \rightarrow 0$ . The bottom mass acts as a effective low momentum cut-off in the calculation. As  $m_B \gg \Lambda_{QCD}$ , the strong coupling  $\alpha_s$  is small ( $\alpha_s(m_B) \approx 0.24$ ) and therefore perturbative QCD should work well. Predictions to order  $\alpha_s^3$  have been calculated [37, 24]. Such calculations include the following subprocesses:

$$g + g \rightarrow b + \bar{b}$$

$$q + \bar{q} \rightarrow b + \bar{b}$$

$$g + g \rightarrow b + \bar{b} + g$$

$$g + q \rightarrow b + \bar{b} + q$$

$$g + \bar{q} \rightarrow b + \bar{b} + \bar{q}$$

$$q + \bar{q} \rightarrow b + \bar{b} + g$$

Figure 1.2 gives an example of some of the Feynman diagrams used in the NLO calculation. Virtual diagrams of  $\mathcal{O}(\alpha_s^4)$  interfere with the  $\mathcal{O}(\alpha_s^2)$  terms. The NLO order contributions to the cross section can be sizeable relative to the LO predictions. The cross section also depends on the renormalization scale ( $\mu^R$ ) used to evaluate the value of  $\alpha_s$ . The scale used is typically of order  $\sqrt{m_b^2 + (p_{T_b}^2 + p_{T_{\bar{b}}}^2)/2}$  which minimizes large logarithmic uncertainties at high  $p_T$ .

Nason, Dawson, and Ellis [37] first calculated the NLO inclusive single bottom differential cross section  $\frac{d^2\sigma}{dydp_T}$ . In the calculation, the kinematical variables of the  $\bar{b}$  quark are integrated over, and therefore correlations between the bottom quarks can not be calculated.

The NLO prediction of the full kinematics of bottom pair production has not yet been calculated in closed form. Mangano, Nason, and Ridolfi [24] have produced a fully exclusive parton cross section for heavy quark hadroproduction using numerical integration techniques. Soft and collinear divergences in the calculation are handled with careful organization of the integrals and the inclusion of large negative counter-terms. The calculation of the differential spectra is not predictive in the usual areas in phase space for  $\mathcal{O}(\alpha_s^3)$  calculations: when the radiated gluon is collinear with either of the bottom quarks or as the radiated gluon's momenta approaches zero. This condition occurs when  $p_T^{b\bar{b}} \rightarrow 0$ ,  $\Delta\phi^{b\bar{b}} \rightarrow \pi$ , and  $R > \pi$ . In such regions, negative differential cross sections are encountered due to the large negative terms originating from the virtual diagrams and the collinear subtractions. In such regions, the bins in the differential cross section should be widened until the predicted cross section is stable, i.e. the shape of the distribution has a fairly smooth second derivative. Positive only differential cross sections can only be guaranteed

with the inclusion of an arbitrary number of soft gluon emissions [38] (summation of the leading Sudakov logarithms), which at the time of the writing of this thesis has yet to be done.

## 2.4 Fragmentation

The principle of color confinement states that colored objects (such as bottom quarks) must bind with other quarks and gluons to produce a colorless object, or hadronize. Such hadronization processes involve soft gluons which have a typical scale of the size of hadrons,  $Q \sim 1/R_{had} \sim 300$  MeV. Due to the low  $Q^2$  of the process and the large value of  $\alpha_s$ , bottom quark hadronization is not described well by perturbation theory and has to be described by an empirical ansatz based on kinematical arguments that is tuned to experimental data. The function describing hadronization, the fragmentation function, is parameterized by the fraction of the bottom quark's momentum carried by the bottom hadron  $z = \frac{E(B)+p_{\parallel}(B)}{E_b+p_b}$  where:  $E(B)$  and  $p_{\parallel}(B)$  are the bottom hadron's energy and momentum parallel to the bottom quark direction and  $E_b$  and  $p_b$  are the bottom quark's energy and momentum. Many different fragmentation models and fragmentation functions exist. Two of the most common models used are independent [39] and string fragmentation [40].

### 2.4.1 Independent and string fragmentation models

Independent and string fragmentation models differ in how the hadronization process are treated. In independent fragmentation model, the hadronization is calculated as an incoherent sum of independent fragmentation processes for each of the partons. This model has the advantage of being easy to implement, but has a few weaknesses. Flavor, energy,

and momentum are not guaranteed to be conserved, as each parton is fragmented independently. In addition, the fragmentation procedure is not Lorentz covariant; hadronization depends on the frame in which the fragmentation is calculated. Momentum and energy conservation can re-established by various schemes of rescaling the momentum and energy of the generated particles. The Lorentz covariance problem can be circumvented by choosing the convention that the fragmentation process must always be done in the center-of-mass frame.

The problems of the independent fragmentation model are not present in the string fragmentation model (LUND model) in which the color of the parton is correctly taken into account. In this model, the energy contained in the color dipole made by two colored objects is assumed to increase linearly with separation between them,  $\sim \kappa l$  where  $\kappa \approx 1 \text{ GeV/fm}$  and  $l$  is the separation between the color charges. The energy between the two color charges is viewed as a one-dimensional 'string', which guarantees the Lorentz covariance of the fragmentation process. Once the energy in the string is sufficient to create a  $q\bar{q}$  pair, the string is 'broken' at its intermediate point. The probability of breaking the string is given by the quantum mechanical probability of tunneling through a potential barrier.

$$\frac{d^2\mathcal{P}}{dxdt} = \exp\left(-\frac{\pi m^2}{\kappa}\right) \cdot \exp\left(-\frac{\pi p_T^2}{\kappa}\right) \quad (2.2)$$

Due to the mass term in the tunneling potential, fragmentation to heavy quark pairs are suppressed.  $u : d : s : c \approx 1 : 1 : .3 : 1^{-11}$  In addition, the cutting of the string with a  $q\bar{q}$  pair guarantees momentum and energy conservation. The  $p_T$  of the quark formed in the tunneling is compensated by the antiquark in the pair. The fragmentation continues until all strings end with quarks and the quark-string-antiquark systems all have a mass below a cut-off value. For more information, see chapter 12 of ref. [41].

The next-to-leading order calculation of bottom production [37, 24] do not include the event's color connections and therefore only independent fragmentation can be used. PYTHIA uses the string fragmentation model.

### 2.4.2 Fragmentation functions

Many fragmentation functions exist which differ by the kinematic arguments used to derive them. Two commonly used fragmentation functions are by Peterson, et. al. [42] and by Bowler [43]. The fragmentation functions are assumed to be universal, to have no dependence on the incoming particle. Thus, fragmentation functions are tuned using measurements of  $e^+e^-$  collisions at the Z pole [44], where the measurement of the fraction  $z$  is most clean. The fragmentation functions evolve with the scale of the fragmentation ( $\mu_H$ ) in a manner similar to the PDFs. A set of equations, similar to the Altarelli–Parisi equations, governs the evolution of the fragmentation functions. These functions should be calculated to the same fixed order as the PDF and parton cross section.  $\mu_H$  is not typically discussed and is set to the same value as the renormalization/factorization scale. The  $\mu_H$  dependence of the fragmentation function is suppressed for the rest of this section.

The Peterson fragmentation function assumes that the energy lost by the heavy quark due to the light antiquark is small. The transition amplitude is determined by the energy difference between the incoming partons and the outgoing hadron. The function has one free parameter  $\epsilon_B$  which is determined experimentally. The Peterson fragmentation function is:

$$F(z) \propto \frac{1}{z(1 - \frac{1}{z} - \frac{\epsilon_B}{1-z})^2} \quad (2.3)$$

All of the previous bottom cross section measurements at Tevatron and  $S\bar{p}\bar{p}S$  have used the Peterson fragmentation functions with independent fragmentation. The Peterson pa-

parameter used in the previous analyses was given in ref. [45] as  $\epsilon_B = 0.006 \pm 0.002$ .  $\epsilon_B$  was extracted using LO perturbation theory with leading-log resummation of large transverse momentum logarithms. As discussed in ref. [46], this value of the Peterson parameter is only appropriate for leading order QCD and leading-log shower Monte Carlos (such as PYTHIA) predictions. As the theoretical predictions in the previous analyses used NLO QCD, the  $\epsilon_B$  used was too large. At next-to-leading order, hard gluon radiation is included in the hard scatter calculation, which decreases the fraction of energy lost in the fragmentation process relative to the leading order calculation. Ref. [46] calculated that a Peterson parameter of  $\epsilon_B = 0.0016\text{--}0.0033$  is appropriate when using NLO QCD cross section predictions. The value is consistent with the  $\epsilon_B \approx 0.002\text{--}0.004$  found in the individual  $e^+e^-$  measurements [44]. According to Cacciari and Nason [16], a fixed order fit to the moments to the Peterson fragmentation function with the addition of next-to-leading logarithm summation reduces the disagreement between the experimental measurement of ref. [14] and the theory prediction from a factor of 2.9 to  $1.7 \pm 0.5$  (expt)  $\pm 0.5$  (theory)

The Bowler fragmentation function is a modification of the LUND fragmentation model which includes the effect of the heavy quark mass. The probability of cutting the string is constant per unit length of the string and unit time. The Bowler fragmentation function is the default function used for heavy flavor in PYTHIA. The Bowler fragmentation function is:

$$F(z) \propto \frac{1}{z^{1+r_b m_t^2}} (1-z)^a \exp\left(-\frac{b m_t^2}{z}\right) \quad (2.4)$$

The quality of the fits of the fragmentation functions to the experimental measurements have been collated by ref. [17]. The Bowler fragmentation function has the best quality of fit of the seven fragmentation functions used. The Peterson fragmentation function is too

broad and has a much lower  $\chi^2$  probability than the Bowler fragmentation function. This analysis uses the Bowler fragmentation function to extrapolate between bottom meson and quark kinematics.

## 2.5 $k_T$ Smearing

As stated in ref. [24], a positive differential cross section for arbitrarily small  $p_T^{b\bar{b}}$  can only be achieved by the resumming the full series of Sudakov logarithms [38], which corresponds to the emission of arbitrarily large number of initial state gluons. Such a resummation has yet to be performed on the NLO QCD prediction of bottom quark production. The resummation of the Sudakov logarithms can be approximated using a  $k_T$  smearing technique. The soft gluons are assumed to generate an initial state parton transverse momenta ( $\vec{k}_T$ ). The average value of the magnitude of the parton transverse momenta ( $\langle k_T \rangle$ ) grows with the  $\sqrt{s}$  of the proton collision. The  $\langle k_T \rangle$  may depend slightly on the process measured and the center-of-mass energy of the initial state partons ( $\sqrt{\hat{s}}$ ), but will still be of the same order of magnitude. At the Tevatron's center-of-mass energies, a  $\langle k_T \rangle$  of 3–4 GeV at  $\hat{s} > 20$  GeV is expected. The  $\langle k_T \rangle$  expected at the Tevatron is supported by the  $p_T^{\gamma\gamma}$  of D0 [47] and CDF [48], shown in figure 2.1. The NLO calculation (without  $k_T$  effects) does not describe the spectrum well. PYTHIA, which includes  $k_T$  effects, describes the data well. The average  $p_T$  of the di-photon system is consistent with 3–4 GeV.

The results of predictions which include  $k_T$  smearing effect are model dependent. The implementation of the  $k_T$  smearing in this thesis is similar to ref. [49]. The size of each parton's initial state momentum is assumed to a Gaussian of the form:



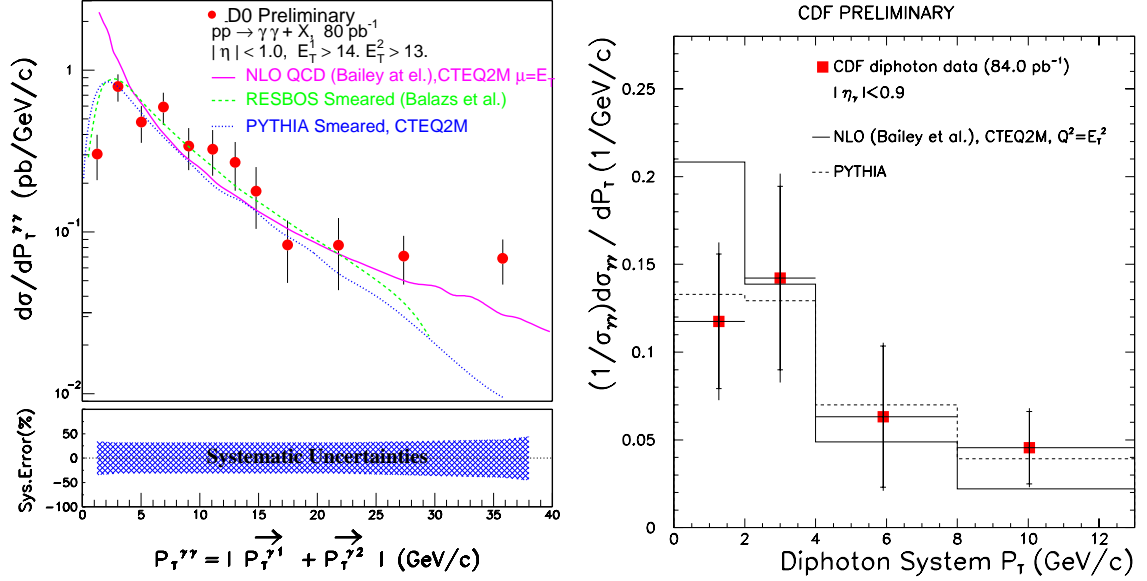


Figure 2.1: Di-photon system transverse momenta. Left: D0 [47]. Right: CDF [48].

$$g(\vec{k}_T) = \frac{e^{-k_T^2/\langle k_T^2 \rangle}}{\pi \langle k_T^2 \rangle} \quad (2.5)$$

The phi direction of the  $k_T$  is random for the two initial state partons. In ref. [49], the Gaussian assumption of the  $k_T$  smearing is shown to be consistent with direct photon production at fixed target and collider experiments at the Tevatron, and fixed target experiments at CERN. The effects of  $\langle k_T^2 \rangle$  on this analysis are discussed in more detail in chapter 6.

## Chapter 3

# Experimental Apparatus

This thesis studies the azimuthal correlations between bottom hadrons produced in  $p\bar{p}$  collisions in the Tevatron accelerator at Fermilab. The decay products of the bottom hadrons are measured using the Collider Detector at Fermilab(CDF). This chapter provides a brief description of the accelerator complex at Fermilab and of the portions of the CDF detector used in this analysis.

### 3.1 The Accelerator Complex

Proton-antiproton collisions at Fermilab are made possible by a series of seven accelerators, culminating in the Tevatron. The Tevatron is currently the world's highest energy accelerator; during the data taking period relevant for this analysis, it produced  $p\bar{p}$  collisions with a center of mass energy of  $\sqrt{s} = 1.8$  TeV. Figure 3.1 shows a schematic of the accelerator complex at Fermilab.

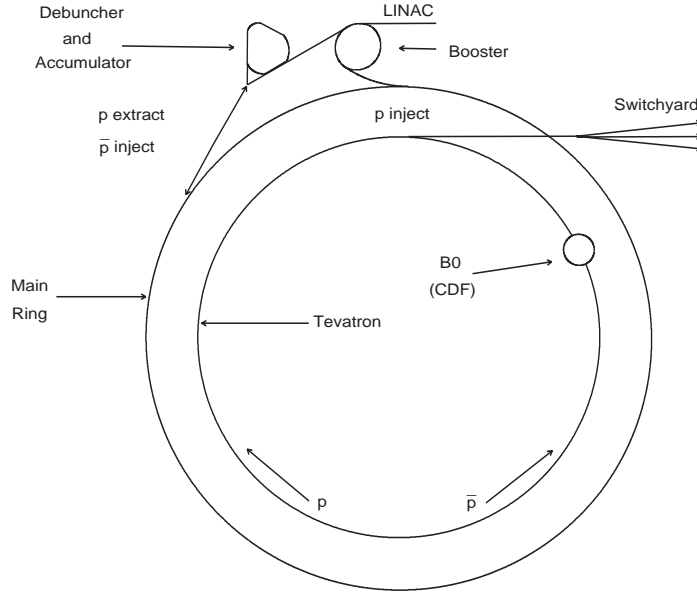


Figure 3.1: *The Fermi National Accelerator Complex.*

### 3.1.1 Proton acceleration

The process of proton acceleration [50] begins with a bottle of molecular hydrogen.  $H^-$  is extracted from the molecular hydrogen with a magnetron source. A 750 KeV electric potential is applied to the resulting ions by a Cockroft-Walton power supply, accelerating the hydrogen ions into a 150 m Linac. The Linac [51] consists of a series of 11 copper RF cavities. A potential difference is applied to alternating cavities, which accelerates the hydrogen ions to 400 MeV. At the end of the Linac, a copper foil strips the electrons from the proton, leaving a bare proton. The protons are then injected into the Booster, an alternating gradient synchrotron with a 475 meter circumference. The Booster accelerates the protons to 8 GeV and then directs them into the Main Ring. The Main Ring was the original, large accelerator at Fermilab; it is a synchrotron with a radius of 1000 meters and accelerates the protons up to 150 GeV. The Tevatron [52] is the last step in proton acceleration and lies directly below the Main Ring. Unlike the previous accelerators, the Tevatron

employs NbTi super-conducting magnets, cooled with liquid helium. The superconducting magnets produce a larger 4.4 Tesla magnetic field, which allows for a larger acceleration than the Main Ring. In colliding mode, the Tevatron accelerates the protons up to 900 GeV.

### 3.1.2 Anti-proton production

Anti-proton [53] production begins by extracting the 120 GeV proton beam from the Main Ring and directing it onto a nickel target. In the resulting nuclear interactions, anti-protons are produced, approximately 1 for every  $10^5$  protons on target. The resulting spray of particles is focused by a cylindrical Lithium lens with an 0.5 MA pulsed axial current. The particles are then filtered by a pulsed di-pole magnetic spectrometer resulting in a 8 GeV beam of anti-protons.

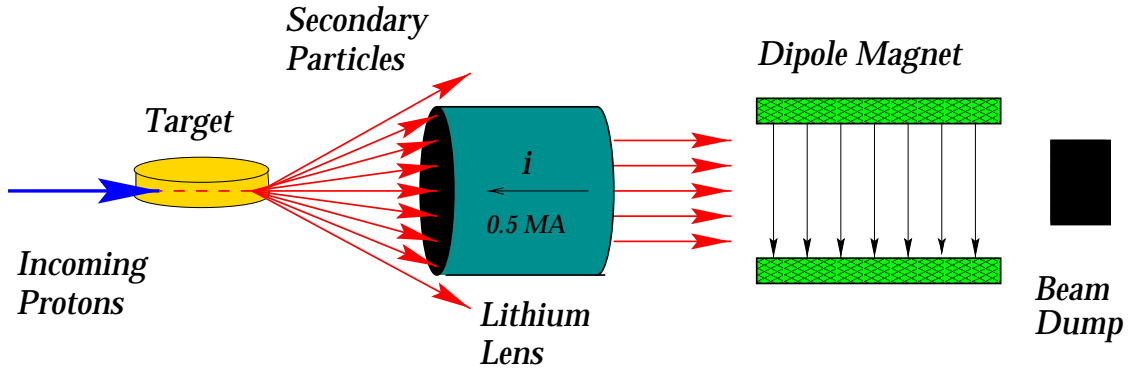


Figure 3.2: *Schematic of anti-proton production.*

The beam of anti-protons is directed to the Debuncher [54], one of two rounded triangular synchrotrons which make up the anti-proton source. The Debuncher reduces the momentum spread of the anti-protons by bunch rotation and stochastic cooling techniques [55]. The cooling process turns narrow bunches with a large momentum spread into a broad beam with a small momentum spread.

Once cooled, the beam is injected into the Accumulator [56], which is co-centric with the Debuncher. Anti-protons are added to the Accumulator at the rate of  $7 \times 10^{10}$ /hour, until enough anti-protons are stored to begin setup for collision. At that point, the anti-protons are loaded into the Main Ring, and eventually the Tevatron for acceleration.

### 3.1.3 Collisions

To begin collisions, the Tevatron is first filled with 6 bunches of proton from the Main Ring; each bunch has  $\sim 2.5 \times 10^{11}$  protons. Next, 6 bunches of anti-protons ( $\sim 7.5 \times 10^{10}$ /bunch) are added to the Main Ring. The anti-protons are accelerated to 150 GeV and then injected into the Tevatron. The 6 bunches of protons and anti-protons are then accelerated in the Tevatron to beam energies of 900 GeV. The beams are focused at the CDF and D0 detector sites with a low  $\beta$  quadrupole magnets and made to collide. The instantaneous luminosity decreases exponentially during the run due to beam losses from collisions, and beam de-focusing from beam-beam interactions. After about 20 hours, the beams are dumped and acceleration process begins again.

The bunches during collision have a longitudinal width of 50 cm, but due to their hour-glass shape, the luminous region only has a longitudinal width of 30 cm. The transverse width the luminous region is  $\approx 30 \mu\text{m}$ . Beam crossings occur every  $3.5 \mu\text{s}$  with  $2.7 \bar{p}p$  inelastic collisions per beam crossing. The instantaneous luminosity is given by

$$\mathcal{L} = \frac{f N_p N_{\bar{p}} B}{4\pi\sigma_t^2} \quad (3.1)$$

where  $f$  is the revolution frequency,  $B$  is the number of bunches, and  $\sigma_t$  is the transverse beam size.

This study uses  $86.5 \pm 3.5 \text{ pb}^{-1}$  of data collected during Run Ib of the Tevatron, between

January 1994 and July 1995. The average and instantaneous luminosity of the Tevatron during that time period [57] was  $1.6 \times 10^{31} \text{ cm}^{-2}\text{s}^{-1}$  and  $2.5 \times 10^{31} \text{ cm}^{-2}\text{s}^{-1}$ , respectively.

## 3.2 The CDF Detector

CDF is a general-purpose detector located at the B0 interaction point of the Tevatron. It is cylindrically symmetric around the beam axis and forward-backward symmetric about the interaction region. It is designed to make precise position, momentum, and energy measurements of particles originating from the proton–anti-proton collisions and their decay products. This section describes the Run 1b configuration of the CDF detector, focusing on the systems that were vital to this analysis. A more complete description of the detector is available [58], but it pre-dates installation of upgrades in 1992 and 1994.

CDF uses an right-handed coordinate system.  $\hat{x}$  points away from the center of the Tevatron (north),  $\hat{y}$  points upward, and  $\hat{z}$  points along the proton beam direction (east). Due to CDF’s geometry, it is convenient to use a cylindrical coordinate system where  $r$  is the distance from the  $z$ -axis,  $\phi$  is the azimuthal angle where 0 radians lie along the  $x$ -axis, and  $\theta$  is the polar angle relative to the  $z$ -axis.

Rapidity ( $y = \frac{1}{2} \ln(\frac{E+p_z}{E-p_z})$ ) is relativistically invariant for boosts along the beam axis, and occurs in phase space descriptions at proton-antiproton colliders. In the ultra-relativistic limit, rapidity is approximated by a purely geometrical variable, pseudo-rapidity ( $\eta = -\ln(\cot \frac{\theta}{2})$ ).

The CDF detector (shown in 3.3) consists of various nested subsystems, described in sections 3.2.1–3.2.7. Nearest to the interaction region, a set of tracking systems measure the trajectory of charged particles. It consists of silicon micro-vertexing chamber (SVX’), a

time-projection chamber (VTX), and a multi-wire drift chamber (CTC). The entire tracking system is contained in a super-conducting solenoidal magnet. Next, a series of calorimeters measure the energy of the particles. The central electromagnetic calorimeter (CEM) measures the energy of photons and electrons, which have electro-magnetic interactions with material. The hadronic calorimeter, which measures the energy of strongly interacting particles, is broken up into two sections, the central (CHA) and end-wall (WHA) calorimeters. The muon systems are located outside of the calorimeters, which are used as absorbers. The central muon system (CMU) lies directly behind the central calorimeters. In 1992, the Central Muon Upgrade (CMP) and the Central Muon Extension (CMX) were added to the detector to improve the purity and coverage of the muon systems.

Charged particles' trajectories are helixes because of the magnetic field. The CDF collaboration uses the following helix parameters:  $c$ ,  $\phi_0$ ,  $d_0$ ,  $z_0$ , and  $\lambda$ .  $c$  is the track curvature and defined to be positive for positively charged particles.  $\phi_0$ ,  $d_0$ , and  $z_0$  are respectively the azimuthal angle, the distance in the  $r$ - $\phi$  plane, and the  $z$  position of the track at the closest approach to the  $z$ -axis.  $\lambda$  is equal to  $\cot\theta$ .

### 3.2.1 Silicon Vertex Detector

The primary purpose of the Silicon Vertex Detector (SVX') is to improve of the measurement of the impact parameter of tracks, which allows for the detection of displaced vertices from the decay of heavy flavor. The SVX' [59] is a 4-layer 46000 channel solid-state micro-strip detector.

A silicon sensor is the charge-sensitive element of the detector. It is a wafer of  $n^-$ -type doped silicon that is 8.5 cm long and 300  $\mu\text{m}$  thick. Using modern lithography technology, finely spaced  $p^+$  implants strips are made on one side of the wafer in the

Figure 3.3: *A r-z Quadrant Schematic Cross-section of the Collider Detector at Fermilab.*

direction parallel to the beam, defining the sensor's channels. The silicon system only provides  $r$ - $\phi$  information. Over the implant, a thin 200  $\mu\text{m}$  silicon oxide layer and a thin aluminum strip are placed, creating a capacitor. The readout electrics are connected to the aluminum strip. The other side of the wafer has a thin layer of  $n^+$  doping introduced, creating a diode. An 80 V potential difference is placed between the  $n^+$  plane and  $p^+$  strips, which reverse biases the diode and creates an area of high electric field, free of space charge. When a particle traverses the sensor, mobile charge carriers (electron-hole pairs) are formed for every 3.6 eV deposited along the path of the particle. A minimum-ionizing particle traversing perpendicular to the silicon surface creates about 22,000 electron-hole pairs. The electrons and holes drift along the electric fields, creating currents in the AC-coupled aluminum readout strips. The drift time to the implant is 10-30 ns, which is much less than the collision rate.

The position resolution of the SVX' is predominately determined by the pitch (spacing)



between the readout strips. The first three layers of the SVX' have a  $60\text{ }\mu\text{m}$  readout pitch and the outer layer has a  $55\text{ }\mu\text{m}$ . The position resolution is improved by using a weighted average of the amount of charge collected on neighboring strips. 1, 2, and 3 strip hits have a resolution of 13, 11, and  $19\text{ }\mu\text{m}$  respectively.

Shown in figure 3.4, the electrical and mechanical unit of the SVX' is the ladder. The ladders is made of 3 silicon sensors, a readout hybrid, and a mechanical support structure. The 3 silicon sensors are connected end-to-end by aluminum wire bonds, creating 25.5 cm long channels. The sensors are supported on a Rohacell foam backing with carbon fiber support ribs. The hybrid readout circuit is made on an Aluminum-Nitride substrate. Called an ear board, the hybrid circuit is mounted on one end of the ladder. The ear board holds the readout integrated circuits, and routes and filters power, command, and data lines. The other end of the ladder has a precision alignment tab.

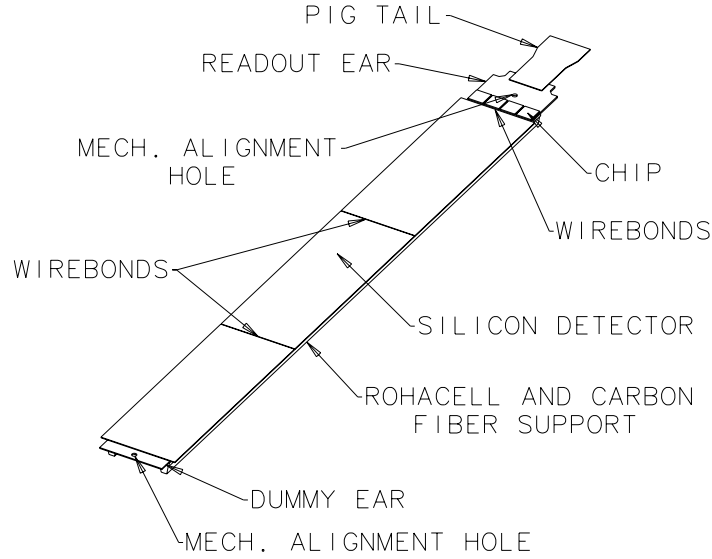


Figure 3.4: *Schematic of a SVX' Ladder.*

The SVX integrated circuit, the SVXH, is a mixed analog-digital device built in  $1.2\text{ }\mu\text{m}$  CMOS technology, which is able to withstand more than 1 MRad of radiation. The

chip's radiation hardness along with the change to AC-coupled sensors allows the SVX' to function much longer than the previous SVX detector. To reduce the event's data size, only channels (and their neighbors) above a chosen threshold are read out. The pre-amplifiers are run in double-sample and hold mode, in which the charge is only integrated 'on-beam'. The signal-to-noise ratio of the SVXH was 15:1.

The ladders are assembled into two barrels, shown in figure 3.5. The two barrels are placed around the interaction point with a 2.15 cm gap between them. A barrel is made up of two Beryllium bulkheads, which positions the ladders precisely. The ear board are placed at the large z end. Each barrel is made up of 4 layers with mean radii of 2.94 cm, 4.37 cm, 5.84 cm, and 8.07 cm, respectively. Each layer consists of 12 ladders. The ladders are given a  $4.5^\circ$  tilt along the longitudinal axis in order to overlap ladders in the same layer. As the active length is 51 cm and the interaction region has a width of 30 cm in z, SVX' only covers  $\sim 60\%$  of the interaction region.

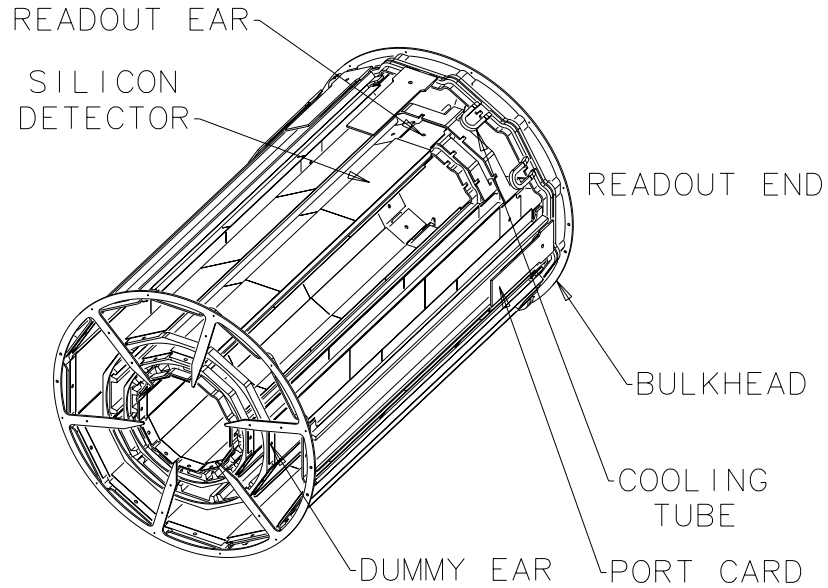


Figure 3.5: *Schematic of a SVX' barrel.*

The impact parameter resolution of the tracks depends on four components: the position resolution of the silicon sensors, the geometry of the detector, the alignment of the detector and the material in the detector. The radii of the ladders and their single hit position resolution sets the absolute scale on the impact parameter resolution. Alignment imperfections degrade the impact parameter resolution further. Detector material causes multiple scattering of the particle, which also decreases the impact parameter resolution. The effect of multiple scattering is inversely proportional to the particle's transverse momentum. The SVX' has about 3% of a radiation length of material for normal incident particles. The impact parameter resolution of combined SVX+CTC tracks is  $(19 \mu\text{m} \oplus \frac{33 \mu\text{m}-\text{GeV}}{p_T})$ . The first term is due to single hit position resolution, detector geometry and alignment. The second term describes multiple scattering effects.

### 3.2.2 Vertex Tracking Chamber

The Vertex Tracking Chamber (VTX) is a time-projection chamber. Its primary purpose is to provide r-z tracking information, which is used to determine the z coordinate of the inelastic interactions for each event and to seed the r-z fit in the drift chamber. It consists of 28 octagonal modules, each 9.4 cm in length. Adjacent modules are rotated by  $11.25^\circ$  in  $\phi$ . As shown in figure 3.6, each module has two drift regions, separated by an aluminum high voltage grid. Near the cathode, sense wires oriented tangentially in the r-z view are used to measure the drift time and therefore the z position of the track. In modules with  $|z| < 85$  cm, there are 16 sense wires between r of 11.5 cm–21.0 cm; modules with  $85 \text{ cm} < |z| < 132$  cm have 24 sense wires between r of 6.5 cm–21 cm. The VTX measures the z position of the primary vertex with a 2 mm resolution.

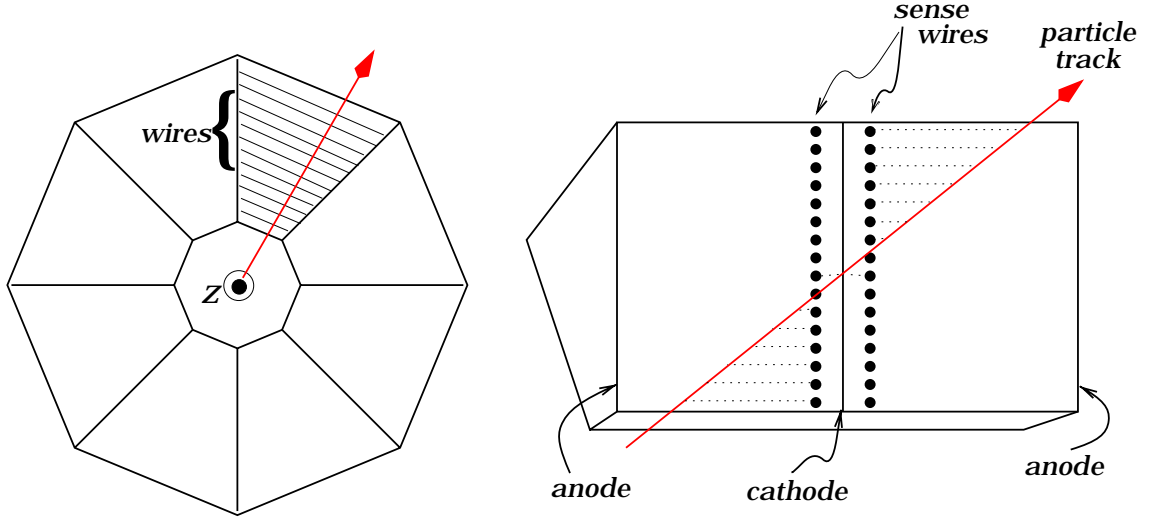


Figure 3.6: *Schematic of a VTX module.*

### 3.2.3 Central Tracking Chamber

The Central Tracking Chamber (CTC) [60] is a 6156 channel, multi-wire cylindrical drift chamber. It measures charged particles trajectories in the region  $0.3 \text{ m} < r < 1.3 \text{ m}$  and  $|z| < 1.6 \text{ m}$ . The chamber, shown in figure 3.7, is organized in 9 'super-layers'. Each super-layer is divided into cells, a set of sense (anode) wires bounded on both sides by rows of field (cathode) wires. 5 of the super-layers have cells with 12 sense wires parallel (axial) to the beam axis, providing  $r$ - $\phi$  tracking information. Interspersed between the axial super-layers are 4 'stereo' super-layers, where the wires are tilted  $\pm 3^\circ$  relative to the beam axis. These layers have 6 sense wires per cell, and provide some  $r$ - $z$  tracking information.

The cells are tilted  $45^\circ$  with respect to the radial direction in order to match the Lorenz angle of the drift electrons; the cells' tilt is chosen so that the drift electrons' trajectories are in the azimuthal direction. The tilted cell geometry ensures that at least one wire per super-layer will have a short ( $< 80 \text{ ns}$ ) drift time, which is used in the level 2 track trigger

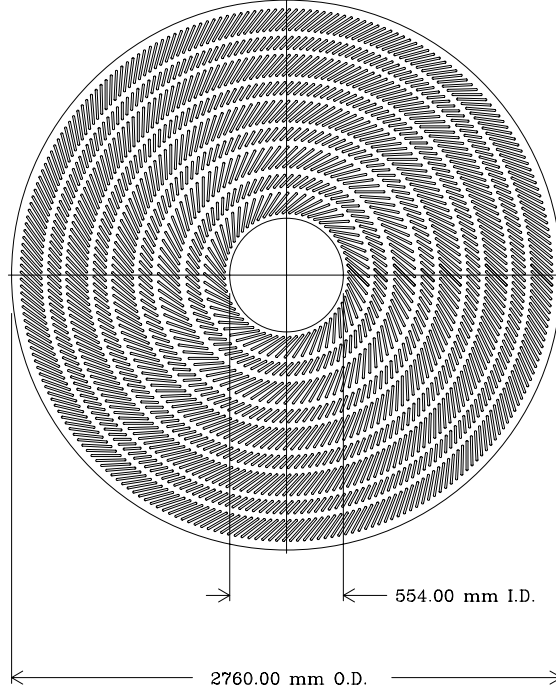


Figure 3.7: *Schematic of a CTC end-plate.*

(see section 3.2.7). The maximum drift time is 800 ns. The hit residuals in the  $r$ - $\phi$  plane vary from  $250\text{ }\mu\text{m}$  in the inner layers to  $160\text{ }\mu\text{m}$  in the outer layers. The  $r$ - $z$  resolution for the stereo super-layers is  $1/\tan(3^\circ)$  larger. In Run 1b, the CTC had the following tracking resolution stand-alone:  $\frac{\sigma_{p_T}}{p_T^2} = 0.1\%$ ,  $\sigma_{d_0} = 0.07\text{ cm}$ , and  $\sigma_{z_0} = 1.0\text{ cm}$ .

In addition, super-layers 4, 6, and 8 are instrumented with electronics that discriminates pulse width (TDC). The pulse width is proportional to the amount of energy deposited in the drift cell by the charged particle ( $dE/dx$ ), which is a function of the  $\beta\gamma$  of the particle. Once calibrated [61], the  $dE/dx$  is an effective tool for distinguishing electrons from hadrons in the momentum region of this thesis.

### 3.2.4 Calorimetry

Calorimetry is used to measure the energy of incident particles. The central calorimeters ( $|\eta| < 1.1$ ) consist of projective towers (“points” back to the nominal interaction point) of size  $\Delta\eta \times \Delta\phi = 0.1 \times 15^\circ$ , shown in figure 3.8 . The calorimeter is broken up into two sections in radius. The section at lower radius is designed to measure electromagnetic showers. At higher radius, the calorimeter is optimized for hadronic showers.

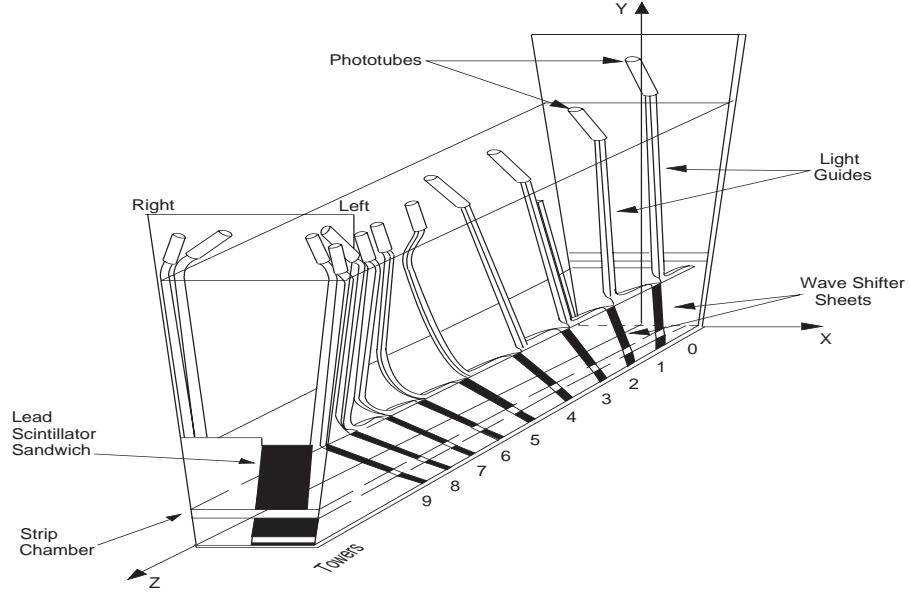


Figure 3.8: *Schematic of a calorimeter tower.*

#### Central Electromagnetic Calorimeter

The Central Electromagnetic Calorimeter [62] (CEM) is a sampling calorimeter consisting of a stack of 1/8" thick lead plates interspersed with 5 mm thick polystyrene scintillators. Electrons and photons incident on the calorimeter interact with the lead producing showers of photons and electrons. The resulting electrons produce blue light in the scintillators. The total amount of light observed is proportional to the energy of the initial

electron or photon. The light is collected by acrylic wavelength shifters at both azimuthal tower boundaries and is guided to photo-multiplier tubes. In order to maintain a constant radiation thickness of  $X_0 = 18$  as a function of  $\eta$ , layers of lead are replaced with acrylic. At  $|\eta| = 0.06$ , there are 30 layers of lead; at  $|\eta| = 1.0$ , there are only 20 layers of lead.

The calorimeter is constructed in 4 arches, each which contain 12  $15^\circ$  wedges. A wedge is made up of 10 towers each. The wedges' edges have low response and cannot be used for electron identification. The energy resolution for electrons is  $\sigma_E/E = 13.5\%/\sqrt{E \cdot \sin(\theta)} \oplus 1.5\%$ . The first term is the 'stochastic' term which depends on shower fluctuations and PMT photo-statistics. The second term is the 'constant' term is due to calibration uncertainties.

At the approximate shower maximum ( $5.9 X_0$ , including the solenoid), the Central Strip Chambers (CES) measure the shower position and transverse shower development. It consists of proportional chambers with anode wires parallel to the beam and segmented cathodes in the z direction. The wires and cathodes provide measurements of position with a resolution of 0.22 cm in the azimuthal direction and 0.46 cm in the z direction. The CES shower shape and position are useful for electron-hadron separation.

Another tool for electron identification is the Central Pre-radiator (CPR); a multi-wire proportional chamber with  $r$ - $\phi$  information only. The CPR samples the early development of electron magnetic showers, using the solenoid as a pre-radiator. The charge collected is used to distinguish between electrons and other particles.

### **Central and End-wall Hadronic Calorimeter**

The Central Hadronic (CHA) and End-wall Hadronic (WHA) Calorimeters [63] are made up of layers of 2.5 cm thick steel sandwiched between 1 cm thick plastic scintilla-

tor. The calorimeter is 4.7 interaction lengths thick. The energy resolution is  $\sigma_E/E = 50.0\%/\sqrt{E \cdot \sin(\theta)} \oplus 3\%$ . In this analysis, the hadronic calorimeter are not used to measure the energy of hadrons. Instead, it is used as a veto for the identification of electrons and an absorber for the muon systems.

### 3.2.5 Central muon detectors

Muons, due to their larger mass, produce much less bremsstrahlung than electrons and therefore do not produce electromagnetic showers. The CDF muons systems use this property by placing detectors behind enough material that only muons have a large likelihood of penetrating the material. The central muon systems consist of three separate subsystems: the original Central Muon Chambers (CMU) [64] built in 1988, and two upgrades [65], the Central Muon Upgrade (CMP) and the Central Muon Extension (CMX), built in 1992. The CMU covers 84% of the solid angle with  $|\eta| < 0.6$ . The CMP covers 63% of the solid angle with  $|\eta| < 0.6$ , with 53% of the solid angle covered by both systems. The CMX covers 71% of the solid angle between  $0.6 < |\eta| < 1.0$ . A schematic of the muon coverage is shown in figure 3.9.

The CMU lies directly outside of the central electromagnetic and hadronic calorimeters at a radial distance of 3.47 m. It is made up of 12  $12.6^\circ$  wedges in  $\phi$  with  $2.4^\circ$  gaps in between the wedges. There are 3 modules per wedge, each consisting of a  $4 \times 4$  grid of rectangular drift cells, shown in figure 3.10. Each drift cell has a  $50 \mu\text{m}$  sense wire running down the middle. Drift time is used to find the  $\phi$  position of the track's intersection and charge division is used for the z measurement. The cells have a  $250 \mu\text{m}$  resolution in  $\phi$  and a 1.2 mm resolution in z.

The CMU has a large fake rate due to non-interacting 'punch-through' hadrons. Fig-



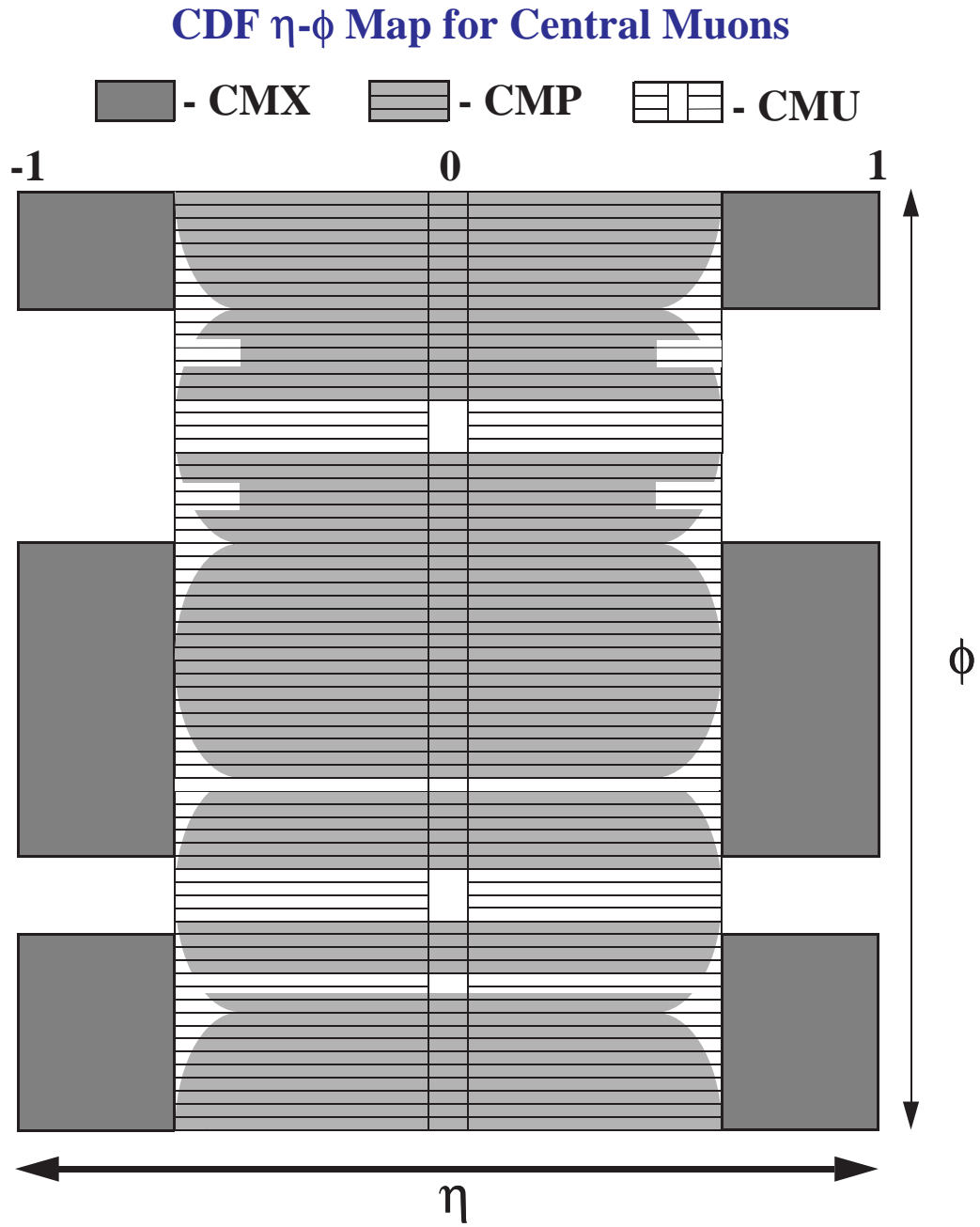


Figure 3.9: *Schematic of the central muon coverage.*

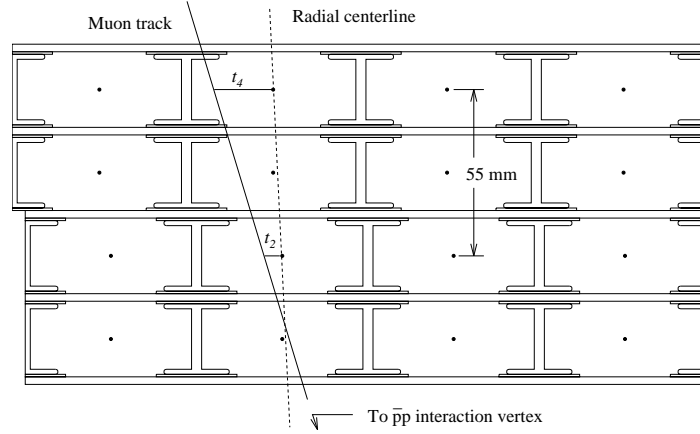


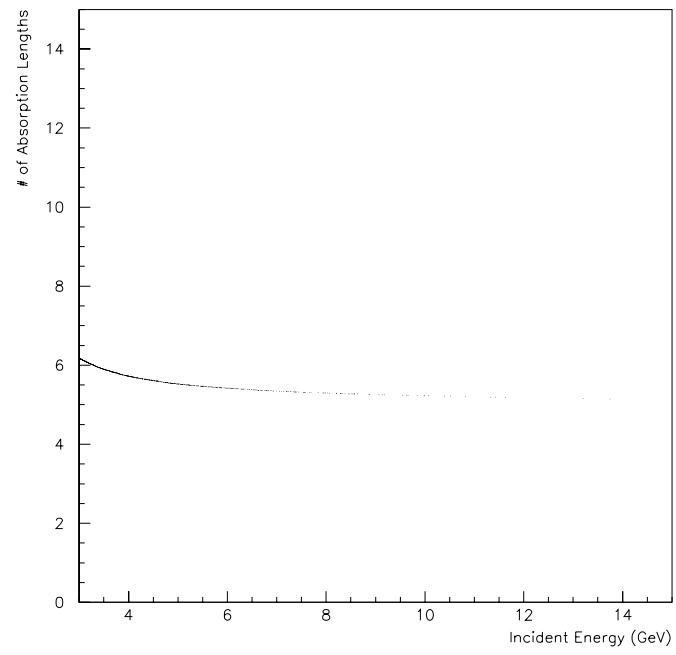
Figure 3.10: *End-view schematic of a CMU modules.*

Figure 3.11 shows the number of absorption lengths<sup>1</sup> traversed by normal incident kaons and pions. About 1 in 20 low momentum  $K^+$  penetrate the calorimeters, leaving only a minimum-ionizing particle (MIP) signal in the calorimeter. In an effort to reduce the punch-through rate, the CMP was constructed behind the CMU with an additional 60 cm of steel shielding. The CMP upgrade is made up of 4 layers of rectangular drift cells with only  $r$ - $\phi$  measurements. The inner and outer surfaces of the detector are lined with scintillator planes (CSP) to provide timing information of the trigger system.

The CMX provides additional coverage at a pseudo-rapidity of  $0.6 < |\eta| < 1.0$ . It consists of 4 arches of drift tubes behind approximately 6.2 absorption lengths of material. The drift tubes provide both  $r$ - $\phi$  and  $z$  information used in matching hits in the muon chamber to tracks seen in the CTC. The arches also are sandwiched between scintillator counters that provide timing for the trigger.

---

<sup>1</sup>The probability that a particle with absorption length ( $l_0$ ) will penetrate to a depth of  $x$  is  $e^{-x/l_0}$ .



### 3.2.7 Data acquisition and trigger

The Tevatron has a 185 kHz collision rate, but CDF can only transfer  $< 10$  Hz of data to tape. In order to reduce the data rate while preferentially saving interesting events, CDF employs a three level trigger. Each level of the trigger has more time to process events and therefore can use more complex information.

The level 1 trigger [67] uses only calorimeter energy and muon chamber hits. The level 1 trigger decision takes less than  $3.5 \mu\text{s}$  and therefore induces no dead time (a period of time during collisions in which the detector can take no data). The level 1 accepts data at a rate of 1 kHz.

At level 2, more detector information is available. Calorimeter energies are summed to form seed towers for jets and electrons. Missing  $E_T$  and  $\Sigma E_T$  are calculated. Preliminary tracking information (discussed below) is available to match to muon stubs and EM energy clusters for electron and muon candidates. The trigger decision is based on combination of these objects. The level 2 decision time is  $40 \mu\text{s}$ , which causes about 3% detector dead time. The trigger rate at level 2 is reduced from 1 kHz to 20-35 Hz.

The level 3 trigger [68] is a Silicon Graphics computer farm running FORTRAN-77 code. All detector elements are digitized and readout, taking approximately 3 ms. A simplified version of the off-line analysis code is run, allowing for a complete reconstruction of the event. Once accepted, the event is written to 8 mm tape. The level 3 trigger reduces the data rate to 8 Hz.

Once to tape, the events are re-analyzed using the full off-line code. Precise alignment and calibration constants are applied. The events are saved with the raw hit information as well as the processed physics objects (tracks, electron and muon banks, etc.).

The following subsections detail the di-muon trigger’s used in this analysis.

### **Level 1 Di-muon Triggers**

The level 1 di-muon trigger [69] uses hit information in the CMU and CMX. It identifies muon candidates by looking at the difference in drift times in two drift cells. The time difference determines the angle relative to the radial direction in which the particle traverses the chamber. The angle of the track in the muon chambers (called a ‘stub’) is approximately inversely proportional to the traverse momentum of the particle. The trigger fires at nominal  $p_T$  of 3.3 GeV. Multiple scattering of muon as it passes through the calorimeter smears the relationship between the angle of the stub in the muon chamber and the particles  $p_T$ ; thus, the trigger does not have a sharp turn-on. The point of 50% efficiency for the stub is 1.7 GeV (2.2 GeV) for the CMU (CMX).

The Run 1B di-muon triggers require either two CMU stubs, two CMX stubs, or one CMU and one CMX stub.

### **Level 2 Di-muon Triggers**

Preliminary tracking in the CTC is available at level 2 using the Central Fast Track (CFT) trigger [70]. The CFT uses only  $r$ - $\phi$  tracking information from the 5 axial super-layers. In every super-layer, the track will pass near a sense wire, producing a ‘prompt’ hit ( $< 90$  ns drift time). 2 ‘delayed’ hits are found in each super-layer using a 530-690 ns drift time window. CFT first looks in the outermost layers, forming ‘stubs’ from a ‘prompt’ hit and two ‘delayed’ hits in a cell. The CFT, using a lookup table, adds hits in the inner super-layers. The track candidates have to have at least 14 of the 15 possible hits to pass the trigger. The track has a momentum resolution of  $\frac{\sigma_{p_T}}{p_T} = 3.5\%$ .

The CFT tracks are projected to the muon chambers using a lookup table. If the track matches the muon cluster to within  $\Delta\phi$  of 5%, it is a muon candidate.

The various level 2 di-muon trigger are summarized in ref. [71]. There are two basic classes of triggers. The first class requires two muon stubs that match to CFT tracks, the CFT tracks have a 50% efficiency at  $p_T$  of 1.9 GeV. The stubs could be in either the CMU or CMX. The second class of triggers requires two muon stubs with only one matching a CFT track. The CFT track is required to be stiffer, with the 50% efficiency point at  $p_T$  of 3.0 GeV.

### **Level 3 Di-muon Triggers**

At level 3, full three-dimensional CTC tracking information is available. The tracks are more precisely projected to the muon stubs and required to match within  $\sim 3\sigma$  in both the  $r$ - $\phi$  and  $z$  projections, taking into account multiple scattering and measurement precision. The mass of the pair of muon candidates is required to be between 2.7 GeV and 4.1 GeV.

## Chapter 4

# Data Set and Event Selection

The signal searched for in this analysis is  $b \rightarrow J/\psi X, \bar{b} \rightarrow \ell X'$  where  $\ell$  can be an electron or muon. In this chapter, the Run 1B  $J/\psi$  data set is described. The off-line selection criteria for both the  $J/\psi$  and the additional lepton are described.

### 4.1 Run 1B Di-muon Triggers and Data Set

This analysis uses the CDF Run 1b  $J/\psi$  data set obtained between January 1994 and July 1995, with an integrated luminosity of  $86.5 \pm 3.5 \text{ pb}^{-1}$ . The CDF three level di-muon trigger is described previously in chapter 3. Events which pass the di-muon triggers are written to 8 mm storage tape. The events are then re-analyzed with the final off-line alignment constants; the events are then saved in a compact YBOS format [72]. The YBOS banks are pre-processed specific physics objects, such as tracks, muons, electrons, etc., which can be unpacked for convenient use.

Di-muon Trigger	$p_T$ requirement
CMU_CMU_TWO_CFT_1B	1.9,1.9
CMU_CMX_TWO_CFT_1B	1.9,1.9
CMUP_CMX_TWO_CFT_1B	2.4,1.9
CMX_CMX_TWO_CFT_1B	1.9,1.9
CMU_CMU_ONE_CFT_1B	3.0,1.65
CMU_CMX_ONE_CFT_1B	3.0,1.65
CMUP_CMU_ONE_CFT_1B	3.0,1.65
CMUP_CMX_ONE_CFT_1B	3.0,1.65
CMU_CMU_SIX_TOW_1B	1.9,1.9

Table 4.1:  $p_T$  requirements on Run 1b di-muon triggers used. CMU/CMX/CMUP indicate which muon subsystems had a stub for the two muons. TWO\_CFT indicates that both muon candidates have stubs matched to CFT tracks, while ONE\_CFT indicates that only one muon stub is matched to a CFT track.

## 4.2 $J/\psi \rightarrow \mu^+\mu^-$ Event Selection

The CDF three level di-muon triggers do not require that an event passes all three levels of the trigger. Instead, 'trigger volunteers' are allowed, where an event passes some other level 2 trigger, but has a  $J/\psi$  candidate found in level 3. In order to understand the trigger efficiencies, the first step of event selection is to confirm that the event passes a level 2 di-muon trigger, made possible by algorithm DIMUTG [73]. The level 2 trigger confirmation guarantees that all events used in this analysis have passed all three levels of the di-muon trigger. The  $J/\psi$  triggers used in this analysis are shown in table 4.1. The  $p_T$  requirements vary for the different triggers and are chosen to be slightly greater than the 50% efficiency point as determined by ref. [71]. These selection criteria are the same as the  $B_c$  discovery analysis [31].

After confirming the level 2 trigger, the position of the extrapolated track at the muon chamber is compared to the position of the muon stub. A  $\chi^2$  matching test is made of these two quantities, taking into account the effects of multiple scattering and energy loss in material [74]. Table 4.2 shows the  $\chi^2$  matching requirements for muon stubs for the



Muon chamber	r- $\phi$ requirement	r-z requirement
CMU	$\chi^2 < 9$	$\chi^2 < 12$
CMP	$\chi^2 < 9$	Not applicable
CMX	$\chi^2 < 9$	$\chi^2 < 12$

Table 4.2:  $\chi^2$  matching cuts for muons. Muon candidates with stubs in two chambers must pass both chambers  $\chi^2$  matching.

various muon subsystems. The  $\chi^2$  has one degree of freedom.

Next, we require a high quality track for both muon candidates. The pseudo-lifetime ( $c\tau$ ) of the  $J/\psi$  candidates is used in this analysis to determine the bottom purity. SVX information is required in order to improve the precision of the  $c\tau$  measurement. A quality track is defined as follows:

- 2 axial super layers in the CTC with at least 4 hits in each layer
- 2 stereo super layers in the CTC with at least 2 hits in each layer
- At least 3 of the possible 4 SVX layers have a hit associated with the track

In order to reject  $J/\psi$  candidates with muons originating from different primary interactions, the z position difference between the two tracks is required to be less than 5 cm at the beam-line.

A time-dependent degradation of the CTC was seen during Run 1B due to aging effects. A time varying scaling of the error covariance matrix for the CTC track [75] takes into account the effects of the drift chamber's degradation. A vertex constrained fit using the program CTVMFT [76] is performed after the error covariance scaling. The  $\chi^2$  probability of the vertex fit is required to be better than 1%. Figure 4.2 shows the sideband subtracted  $\chi^2$  probability of the  $J/\psi$  vertex before and after the scaling; the time-varying covariance

scaling clearly yields a more uniform vertex probability. The vertex constrained mass of the  $J/\psi$  candidate is required to be  $2.9 \text{ GeV} < M_{J/\psi} < 3.3 \text{ GeV}$ .

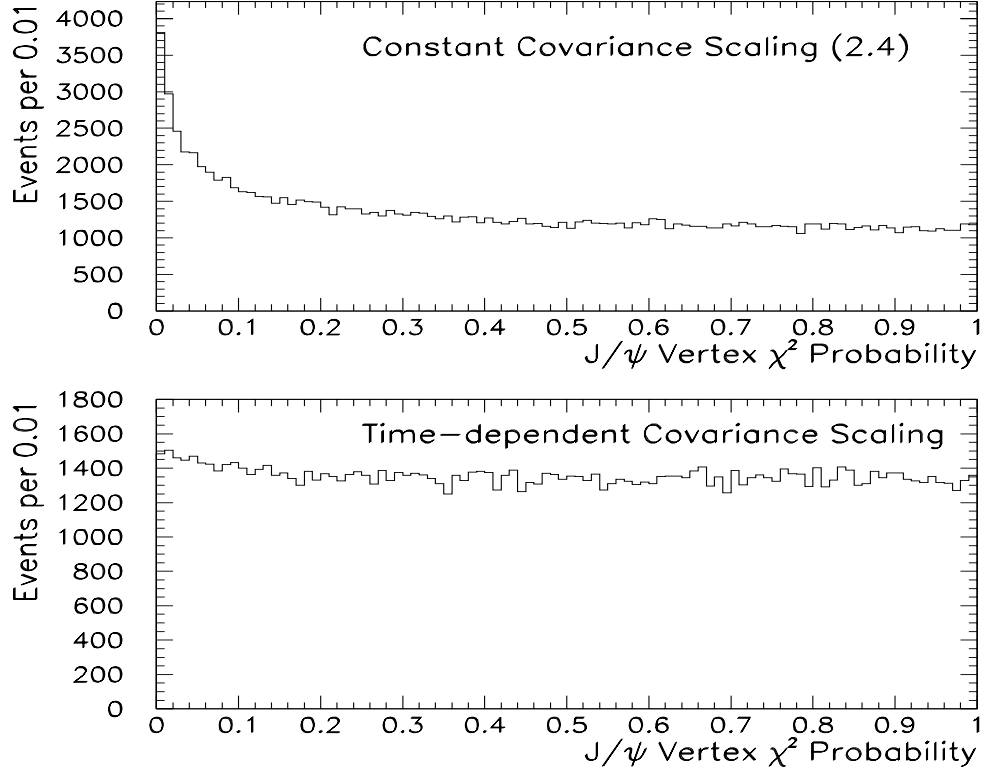


Figure 4.1:  $\chi^2$  probability of the  $J/\psi$  vertex fit.

A total of 177,650 events pass the above selection cuts. Figure 4.1 shows the  $J/\psi$  mass distribution for these events. In order to estimate the number of  $J/\psi \rightarrow \mu^+\mu^-$  candidates, the mass has been fit with two Gaussians (which fit the  $J/\psi$  signal) and a linear background term. Two Gaussians are necessary to describe the signal shape because of final state radiation effects. A linear background has been assumed in many previous CDF  $J/\psi$  analyses [31, 77, 78]. The background under the mass peak is caused by: irreducible decay-in-flight and punch-through backgrounds, Drell-Yang muons and double sequential

semi-leptonic decays where  $b \rightarrow c\mu^-X, c \rightarrow s\mu^+X'$ . From the fit,  $137780 \pm 440$   $J/\psi$  candidates are in the sample. For this measurements, the  $J/\psi$  mass signal region is defined to be within  $\pm 50$  MeV of the Particle Data Group's [79] world average value (3096.87 MeV). The sideband regions are chosen to be  $2.900 \text{ GeV} \leq M_{J/\psi} \leq 3.000 \text{ GeV}$  and  $3.200 \text{ GeV} \leq M_{J/\psi} \leq 3.300 \text{ GeV}$ . The sideband regions contain 20,180 events. The events in these regions are used later in the analysis to describe the  $c\tau$  shape of fake  $J/\psi$  background in the mass signal region.

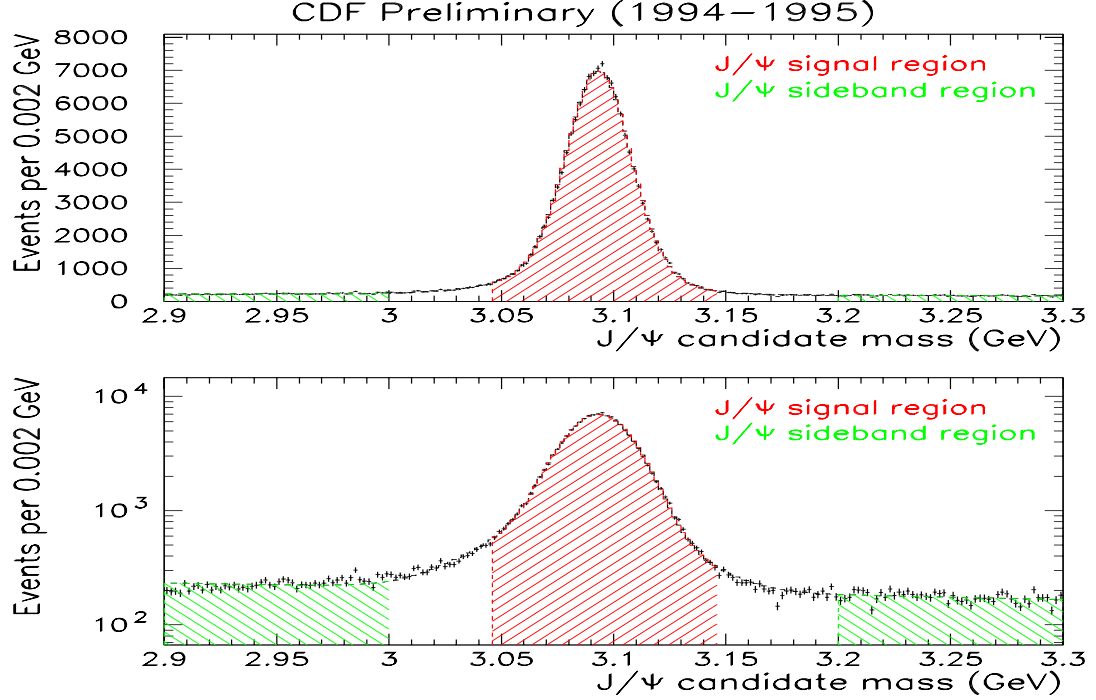


Figure 4.2: *Di-muon invariant mass distribution from events passing selection criteria. Top: Linear scale. Bottom: Logarithmic scale.*

The ratio between the number of fake  $J/\psi$  events in the mass signal region to the mass sideband region ( $R_{side}$ ) was determined to be  $R_{side} = 0.501 \pm 0.000043$ <sup>1</sup> by the mass fit. To estimate the systematic uncertainty of this ratio, a 2nd order polynomial is used to describe the background term. The resulting fit value is  $R_{side} = 0.545 \pm 0.008$ .

<sup>1</sup>In this thesis, constraints are always written in a capital letters.

The difference between the two fits is taken to be the systematic uncertainty yielding  $R_{side} = 0.501 \pm 0.000043(\text{stat}) \pm 0.044(\text{syst})$ .

### 4.3 CMUP $\mu$ Selection Requirements

The additional (non- $J/\psi$ ) muon is required to have muon stubs in both the CMU and CMP (a CMUP muon). Requiring both CMU and CMP muon stubs maximizes the amount of material traversed by the candidate, reducing the background due to hadronic punch-through of the calorimeter. The  $\chi^2$  matching requirements are the same as for the  $J/\psi$  muons. The muons candidates are required to have a  $p_T > 3$  GeV; muons with lower  $p_T$  will typically range out prior to the CMP due to energy loss in the calorimeter and the CMP steel.

As the impact parameter is used to estimate the bottom purity of the muons, the same track quality is required as for the  $J/\psi$  muons. Additionally, the muon candidate's track is projected into the CMU and the CMP chamber regions. Any candidate which projects more than 2 cm outside of the CMU chamber boundary and more than 5 cm outside of the CMP chamber boundary are rejected. The z positions of the  $J/\psi$  candidate and the CMUP muon are required to be within 5 cm of each other at the beam-line.

247 CMUP candidate muons are found in the  $J/\psi$  sample, with 51 in the  $J/\psi$  mass sideband and 142 in the  $J/\psi$  mass signal region.

Of the 142 candidates in the  $J/\psi$  mass signal region, 64 candidates have the CMUP muon and the  $J/\psi$  candidates in the same hemisphere in the azimuthal angle (which will be known as toward) and the other 78 candidates are in the opposite hemisphere in the azimuthal angle (which is denoted away). Figure 4.3 shows the distribution of the

requirement variables of the candidates.

## 4.4 SLT Electron Selection Criteria

A method of the finding soft electrons (SLT's) was developed for bottom flavoring tagging in  $B_d$  mixing and  $\sin(2\beta)$  measurements [8, 80]. These electrons have a relatively high purity, low momenta ( $p_T > 2$  GeV), and an understood efficiency. The rate of hadrons faking an electron was studied extensively in ref. [31], making it possible to estimate the background due to fake electrons. The selection criteria is identical to ref. [31] in order to use these fake rate estimates.

### 4.4.1 General selection criteria

The soft electron candidates have the same track quality cuts as the  $J/\psi$  muons. The candidates must have a  $p_T > 2$  GeV. In order to ensure that the electrons come from the same primary interaction, the z position of the track at the beam axis must be within 5 cm of the  $J/\psi$  candidate.

### 4.4.2 Calorimeter requirements

The difference between electromagnetic and hadronic showers can be used to improve the purity of the soft electron selection. Two quantities which measure the electromagnetic quality of the shower are  $E/p$  and  $E_{had}/E_{em}$ .  $E/p$  is defined to be the energy measured in the electro-magnetic calorimeter (CEM) divided by the track momentum measured in the drift chamber. The  $E/p$  is required to be  $0.7 \leq E/p \leq 1.5$ .

$E_{had}/E_{em}$  is the ratio between the energy measured in the hadronic and electromagnetic calorimeters. As the CEM is 18 radiation lengths deep, the majority of energy will be

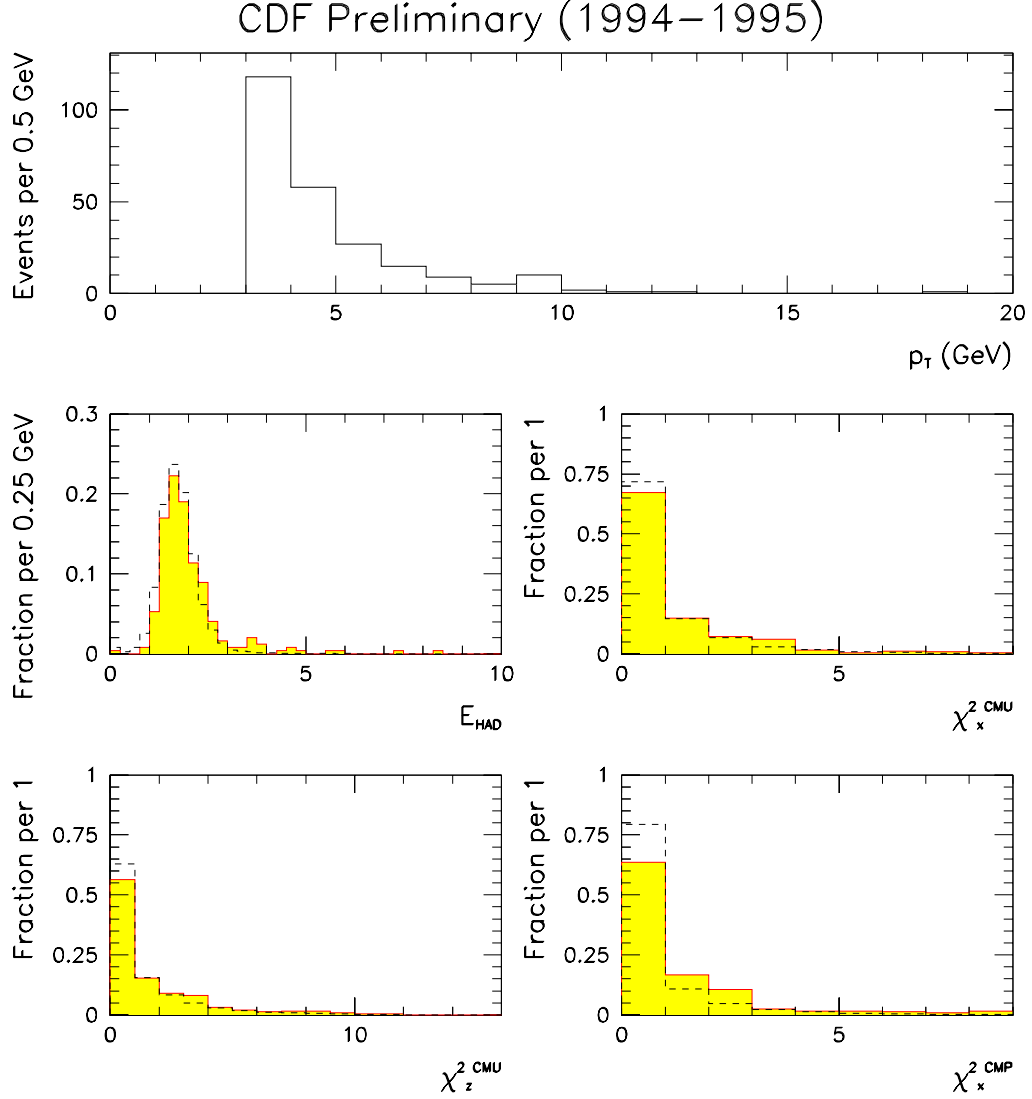


Figure 4.3: Top: The  $p_T$  of the CMUP muon candidates. Middle Left: Hadronic energy deposited by the SLT CMUP muon candidates (solid, filled) and by CMUP muons from  $J/\psi$  decay. Middle Right:  $\chi^2$  of r- $\phi$  stub matching in the CMU for the SLT CMUP muon candidates (solid, filled) and for CMUP muons from  $J/\psi$  decay. Bottom Left:  $\chi^2$  of r-z stub matching in the CMU for the SLT CMUP muon candidates (solid, filled) and for CMUP muons from  $J/\psi$  decay. Bottom Right:  $\chi^2$  of r- $\phi$  stub matching in the CMP for the SLT CMUP muon candidates (solid, filled) and for CMUP muons from  $J/\psi$  decay.

deposited by an electron in the electromagnetic calorimeter.  $E_{had}/E_{em}$  is required to be  $E_{had}/E_{em} < 0.1$ .

#### 4.4.3 CES and CPR requirements

The soft electron candidates passing the above criteria are extrapolated to the CES and the CPR. Fiducial requirements are made to ensure a good shower position and shape measurement. The track extrapolation is required to be at least 2 cm away from the phi edge of the tower (a tower is 48 cm wide) and lie within  $6.22 \text{ cm} \leq |Z_{CES}| \leq 237.45 \text{ cm}$  in the z position within the arch, where  $Z_{CES}$  is the local z position in the CES. The track extrapolation is also required to be away from the edges of the CPR chambers:  $|X_{CPR}| \leq 17.78 \text{ cm}$ , and  $9.0 \text{ cm} \leq |Z_{CPR}| \leq 118.0 \text{ cm}$  or  $125.0 \text{ cm} \leq |Z_{CPR}| \leq 235.26 \text{ cm}$  where  $X_{CPR}$  and  $Z_{CPR}$  are the local CPR x and z position respectively.

The CES cluster position is calculated with a energy-weighted mean of the 3 wires and 3 strips around the extrapolated track position. The following cuts are made on the  $\Delta x$  and  $\Delta z$  between cluster position and the track extrapolation.

- $\Delta z < 2.0 \text{ cm}$
- $\Delta x < 1.82 - 0.1867p \text{ cm}$  ( $p < 6.0 \text{ GeV}$ )
- $\Delta x < 0.7 \text{ cm}$  ( $p > 6.0 \text{ GeV}$ )

The track is then matched to a cluster within the CES. The energy of the cluster is measured in both the strips and wires. The energy is calculated by adding the 5 strips ( $E_{strip}$ ) and 5 wires ( $E_{wires}$ ) around the track extrapolation. A requirement is made on the ratio of the energy measured versus the track momentum ( $p$ ). The requirement is the same for both the strips and wires.

- $E_{strip,wires}/p > 0.24 + 0.03p$  ( $p < 12$  GeV)
- $E_{strip,wires}/p > 0.6$  ( $p > 12$  GeV)

Finally, a  $\chi^2$  comparison is made between the lateral shower shape of 7 channel CES clusters and test beam data [81] for both the wires ( $\chi^2_{wires}$ ) and strips ( $\chi^2_{strips}$ ).

- $\chi^2_{wires}/6 \leq 16$
- $\chi^2_{strips}/6 \leq 16$

The energy in the pre-radiator is measured by summing the energy of 3 adjacent CPR wires ( $Q_{CPR}$ ). The amount of energy deposited in the pre-radiator depends on the path length traversed through the solenoid coil by the incident electron. The requirement of the CPR energy varies as a function of  $p/p_T$ , which accounts for the energy variation as a function of path length.

- $Q_{CPR} \geq 4744 - 11592(p/p_T) + 7923(p/p_T)^2$  fC

#### 4.4.4 $dE/dx$ requirements

Electrons also can be identified by rate of ionization ( $dE/dX$ ) of the track in the CTC. A truncated mean of the charge measured in super-layers 4, 6, and 8 is used to measure the  $dE/dx$  of the track. The  $dE/dx$  is then corrected for the aspect angle of the track in the drift cell, the number of  $dE/dx$  measurements, aging effects, etc., by the routine DEDX\_MASTER [61], yielding both the corrected  $dE/dx$  ( $Q_{ctc}$ ) and the resolution of the measurement ( $\sigma$ ). The significance ( $S_e$ ) of the difference between the measured and the expected  $dE/dx$  for an electron( $Q_e$ ) is calculated ( $S_e \equiv \frac{Q_{ctc}-Q_e}{\sigma}$ ). The requirement on  $S_e$  is:



- $S_e > -0.9$  ( $2 < p < 3$  GeV)
- $S_e > -1.1$  ( $3 < p < 5$  GeV)
- $S_e > -1.3$  ( $5 < p < 6$  GeV)
- $S_e > -1.5$  ( $6 < p < 8$  GeV)
- $S_e > -1.9$  ( $8 < p < 10$  GeV)
- Not Applied ( $p > 10$  GeV)

In ref. [31], the required value of  $S_e$  was optimized as a function of  $p_T$ ; the fake electron fraction increases with decreasing track  $p_T$ . Thus, the  $S_e$  becomes more stringent (less efficient) with decreasing  $p_T$ . As these measurement uses the electron fake rates from ref. [31], the same  $S_e$  requirements are used.

#### 4.4.5 Conversion removal

One source of background to electrons from bottom decay is photon conversions, where a photon interacts with detector material and converts into a  $e^+e^-$  pair. In addition, 1.2% of all neutral pion decays into  $\gamma e^+e^-$  directly (Dalitz decay). To reduce this background, conversions are searched for and vetoed by looking for a conversion partner track that satisfies the following requirements:

- r- $\phi$  separation at point of tangency  $< 0.2$  cm
- Difference of tracks cotangents  $< 0.03$
- z mismatch at point of tangency  $< 2.0$  cm
- Radius of conversion between -5 cm to 50 cm

- $\Delta\phi$  at radius of conversion  $< 0.01$
- Pointing residual to origin  $< 1.0$  cm

The conversion requirements are the same as ref. [8]. The conversion removal is not totally efficient. Some of the soft electron candidates are residual conversion electrons, where either the conversion pair track is not found due to tracking inefficiencies at low  $p_T$  or the conversion electron selection is not fully efficient. The rate of residual conversions is studied more in section 5.1.4.

#### 4.4.6 Results of electron selection

514 candidate electrons are found, with 92 in the  $J/\psi$  mass sidebands and 312 in the  $J/\psi$  mass signal region. 107(205) of the events in the mass signal region are in the toward(away) regions in  $\Delta\phi$  between the electron and  $J/\psi$ . In the  $J/\psi$  mass signal region, 6(9) events were vetoed as conversions in the toward(away)  $\Delta\phi$  bin. In the  $J/\psi$  mass sideband region, 5(4) events were vetoed as conversions. Figures 4.4 and 4.5 shows the distributions of the selection variables for SLT candidates and conversions.

# CDF Preliminary (1994–1995)

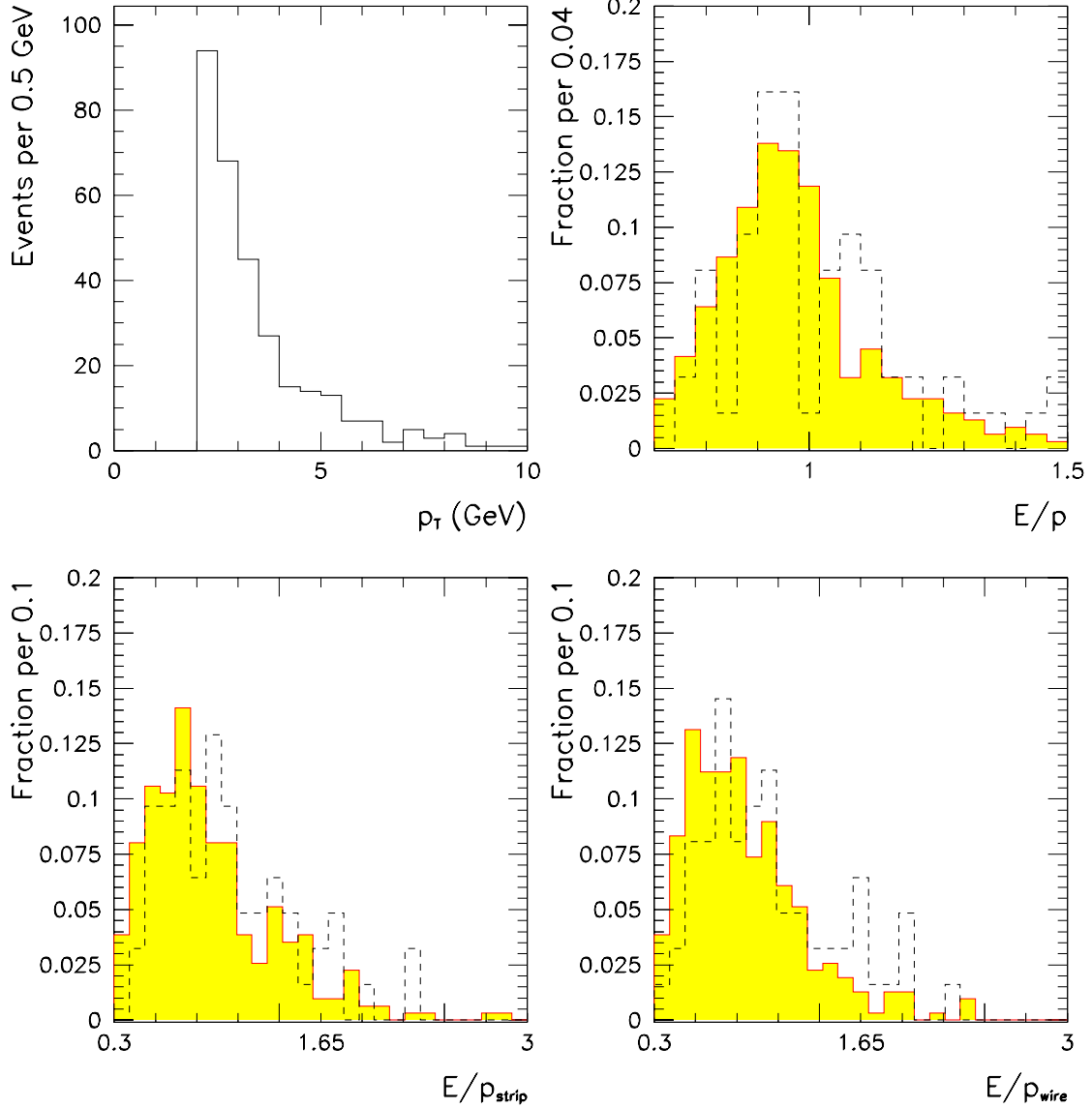


Figure 4.4: Top Left:  $p_T$  of the SLT electron candidates. Top Right:  $E/p$  of SLT electron candidates (filled,solid) and conversion candidates (dotted). Bottom Left:  $E_{strip}/p$  of SLT electron candidates (filled,solid) and conversion candidates (dotted). Bottom Right:  $E_{wire}/p$  of SLT electron candidates (filled,solid) and conversion candidates (dotted).

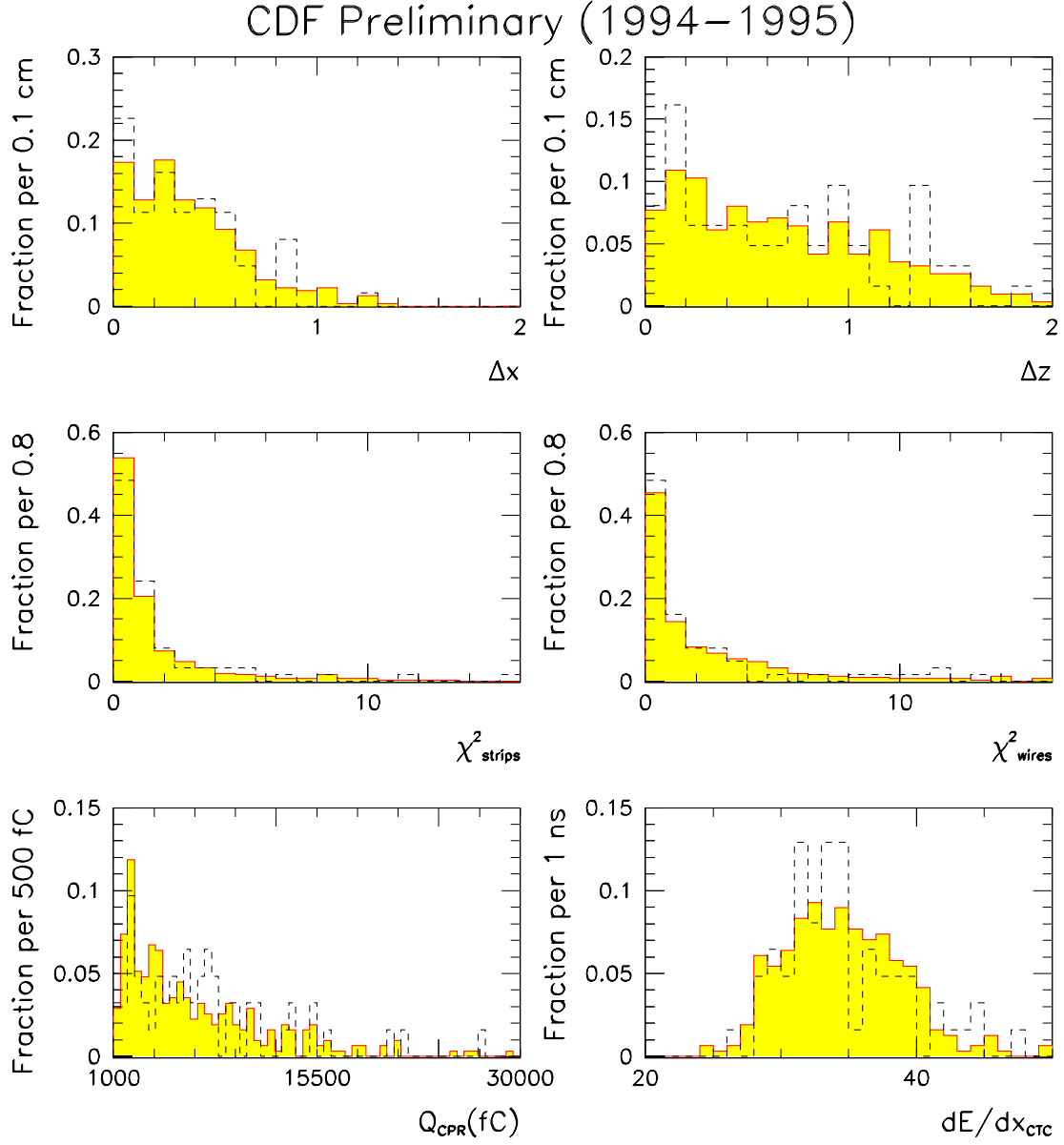


Figure 4.5: Distribution of electron selection variables for SLT candidates (solid, filled) and conversion candidates (dotted). Top Left:  $\Delta x$ . Top Right:  $\Delta z$ . Middle Left:  $\chi^2_{wire}$ . Middle Right:  $\chi^2_{strip}$ . Bottom Left:  $Q_{CPR}$ . Bottom Right:  $dE/dx$ .

## Chapter 5

# Physics Analysis

This chapter describes the analysis techniques used to measure of the fraction of the  $b\bar{b}$  pairs produced in the semi-hemisphere in the azimuthal angle ( $f_{toward}$ ). First, the  $c\tau$  and impact parameter distributions of the signal and backgrounds are described. In addition, the size of some backgrounds is estimated. Next, the unbinned-likelihood function used to determine the relative rates of the signal and background components is described. Finally, the results of the fit is presented along with an estimate of systematic uncertainties.

### 5.1 Signal and Background Description

The signal and backgrounds for both the  $J/\psi + \mu$  and  $J/\psi + e$  samples are very similar. The basic technique is to determine the amounts of the various signal and background components of the sample with a simultaneous fit of the pseudo- $c\tau$  (defined in section 5.1.1) of the  $J/\psi$ <sup>1</sup> and the signed impact parameter of the non- $J/\psi$  lepton. The impact parameter is signed to distinguish between residual electron conversions and electrons from bottom

---

<sup>1</sup>Unless explicitly noted,  $c\tau$  is actually pseudo- $c\tau$

decay<sup>2</sup>, described more fully in section 5.1.5. The impact parameter is signed positive if the primary vertex lies outside  $r$ - $\phi$  projection of the particle's helix fit.

The signal in this analysis is  $b \rightarrow J/\psi X, \bar{b} \rightarrow \ell X'$  where  $\ell$  can be an electron or muon. As the  $J/\psi$  and additional lepton originate from separate bottom hadron decays, the impact parameter of the additional lepton and the  $c\tau$  of the  $J/\psi$  are not strongly correlated for the signal. The backgrounds in this analysis have two categories: one in which the impact parameter and  $c\tau$  are uncorrelated, and other where the impact parameter and  $c\tau$  are strongly correlated. The impact parameter and the  $c\tau$  become strongly correlated when both the  $J/\psi$  and the additional lepton candidate originate from the same displaced vertex.

In uncorrelated sources, the impact parameter and  $c\tau$  shapes describing the background are determined independently.  $J/\psi$  candidates are assumed to originate from three sources: direct  $J/\psi$  production (including feed-down from  $\chi_{c1}$ ,  $\chi_{c2}$ , and  $\psi(2s)$ ) where the  $J/\psi$  decays at the primary vertex,  $J/\psi$  from bottom decay (including the feed-down from higher  $c\bar{c}$  resonances), and the non- $J/\psi$  background described by the events in the  $J/\psi$  mass sidebands. Leptons candidates are assumed to originate from the following sources: directly produced fake or real leptons from the primary vertex, leptons from bottom decay (including  $b \rightarrow cX \rightarrow \ell X'$ ), lepton candidates with the fake  $J/\psi$  candidate, and residual conversion electrons (for electrons only).

In addition, two correlated sources of backgrounds exist. The first source is  $B_c \rightarrow J/\psi \ell^+ X$ , which is a small but irreducible background. The impact parameter of the additional lepton and the  $c\tau$  of the  $J/\psi$  is described by Monte Carlo techniques and the overall size of the background is also estimated (see section 5.1.7).

---

<sup>2</sup>In this thesis, leptons from bottom decay include sequential charm lepton where  $b \rightarrow cX \rightarrow \ell X'$  unless explicitly noted.

The other correlated source of background occurs when a bottom hadron decays into a  $J/\psi$  and a hadron which is mis-identified as a lepton. For electrons, this background is due to hadrons (mostly  $\pi^{+/-}$  and  $K^{+/-}$ ) showering early in the calorimeter and passing the electron identification selection. For muons, there are two sources of this background. The largest source of correlated background is due to decay-in-flight of charged pions and kaons, which result in a real muon. These real muons are denoted as 'fakes' in this analysis. The other, smaller correlated fake muon background is caused by hadrons punching-through the calorimeter and muon steel shielding. These background sources are more fully described in section 5.1.8.

The following sections provide a description of the techniques used to determine the impact parameter and  $c\tau$  shapes of the various sources and to estimate of the number of  $B_c \rightarrow J/\psi \ell X$  and  $b \rightarrow J/\psi \ell_{\text{fake}} X$  events in the sample.

### 5.1.1 Direct and bottom decay $c\tau$ shapes

The direct  $J/\psi$  and bottom decay  $J/\psi$   $c\tau$  shapes are determined from a fit to the data. The relatively long average lifetime of the bottom hadron ( $(1.564 \pm 0.014) \times 10^{-12}$  s [79]) allows one to distinguish between these two sources. First, the signed transverse decay length  $L_{xy}$  is determined in the  $r$ - $\phi$  plane.

$$L_{xy} \equiv \frac{(\vec{X}_{SV} - \vec{X}_{PV}) \cdot \vec{p}_T^{J/\psi}}{p_T^{J/\psi}} \quad (5.1)$$

where  $\vec{X}_{SV}$  and  $\vec{X}_{PV}$  are the locations of the  $J/\psi$  and primary vertex in the transverse plane, and  $\vec{p}_T^{J/\psi}$  is the vector transverse momentum of the  $J/\psi$  (depicted in figure 5.1). Directly produced  $J/\psi$  have a symmetric distribution around zero and bottom  $J/\psi$  events have a positive sign. If the bottom decay was fully reconstructed, one could determine the

proper decay length exactly ( $c\tau_{proper}$ ) from the measured  $L_{xy}$  with:

$$c\tau_{proper} \equiv \frac{L_{xy}^B \cdot m_B}{p_T^B} \quad (5.2)$$

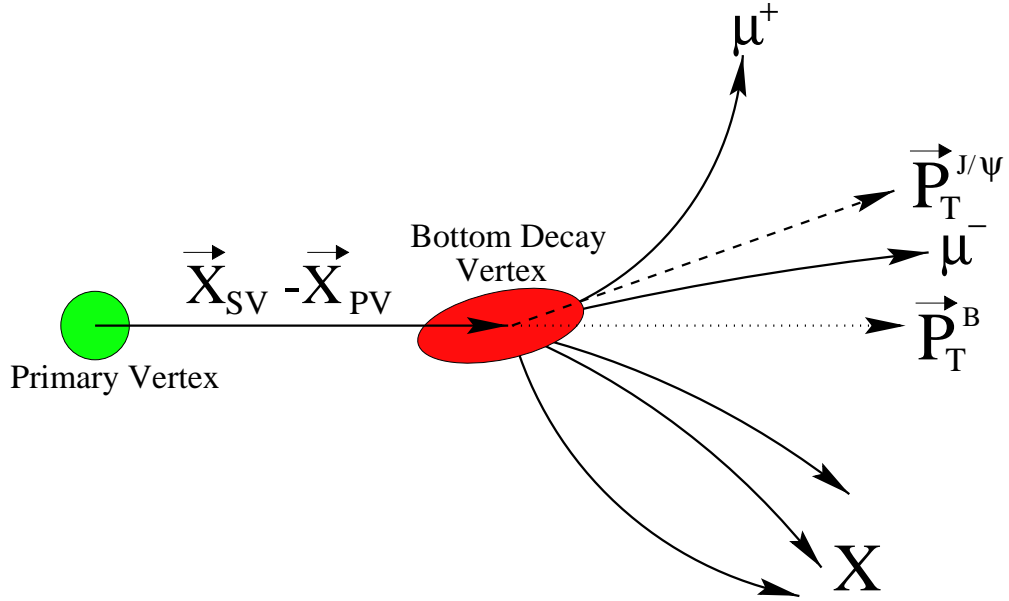


Figure 5.1: *Cartoon of  $L_{xy}$  measurement in  $b \rightarrow J/\psi X$  decays.*

Because the bottom hadron is not fully reconstructed, a 'pseudo-proper decay length' ( $c\tau$ ) is constructed using the kinematics of the  $J/\psi$  only:

$$c\tau \equiv \frac{L_{xy} \cdot m_{J/\psi}}{p_T^{J/\psi} \cdot F_{corr}(p_T^{J/\psi})} \quad (5.3)$$

$F_{corr}(p_T^{J/\psi})$ , determined by Monte Carlo [77], is the average correction factor for the partial reconstruction of the bottom hadron. The  $F_{corr}(p_T^{J/\psi})$  dependence on the  $J/\psi$  transverse momentum is:

$$F_{corr}(p_T^{J/\psi}) = 2.438e^{-1.177p_T^{J/\psi}} + 0.8357 \quad (5.4)$$



### **$J/\psi$ mass sideband $c\tau$ fit**

The events in the  $J/\psi$  mass sidebands are used in order to model the fake  $J/\psi$  background under the  $J/\psi$  mass signal peak. Two components are fit for using an unbinned log-likelihood technique: events from the primary vertex (direct) and events with lifetime from heavy flavor (predominantly from  $b \rightarrow c\mu^- X \rightarrow \mu^+ X'$ ). The direct events are described by a symmetric resolution function chosen to be a Gaussian plus 2 symmetric exponentials. The events with lifetime are fit with a positive only exponential.

The sideband fit function is:

$$g_{back}(x) = (1 - f_B)[(1 - f_1 - f_2) \cdot G(x, \sigma) + f_1 \cdot E(|x|, \lambda_1) + f_2 \cdot E(|x|, \lambda_2)] + f_B \cdot E(x, \lambda_B) \quad (5.5)$$

where  $G(x, \sigma) = \frac{1}{\sqrt{2\pi}\sigma} e^{-x^2/2\sigma^2}$ ,  $E(x, \lambda) = \frac{1}{\lambda} e^{-x/\lambda}$  ( $x \geq 0.0$ ), and  $E(|x|, \lambda) = \frac{1}{2\lambda} e^{-|x|/\lambda}$ .

The fit parameters are:

$f_B$ : fraction of events in sideband with lifetime

$\lambda_B$ : length scale of sideband events with lifetime

$f_1$ : fraction of direct events in first symmetric exponential

$\lambda_1$ : length scale of the first symmetric exponential

$f_2$ : fraction of direct events in second symmetric exponential

$\lambda_2$ : length scale of the second symmetric exponential

$\sigma$ : width of the direct resolution Gaussian

The log-likelihood function ( $\mathcal{L} = -2 \ln \prod_i g_{back}(c\tau_i)$ ) is minimized, returning the fit shown in table 5.1 and figure 5.2.

Parameter	Fit
$f_B$	$12.7\% \pm 0.5\%$
$\lambda_B$	$606\mu\text{m} \pm 23\mu\text{m}$
$f_1$	$32.3\% \pm 0.9\%$
$\lambda_1$	$219\mu\text{m} \pm 9\mu\text{m}$
$f_2$	$8.0\% \pm 0.3\%$
$\lambda_2$	$4142\mu\text{m} \pm 151\mu\text{m}$
$\sigma$	$46.1\mu\text{m} \pm 0.7\mu\text{m}$

Table 5.1: *Fit result of  $J/\psi$  mass sideband data.*

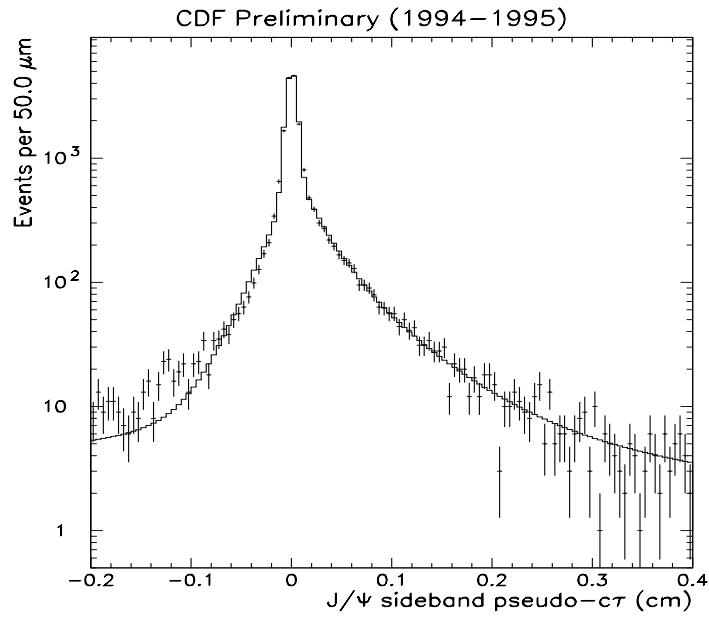


Figure 5.2: *Fit of  $J/\psi$  mass sideband data.*

### **$J/\psi$ mass signal region $c\tau$ fit**

Once the  $c\tau$  shape of the mass sideband event is found, the  $c\tau$  shapes of directly produced and bottom decay  $J/\psi$  can be determined. The shape of the directly produced  $J/\psi$  ( $F_{direct}^{c\tau}(x)$ ) is parameterized by a Gaussian with two symmetric exponential tails; this shape is the assumed resolution function of the  $c\tau$  measurement. The shape of  $J/\psi$  events from bottom decay ( $F_b^{c\tau}(x)$ ) is therefore described as a positive exponential convoluted with the  $c\tau$  resolution function. The background shape ( $g_{back}$ ) is fixed to the value obtained in the fit of the sideband region and the background fraction ( $f_{back}$ ) is fixed to the value predicted by the  $J/\psi$  candidate mass fit.

The unbinned log-likelihood is:

$$\mathcal{L} = -2 \ln \prod_i (f_{back} \cdot g_{back}(c\tau_i) + (1 - f_{back})[(1 - f_B^s) \cdot F_{direct}^{c\tau}(c\tau_i) + f_B^s \cdot F_b^{c\tau}(c\tau_i)]) \quad (5.6)$$

The functional forms of  $F_{direct}^{c\tau}(x)$  and  $F_b^{c\tau}(x)$  are shown below:

$$F_{direct}^{c\tau}(x) = (1 - f_1^s - f_2^s) \cdot G(x, \sigma^s) + f_1^s \cdot E(|x|, \lambda_1^s) + f_2^s \cdot E(|x|, \lambda_2^s) \quad (5.7)$$

$$F_b^{c\tau}(x) = E(y, \lambda_B^s) * F_{direct}^{c\tau}(x - y) = \int_0^\infty F_{direct}^{c\tau}(x - y) \cdot E(y, \lambda_B^s) dy \quad (5.8)$$

The fit parameters are:

$f_{back}$ : fraction of background events in the signal region

$f_B^s$ : bottom fraction

$\lambda_B^s$ : average bottom proper decay length

$f_1^s$ : fraction of the resolution function in the first symmetric exponential

$\lambda_1^s$ : length scale of the first symmetric exponential

$f_2^s$ : fraction of the resolution function in the second symmetric exponential

$\lambda_2^s$ : length scale of the second symmetric exponential

$\sigma^s$ : Gaussian width in the resolution function

Table 5.2 and figure 5.3 shows the fit result of the signal region. The fit average bottom proper decay length of  $442 \pm 5 \mu\text{m}$  is consistent with previous measurements at the Tevatron [77, 78]. The fit yields a bottom fraction of  $16.6\% \pm 0.2\%$  or equivalently  $22150 \pm 270$   $J/\psi$  from bottom decay.

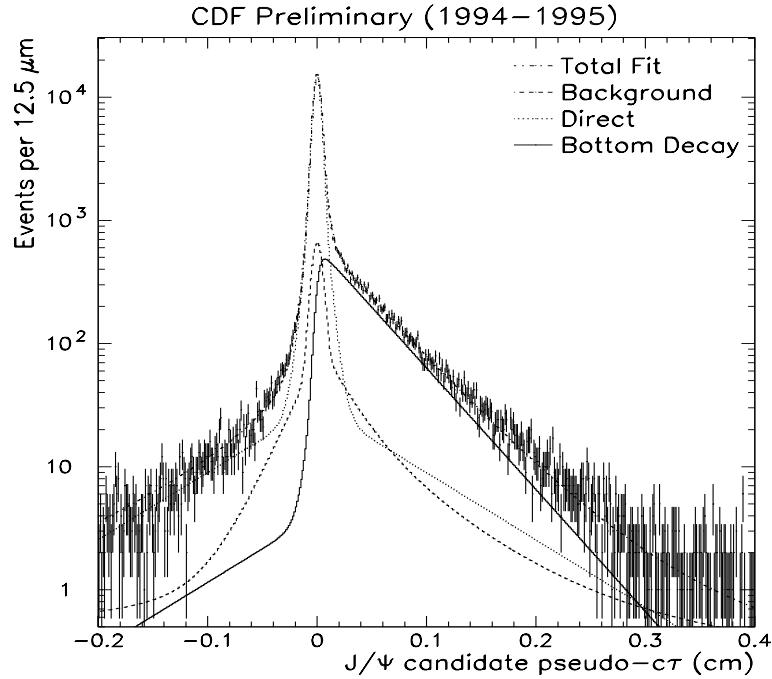


Figure 5.3: *Fit of  $J/\psi$  signal region.*

### 5.1.2 Direct impact parameter shape

In previous analyses [27, 28], the impact parameter distributions for particles originating at the primary vertex was determined using jet data. Unfortunately, any data sample will have low level contamination of heavy flavor (charm or bottom) at the  $\approx 0.1 - 1\%$  level, which is larger than the non-Gaussian effects in the impact parameter resolution. In this

Parameter	Fit
$f^{back}$	7.04% ( <i>fixed</i> )
$f_B^s$	$16.6\% \pm 0.2\%$
$\lambda_B^s$	$442\mu\text{m} \pm 5\mu\text{m}$
$f_1^s$	$34.2\% \pm 1.5\%$
$\lambda_1^s$	$46.7\mu\text{m} \pm 1.1\mu\text{m}$
$f_2^s$	$3.60\% \pm 0.12\%$
$\lambda_2^s$	$797\mu\text{m} \pm 27\mu\text{m}$
$\sigma^s$	$34.2\mu\text{m} \pm 0.2\mu\text{m}$

Table 5.2: *Fit result of signal region of  $J/\psi$  data.*

analysis, the impact parameter shapes of directly produced particles are determined with a Monte Carlo technique.

PYTHIA is used to generate the light quark and gluon subprocesses, which is then passed through a detector simulation. To be included in the electron direct shape, the candidates must be a quality track with a  $p_T > 2$  GeV and extrapolate into the electron fiducial region described in section 4.4. For the muon direct shape, the candidates must be a quality track with a  $p_T > 3$  GeV and extrapolate into the CMUP muon fiducial region described in section 4.3.

The Monte Carlo events which pass the selection criteria are fit with two symmetric exponentials and a Gaussian :

$$F_{direct}^{d_0}(x) = (1 - f_1 - f_2) \cdot G(x, \sigma_d) + f_1 \cdot E(|x|, \lambda_1) + f_2 \cdot E(|x|, \lambda_2) \quad (5.9)$$

The fit results for both electron and muon samples are shown in table 5.3. Figures 5.4 and 5.5 show the fit results to the electron and muon direct Monte Carlo samples.

### 5.1.3 Bottom impact parameter shapes

The impact parameter shape of bottom decay leptons is determined by Monte Carlo simulation, using the prescription from ref. [21] for leading-log order showering Monte

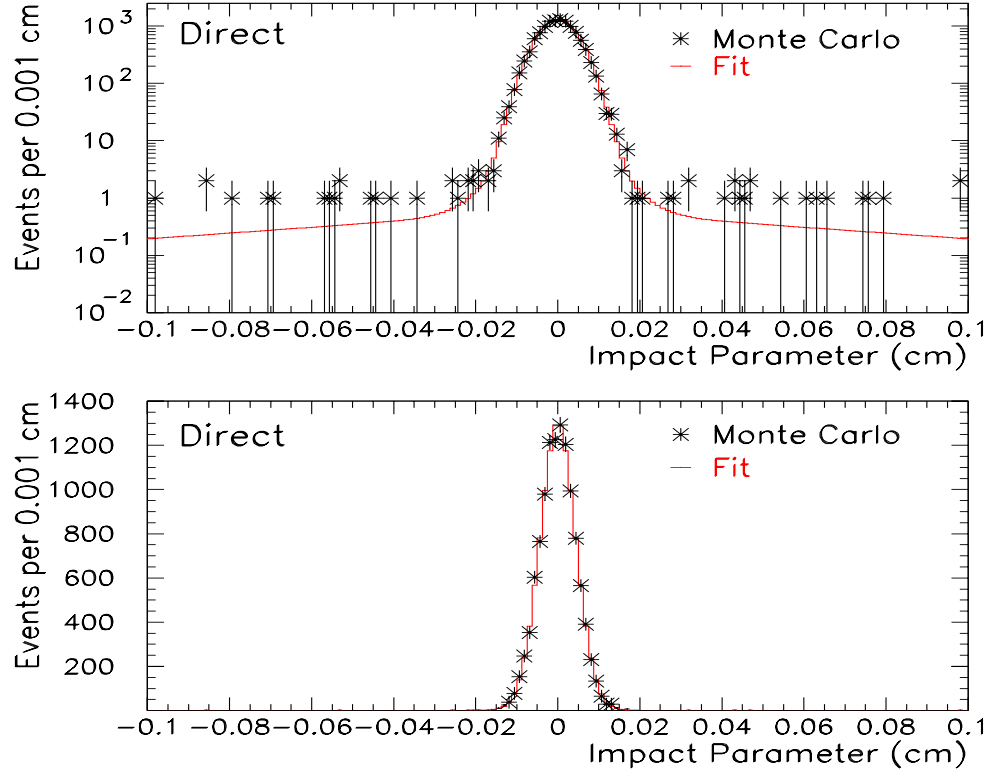


Figure 5.4: The signed impact parameter distribution for the simulated electron direct production. Top: Logarithmic scale. Bottom: Linear scale.

Parameter	Electron	Muon
$f_1$	$5.1 \pm 2.7\%$	$3.0 \pm 2.7\%$
$\lambda_1$	$42.2 \pm 6.9\mu\text{m}$	$76.3 \pm 38.7\mu\text{m}$
$f_2$	$0.7 \pm 0.1\%$	$0.5 \pm 0.3\%$
$\lambda_2$	$862 \pm 109\mu\text{m}$	$937 \pm 483\mu\text{m}$
$\sigma_d$	$44.1 \pm 0.4\mu\text{m}$	$40.2 \pm 1.1\mu\text{m}$

Table 5.3: Fit results for the direct electron and muon Monte Carlo samples.

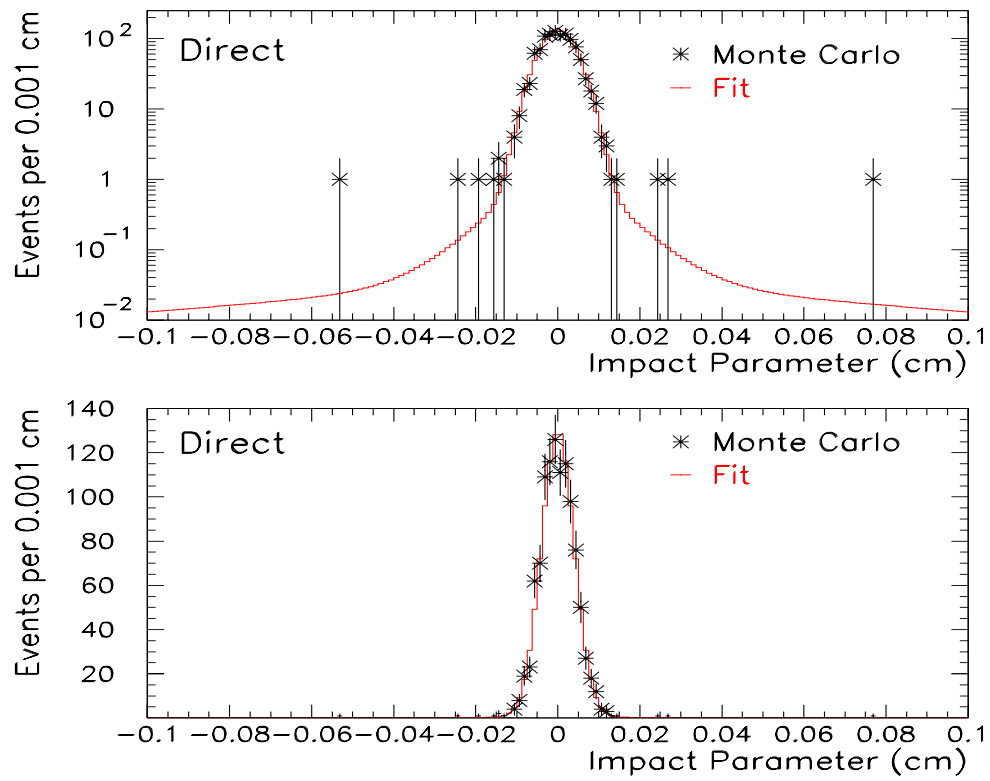


Figure 5.5: The signed impact parameter distribution for the simulated direct muon production. Top: Logarithmic scale. Bottom: Linear scale.

Carlo. In this prescription, separate samples of flavor creation, flavor excitation, and gluon splitting Monte Carlo are generated and then combined with the relative rates predicted by the Monte Carlo. As will be shown later, the impact parameter from all three mechanisms are very similar.

PYTHIA [40] with the CTEQ3L [35] parton distribution functions is used. The bottom quarks are hadronized using the Bowler fragmentation function [43] and using the LUND string fragmentation model. The resulting bottom hadrons are decayed using the CLEO decay model [82]. The events are then placed through a detector simulation [83] and the trigger simulation [73]. The same selection criteria is applied to the  $J/\psi$  candidates in Monte Carlo as in data.

For the bottom decay impact parameter shape for muons, the muons are required to be fiducial in both the CMU and the CMP muon subsystems (as described in section 4.3) with a quality track with a  $p_T > 3$  GeV. The efficiency of  $\chi^2$  matching in the CMU and CMP is constant above 3 GeV [71]<sup>3</sup>. Since the measurement is a fraction, the efficiency cancels and is not applied to the Monte Carlo.

For the bottom decay shapes for electrons, the electrons are required to be fiducial (as described in section 4.4) with a quality track with  $p_T > 2$  GeV. The efficiency of the electron identification criteria is simulated in the same manner as ref. [31]. The CPR, the CES, and the CTC  $dE/dx$  selection criteria do not depend on the isolation of the electron, due to the fine segmentation of the CPR, the CES and the CTC. Therefore, the efficiencies as a function of  $p_T$  of the CPR and the CES selection derived by ref. [84] using conversions can be used. The CTC  $dE/dx$  efficiency as a function of  $p$  is defined by the selection criteria. Figure 5.6 shows the efficiencies used. The conversion removal over-efficiency, and

---

<sup>3</sup>The CMU/CMP efficiency is  $97 \pm 5\%$



the  $E_{had}/E_{EM}$  and  $E/p$  efficiencies depend on the isolation of the track; therefore, the values simulated in the Monte Carlo have to be used to determine the efficiency.

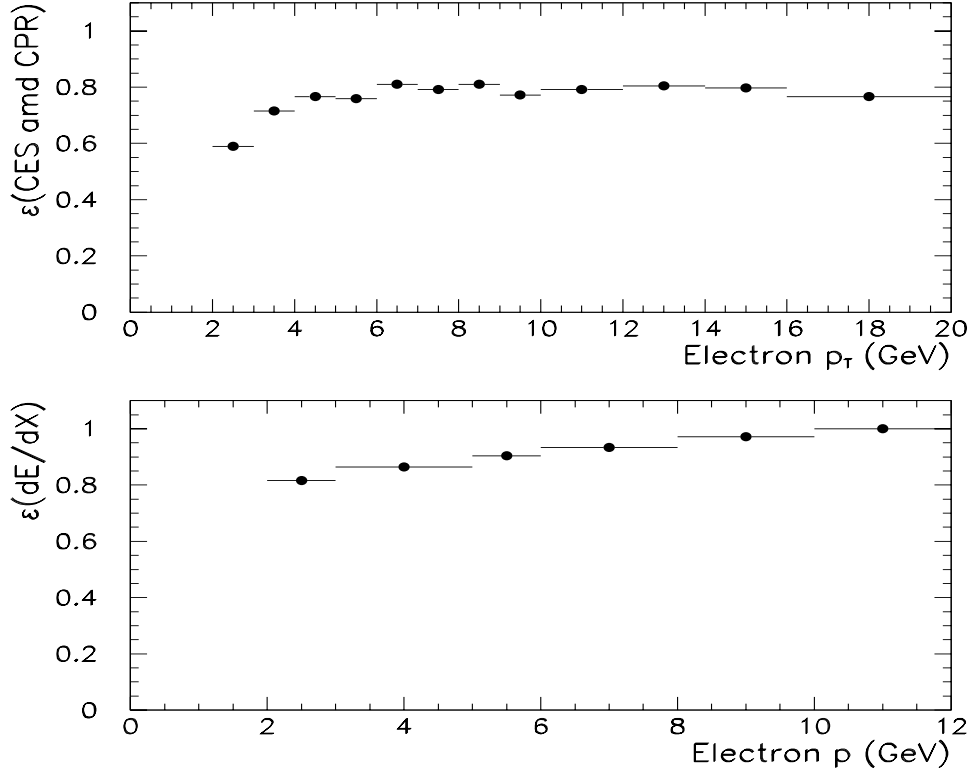


Figure 5.6: Top: Combined CES and CPR electron selection efficiency from [84]. Bottom: CTC  $dE/dX$  selection efficiency.

Figure 5.7 shows the unsigned impact parameter for direct bottom electrons ( $b \rightarrow ce^-$ ) and sequential charm electrons ( $b \rightarrow c \rightarrow se$ ) in the flavor creation Monte Carlo. As stated before, the impact parameter distributions are similar and cannot be fit for separately. Table 5.4 shows the sequential charm fractions ( $f_{seq} = \frac{N_{b \rightarrow cX \rightarrow stY}}{N_{b \rightarrow cX \rightarrow stY} + N_{b \rightarrow clX}}$ ) for flavor creation, flavor excitation, and gluon splitting Monte Carlo. The fractions are slightly higher in the flavor creation Monte Carlo because the  $p_T$  spectra of the non- $J/\psi$  bottom hadron is slightly higher. The uncertainty on the sequential fraction is one of the

	FC	FE	GS
Electron	$16.9 \pm 0.7\%$	$16.1 \pm 0.7\%$	$13.0 \pm 0.5\%$
Muon	$15.6 \pm 1.0\%$	$12.9 \pm 1.0\%$	$13.2 \pm 0.8\%$

Table 5.4: *Sequential charm fractions predicted by PYTHIA Monte Carlo.*

systematic uncertainties treated in section 5.4.

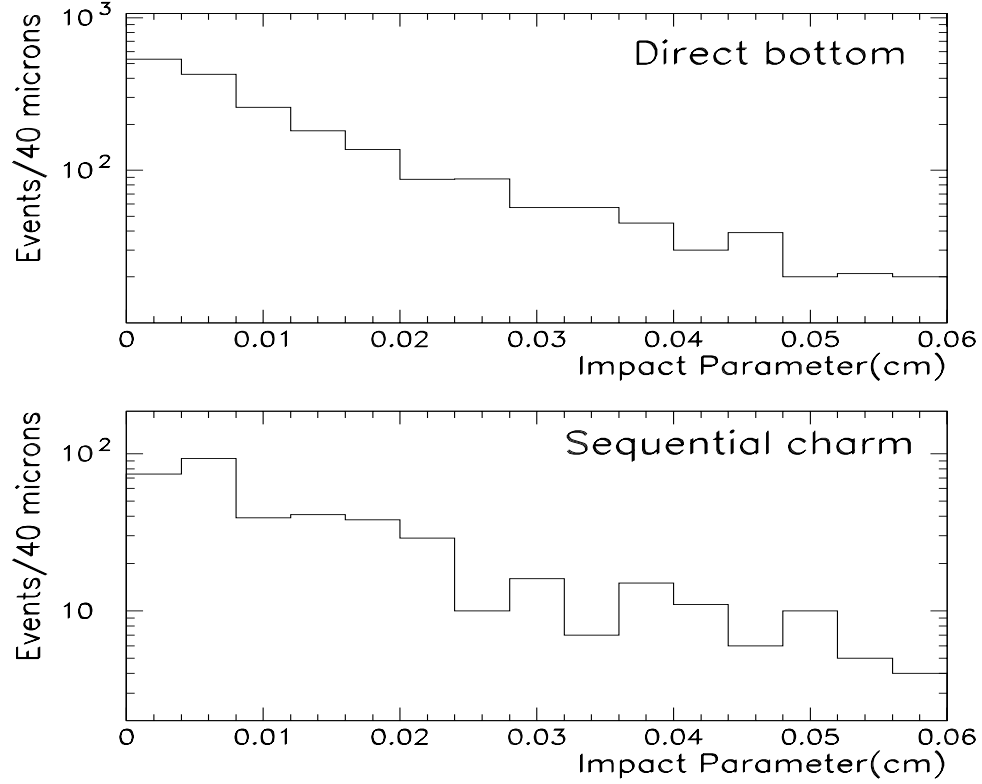


Figure 5.7: *The impact parameter of events with electrons passing requirement in the flavor creation Monte Carlo sample. Top: Direct bottom. Bottom: Sequential charm.*

The bottom decay impact parameter shape is fit with two symmetric exponentials and a Gaussian.

The fit function is:

$$F_b^{d_0} = (1 - f_1 - f_2) \cdot G(d_0 - c_b, \sigma_b) + f_1 \cdot E(|d_0|, \lambda_1) + f_2 \cdot E(|d_0|, \lambda_2) \quad (5.10)$$

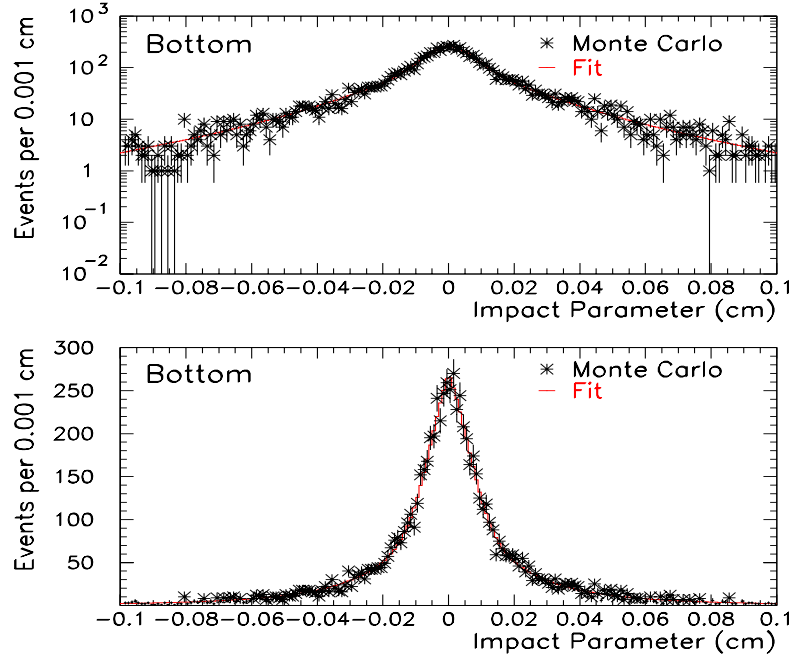


Figure 5.8: *The signed impact parameter distribution for the combined electron bottom Monte Carlo. Top: Logarithmic scale. Bottom: Linear scale.*

The impact parameter distribution is fit separately for each production mechanism as well the combination of the three mechanisms predicted by PYTHIA for both the electron and muon samples. The results of the combined fit are shown in table 5.5 and in figures 5.8 and 5.9. Figure 5.10 shows the shapes fit for the three production mechanisms separately for the electron sample. The fit shapes for the three mechanisms are very similar.

Parameter	Electron	Muon
$f_1$	$48.2 \pm 4.6\%$	$57.3 \pm 5.9\%$
$\lambda_1$	$135 \pm 15\mu\text{m}$	$129 \pm 24\mu\text{m}$
$f_2$	$30.5 \pm 4.6\%$	$23.1 \pm 6.3\%$
$\lambda_2$	$367 \pm 22\mu\text{m}$	$406 \pm 45\mu\text{m}$
$\sigma_b$	$66 \pm 4\mu\text{m}$	$64 \pm 7\mu\text{m}$
$c_b$	$3.9 \pm 3.4\mu\text{m}$	$0.7 \pm 5.2\mu\text{m}$

Table 5.5: *Fit results of bottom impact parameter shape.*

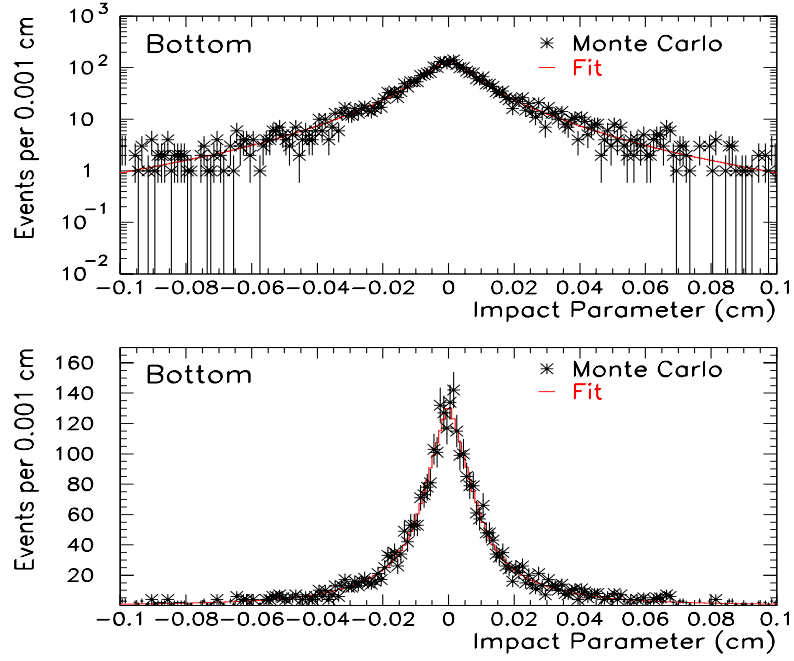


Figure 5.9: *The signed impact parameter distribution for the combined muon bottom Monte Carlo. Top: Logarithmic scale. Bottom: Linear scale.*

#### 5.1.4 Residual conversion background rate ( $R_{conv}$ )

One obvious source of electron background is residual conversions left in the sample, due to the inefficiency of finding the conversion pair. The number of residual ( $N_{resid}$ ) and found conversions ( $N_{found}$ ) is greatly reduced by the SVX hit requirement on the candidates, as conversions that occur outside the second layer of SVX do not have enough real attached hits to pass the requirements. The large impact parameter of conversion electrons at large conversion radii still allows for the attachment of SVX clusters not associated with the track at a decreased rate. The large impact parameter leads to large silicon hit search roads, causing the increase in the attachment of incorrect SVX hits relative to tracks originating closer to the primary vertex.

In order to estimate the number of residual conversions, a technique similar to ref. [85]

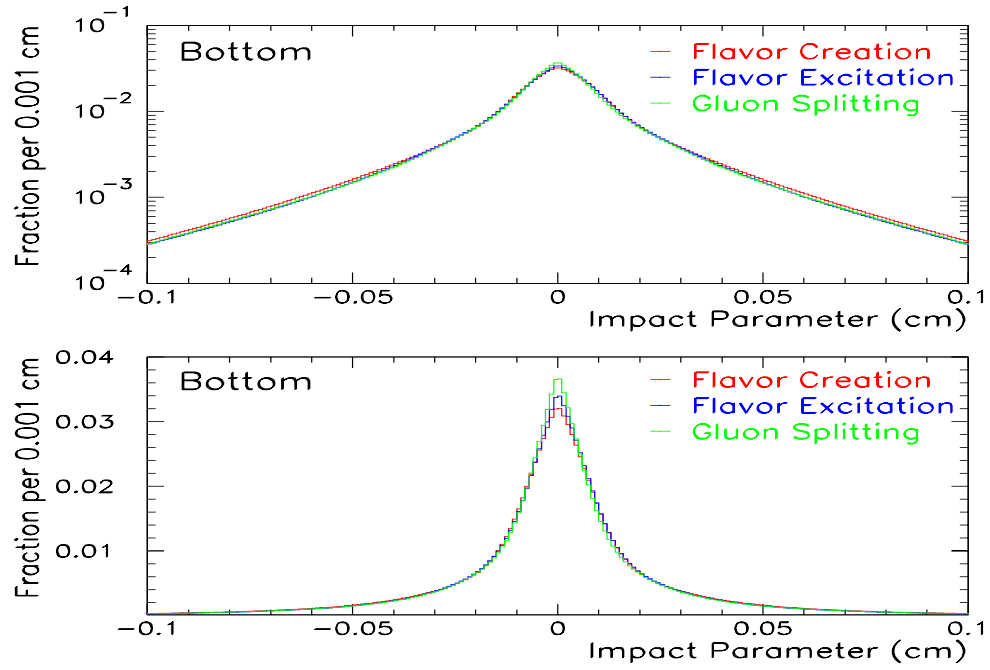


Figure 5.10: The signed impact parameter distributions of electron Monte Carlo for the three bottom production mechanisms. Both directly produced and sequential muons are included in the distribution. Top: Logarithmic scale. Bottom: Linear scale.

is used. In the technique, one assumes that there are two independent causes for the lack of removal of a conversion electron: the track pair is lost due to tracking inefficiencies at low momenta or the selection requirements are not fully efficient. By measuring these two efficiencies and the rate of conversion removal with the chosen conversion selection requirements, one determines the residual electrons ( $N_{resid}$ ). The conversion electron that passes the electron identification criteria is denoted as the SLT conversion candidate, and other electron that did not pass the electron identification criteria is denoted as the pair candidate.

The number of residual electrons is equal to:

$$N_{resid} = N_{tag} \cdot P_{cnv} \cdot \left( \frac{1}{\epsilon_{cnv}(cut)} \cdot \frac{1}{\epsilon_{cnv}(p_T)} - 1 \right) \quad (5.11)$$

where:

$N_{tag}$  is the number of the conversions removed,  $P_{cnv}$  is the purity of the conversions removed,  $\epsilon_{cnv}(cut)$  is the conversion finding efficiency, and  $\epsilon_{cnv}(p_T)$  is the tracking efficiency of the conversion pair.

$P_{cnv}$  is assumed to be 100% in this analysis and in previous measurements at CDF [31], when SVX hits are required for the SLT conversion candidate. As an estimate of the systematic uncertainty, the  $dE/dx$  measured in the CTC for both SLT conversion and pair candidate are fit simultaneously; the fit is described in appendix A. The  $J/\psi$  mass and vertex probability requirements are removed in order to increase statistics. In addition, the  $dE/dx$  requirement on the conversion leg is removed in order to fit the hadron fractions.  $66.5 \pm 8.2$  of the 69 candidates fit to the hypothesis of an conversion (both legs being an electron). The fit result is consistent with the sample containing only conversions. The difference between the fraction fit from 100% is use to estimate of the systematic

Parameter	Tight	Loose	Looser	Loosest
r- $\phi$ Separation	0.2 cm	0.5 cm	1.0cm	2.0cm
$\Delta\cot(\theta)$	0.03	0.06	0.12	0.24
$\Delta z$	2.0 cm	5.0cm	10.0cm	10.0cm
Conversion radius	-5 cm to 50 cm	-10 cm to 50 cm	-20 cm to 50 cm	
$\Delta\phi$	0.01	0.05	0.1	0.1
Pointing residual	1.0 cm	1.0 cm	2.0 cm	2.0cm

Table 5.6: *Tight and looser sets of cuts used in conversion finding.*

uncertainty. Thus,  $P_{cnv} = 100.0 \pm 3.7\%$ .

$\epsilon_{cnv}(cut)$  is measured using different sets of conversion requirements, the standard (tight) and a loose set cuts. The number of conversions candidates is determined with the  $dE/dx$  fitter using both sets of cuts. First, the events passing the tight selection are fit. Next, the events passing the loose selection, but not the tight selection are fit in order to get a statistically independent sample. Assuming that the loose cuts are fully efficient, the number of conversion pairs fit with tight and loose cuts yields  $\epsilon_{cnv}(cut)$ . In order to test this assumption, 2 additional wider sets of cuts are used.

Table 5.6 lists the requirements and the results of the fit are shown in table 5.7. No events are fit where the SLT conversion candidate is a kaon or proton, and therefore these quantities are fixed to zero.

Figure 5.11 and 5.12 show the fit results for the tight and loosest conversion selection requirements. The increased pions and kaon fractions as the selection criteria is loosened can be seen by the increase in the events with low  $dE/dx$ . Table 5.8 shows  $\epsilon_{cnv}(cut)$  assuming a given set of selection criteria is fully efficient. The fit number of electron pairs is same within errors for the three wider set of conversion requirements. The ratio between the tight and loose selection criteria is chosen to be  $\epsilon_{cnv}(cut) = 72.3 \pm 6.5\%$ .

The tracking efficiency of the pair candidates ( $\epsilon_{cnv}(p_T)$ ) is estimated with a Monte

Cut	N(e,e)	N(e, $\pi$ )	N(e,k)	N(e,p)
Tight	$66.5 \pm 8.2$	$0 \pm 1.6$	$0 \pm 3.0$	$0 \pm 2.3$
Loose	$25.4 \pm 7.7$	$14.2 \pm 11.4$	$3.3 \pm 11.2$	$0 \pm 1.4$
Looser	$27.0 \pm 10.2$	$48.4 \pm 14.4$	$9.3 \pm 12.7$	$0 \pm 4.1$
Loosest	$26.9 \pm 10.8$	$144.4 \pm 18.9$	$2.9 \pm 14.2$	$0 \pm 2.4$

Cut	N( $\pi$ ,e)	N( $\pi$ , $\pi$ )	N( $\pi$ ,k)	N( $\pi$ ,p)
Tight	$0 \pm 3.0$	$0 \pm 1.5$	$2.4 \pm 2.1$	$0 \pm 3.3$
Loose	$2.4 \pm 5.2$	$19.9 \pm 9.1$	$0.6 \pm 18.0$	$0 \pm 1.6$
Looser	$6.5 \pm 7.5$	$53.1 \pm 15.2$	$7.1 \pm 13.4$	$3.2 \pm 3.5$
Loosest	$21.7 \pm 10.8$	$123.3 \pm 20.4$	$16.5 \pm 16.8$	$11.9 \pm 5.3$

Table 5.7: Results of the fitting the  $dE/dx$  of conversion candidates using the tight and looser sets of cuts. For the looser set of cuts, candidates which pass the tight set of selection requirements are excluded.

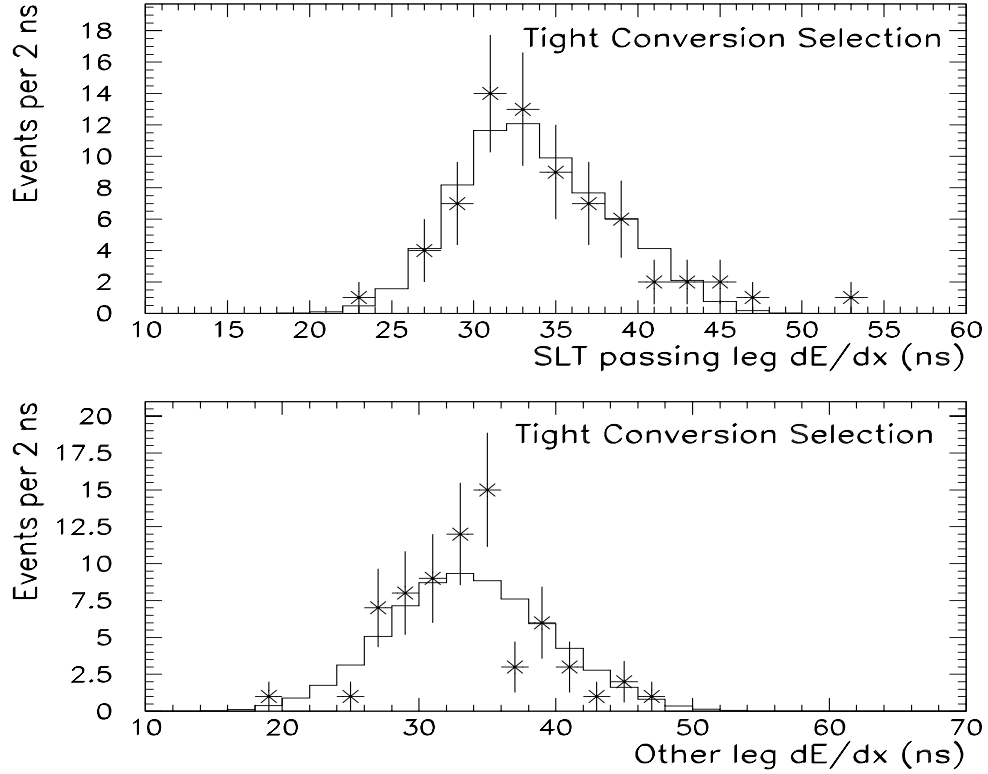


Figure 5.11: Fit of the CTC  $dE/dx$  measured of events with the tight conversion selection criteria. Top: SLT conversion candidate. Bottom: Pair candidate.



Cut	$\epsilon_{cnn}(cut)$
Loose	$0.723 \pm 0.065$
Looser	$0.711 \pm 0.082$
Loosest	$0.712 \pm 0.086$

Table 5.8: The conversion selection requirement efficiency( $\epsilon_{cnn}(cut)$ ) for the standard (tight) selection requirements assuming a given set of loosened cuts is fully efficient.

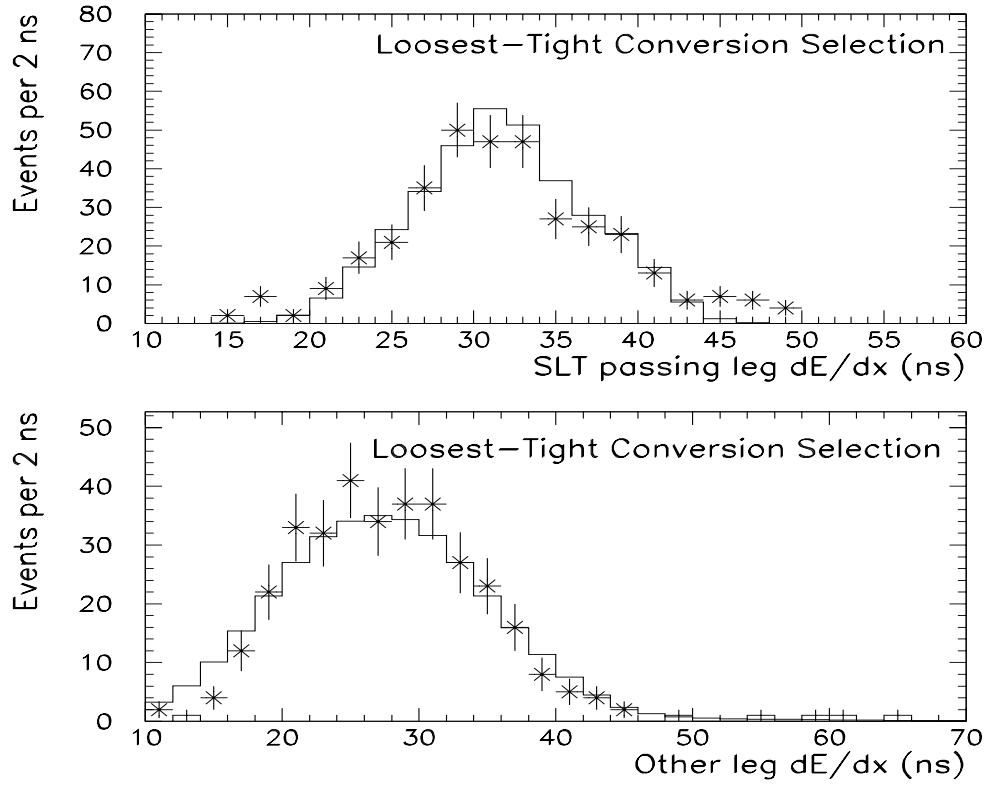


Figure 5.12: Fit of the CTC  $dE/dx$  measured for events passing the loosest conversion selection criteria, but not the tight selection criteria. Top: SLT conversion candidate. Bottom: Pair candidate.

Carlo technique similar to ref. [31]. A sample of  $\pi^0$  is simulated in the detector. A SLT conversion candidate is required to have a quality track in the electron fiducial region with a  $p_T > 2$  GeV. The efficiency of electron identification requirements is simulated in the same manner as section 5.1.3.  $\epsilon_{cnv}(p_T)$  is estimated by comparing the Monte Carlo truth information of the conversion partner to the  $p_T$  of the conversion partners found in data. The simulation is normalized to the data in the  $p_T$  range where the tracking is assumed to be fully efficient; in this analysis,  $p_T > 0.5$  GeV is the region chosen. The ratio of the number of events seen in data versus the number of normalized conversion candidates in Monte Carlo is the estimate of  $\epsilon_{cnv}(p_T)$ . The data sample is the same one used to determine  $\epsilon_{cnv}(cut)$  with the CTC  $dE/dx$  requirement applied to the SLT conversion candidate. 62 of the 69 conversion candidates pass the additional  $dE/dx$  requirement.

The simulated  $\pi^0$  are generated with a power law spectra for  $p_T$  and a flat  $\eta$  distribution. The order of the power law is varied in order to match the  $p_T$  spectra of the found SLT conversion candidates in data. The shape of the found pair candidates'  $p_T$  is used as a cross check of the power law description of the conversions. Figure 5.13 shows the Monte Carlo spectra normalized to the data for a power law of 3, 3.5, 4, and 5. The 3.5 order power law describes the data well and is used for the calculation of the efficiency. The 3rd and 4th order power law is used as a estimate of the systematic uncertainty.

The  $p_T$  of the pair candidates is shown in figure 5.14. The 3.5 order power law describes the shape of events with  $p_T > 0.5$  GeV (where the tracking is assumed to be fully efficient). Table 5.9 shows the average and rms  $p_T$  for both conversion legs, which also confirms the choice of 3.5. Table 5.10 shows the estimated  $\epsilon_{cnv}(p_T)$  for the different power law Monte Carlo. Half the difference between the 3rd and 4th order power law spectra is used as the

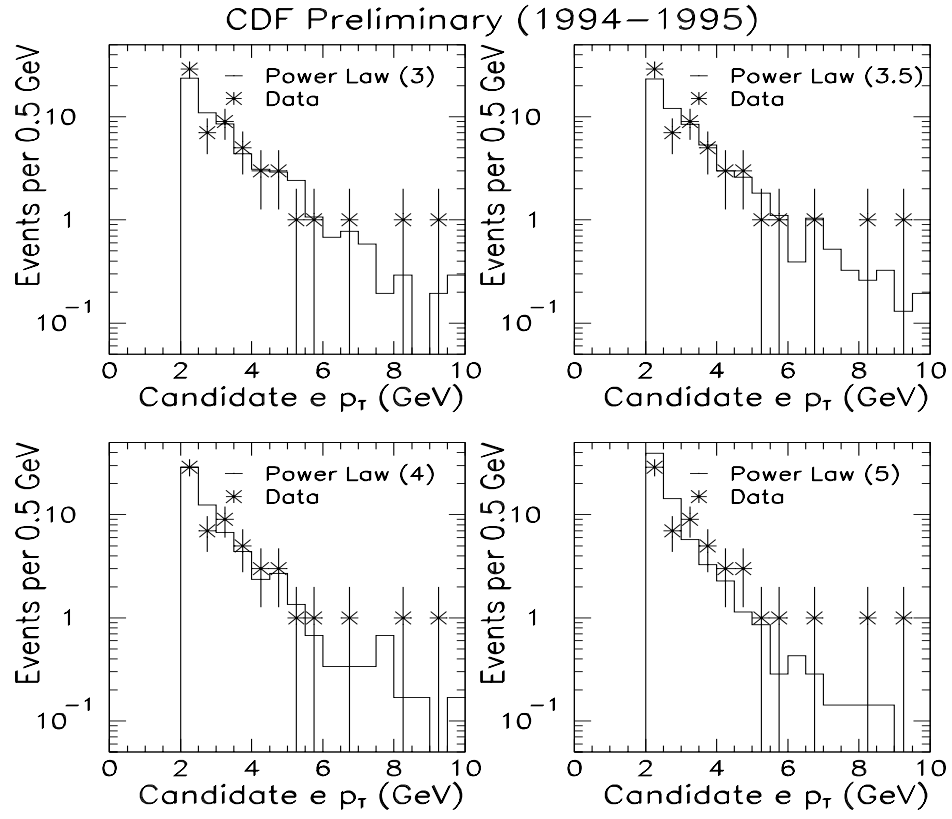


Figure 5.13: The  $p_T$  spectra of the SLT conversion candidates. Top Left: 3rd order power law. Top Right: 3.5 order power law. Bottom Left: 4th order power law. Bottom Right: 5th order power law.

systematic uncertainty of the estimate.  $\epsilon_{conv}(p_T)$  is determined to be  $69 \pm 5(\text{stat}) \pm 9(\text{syst})\%$ .

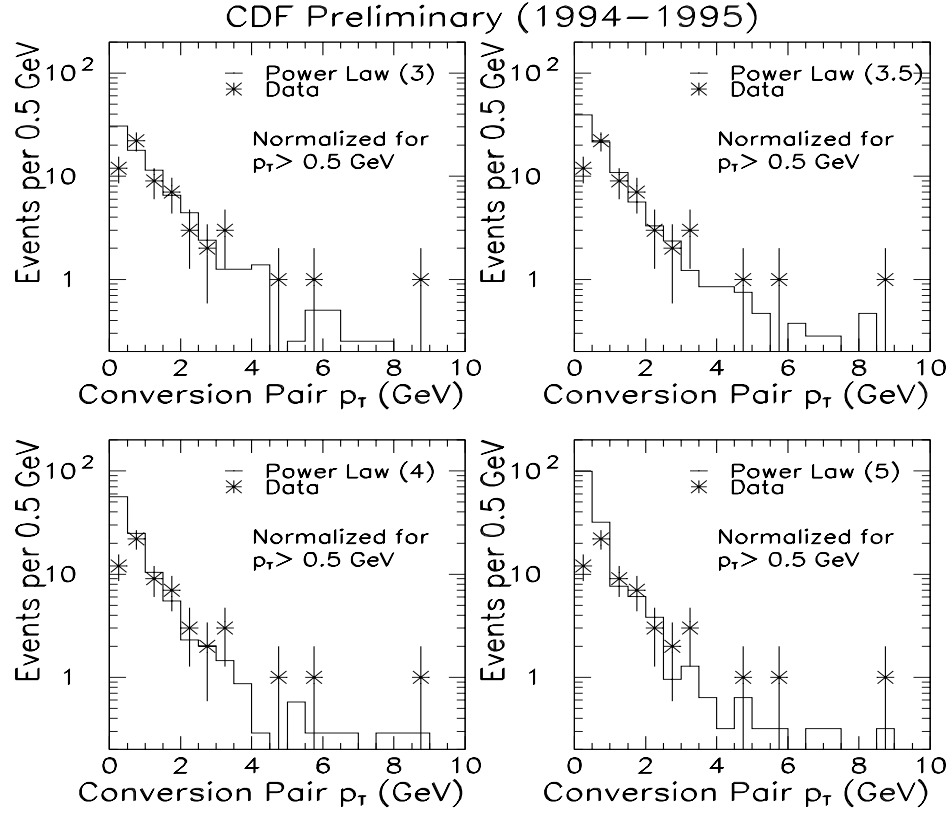


Figure 5.14: The  $p_T$  spectra of the pair candidates. The Monte Carlo is normalized to the data with  $p_T > 0.5$  GeV. Top Left: 3rd order power law. Top Right: 3.5 order power law. Bottom Left: 4th order power law. Bottom Right: 5th order power law.

Using equation 5.11, the estimate of the number of residual conversions is  $N_{resid} = (1.00 \pm 0.38) \cdot N_{found}$ . The ratio of the number of residual to found conversions is called  $R_{conv} = 1.00 \pm 0.38$ . The conversion veto removes 6(9) SLT electron candidates in the toward(away)  $\Delta\phi$  region. Thus, approximately 6.0(9.0) residual conversion are in toward(away)  $\Delta\phi$  region. About 5% of the SLT electron candidates are residual conversions and have to be included in the  $c\tau$ -impact parameter fit. A total of 9 conversions (4 toward, 5 away) are found in events with the  $J/\psi$  candidate in the mass sideband region.

	Data	3rd	3.5	4th	5th
Ave $p_T$ SLT leg	3.32	3.46	3.36	3.09	2.81
RMS $p_T$ SLT leg	1.74	1.99	1.75	1.34	1.20
Ave $p_T$ other leg	1.91	1.97	1.74	1.53	1.40
RMS $p_T$ other leg	2.29	2.00	1.69	1.39	1.24

Table 5.9: Average and RMS of  $p_T$  spectra (in GeV) for both the SLT conversion candidate and the pair candidate.

Power law	$\epsilon_{conv}(pt)$
3rd	$0.77 \pm 0.04$
3.5	$0.69 \pm 0.05$
4th	$0.58 \pm 0.04$
5th	$0.44 \pm 0.03$

Table 5.10:  $\epsilon_{conv}(pt)$  calculated using the given order of Monte Carlo power law spectra for the  $\pi^0$ .

### 5.1.5 Residual conversion impact parameter shape

Initially, unsigned impact parameters were used for this measurement. Figure 5.15 shows the bottom Monte Carlo and the measured impact parameter of the conversion candidates. The distributions are very similar and attempts at fitting the conversion fraction using unsigned impact parameters were unsuccessful.

Conversion electrons originate from a massless decay. The two electrons are co-linear at the point of decay. If the photon originates at the primary vertex, the two tracks also point at the primary vertex at the conversion point. Using the constraint that the photon originates at the primary vertex and has a massless decay, one arrives at the following equation:

$$R_{conv}^2 = d_0^2 + d_0/c \quad (5.12)$$

where  $R_{conv}$  is the conversion radius and  $c$  is the curvature of the track. As  $1/c$  is always much bigger than the impact parameter,  $d_0 \cong cR_{conv}^2$ . Dalitz decay electrons have impact

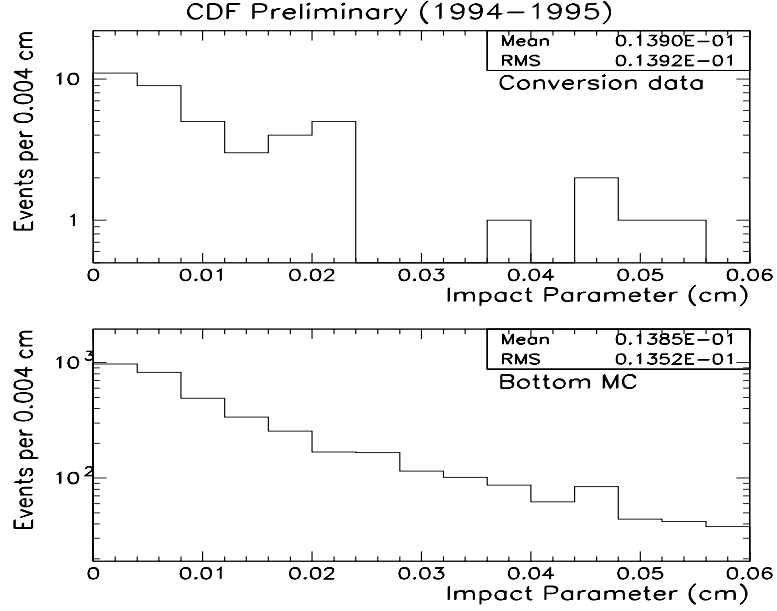


Figure 5.15: *Top: Conversion impact parameter distribution. Bottom: Impact parameter distribution of bottom flavor creation Monte Carlo.*

parameter distribution similar to directly produced tracks.

For conversion electrons from a primary photon, the primary vertex always lies outside of the helix projection with perfect tracking. To distinguish between conversions and bottom decay electrons, the impact parameter is signed such that the impact parameter is positive if the primary vertex is outside the  $r$ - $\phi$  projection of the track's helix, and the sign of the impact parameter is negative otherwise. Conversion electrons are positively signed, and dalitz decay electrons and bottom decay electrons are equally negatively and positively signed, as shown in figure 5.16

Figure 5.17 shows the impact parameter and conversion radius of the conversion candidates. The vast majority of the conversion candidates are signed positive as predicted. Unfortunately, there is a large positive tail which is not consistent with the number of SVX hits assigned to the track. Since at least 3 SVX hits are required, one would expect the

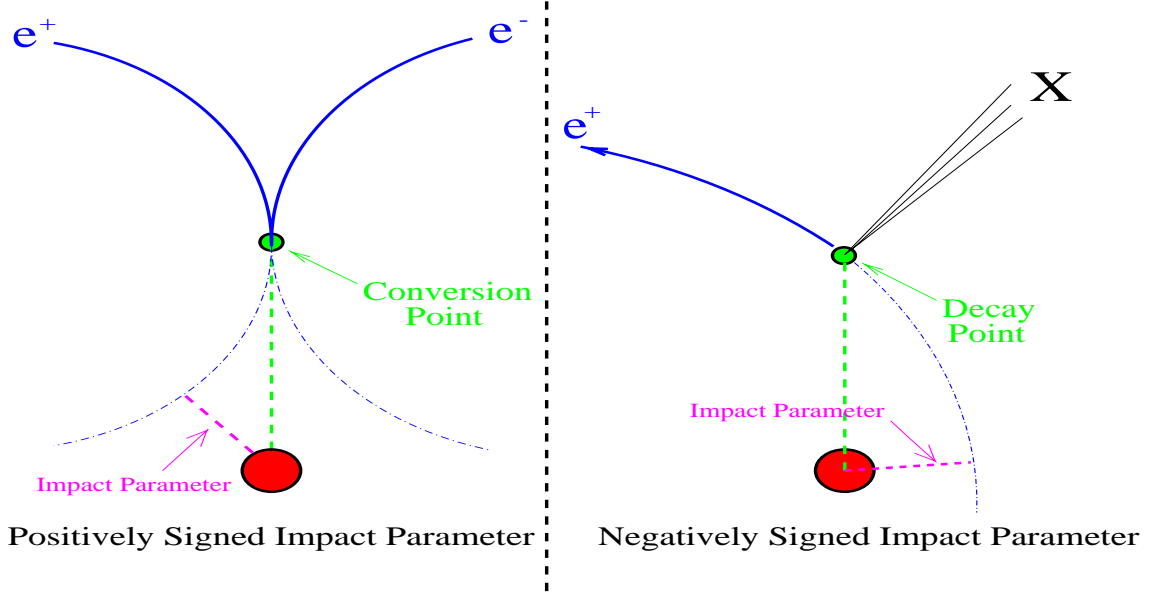


Figure 5.16: *Cartoon of impact parameter signing. With perfect tracking, conversion electrons are always positively signed due to the fact that the photon is massless. Bottom decay electrons have a symmetric impact parameter distribution due to the bottom hadron's mass.*

conversion candidates are either originate from the first two SVX layers or the beam pipe, or be a  $\pi^0$  Dalitz decays from the primary. These sources would produce conversions with a impact parameter less than 0.04 cm. Therefore, a fraction of the conversion candidates must have mis-assigned SVX hits and originate outside of the SVX. The conversion radius plot supports this claim<sup>4</sup>. 25 of the 62 conversion candidates have a radius greater than 6 cm, which is outside of the second SVX' layer. The SVX track quality is studied (see appendix B) and no track quality cuts are found which would remove these events. The  $dE/dx$  measurements are consistent with the entire sample being conversions. In addition, the data lies along the predicted relationship between the impact parameter and the conversion radius as shown in figure 5.18. The increased scatter relative to the  $d_0 = cR_{conv}^2$  prediction at large  $R_{conv}$  is due to the fact the SVX hits assigned to the tracks are incorrect; therefore, the tracks have the impact parameter resolution typical of a CTC only

<sup>4</sup>The conversion radius calculation only used CTC information and has a resolution of  $\approx 1$  cm.

track ( $\approx 700 \mu\text{m}$ ). At small  $R_{conv}$ , the SVX hits are typically correctly assigned, yielding an impact parameter resolution of  $\approx 40 \mu\text{m}$ .

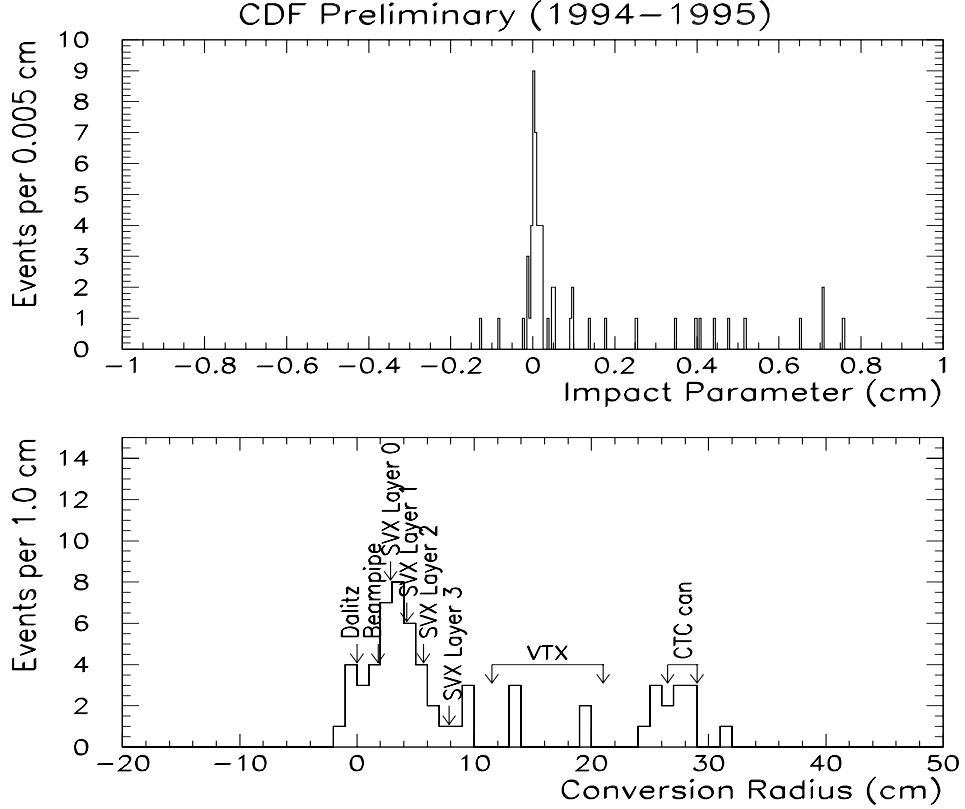


Figure 5.17: *Top: Signed impact parameter of conversion candidates. Bottom: Conversion radius of candidates.*

As there is not enough conversion candidates in order to determine a conversion impact parameter shape from data, a Monte Carlo technique is used. The  $\pi^0$  power law Monte Carlo described in section 5.1.4 is used to derive the impact parameter shape. The Monte Carlo does not predict accurately number of candidates with mis-assigned SVX hits at large radius. Thus, the impact parameter shape is constructed to two parts: a component where the Monte Carlo correctly describes the assignment of SVX hits (mostly low conversion radius,  $R_{conv} < 6 \text{ cm}$ ), and a component where the Monte Carlo does not describe correctly



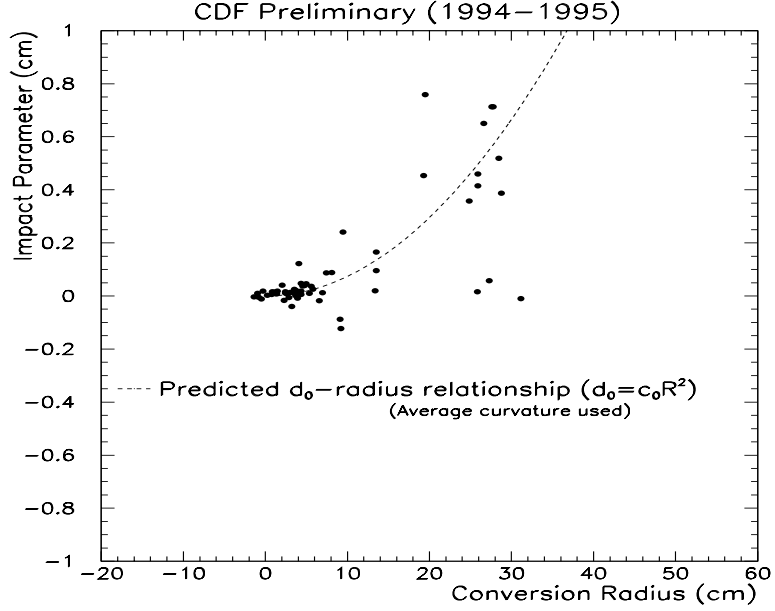


Figure 5.18: *Top: Signed impact parameter of conversion candidates versus the conversion radius.*

the mis-assignment of SVX hits (mostly at high conversion radius,  $R_{conv} > 6$  cm)). The relative fractions of the two components are determined by data. The fraction of conversions with  $R_{conv} > 6$  cm in data and Monte Carlo are matched, with the uncertainty in the fraction in data included as a systematic uncertainty in the fit.  $f_{conv}^{GoodSVX} = 59.7 \pm 6.2\%$  is the fraction of conversion pairs found in data with a conversion radius less than 6 cm.

### “Good” SVX conversion impact parameter shape

To be included in the “Good” SVX conversion shape, the simulated conversion electron must be in the electron fiducial region, with a quality track and a  $p_T > 2$  GeV. The electron identification efficiency is simulated using the same method as for the bottom impact parameter template. The true conversion radius of the candidates is required to be smaller than or equal to the location of the 2nd SVX layer. The resulting events are fit with four Gaussians. The Gaussians are determined from a single Gaussian fit of the

Source	$f_i$	$c_i$	$\sigma_i$
Dalitz	0.313	$3.0 \pm 3.0\mu\text{m}$	$49.6 \pm 2.0\mu\text{m}$
Beam pipe	0.063	$47.5 \pm 7.0\mu\text{m}$	$54.2 \pm 5.0\mu\text{m}$
SVX layer 1	0.336	$68.8 \pm 3.1\mu\text{m}$	$55.0 \pm 2.2\mu\text{m}$
SVX layer 2	0.287	$139.3 \pm 5.0\mu\text{m}$	$82.9 \pm 3.6\mu\text{m}$

Table 5.11: *Parameters used in fit to “Good” SVX portion of the conversion impact parameter shape.*

conversions from each of the four sources of conversions with at least three real SVX hits (Dalitz decays, beam-pipe, SVX layers 1 & 2). The relative normalization between the Gaussian is forced to the relative number of conversions from each source.

$$F_{cnv}^{GoodSVX}(d_0) = \prod_1^4 f_i * G(d_0 - c_i, \sigma_i) \quad (5.13)$$

where:  $f_i$  is the fraction of conversions from source i and  $G(x, \sigma_i)$  is a normalized Gaussian with center of  $c_i$  and width of  $\sigma_i$ . Table 5.11 shows the values used in the fit. The resulting fit is shown in figure 5.19.

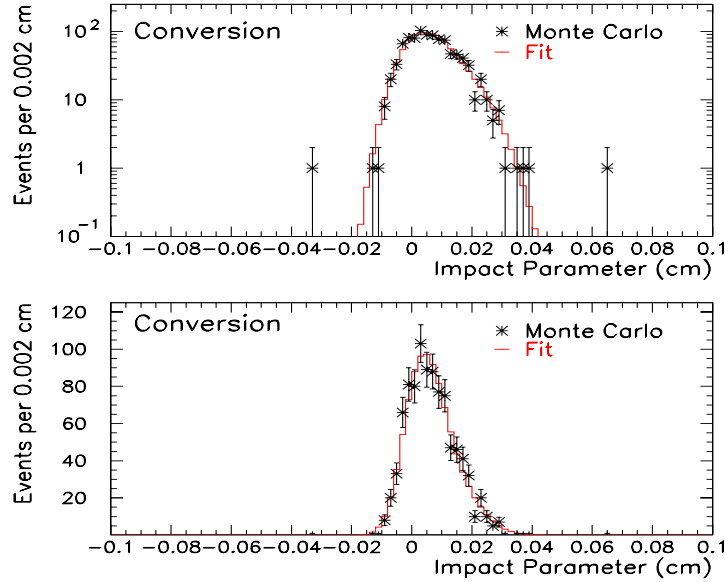


Figure 5.19: *The signed impact parameter distribution for the conversions with correct SVX assignment in Monte Carlo. Top: Logarithmic scale. Bottom: Linear scale.*

### “Bad” SVX conversion impact parameter shape

The “Bad” SVX conversion shape describes the impact parameter distribution of conversions in which at least one SVX hit is mistakenly assigned to the track. To determine the shape, the same Monte Carlo sample and requirements as the “Good” SVX conversion shape are used, except that less than 3 SVX hits are required. Figure 5.20 shows the impact parameter of simulated events that pass this selection. The low impact parameter region consists of conversion electrons which are inside the radius of the second SVX layer but missed at least one of the SVX layers, or which converted in the outside two SVX layers. The large, high impact parameter tail originates from conversion electrons from the VTX and the CTC inner support structure.

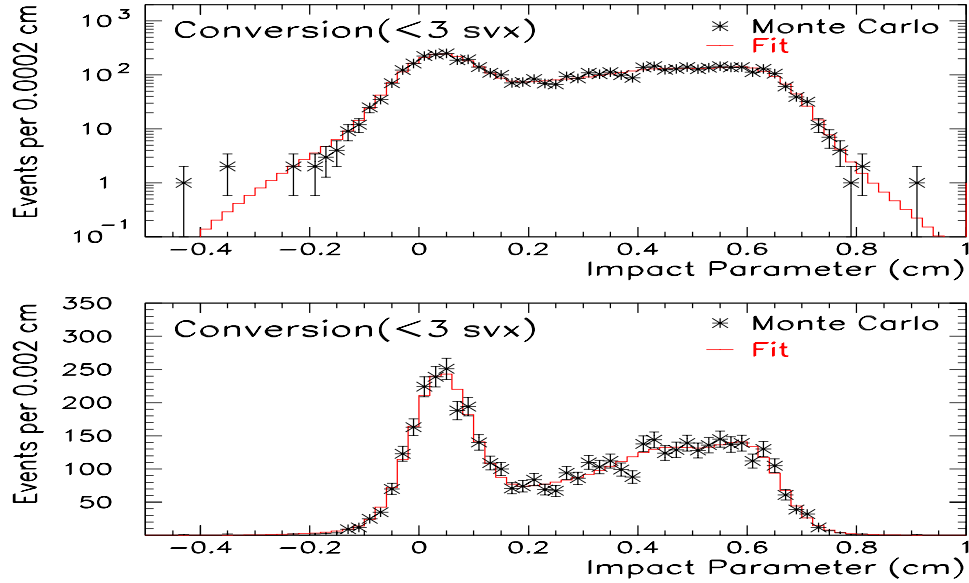


Figure 5.20: The signed impact parameter distribution for the conversions with less than 3 SVX hits assigned in Monte Carlo. Top: Logarithmic scale. Bottom: Linear scale.

The simulated events which pass the selection criteria are fit with four gaussians with the same functional forms as eqn. 5.13. Unlike the “Good” SVX fit, the Gaussians do not

	$f_i$	$c_i$	$\sigma_i$
1	$0.296 \pm 0.042$	$0.0388 \pm 0.0022\text{cm}$	$0.0540 \pm 0.0019\text{cm}$
2	$0.368 \pm 0.032$	$0.272 \pm 0.015\text{cm}$	$0.1864 \pm 0.0051\text{cm}$
3	$0.214 \pm 0.040$	$0.478 \pm 0.019\text{cm}$	$0.0943 \pm 0.0104\text{cm}$
4	$0.122 \pm 0.031$	$0.611 \pm 0.009\text{cm}$	$0.0545 \pm 0.0060\text{cm}$

Table 5.12: *Parameters used in fit to “BAD” SVX portion of the conversion impact parameter shape.*

represent different sources of conversions, but instead just parameterize the shape. The fit results are shown in figure 5.20 and table 5.12.

### Combined conversion impact parameter shape

As stated previously, the “Good” and “Bad” conversion impact parameter shape are combined, such that the fraction of candidates with  $R_{conv} < 6$  cm is the same in data and Monte Carlo.

$$F_{conv} = f_{conv}^{GoodSVX} \cdot F_{cnv}^{GoodSVX}(d_0) + (1 - f_{conv}^{GoodSVX}) \cdot F_{cnv}^{BadSVX}(d_0) \quad (5.14)$$

Figure 5.21 shows the impact parameter of the candidates found in data and the combined conversion impact parameter shape normalized to data. The combined impact parameter shape describes the data surprisingly well, including both the negative tail and large positive tail.

#### 5.1.6 Sideband impact parameter- $c\tau$ shape

Events in the  $J/\psi$  mass sideband region in data are used to describe the impact parameter- $c\tau$  shape of the fake  $J/\psi$  background in the  $J/\psi$  mass signal region. The composition of events in the  $J/\psi$  mass sidebands are unknown; therefore, the shapes have to be fit in a similar manner as section 5.1.1. Due to the limited statistics, the fit shape assumes that the impact parameter and  $c\tau$  are uncorrelated.

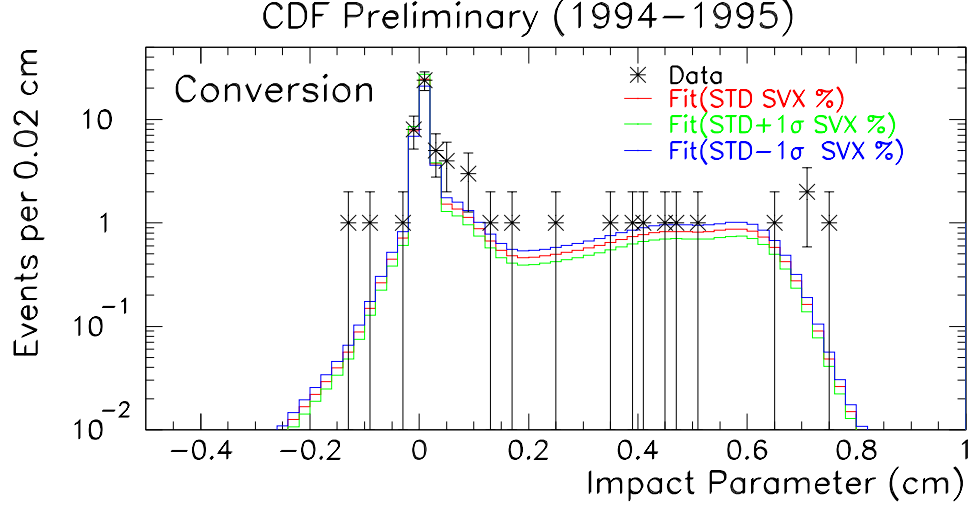


Figure 5.21: The signed impact parameter distribution for conversions found in data. Red: Monte Carlo fit using the central value of  $f_{conv}^{GoodSVX}$ . Green: Monte Carlo fit increasing  $f_{conv}^{GoodSVX}$  by one sigma. Blue: Monte Carlo fit decreasing  $f_{conv}^{GoodSVX}$  by one sigma.

The combined fit function is:

$$F_{sideband}^{\mu}(d_0, c\tau) = F_{sideband}(d_0) \cdot F_{sideband}(c\tau) \quad (5.15)$$

The  $c\tau$  fit function is the same for both samples. The fit shape is:

$$F_{sideband}(c\tau)^e = (1 - f_b^{c\tau}) [(1 - f_1^{c\tau}) \cdot G(d_0, \sigma^{c\tau}) + f_1 \cdot E(|d_0|, \lambda_1^{c\tau})] + f_b \cdot E(x, \lambda_B^{c\tau}) \quad (5.16)$$

For the muon sample, there is no knowledge of the contributions to the muon's impact parameter distribution. Therefore, the shape has to be parameterized. The impact parameter fit function for the muon sample is:

$$F_{sideband}(d_0) = (1 - f_1^{d_0}) \cdot G(d_0, \sigma^{d_0}) + f_1^{d_0} \cdot E(|d_0|, \lambda_1^{d_0}) \quad (5.17)$$

The events with the  $J/\psi$  candidate in the sideband are then fit to determine the impact parameter- $c\tau$  shape for fake  $J/\psi$  in the muon sample. The fit result is shown in table 5.13. Figure 5.22 show the fit results projected onto the  $c\tau$  and impact parameter axis for regions in  $\Delta\phi$  for the muon sample.

Parameter	Muon
$f_1^{d_0}$	$22.4\% \pm 9.4\%$
$\lambda_1^{d_0}$	$301 \mu\text{m} \pm 116 \mu\text{m}$
$\sigma^{d_0}$	$60 \mu\text{m} \pm 9 \mu\text{m}$
$f_B^{c\tau}$	$23.9\% \pm 9.4\%$
$\lambda_B^{c\tau}$	$1100 \mu\text{m} \pm 391 \mu\text{m}$
$f_1^{c\tau}$	$63.1\% \pm 18.0\%$
$\lambda_1^{c\tau}$	$227 \mu\text{m} \pm 82 \mu\text{m}$
$\sigma^{c\tau}$	$49.2 \mu\text{m} \pm 2.1 \mu\text{m}$

Table 5.13: *Fit result of addition muon with the  $J/\psi$  candidate in the sideband region.*

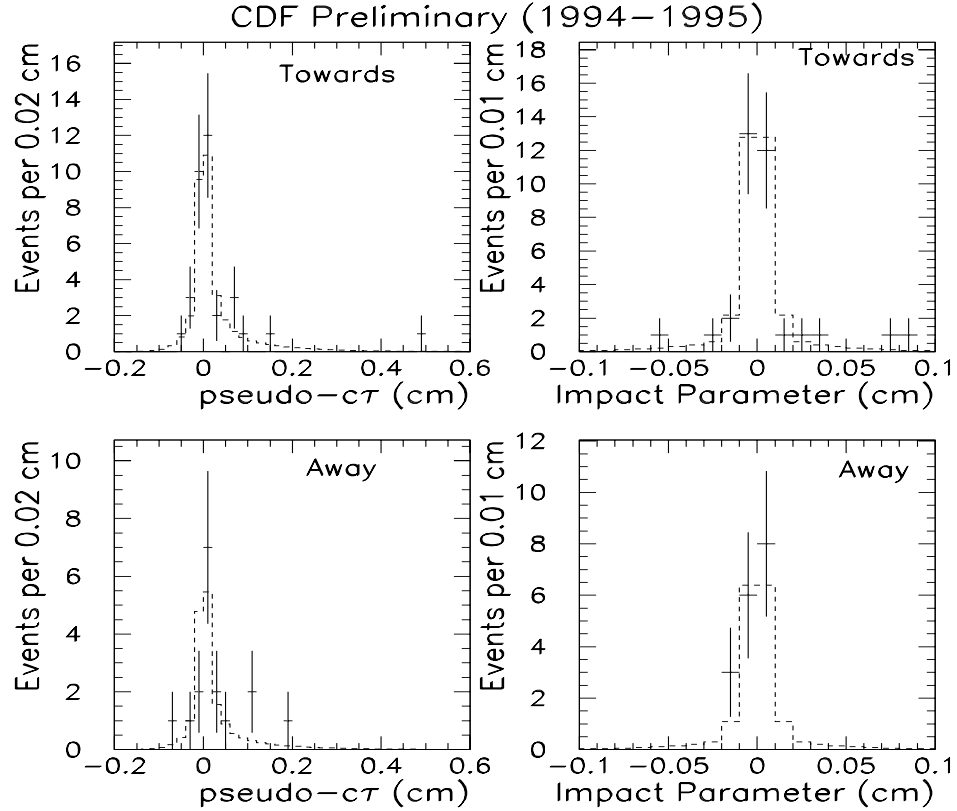


Figure 5.22: *The fit of the muon sample's signed impact parameter and  $c\tau$  distributions in the  $J/\psi$  mass sideband region.*

The sideband impact parameter shape in the electron sample has an additional complication; the electron sample's sideband contains residual conversions. The number of found conversions in the signal region is used as a constraint on the number of residual conversion events in the signal region. Thus, the number of residual conversion event fit in the sideband region has to be known. In the sidebands, the residual conversion fraction is fit for  $f_{conv} = \frac{r_{conv} \cdot n_{convside}}{N_{sideband}}$ .  $r_{conv}$  and  $n_{convside}$  are the fit ratio of residual to found conversions, and fit number of “found” conversions. These quantities are constrained by the estimate of  $R_{conv}$  and the number of found conversions in the sidebands,  $N_{convside}$ . Since  $r_{conv}$  is a component of the signal region fit, the signal and sideband regions have to be fit simultaneously. The signal fit (and how the electron sideband component of the fit is added) are described more thoroughly in section 5.2.

For the electron sample, the impact parameter fit shape is:

$$F_{sideband}(d_0) = (1 - f_{conv}^{d_0}) \cdot \left[ (1 - f_1^{d_0}) \cdot G(d_0, \sigma^{d_0}) + f_1^{d_0} \cdot E(|d_0|, \lambda_1^{d_0}) \right] + f_{conv}^{d_0} \cdot F_{conv}(x) \quad (5.18)$$

The results of the electron impact parameter- $c\tau$  shape fit are shown later (along with the signal fit results) in section 5.3.

### 5.1.7 $B_c \rightarrow J/\psi \ell^+ X$

$B_c$  decay is the only known process that yields a lepton and a  $J/\psi$  from the same displaced vertex. Recent measurements [31] of the  $\frac{\sigma(B_c) \cdot BR(B_c \rightarrow J/\psi \ell \nu)}{\sigma(B^+) \cdot BR(B^+ \rightarrow J/\psi K)}$  and the  $B_c$  lifetime allow one to estimate both the number and impact parameter- $c\tau$  shape of this background. The estimated number of  $B_c \rightarrow J/\psi \ell X$  events in the samples is used as a constraint in the fit.

The number of electron  $B_c$  events in the sample is estimated to be:

$$N^e = \frac{N^K \cdot \mathcal{L} \cdot \sigma(B_c) \cdot BR(B_c \rightarrow J/\psi \ell \nu) \cdot \epsilon_e}{\mathcal{L} \cdot \sigma(B^+) \cdot BR(B^+ \rightarrow J/\psi K) \cdot \epsilon_K \cdot R_c} = N^K \cdot \frac{\sigma(B_c) \cdot BR(B_c \rightarrow J/\psi \ell \nu)}{\sigma(B_u) \cdot BR(B_u \rightarrow J/\psi K)} \cdot R^K / R_c \quad (5.19)$$

Similarly, the number of muon  $B_c$  events will be:

$$N^\mu = N^K \cdot \frac{\sigma(B_c) \cdot BR(B_c \rightarrow J/\psi \ell \nu)}{\sigma(B_u) \cdot BR(B_u \rightarrow J/\psi K)} \cdot R^K \left( \frac{1}{R^e} - 1 \right) / R_c \quad (5.20)$$

where:  $\mathcal{L}$  is the integrated luminosity,  $\sigma(B_c)$  and  $\sigma(B^+)$  are the production cross-sections for  $B_c$  and  $B^+$  at the Tevatron,  $\epsilon_e$ ,  $\epsilon_\mu$ ,  $\epsilon_K$  is the efficiencies for the processes  $B_c \rightarrow J/\psi e \nu$ ,  $B_c \rightarrow J/\psi \mu \nu$  and  $B^+ \rightarrow J/\psi K^+$ ,  $R^K \equiv \frac{\epsilon_e}{\epsilon_K}$ ,  $R^e \equiv \frac{\epsilon_e}{\epsilon_\mu + \epsilon_e}$ ,  $R_c$  is the estimated fraction of  $B_c \rightarrow J/\psi \ell X$  events passing the selection criteria originating from  $B_c \rightarrow J/\psi \ell \nu$ , and  $N^K$  is the number of  $B^+ \rightarrow J/\psi K^+$  events measured in data using selection criteria described below.

The  $J/\psi$  candidate is required to satisfy the selection criteria given in section 4.2. The  $K^+$  candidate is required to be in the SLT electron fiducial region with a quality track and  $p_T$  greater than 2 GeV. The  $J/\psi$  candidate mass is required to be within 50 MeV of the PDG mass [79], and the  $B^+$  candidate is required to be within 400 MeV of its PDG mass. 6871 events pass these requirement. The large amount of background makes a systematic fit of the number of  $B_u \rightarrow J/\psi K$  events problematic.

In order to reduce the background, I required the  $c\tau$  of the  $J/\psi$  to be positive. This requirement removes half of the direct  $J/\psi$  events from the sample with removing minimal  $B^+$  events. 4070 events pass the requirement. Figure 5.23 shows mass spectra and the fit with the additional cut. The fit is a Gaussian signal with a linear background.  $245 \pm 39$  signal events are fit.

$R^K$ ,  $R^e$ ,  $R_c$  and  $\frac{\sigma(B_c) \cdot BR(B_c \rightarrow J/\psi \ell \nu)}{\sigma(B_u) \cdot BR(B_u \rightarrow J/\psi K)}$  has all been measured previously in ref. [31].



- $R^K = 0.263 \pm 0.035(\text{syst.})^{+0.038}_{-0.062}(\text{lifetime})$
- $R^e = 0.58 \pm 0.04$
- $R_c = 0.85 \pm 0.15$
- $\frac{\sigma(B_c) \cdot BR(B_c \rightarrow J/\psi \ell \nu)}{\sigma(B_u) \cdot BR(B_u \rightarrow J/\psi K)} = 0.132^{+0.041}_{-0.037}(\text{stat.}) \pm 0.031(\text{syst.})^{+0.032}_{-0.020}(\text{lifetime})$

Taking into account correlated uncertainties, the number of  $B_c \rightarrow J/\psi \ell X$  events estimated in the sample are  $N_{B_c}^e = 10.0^{+3.5}_{-3.3}$  and  $N_{B_c}^\mu = 7.2^{+2.6}_{-2.4}$ . According to Monte Carlo, over 99% of the  $B_c$  passing the selection requirements have  $\Delta\phi < \frac{\pi}{2}$  between the lepton and the  $J/\psi$ . Thus, this background is only fit for in toward  $\Delta\phi$  region in the measurement.

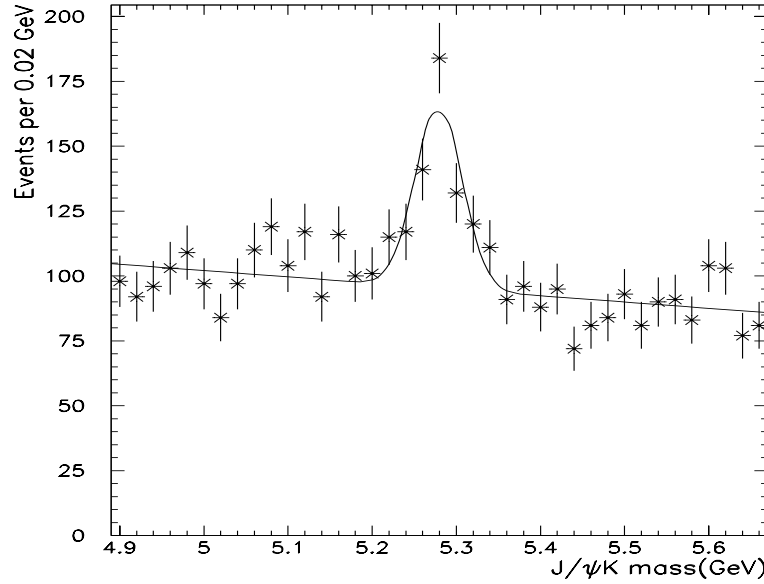


Figure 5.23: Mass of  $B^+ \rightarrow J/\psi K^+$  candidates found in the Run 1b  $J/\psi$  sample.

Using a  $B_c \rightarrow J/\psi \ell \nu$  Monte Carlo sample, the impact parameter- $c\tau$  shape is determined. The  $B_c$  mesons are generated according to the NLO fragmentation model from ref. [86] with a flat rapidity spectra. The particles are decayed using the semi-leptonic decay model of ref. [87] and passed through a detector and trigger simulation. The selection

criteria used is identical to section 5.1.3. The Monte Carlo events passing the selection criteria are fit using a shape described in appendix C. Figures 5.24 and 5.25 show the results of the fit for the electron and muon samples, which describe the correlations between the impact parameter and  $c\tau$  well.

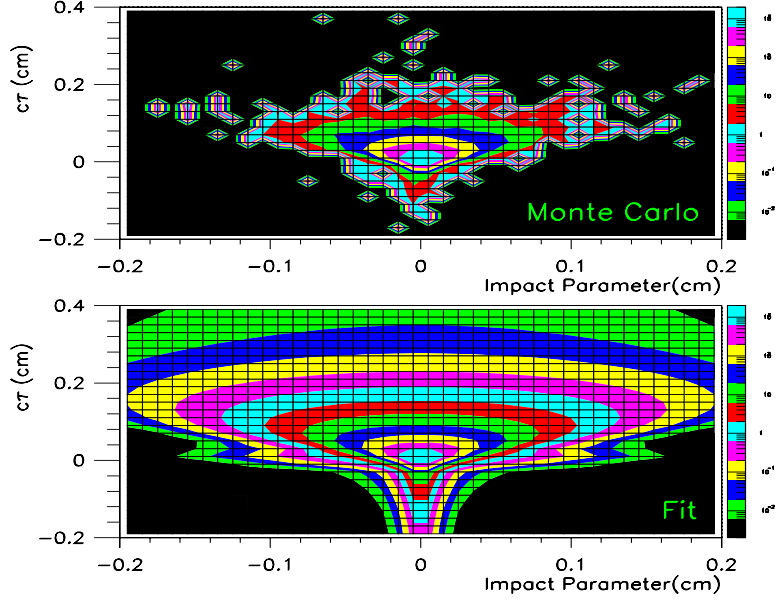


Figure 5.24: *Impact parameter- $c\tau$  contour plots of Monte Carlo  $B_c \rightarrow J/\psi e \nu$  events and the fit. Top: Monte Carlo. Bottom: Fit to Monte Carlo.*

### 5.1.8 $b \rightarrow J/\psi \ell_{\text{fake}}$

The other source of background where the impact parameter and  $c\tau$  are correlated is bottom hadrons decaying to a real  $J/\psi$  with a hadron from the same decay faking an lepton. The sources and rates for faking leptons were studied extensively in ref. [31] and are used in this thesis.

The estimates of the amount and shapes of these backgrounds are made using a Monte Carlo sample of  $b \rightarrow J/\psi X$  events. Single bottom quarks are generated according the

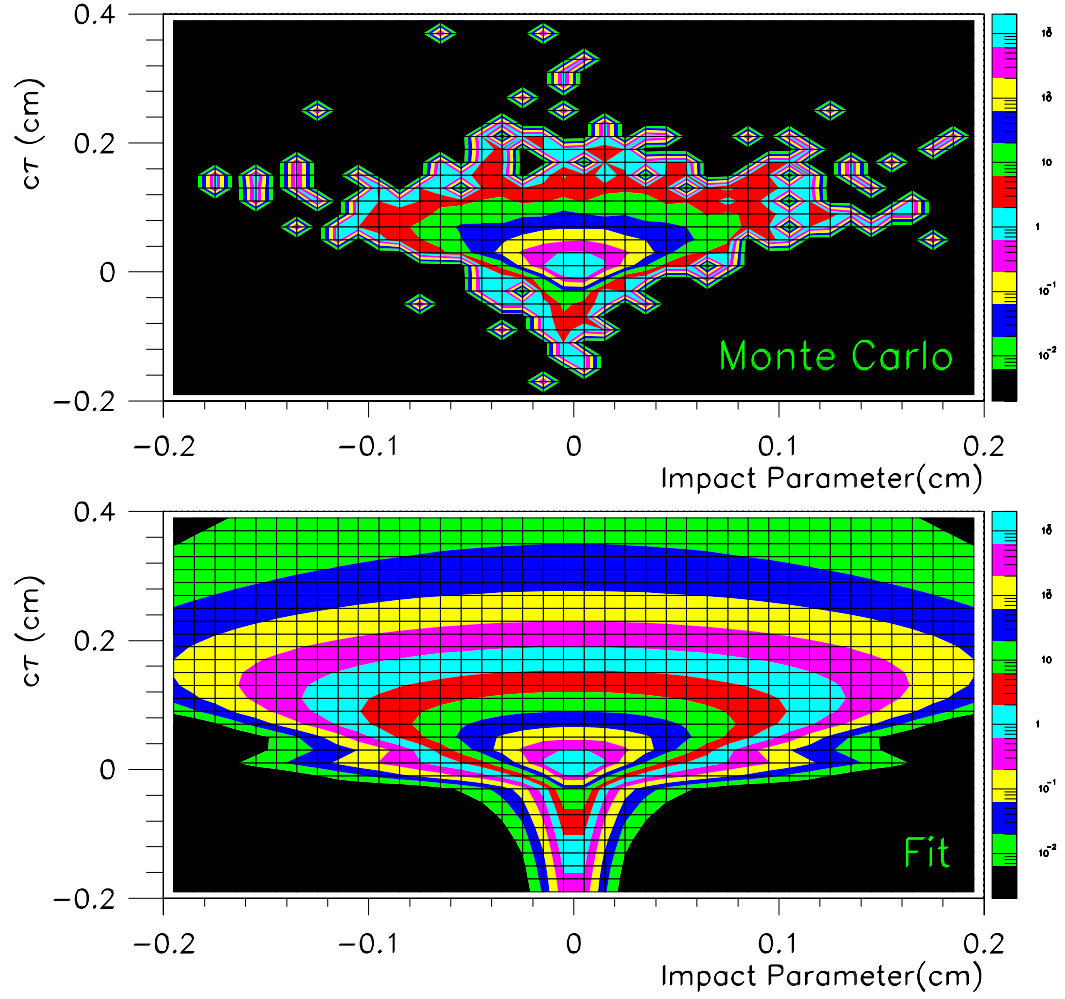


Figure 5.25: Impact parameter- $c\tau$  contour plots of Monte Carlo  $B_c \rightarrow J/\psi \mu \nu$  events and the fit. Top: Monte Carlo. Bottom: Fit to Monte Carlo.

next-to-leading order QCD predictions by ref. [37], and fragmented using the Peterson fragmentation model [42]. The resulting bottom hadrons are decayed using the CLEO decay model [82], requiring a  $J/\psi \rightarrow \mu^+ \mu^-$  decay. The events are then placed through a detector simulation [83] and the trigger simulation [73]. For both the calculation of electron and muon fake rates, the  $J/\psi$  is required to pass the same selection criteria as data. The sample is normalized to the number of  $J/\psi$  events from bottom decay fit in data in section 5.1.1.

### **Fake electron background**

Hadrons can mimic the detector response of an electron in the calorimeter if it interacts with material in front of the CEM, beginning its hadronic shower early. The rate that a hadron will fake an electron was studied in ref. [31] using two data samples. The larger of the two samples is the inclusive jet trigger data with a traverse energy requirement of 20 GeV, as known as the JET20 data set. The other sample used is the Minimum Bias (minbias) trigger data; this trigger has minimal physics requirements but a large pre-scale. The rate determined using minbias data set is used in ref. [31] as a measure of the systematic uncertainty of the fake rate. The fake rate found is parameterized by the track's  $p_T$  and isolation (I). The isolation is defined as the ratio between the scalar sum of the momenta of all tracks within a cone radius of 0.2 of the track in  $\eta - \phi$  space (excluding the track itself) and the track's scalar momenta ( $I = \frac{\sum p_{other}}{p_{track}}$ ). Figure 5.26 shows the fake probability measured in ref. [31].

As stated previously, the number of  $b \rightarrow J/\psi e_{\text{fake}} X$  events is determined by using these fake rates and a Monte Carlo sample. To be included in the fake rate calculation, an event must pass the  $J/\psi$  selection and have an charged hadron in the electron identification

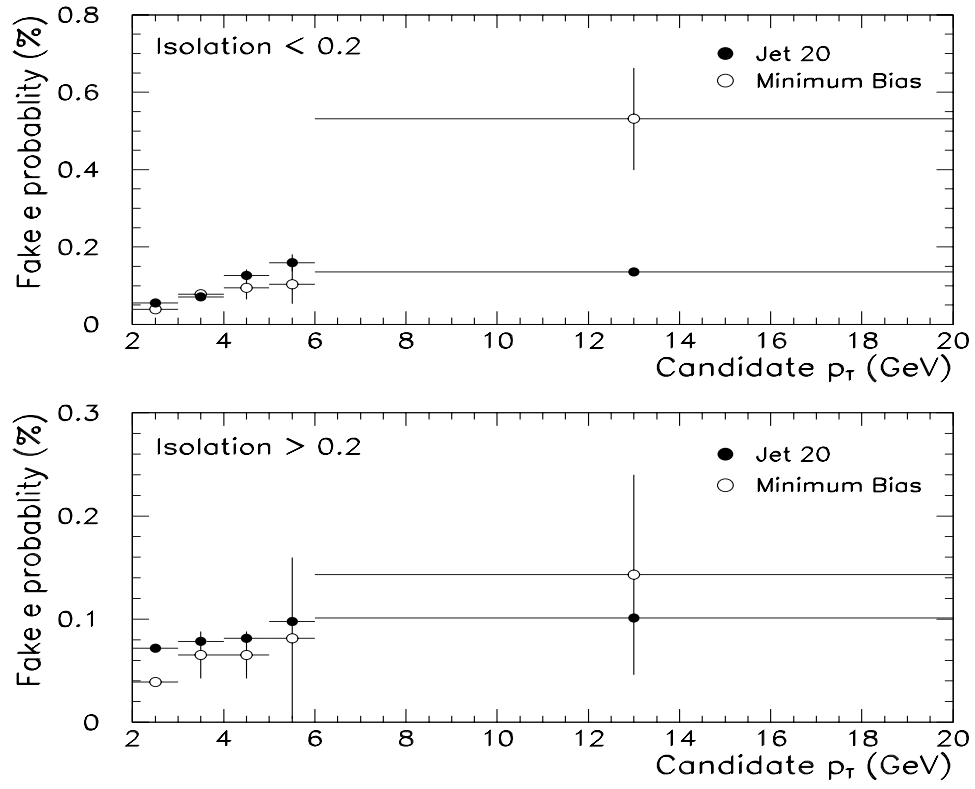


Figure 5.26: Fake SLT electron probability as a function of  $p_T$  from [31].

fiducial (as defined in section 4.4) with a quality track and a  $p_T > 2$  GeV. Ideally, one then would apply the appropriate fake rate for the particle's  $p_T$  and isolation for each track passing the selection, yielding the fake rate. Unfortunately, the Monte Carlo used does not include particles from the underlying event, fragmentation, gluon radiation or the other bottom hadron in the event. Thus, the isolation in the simulation does not represent the data. Figure 4.1 in ref. [88] shows that about  $\approx 70\%$  of the tracks have a  $I < 0.2$  in the CDF  $J/\psi$  data set. I apply the Jet20  $I < 0.2$  fake rates to entire Monte Carlo sample and use the Jet20  $I > 0.2$ , minbias  $I < 0.2$ , and minbias  $I > 0.2$  fake rates to estimate the systematic uncertainty.

Normalizing the Monte Carlo to the estimated number of  $b \rightarrow J/\psi X$  events in data yields a estimate of  $2.85 \pm 0.03$  events using the jet20  $I < 0.2$  fake rates.  $2.86 \pm 0.03$ ,  $3.41 \pm 0.04$ , and  $2.10 \pm 0.03$  are the fake electron event estimates using the jet20  $I > 0.2$ , minbias  $I < 0.2$ , and minbias  $I > 0.2$  fake rates. The greatest difference between the jet20  $I < 0.2$  fake rate estimate and the other fake rates is used as an over-estimate of the systematic uncertainty due to modeling (or lack of) of the track isolation, which yields an estimate of  $N_{B_{fake}}^e = 2.85 \pm 0.03(\text{stat.}) \pm 0.75(\text{isolation})$ .

In order to cross-check the ability of the Monte Carlo to represent the data, a comparison is made with the fake electron estimate made in ref.[31]. In that analysis, the fake electron estimate was made using the data. A three track vertex was made between the  $J/\psi$  candidate and all tracks in the electron fiducial region with a  $p_T > 2$  GeV. The mass of the candidates was required to be  $4.0 < M(J/\psi e) < 6.0$  GeV and  $|M(J/\psi e) - 5.2789| > 0.050$  GeV, which is the expected mass region for  $B_c$  candidates excluding  $B^+ \rightarrow J/\psi K^+$  mass region.  $\frac{M(J/\psi e) \cdot L_{xy}}{|p_T(J/\psi e)|} > 60 \mu\text{m}$  was also required. The number of fake electron events

was estimated to be  $2.6 \pm 0.3$ .

Applying the additional requirements and renormalizing the Monte Carlo to the larger data set used in ref. [31],  $1.8 \pm 0.6(\text{stat} + \text{syst})$  events are predicted in Monte Carlo. The estimates agrees at the  $1.2\sigma$  level; the Monte Carlo appears to describe the data adequately.

The impact parameter- $c\tau$  shape of this background is determined by a fit to the Monte Carlo. The Monte Carlo sample used in the fit are events which can included in the electron fake rate calculation. The fit shape is described in appendix C. Figure 5.27 shows the fit result.

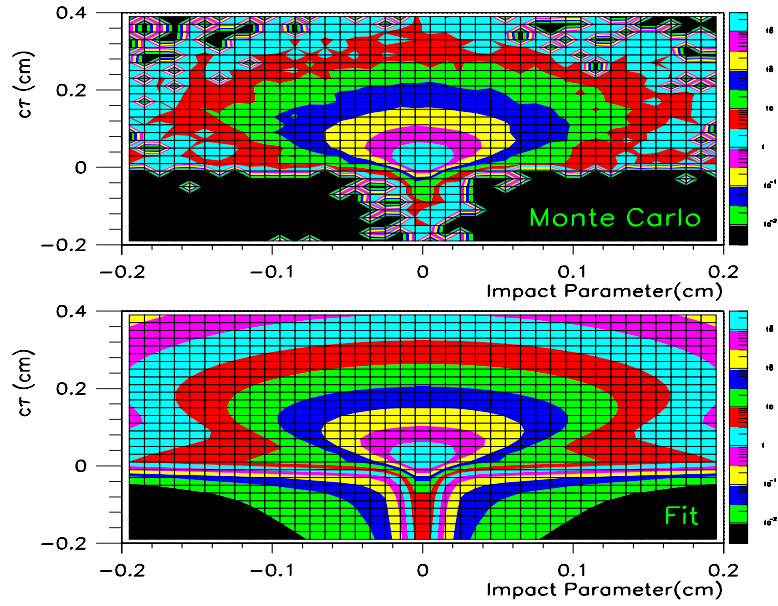


Figure 5.27: Impact parameter- $c\tau$  contour plots of Monte Carlo  $b \rightarrow J/\psi e_{Fake} X$  events and the fit. Top: Monte Carlo. Bottom: Fit to Monte Carlo.

### Fake muon background (Decay-in-flight)

Decay-in-flight(DIF) of charged pions and kaons to muons is a source of correlated background, as long as the track is reconstructible. The probability of a decay-in-flight

to have a reconstructible track is greatly reduced by the SVX requirements as shown in ref. [31]. In that study, the probability of a kaon or pion to decay-in-flight (with a reconstructible track) and 'fake' an muon was calculated using a full simulation of the detector. The kaon or pion was forced to decay previous to the calorimeter. The tracking software was applied to the simulated track and the fraction of events which the hadron and decay muon were reconstructed as a single track of sufficient quality was determined as a function of track  $p_T$ . The results of the study is shown in figure 5.28.

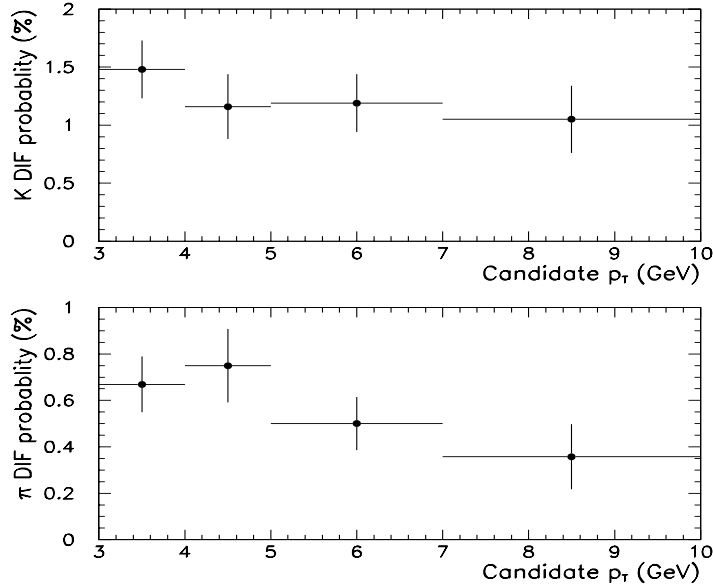


Figure 5.28: *Decay-in-flight probability as a function of  $p_T$  in ref. [31].*

The number of correlated background events from decay-in-flight is determined in a manner similar to the fake electron estimate. The Monte Carlo is normalized in the same manner as the fake electron calculation. The  $J/\psi$  candidate is required to pass the selection criteria in section 4.2, and the decay-in-flight candidates are required to have a quality track with  $p_T > 3$  GeV and project into the CMU and CMP fiducial volumes (described in section 4.3). The probability of decaying-in-flight is determined for the given  $p_T$  and



particle species.  $64.2 \pm 0.3\%$  of the particles passing the requirements are kaons. The decay-in-flight background is estimated to average  $9.9 \pm 2.1$  events. The error includes a 12% Monte Carlo calculation systematic uncertainty and a 17% reconstruction efficiency systematic uncertainty quoted in ref. [31].

In ref. [31], the decay-in-flight estimate was done using data. The third (non- $J/\psi$ ) tracks was required to be in the CMUP fiducial region and the combined three track vertex  $\chi^2$  probability had to be larger than 1%. In that analysis, the kaon fraction was measured to be  $(44 \pm 4.4)\%$ . The difference between the kaon fraction in ref. [31] and the simulation could lead to a large systematic uncertainty due to the difference in the kaon and pion decay-in-flight probabilities. To estimate this uncertainty, the Monte Carlo events are re-weighted in order to match the kaon fraction measured by [31]. With the re-weighting, the estimated number of correlated decay-in-flight background is estimated to be  $8.7 \pm 2.0$ . The difference between the two estimates is conservatively used as the systematic error, yielding a final decay-in-flight estimate of  $N_{B_{fake}}^{\mu, DIF} = 9.9 \pm 2.4$ .

As in the electron fake rate, the Monte Carlo ability to represent the data is tested with a comparison to the decay-in-flight estimate made with data in ref. [31]. The following additional requirements were made in the study:

- $4.0 < M(J/\psi\mu) < 6.0$  GeV
- $\frac{M(J/\psi\mu) \cdot L_{xy}}{|p_T(J/\psi\mu)|} > 60\mu\text{m}$
- $|M(J/\psi\mu) - 5.2789| > 0.050$  GeV

The kaon fraction is re-weighted to match the data and the Monte Carlo is renormalized to sample used in ref. [31].  $6.0 \pm 1.3$  events are predicted, which agrees well with the

estimate produced with data of  $5.5 \pm 0.5 \pm 1.3$ . This agreement indicates that the Monte Carlo describes the multiplicity and  $p_T$  spectra of the bottom decay product well enough to use it to estimate the decay-in-flight background in this analysis.

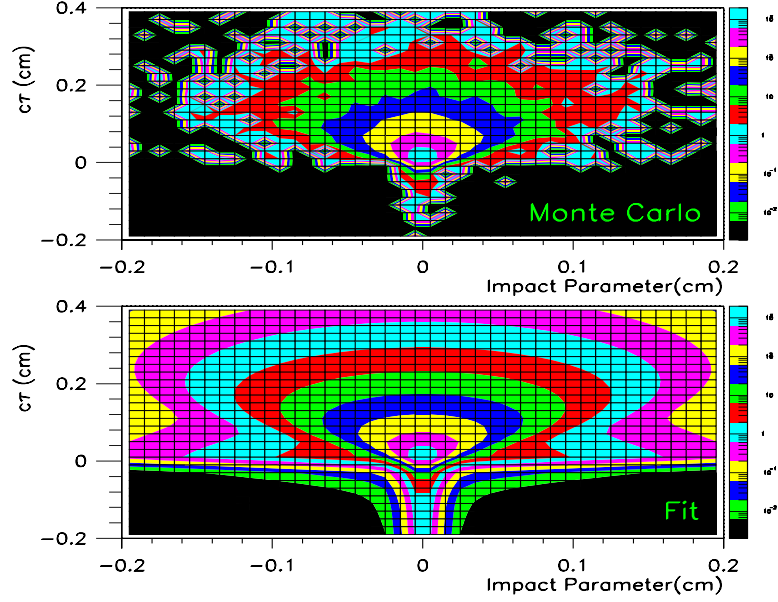


Figure 5.29: Impact parameter- $c\tau$  contour plots of Monte Carlo  $b \rightarrow J/\psi \mu_{Fake} X$  events and the fit. Top: Monte Carlo. Bottom: Fit to Monte Carlo.

The impact parameter- $c\tau$  shape of the decay-in-flight background is determined by the same Monte Carlo sample. In ref. [27, 31], it is shown that the impact parameter distribution of reconstructible decay-in-flight particles with SVX information have the same impact parameter distribution of the parent particle. Similar to the fake electron shape, the Monte Carlo events which could be used in the DIF rate calculation are fit in order to determine the DIF impact parameter- $c\tau$  shape, using the function described in appendix C. Figure 5.27 shows the fit result.

### Fake muon background (Punch-through)

Hadrons can mimic muons by not being completely absorbed by the calorimeter and leaving hits the muon chambers. The probability of a track punching-through the calorimeter was determined in ref. [31]. To summarize their method, a model of the CDF detector and the absorption cross section for charged pions and kaons were used to determine the total number of nuclear absorption lengths traversed by a particle. The number of absorption lengths traversed was corrected for the angle of the track and the ionization energy loss of the particle. The probability of punch-through is the probability of the particle punching-through to both the CMU and the CMP plus the probability of the particle punching-through the CMU and decaying-in-flight before the CMP. Figure 3.11 shows the number of absorption length traversed by a zero rapidity particle for  $K^+$ ,  $K^-$ , and  $\pi^\pm$ .

The selection criteria of the punch-through estimate is the same as the the decay-in-flight estimate. The punch though probability of the tracks passing the requirements is calculated from its particle type and momentum, yielding the final estimate. An average  $1.76 \pm 0.70$  punch though events are expected in the data, including a 40% systematic error used in [31].

As the punch-though rate is much larger for  $K^+$  than  $K^-$  or  $\pi^{+/-}$ , the large difference in kaon fraction between [31] and Monte Carlo (shown in the decay-in-flight estimate) is a significant systematic uncertainty to the punch-through estimate. To be conservative, we re-weight the data with the kaon fraction measured in ref. [31];  $1.23 \pm 0.46$  events are expected. The difference between the two predictions is used as the estimate of the systematic uncertainty in the prediction. Thus, the final estimate of the average number of correlated backgrounds from punch though is  $N_{B_{fake}}^{\mu,PT} = 1.76 \pm 0.88$  events. In Monte

Carlo, more than 99% of the events have the  $J/\psi$  and the fake muon candidate in the same azimuthal hemisphere, and therefore this background is only fit for in the toward  $\Delta\phi$  region. In ref. [88], the decay-in-flight and punch-through backgrounds are shown to have the same lifetime shape in the  $B_c$  lifetime fit. The decay-in-flight and punch-through backgrounds are assumed to have the same impact parameter- $c\tau$  shape. As with the decay-in-flight background, the number of punch-through background events is estimated using the [31] analysis cuts as a cross-check of the calculation.  $0.83 \pm 0.33$  events is estimated from Monte Carlo after re-scalings to the kaon fraction measured in ref. [31]. In ref. [31],  $0.88 \pm 0.13 \pm 0.33$  is predicted. The two estimates agree within the statistical error on the measurement in ref. [31].

## 5.2 Fit Description

In order to make a toward <sup>5</sup> fraction measurement in  $\Delta\phi$  for bottom production, the  $b\bar{b}$  component of the data has to be measured in the regions of  $\Delta\phi$ . In this analysis, a simultaneous fit of the  $c\tau$  of the  $J/\psi$  and the impact parameter of the additional lepton extracts the  $b\bar{b}$  component in the data. The fit is a binned, unbinned extended log-likelihood, with binning in  $\Delta\phi$  (toward/away) and in  $J/\psi$  candidate mass (signal/sideband). Within each bin in  $\Delta\phi$ , the shape of the impact parameter and  $c\tau$  distributions in data is fit with continuous functions, which describe the signal and the various backgrounds in the sample. Constraints are used both within the regions of  $\Delta\phi$  and  $M_{J/\psi}$ , and over the entire sample. For each constraint, there is a corresponding fit parameter. The fit parameter is constrained to the estimate or measurement within its uncertainty, which propagates the

---

<sup>5</sup>Toward is  $\Delta\phi < \frac{\pi}{2}$ . Away is  $\Delta\phi > \frac{\pi}{2}$ .

errors in the constraints properly. The constraints are introduced into the log-likelihood as additional Gaussian or Poisson terms, depending on the which statistic that the constraint follows.

The fit parameters will be in lower case, the constraints will be upper case, and the errors on the constraints (if applicable) is denoted  $\Delta(\text{Constraint})$ . The superscripts indicate the additional lepton used (e for electrons,  $\mu$  for muons) and the  $\Delta\phi$  region (t for toward, a for away). For example,  $N_{B_c}^{e,t}$  is the number of  $B_c \rightarrow J/\psi e X$  background events estimated in the electron sample in the toward  $\Delta\phi$  region.

### 5.2.1 Data

The inputs to the fit on an event-by-event basis are the  $J/\psi$  candidate's  $c\tau$  and the additional lepton candidate's impact parameter. In the following sections, x with denote the impact parameter, and y will denote the  $c\tau$ . The number of candidates in the  $J/\psi$  mass sideband and signal regions in both  $\Delta\phi$  regions is used as a constraint in the likelihood. In the electron sample, the number of found conversions in  $J/\psi$  mass sideband and signal regions in both  $\Delta\phi$  regions is also used as a constraint. Conversion constraints are discussed later in their respective sections.

The number of candidates in the electron samples is  $N_{signal}^{e,t} = 107$  and  $N_{signal}^{e,a} = 205$  for the toward and away  $\Delta\phi$  regions. The equivalent numbers for the muon sample are  $N_{signal}^{\mu,t} = 64$  and  $N_{signal}^{\mu,a} = 78$ . The number of candidates in the data is used as a constraint on the number of candidates fit ( $n_{signal}$ ). The constraint is expressed as the Poisson probability of measuring  $N_{signal}$  events with mean value of  $n_{signal}$ .

$$P(n_{signal}, N_{signal}) = \frac{(n_{signal})^{N_{signal}}}{N_{signal}!} e^{-n_{signal}} \quad (5.21)$$

with the appropriate  $n_{signal}$  and  $N_{signal}$  for the given sample and  $\Delta\phi$  region.  $n_{signal}$  is not a fit parameter, but is a function of the other fit parameters, shown in section 5.2.8.

### 5.2.2 $b \rightarrow J/\psi X; \bar{b} \rightarrow \ell X'$ signal

The shapes which are used for the  $b \rightarrow J/\psi X; \bar{b} \rightarrow \ell X'$  signal are described by the fit functions in sections 5.1.1 and 5.1.3. The impact parameter and  $c\tau$  are assumed to be uncorrelated. Therefore, the shape which describes the signal is the product of the impact parameter shape ( $F_b^{d_0}(x)$ ) and the  $c\tau$  shape ( $F_b^{c\tau}(y)$ ) for bottom decay. The parameters that are used in  $F_b^{d_0}(x)$  are different for the electron and muon fits.

The number of  $b\bar{b}$  events fit is  $n_{b\bar{b}}$  with the superscripts given by sample and  $\Delta\phi$  region. For example, the number of  $b\bar{b}$  events fit in the toward  $\Delta\phi$  region in the electron sample is  $n_{b\bar{b}}^{e,t}$ . The  $b\bar{b}$  contribution of the shape component of the likelihood is given by  $\frac{n_{b\bar{b}}}{n_{signal}} \cdot F_b^{d_0}(x) \cdot F_b^{c\tau}(y)$  with the appropriate superscripts for the additional lepton type and  $\Delta\phi$  region.

### 5.2.3 Unconstrained, uncorrelated backgrounds

The impact parameter- $c\tau$  shapes of the three sources of uncorrelated backgrounds without constraints, considered in this analysis, are constructed using the functions derived in sections 5.1.1–5.1.3. The fit parameters for these three backgrounds are:

- $n_{dd}$ : the number of events with the  $J/\psi$  candidate and with the additional lepton candidate both directly produced
- $n_{bd}$ : the number of events with the  $J/\psi$  candidate from bottom decay and with the additional lepton candidate produced directly

- $n_{db}$ : the number of events with a directly produced  $J/\psi$  candidate and with an additional lepton candidate from bottom decay

where the superscripts indicate of the sample and  $\Delta\phi$  region. The number of events with a directly produced  $J/\psi$  candidate and an additional lepton candidate from bottom decay is assumed to be small and  $n_{db}$  is fixed to zero. The parameter is released and fit for as an estimate of systematic uncertainty due to this assumption.

The shape component of the likelihood for these three backgrounds is assembled in the same manner as the  $b\bar{b}$  signal;  $\frac{n_{dd}}{n_{signal}} \cdot F_{direct}^{d_0}(x) \cdot F_{direct}^{c\tau}(y)$ ,  $\frac{n_{bd}}{n_{signal}} \cdot F_{direct}^{d_0}(x) \cdot F_b^{c\tau}(y)$ , and  $\frac{n_{db}}{n_{signal}} \cdot F_b^{d_0}(x) \cdot F_{direct}^{c\tau}(y)$  are the forms of the shape components for the three uncorrelated, unconstrained backgrounds.

#### 5.2.4 Fake $J/\psi$ backgrounds

The fake  $J/\psi$  impact parameter- $c\tau$  background shape ( $F_{sideband}^\mu$ ) is determined in section 5.1.6 from a fit to the data for the muon sample. The predicted number of events for this background is the ratio between the number of fake  $J/\psi$  events in the  $J/\psi$  mass signal and sideband region ( $R_{side}$ ) times the number of events seen in data with the  $J/\psi$  candidate in the mass sideband regions ( $N_{side}$ ) for the given sample and  $\Delta\phi$  region.

In section 4.2, the ratio is determined to be  $R_{side} = 0.501 \pm 0.044$  from a fit of the total  $J/\psi$  data sample. The same value for the fit parameter  $r_{side}$  is used in both  $\Delta\phi$  regions in the sample, but can be different in the electron and muon samples. The fit value of  $r_{side}$  is constrained using a Gaussian factor in the likelihood function.

$$G(r_{side} - R_{side}, \Delta R_{side}) = \frac{1}{\sqrt{2}\Delta R_{side}} e^{-\frac{1}{2}\left(\frac{r_{side} - R_{side}}{\Delta R_{side}}\right)^2} \quad (5.22)$$

The number of candidates found in the  $J/\psi$  mass sideband region for the two samples

and  $\Delta\phi$  regions is  $N_{side}^{e,t} = 45$ ,  $N_{side}^{e,a} = 47$ ,  $N_{side}^{\mu,t} = 34$ ,  $N_{side}^{\mu,a} = 17$ . The corresponding fit parameter  $n_{side}$ , for the given sample and  $\Delta\phi$  region, is constrained using the Poisson probability of measuring  $N_{side}$  events for a sample with an average of  $n_{side}$  events.

$$P(n_{side}, N_{side}) = \frac{(n_{side})^{N_{side}}}{N_{side}!} e^{-n_{side}} \quad (5.23)$$

The contribution of the shape component of the likelihood is  $\frac{r_{side} n_{side}}{n_{signal}} \cdot F_{side}(x, y)$  for the given sample and  $\Delta\phi$  region.

The fake  $J/\psi$  background component in the electron sample is treated differently due to the presence of residual conversions in the background. The functional form of the shape of the background is given by equation 5.18. The fake  $J/\psi$  shape is fit at the same time as the  $J/\psi$  signal region. The  $f_{conv}$  component of the fake  $J/\psi$  impact parameter- $c\tau$  shape is a composite of two variables which are constrained.  $f_{conv} = \frac{r_{conv} \cdot n_{convside}}{N_{sideband}}$  where  $r_{conv}$ ,  $n_{convside}$ , and  $N_{sideband}$  are the fit ratio of residual to found conversion, fit number of “found” conversions, and  $N_{sideband} = N_{side}^{e,t} + N_{side}^{\mu,a}$ .  $n_{convside}$  is constrained by the number of conversions found in the sideband  $N_{convside} = 9$  using the Poisson probability:

$$P(n_{convside}, N_{convside}) = \frac{(n_{convside})^{N_{convside}}}{N_{convside}!} e^{-n_{convside}} \quad (5.24)$$

$r_{side}$  is constrained by the estimate in section 5.1.6. The form of the constraint is described in section 5.2.7.

### 5.2.5 $B_c \rightarrow J/\psi \ell X$ backgrounds

As stated in section 5.1.7,  $B_c \rightarrow J/\psi \ell X$  background is predicted to only populate the toward region in  $\Delta\phi$ . Therefore, this background is only fit for in the toward region in the two samples. In section 5.1.7, number of  $B_c$  background events is estimated to be



$N_{B_c}^{e,t} = 10.0^{+3.5}_{-3.3}$  and  $N_{B_c}^{\mu,t} = 7.2^{+2.6}_{-2.4}$  for the electron and muon samples. The constraint is added to the likelihood as a Gaussian probability factor.

$$G(n_{B_c} - N_{B_c}, \Delta N_{B_c}) = \frac{1}{\sqrt{2\Delta N_{B_c}}} e^{-\frac{1}{2} \left( \frac{n_{B_c} - N_{B_c}}{\Delta N_{B_c}} \right)^2} \quad (5.25)$$

where  $\Delta N_{B_c}$  is the positive-sided error of  $N_{B_c}$  if  $(n_{B_c} - N_{B_c}) \geq 0.0$ , and the negative-sided error otherwise.

The impact parameter- $c\tau$  shape ( $F_{B_c}$ ) of the  $B_c$  background is fit for in section 5.1.7.

$\frac{n_{B_c}^e}{n_{signal}^e} \cdot F_{B_c}^e(x, y)$  and  $\frac{n_{B_c}^\mu}{n_{signal}^\mu} \cdot F_{B_c}^\mu(x, y)$  are the contributions to the toward shape component of the log-likelihood for the electron and muon samples.

### 5.2.6 $b \rightarrow J/\psi \ell_{fake} X$ backgrounds

As in the  $B_c$  background,  $b \rightarrow J/\psi \ell_{fake} X$  background events are only expected to populate the toward region in  $\Delta\phi$ , and therefore the background is only fit for in the toward region in the two samples. In section 5.1.8, the size of  $b \rightarrow J/\psi \ell_{fake} X$  is estimated. For the electron sample,  $N_{B_{fake}}^{e,t} = 2.85 \pm 0.75$  is the expected fake electron correlated background. The fake muon background has two sources: decay-in-flight and punch-through. As the impact parameter- $c\tau$  shapes for both sources are assumed to be the same, the sum of these two backgrounds is the fit variable.  $N_{B_{fake}}^{\mu,t} = 11.7 \pm 2.6$  is the estimated number of fake muon correlated backgrounds. The constraint is added to the likelihood in the same way as  $B_c$ .

$$G(n_{B_{fake}} - N_{B_{fake}}, \Delta N_{B_{fake}}) = \frac{1}{\sqrt{2\Delta N_{B_{fake}}}} e^{-\frac{1}{2} \left( \frac{n_{B_{fake}} - N_{B_{fake}}}{\Delta N_{B_{fake}}} \right)^2} \quad (5.26)$$

The construction of the  $b \rightarrow J/\psi \ell_{fake} X$  contribution of the shape is similar to the  $B_c$ :

$\frac{n_{B_{fake}}^e}{n_{signal}^e} \cdot F_{B_{fake}}^e(x, y)$  and  $\frac{n_{B_{fake}}^\mu}{n_{signal}^\mu} \cdot F_{B_{fake}}^\mu(x, y)$  for the electron and muon samples, respectively.

### 5.2.7 Residual conversion background

The total number of predicted residual conversions is  $R_{conv} \cdot N_{conv}$ , where  $R_{conv}$  is the ratio between the number of residual versus found conversions and  $N_{conv}$  is the number of found conversions in the sample. The number of found conversions removed from the two  $\Delta\phi$  regions with the  $J/\psi$  candidate in the mass signal region is  $N_{conv}^t = 6$  and  $N_{conv}^b = 9$ , respectively. In section 5.1.4,  $R_{conv}$  is estimated to be  $1.00 \pm 0.37$ , using data and Monte Carlo techniques. Residual conversions are assumed to pair with all three sources of uncorrelated  $J/\psi$  candidates: fake  $J/\psi$ , directly produced  $J/\psi$ , and bottom decay  $J/\psi$ . The same value of the fit parameter  $r_{conv}$  is used for all sources of  $J/\psi$  candidates that pair with the residual conversions. The value of  $r_{conv}$  is constrained as a Gaussian probability in the likelihood.

$$G(r_{conv} - R_{conv}, \Delta R_{conv}) = \frac{1}{\sqrt{2}\Delta R_{conv}} e^{-\frac{1}{2}\left(\frac{r_{conv}-R_{conv}}{\Delta R_{conv}}\right)^2} \quad (5.27)$$

The fit parameters that set the scale for the number of residual conversions events with the  $J/\psi$  candidate from bottom decay and direct production are  $n_{bconv}$  and  $n_{dconv}$ . The parameters represent the number of **found** conversions with the  $J/\psi$  candidate from the given source. The number of residual conversions fit from these two sources are  $r_{conv} \cdot n_{bconv}$  and  $r_{conv} n_{dconv}$ . The number of residual conversions already included in the sideband shape component is  $r_{side} n_{side}^e f_{conv}^{d_0}$ , where  $f_{conv}^{d_0} = \frac{r_{conv} \cdot n_{convside}}{N_{sideband}}$  is the fit fraction of  $J/\psi$  mass sideband events where the electron is a residual conversion.

Due the relatively small number of residual conversions, fitting all three pairing of  $J/\psi$  candidate types with conversions is not possible. In order to constrain this component of the fit farther, the ratio of between  $n_{bconv}$  and  $n_{dconv}$  is assumed to be the same as the ratio between  $J/\psi$  mesons from bottom decay and  $J/\psi$  mesons produced directly (at the

primary vertex). The fraction of  $J/\psi$  mesons from bottom decay is fit to be  $16.6\% \pm 0.2\%$  in section 5.1.1, yielding the relationship  $n_{bconv}^{t/a} = 0.2 \cdot n_{dconv}^{t/a}$ . As an estimate of the systematic uncertainty,  $n_{bconv}^{t/a}$  and  $n_{dconv}^{t/a}$  are fixed to zero in separate fits in order to probe the full range of ratio  $n_{bconv}^{t/a} : n_{dconv}^{t/a}$ .

The number of found conversions in the two  $\Delta\phi$  regions is used as a constraint on the fit of the residual conversions. The number of 'found' conversions fit is the number of residual conversions fit divided by the ratio of residual versus found conversions:

$$n_{conv} \equiv n_{bconv} + n_{dconv} + \frac{r_{side} n_{side}^e n_{convside}}{N_{sideband}} \quad (5.28)$$

The constraint using the number of found conversions is the Poisson probability of finding  $N_{conv}$  conversion candidates with a mean value of number of found conversion fit.

$$P(n_{conv}, N_{conv}) = \frac{(n_{conv})^{N_{conv}}}{N_{conv}!} e^{-(n_{conv})} \quad (5.29)$$

The shape components of residual conversions with a  $J/\psi$  from bottom decay and direct production have the form  $\frac{r_{conv} n_{bconv}}{n_{signal}^e} F_{conv}(x) F_b^{c\tau}(y)$  and  $\frac{r_{conv} n_{dconv}}{n_{signal}^e} F_{conv}(x) F_{direct}^{c\tau}(y)$ , respectively. The residual conversions with a fake  $J/\psi$  have already been included in the sideband fit shape.

### 5.2.8 $n_{signal}$ sums

The number of events fit in the  $J/\psi$  mass signal region is a function of fit parameters described previously in this section. Listed below are the functions for number of events fit for the two samples and  $\Delta\phi$  regions.

$$\begin{aligned} n_{signal}^{\mu,t} &= n_{bb}^{\mu,t} + n_{bd}^{\mu,t} + n_{db}^{\mu,t} + n_{dd}^{\mu,t} + r_{side}^{\mu} \cdot n_{side}^{\mu,t} + n_{B_c}^{\mu,t} + n_{B_{fake}}^{\mu,t} \\ n_{signal}^{\mu,a} &= n_{bb}^{\mu,a} + n_{bd}^{\mu,a} + n_{db}^{\mu,a} + n_{dd}^{\mu,a} + r_{side}^{\mu} \cdot n_{side}^{\mu,a} \end{aligned}$$

$$\begin{aligned}
n_{signal}^{e,t} &= n_{b\bar{b}}^{e,t} + n_{bd}^{e,t} + n_{db}^{e,t} + n_{dd}^{e,t} + r_{side}^e \cdot n_{side}^{e,t} + n_{B_c}^{e,t} + n_{B_{fake}}^{e,t} \\
&+ r_{conv} \cdot n_{bconv}^t + r_{conv} \cdot n_{dconv}^t \\
n_{signal}^{e,a} &= n_{b\bar{b}}^{e,a} + n_{bd}^{e,a} + n_{db}^{e,a} + n_{dd}^{e,a} + r_{side}^e \cdot n_{side}^{e,a} \\
&+ r_{conv} \cdot n_{bconv}^t + r_{conv} \cdot n_{dconv}^t
\end{aligned}$$

### 5.2.9 Impact parameter- $c\tau$ shape component

The complete functions for the shape components of the fit are given below for the two samples and  $\Delta\phi$  regions. As a reminder,  $x$  is the additional lepton candidate's impact parameter and  $y$  is the  $J/\psi$  candidate's  $c\tau$ .

$$\begin{aligned}
F_{shape}^{\mu,t}(x,y) &= \frac{1}{n_{signal}^{\mu,t}} \left[ n_{b\bar{b}}^{\mu,t} F_b^{c\tau,\mu}(y) F_b^{d_0,\mu}(x) + n_{bd}^{\mu,t} F_b^{c\tau,\mu}(y) F_{direct}^{d_0,\mu}(x) \right. \\
&+ n_{db}^{\mu,t} F_{direct}^{c\tau,\mu}(y) F_b^{d_0,\mu}(x) + n_{dd}^{\mu,t} F_{direct}^{c\tau,\mu}(y) F_{direct}^{d_0,\mu}(x) \\
&\left. + n_{B_{fake}}^{\mu,t} F_{B_{fake}}^\mu(x,y) + n_{B_c}^{\mu,t} F_{B_c}^\mu(x,y) + r_{side}^\mu n_{side}^{\mu,t} F_{side}^\mu(x,y) \right]
\end{aligned}$$

$$\begin{aligned}
F_{shape}^{\mu,a}(x,y) &= \frac{1}{n_{signal}^{\mu,a}} \left[ n_{b\bar{b}}^{\mu,a} F_b^{c\tau,\mu}(y) F_b^{d_0,\mu}(x) + n_{bd}^{\mu,a} F_b^{c\tau,\mu}(y) F_{direct}^{d_0,\mu}(x) \right. \\
&+ n_{db}^{\mu,a} F_{direct}^{c\tau,\mu}(y) F_b^{d_0,\mu}(x) + n_{dd}^{\mu,a} F_{direct}^{c\tau,\mu}(y) F_{direct}^{d_0,\mu}(x) \\
&\left. + r_{side}^\mu n_{side}^{\mu,a} F_{side}^\mu(x,y) \right]
\end{aligned}$$

$$\begin{aligned}
F_{shape}^{e,t}(x,y) &= \frac{1}{n_{signal}^{e,t}} \left[ n_{b\bar{b}}^{e,t} F_b^{c\tau,e}(y) F_b^{d_0,e}(x) + n_{bd}^{e,t} F_b^{c\tau,e}(y) F_{direct}^{d_0,e}(x) \right. \\
&+ n_{db}^{e,t} F_{direct}^{c\tau,e}(y) F_b^{d_0,e}(x) + n_{dd}^{e,t} F_{direct}^{c\tau,e}(y) F_{direct}^{d_0,e}(x) \\
&+ n_{B_{fake}}^{e,t} F_{B_{fake}}^e(x,y) + n_{B_c}^{e,t} F_{B_c}^e(x,y) + r_{side}^e n_{side}^{e,t} F_{side}^e(x,y) \\
&\left. + r_{conv} n_{bconv}^t F_{conv}(x) F_b^{c\tau,e}(y) + r_{conv} n_{dconv}^t F_{conv}(x) F_{direct}^{c\tau,e}(y) \right]
\end{aligned}$$

$$\begin{aligned}
F_{shape}^{e,a}(x,y) = & \frac{1}{n_{signal}^{e,a}} \left[ n_{bb}^{e,a} F_b^{c\tau,e}(y) F_b^{d_0,e}(x) + n_{bd}^{e,a} F_b^{c\tau,e}(y) F_{direct}^{d_0,e}(x) \right. \\
& + n_{db}^{e,a} F_{direct}^{c\tau,e}(y) F_b^{d_0,e}(x) + n_{dd}^{e,a} F_{direct}^{c\tau,e}(y) F_{direct}^{d_0,e}(x) + r_{side}^e n_{side}^{e,a} F_{side}^e(x,y) \\
& \left. + r_{conv} n_{bconv}^a F_{conv}(x) F_b^{c\tau,e}(y) + r_{conv} n_{dconv}^a F_{conv}(x) F_{direct}^{c\tau,e}(y) \right]
\end{aligned}$$

### 5.2.10 Bin constraints component

The constraints which are specific to a given region in  $\Delta\phi$  and sample are listed below:

$$\begin{aligned}
C_{bin}^{\mu,t} = & P(n_{signal}^{\mu,t}, N_{signal}^{\mu,t}) \cdot P(n_{side}^{\mu,t}, N_{side}^{\mu,t}) \cdot G(n_{B_c}^{\mu,t} - N_{B_c}^{\mu,t}, \Delta N_{B_c}^{\mu,t}) \\
& \cdot G(n_{B_{fake}}^{\mu,t} - N_{B_{fake}}^{\mu,t}, \Delta N_{B_{fake}}^{\mu,t})
\end{aligned}$$

$$C_{bin}^{\mu,a} = P(n_{signal}^{\mu,a}, N_{signal}^{\mu,a}) \cdot P(n_{side}^{\mu,a}, N_{side}^{\mu,a})$$

$$\begin{aligned}
C_{bin}^{e,t} = & P(n_{signal}^{e,t}, N_{signal}^{e,t}) \cdot P(n_{side}^{e,t}, N_{side}^{e,t}) \cdot G(n_{B_c}^{e,t} - N_{B_c}^{e,t}, \Delta N_{B_c}^{e,t}) \\
& \cdot G(n_{B_{fake}}^{e,t} - N_{B_{fake}}^{e,t}, \Delta N_{B_{fake}}^{e,t}) \cdot P(n_{conv}^t, N_{conv}^t)
\end{aligned}$$

$$C_{bin}^{e,a} = P(n_{signal}^{e,a}, N_{signal}^{e,a}) \cdot P(n_{side}^{e,a}, N_{side}^{e,a}) \cdot P(n_{conv}^a, N_{conv}^a)$$

### 5.2.11 Global constraints component

The global constraints are the simplest component of the likelihood. The functions of the global constraints are listed below:

$$C_{global}^{\mu} = G(r_{side}^{\mu} - R_{side}, \Delta R_{side})$$

$$C_{global}^e = G(r_{side}^e - R_{side}, \Delta R_{side}) \cdot G(r_{conv} - R_{conv}, \Delta R_{conv})$$

### 5.2.12 Log-likelihood function

Finally, the log-likelihood can be assembled from the functions developed in the previous sections. The likelihood function for the muon sample is:

$$\mathcal{L} = C_{global}^\mu \prod_i^{t,a} \left[ C_{bin}^{\mu,i} \prod_j^{N_{signal}^{\mu,i}} \left( F_{shape}^{\mu,i}(x_{i,j}^\mu, y_{i,j}^\mu) \right) \right]$$

where  $x_{i,j}^\mu$  and  $y_{i,j}^\mu$  are the impact parameter of the additional muon candidate and the  $c\tau$  of the  $J/\psi$  candidate for  $j^{th}$  event in the  $i^{th}$   $\Delta\phi$  region in the  $J/\psi$  signal region.

The likelihood function for the electron sample is similar to the muon likelihood. The electron likelihood includes conversion terms and the fit of the  $J/\psi$  mass sideband region.

$$\begin{aligned} \mathcal{L} = & C_{global}^e \prod_i^{t,a} \left[ C_{bin}^{e,i} \prod_j^{N_{signal}^{e,i}} \left( F_{shape}^{e,i}(x_{i,j}^e, y_{i,j}^e) \right) \right] \\ & \cdot P(n_{convside}, N_{convside}) \cdot \prod_k^{N_{sideband}} (F_{conv}(x_k^e, y_k^e)) \end{aligned}$$

where  $x_{i,j}^e$  and  $y_{i,j}^e$  are the impact parameter of the additional electron candidate and the  $c\tau$  of the  $J/\psi$  candidate for  $j^{th}$  event in the  $i^{th}$   $\Delta\phi$  region in the  $J/\psi$  signal region, and  $x_k^e$  and  $y_k^e$  are the impact parameter of the additional electron candidate and the  $c\tau$  of the  $J/\psi$  candidate for  $k^{th}$  event in the  $J/\psi$  sideband region.

## 5.3 Fit Results

The log-likelihood ( $-2 \ln \mathcal{L}$ ) is minimized for both data sets using MINUIT [89]. The fit parameter errors are defined by  $\pm 1\sigma$  ( $\Delta\mathcal{L} = 1$ ) contours of the likelihood function using

the MINOS option. The results of the fit are shown in table 5.14. In order to display the fit result, the log-likelihood function has been integrated in regions of impact parameter- $c\tau$  space. Figure 5.30 shows the fit result of the  $J/\psi$  mass sideband region for the electron sample. Figures 5.31–5.34 show the fit results for the additional electron sample with a 2-d contour plot and 1-d projections onto the impact parameter and  $c\tau$  axis for the toward and away  $\Delta\phi$  regions. Figures 5.35–5.38 show the equivalent distributions for the additional muon sample.

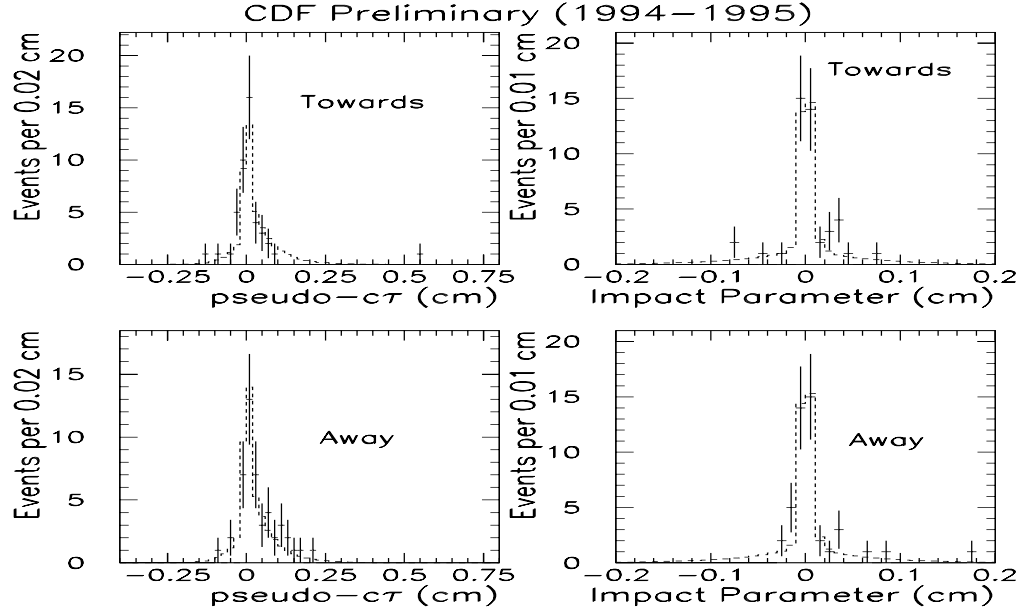


Figure 5.30: The fit of the electron sample's signed impact parameter and  $c\tau$  distribution for the  $J/\psi$  mass sideband.

The toward fraction measured in the two samples are:

$$f_{toward}^{\mu} = 34.5_{-8.2}^{+9.2}\% \quad (5.30)$$

$$f_{toward}^e = 19.2_{-5.9}^{+6.5}\% \quad (5.31)$$

The measurement error includes both the statistical error as well as systematic uncertainties due to the constraints.

As a test of the fitting technique, a set of 1000 toy Monte Carlo 'experiments' is generated. The results of the study are shown in appendix D. The study shows that the fit results are unbiased and have proper errors.

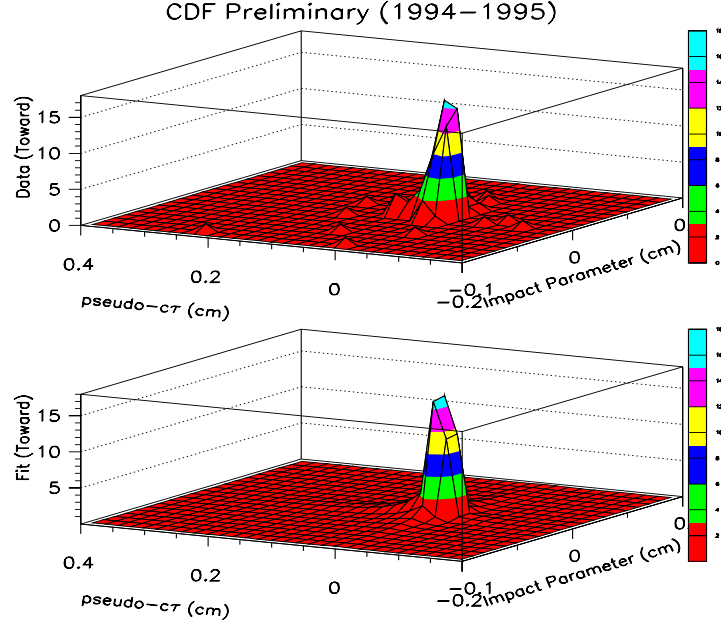


Figure 5.31: Result of the  $c\tau$ -impact parameter fit for the electron sample in the toward bin. Top: Data. Bottom: Fit.

## 5.4 Systematic Uncertainties

In this section, the systematic uncertainties on the  $f_{toward}$  measurement, not already included in the impact parameter- $c\tau$  likelihood, are evaluated.

### 5.4.1 Sequential charm fraction

The sequential charm fraction ( $f_{seq}$ ) that is used in the bottom impact parameter shape ( $F_b^{d_0}$ ) is derived by the simulation. The uncertainty in the sequential charm fraction leads to a systematic uncertainty in the determination of  $F_b^{d_0}$ , as sequential charm leptons



Fit parameter	Electron	Electron Constraint	Muon	Muon Constraint
$n_{b\bar{b}}^t$	$29.6^{+11.7}_{-10.4}$		$23.0^{+7.6}_{-6.9}$	
$n_{bd}^t$	$1.5^{+8.5}_{-8.1}$		$1.6^{+4.6}_{-2.9}$	
$n_{bconv}^t$	0.6(fixed)		N/A	
$n_{db}^t$	0 (fixed)		0 (fixed)	
$n_{dd}^t$	$37.0^{+8.0}_{-7.3}$		$11.3^{+5.1}_{-4.5}$	
$n_{dconv}^t$	$2.8^{+2.1}_{-1.7}$		N/A	
$n_{side}^t$	$45.4^{+6.9}_{-6.2}$	45	$32.9^{+5.7}_{-5.1}$	34
$n_{Bfake}^t$	$2.8^{+0.7}_{-0.7}$	$2.85 \pm 0.75$	$10.7^{+2.5}_{-2.5}$	$11.7 \pm 2.6$
$n_{Bc}^t$	$10.0^{+3.2}_{-3.3}$	$10.0^{+3.5}_{-3.3}$	$5.1^{+2.5}_{-2.5}$	$7.2^{+2.6}_{-2.4}$
$n_{signal}^t$	107.1	107	68.2	64
$n_{conv}^t$	5.6	6	N/A	
$n_{b\bar{b}}^a$	$124.7^{+17.9}_{-16.7}$		$43.6^{+10.2}_{-9.0}$	
$n_{bd}^a$	$-1.4^{+12.5}_{-12.2}$		$8.1^{+8.0}_{-7.5}$	
$n_{bconv}^a$	1.2(fixed)		N/A	
$n_{db}^a$	0 (fixed)		0 (fixed)	
$n_{dd}^a$	$49.5^{+9.2}_{-8.5}$		$16.0^{+5.5}_{-5.2}$	
$n_{dconv}^a$	$6.0^{+2.6}_{-2.2}$		N/A	
$n_{side}^a$	$47.6^{+7.1}_{-6.5}$	47	$18.2^{+4.5}_{-3.9}$	17
$n_{signal}^a$	204.9	205	76.8	78
$n_{conv}^a$	9.5	9	N/A	
$r_{side}$	$0.505^{+0.043}_{-0.0043}$	$0.501 \pm 0.44$	$0.501^{+0.043}_{-0.043}$	$0.501 \pm 0.044$
$r_{conv}$	$0.99^{+0.31}_{-0.28}$	$1.00 \pm 0.37$	N/A	
$f_1^{d_0}$	$0.494^{+0.096}_{-0.085}$		N/A	
$\lambda_1^{d_0}$	$303^{+99}_{-77} \mu\text{m}$		N/A	
$\sigma^{d_0}$	$43^{+9}_{-7} \mu\text{m}$		N/A	
$n_{convside}$	$8.9^{+2.9}_{-2.4}$	9	N/A	
$f_1^{c\tau}$	$0.54^{+0.11}_{-0.11}$		N/A	
$f_B^{c\tau}$	$0.35^{+0.08}_{-0.9}$		N/A	
$f_1^{c\tau}$	$382^{+106}_{-75} \mu\text{m}$		N/A	
$\lambda_B^{c\tau}$	$825^{+224}_{-165} \mu\text{m}$		N/A	
$\sigma^{c\tau}$	$49^{+10}_{-9} \mu\text{m}$		N/A	

Table 5.14: Fit results and constraints for the electron and muon samples.  $n_{signal}$  and  $n_{conv}$  are not fit parameters but are functions of fit parameters.

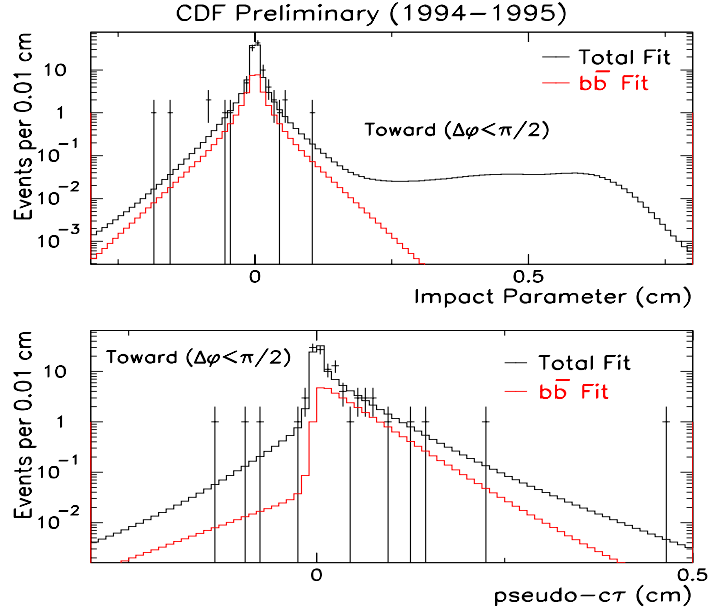


Figure 5.32: Result of the  $c\tau$ –impact parameter fit for the electron sample in the toward bin. Top: Projection onto impact parameter axis. Bottom: Projection onto  $c\tau$  axis..

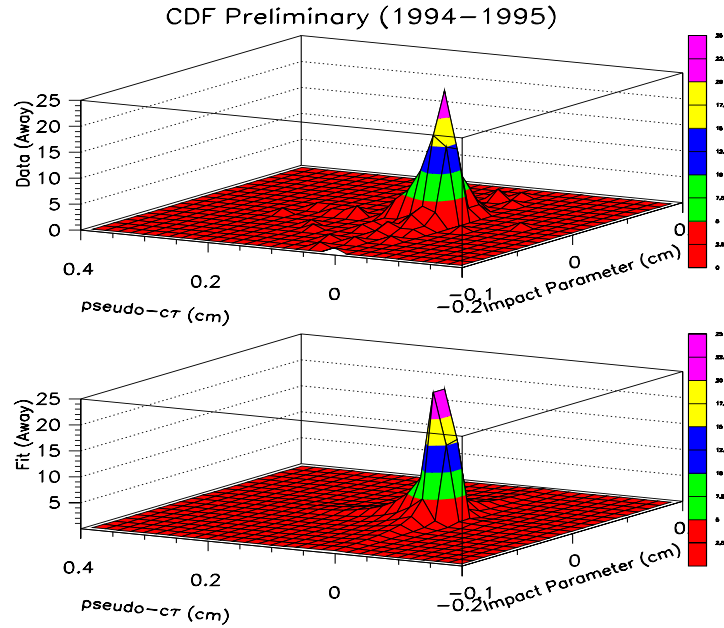


Figure 5.33: Result of the  $c\tau$ –impact parameter fit for the electron sample in the away bin. Top: Data. Bottom: Fit.

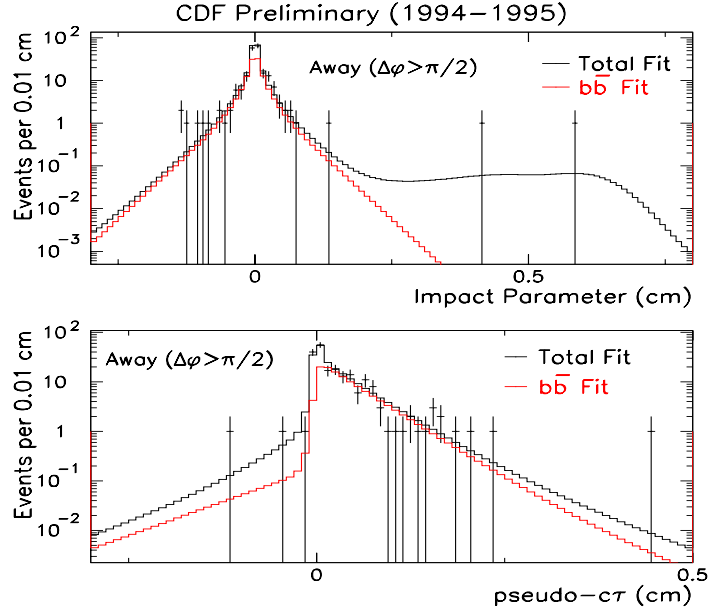


Figure 5.34: Result of the  $c\tau$ -impact parameter fit for the electron sample in the away bin. Top: Projection onto impact parameter axis. Bottom: Projection onto  $c\tau$  axis..

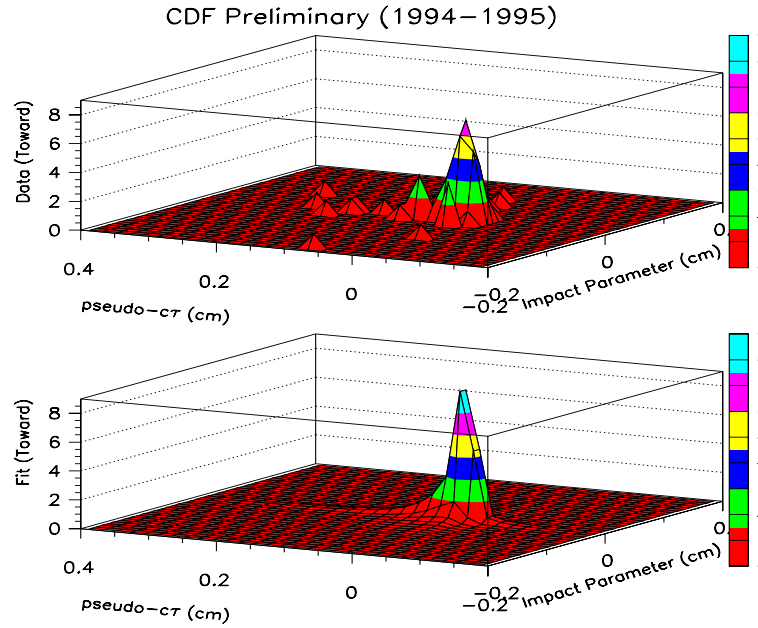


Figure 5.35: Result of the  $c\tau$ -impact parameter fit for the muon sample in the toward bin. Top: Data. Bottom: Fit.

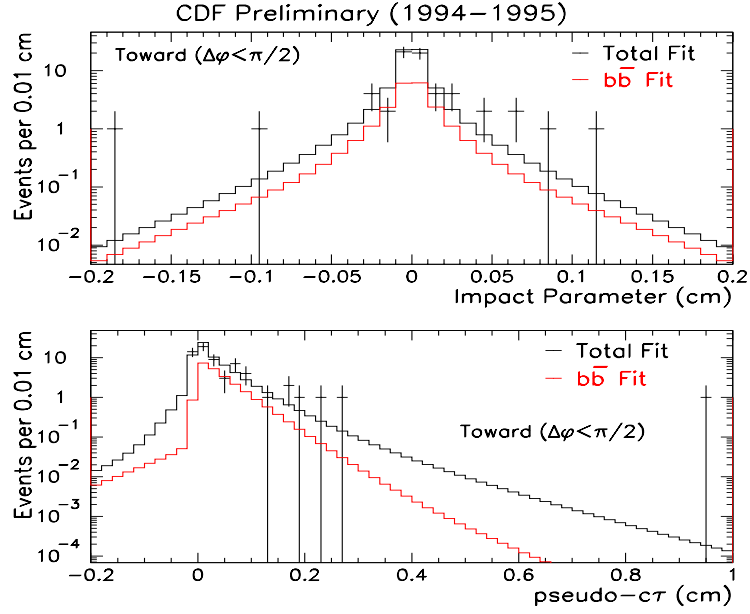


Figure 5.36: Result of the  $c\tau$ –impact parameter fit for the muon sample in the toward bin. Top: Projection onto impact parameter axis. Bottom: Projection onto  $c\tau$  axis..

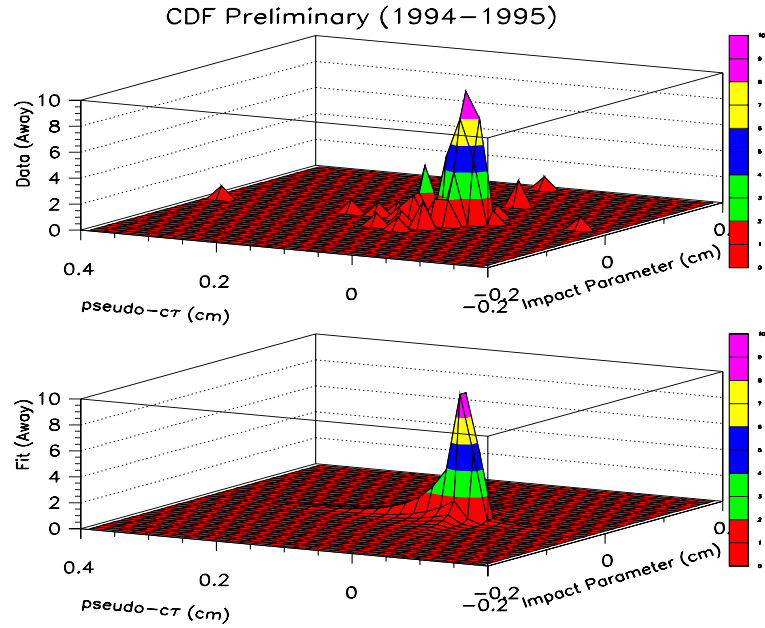


Figure 5.37: Result of the  $c\tau$ –impact parameter fit for the muon sample in the away bin. Top: Data. Bottom: Fit.

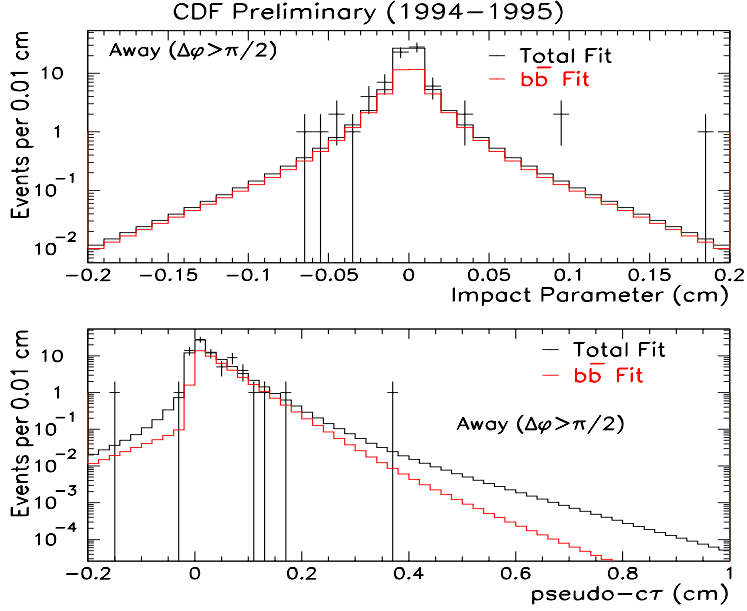


Figure 5.38: Result of the  $c\tau$ -impact parameter fit for the muon sample in the away bin. Top: Projection onto impact parameter axis. Bottom: Projection onto  $c\tau$  axis..

have a larger impact parameter than direct bottom leptons. In ref. [27, 90], the relative systematic uncertainty in  $f_{seq}$  was studied. In both measurements, the uncertainty included the systematic error due to the PDF as well as branching fraction uncertainties. The relative uncertainty in  $f_{seq}$  was  $\pm 19\%$  in both analyses. As both measurements used samples very similar to this analysis,  $\pm 19\%$  is used as the same relative uncertainty in  $f_{seq}$ . The effect on the uncertainty of  $f_{seq}$  is estimated by changing the  $f_{seq}$  by  $\pm 1\sigma$  and re-fitting  $F_b^{d_0}$ . The new  $F_b^{d_0}$  shapes are then used to re-fit  $f_{toward}$ , with the results shown in table 5.15. The maximum differences of  $\pm 0.1\%$  and  $\pm 0.3\%$  are assigned as the systematic uncertainty for the electron and muon samples, respectively.

#### 5.4.2 Bottom lifetime

The bottom hadrons' lifetimes ( $B^+$ ,  $B^0$ ,  $B_s$ , and  $\Lambda_b$ ) and their decay products' impact parameters are strongly correlated. In order to estimate the uncertainty in  $f_{toward}$  caused

	$f_{seq} - 1\sigma$	$f_{seq} + 1\sigma$
Electron	$19.08^{+6.5\%}_{-5.9\%}$	$19.13^{+6.5\%}_{-5.9\%}$
Muon	$34.27^{+9.1\%}_{-8.2\%}$	$34.43^{+9.2\%}_{-8.2\%}$

Table 5.15: *Fit results of  $f_{toward}$  varying  $f_{seq}$  in the bottom impact parameter shape by  $\pm 1\sigma$ .*

	B Lifetime $-1\sigma$	B Lifetime $+1\sigma$
Electron	$18.89^{+6.6\%}_{-5.7\%}$	$19.11^{+6.5\%}_{-5.9\%}$
Muon	$33.40^{+9.1\%}_{-8.2\%}$	$36.75^{+9.2\%}_{-8.4\%}$

Table 5.16: *Fit results of  $f_{toward}$  varying the bottom lifetimes in the bottom impact parameter shape by  $\pm 1\sigma$ .*

by the uncertainties in the bottom hadrons' lifetimes, two additional Monte Carlo samples are generated using BGENERATOR [91], a fast  $b\bar{b}$  Monte Carlo that approximates the NLO prediction by ref. [24]. In one sample, all the bottom hadrons lifetimes are shifted up by  $1\sigma$  from their PDG values ref. [79]. In the other sample, the lifetimes are shifted down by  $1\sigma$ . The  $F_b^{c\tau}$  shapes determined by these samples are then used in a re-fit of  $f_{toward}$ . Table 5.16 shows the  $f_{toward}$  values fit. The estimate of the systematic uncertainty due to the bottom lifetime is chosen to be the greatest differences from the standard fit.  $\pm 0.3\%$  and  $\pm 2.2\%$  are the uncertainties estimated in the electron and muon samples.

### 5.4.3 Bottom fragmentation ratios

$B_s$ ,  $B^+$ , and  $B^-$  have proper decay lengths of  $\sim 470 \mu\text{m}$ , whereas  $\Lambda_B$  has a proper decay length of  $387 \mu\text{m}$ . Thus, the uncertainty in the fraction of bottom quarks fragmenting to  $\Lambda_b$  leads to the largest uncertainty of the  $F_b^{c\tau}$  shape. Using BGENERATOR, two samples are generated shifting the  $\Lambda_b$  fragmentation function by  $\pm 1\sigma$ , with  $\sigma$  given by ref. [7]. The new  $F_b^{c\tau}$  shapes are used to re-fit  $f_{toward}$ , with the maximum difference from the standard

	$F_{\Lambda_b} - 1\sigma$	$F_{\Lambda_b} + 1\sigma$
Electron	$19.08^{+6.5\%}_{-5.9\%}$	$19.14^{+6.5\%}_{-5.9\%}$
Muon	$34.37^{+9.2\%}_{-8.2\%}$	$34.44^{+9.2\%}_{-8.2\%}$

Table 5.17: *Fit results of  $f_{toward}$  varying the  $\Lambda_b$  fragmentation fraction in  $F_b^{d_0}$  shape by  $\pm 1\sigma$ .*

	$n_{dconv} = 0$	$n_{bconv} = 0$
Electron	$19.0^{+6.6\%}_{-5.9\%}$	$19.2^{+6.5\%}_{-5.8\%}$

Table 5.18: *Fit results of  $f_{toward}$  fixing either  $n_{dconv}$  or  $n_{bconv}$  to zero.*

fit used as the estimate of the systematic uncertainty. Table 5.17 shows the  $f_{toward}$  fit results, yielding a systematic uncertainty of  $\pm 0.1\%$  and  $\pm 0.2\%$  for the electron and muon samples.

#### 5.4.4 $n_{bconv}/n_{dconv}$ ratio

Due to the limited number of residual conversions in the sample, the ratio between  $n_{bconv}$  and  $n_{dconv}$  is fixed to the fit ratio between  $J/\psi$  from bottom decay and directly produced  $J/\psi$ . In order to estimate the systematic uncertainty due to this assumption, the fit of the data is re-done with either  $n_{bconv}$  or  $n_{dconv}$  fixed to zero; the difference between fits are used as an estimate of the systematic uncertainty. Table 5.18 shows the  $f_{toward}$  fit results, yielding a systematic uncertainty of  $\pm 0.1\%$  for the electron sample.

#### 5.4.5 Residual conversion impact parameter shape

The residual conversion shape ( $F_{conv}$ ) is determined using data and simulation. In data, the conversion radii of the found conversions indicate that a large fraction ( $f_{conv}^{BadSVX} = 40.3 \pm 6.2\%$ ) of the conversion candidates have at least 1 SVX hit mis-assigned to the

	$f_{conv}^{BadSVX} - 1\sigma$	$f_{conv}^{BadSVX} + 1\sigma$
Electron	$19.0^{+6.6\%}_{-5.9\%}$	$19.3^{+6.5\%}_{-5.8\%}$

Table 5.19: *Fit results of  $f_{toward}$  varying  $f_{conv}^{BadSVX}$  in the residual conversion shape by  $\pm 1\sigma$ .*

track.  $F_{conv}$  is the sum of two shapes:  $F_{conv}^{GoodSVX}$ , which describes the shape of residual conversion where SVX hits are assumed to be correctly assigned (small conversion radii), and  $F_{conv}^{BadSVX}$ , which describes the shape of residual conversion where at least 1 SVX hit is assumed to be incorrectly assigned (large conversion radii).  $F_{conv}^{GoodSVX}$  and  $F_{conv}^{BadSVX}$  are determined using Monte Carlo in section 5.1.5. The value of  $f_{conv}^{GoodSVX}$  is changed by  $\pm 1\sigma$  in  $F_{conv}$  in order to estimate the systematic uncertainty due to the  $F_{conv}$  shape used. The values of  $f_{toward}$  fit using the varied  $F_{conv}$  shapes are shown in table 5.19. The maximum difference of  $\pm 0.2\%$  is assigned as a conservative estimate of the systematic uncertainty due to the residual conversion impact parameter shape used.

#### 5.4.6 Direct impact parameter shape

The direct impact parameter shapes ( $F_{direct}^{d_0}$ ) are determined by a fit to Monte Carlo samples in section 5.1.2. The finite size of the Monte Carlo samples lead to an uncertainty in the fit parameters of the shapes. In order to estimate the uncertainty in  $f_{toward}$  due the  $F_{direct}^{d_0}$  shape uncertainty, each parameter is fixed to a value  $\pm 1\sigma$  from the best fit value and the  $F_{direct}^{d_0}$  shape is re-fit. The new shape is then used in the impact parameter- $c\tau$  fit. Table 5.20 shows the result of the fits. The largest negative and positive differences from the standard fit is conservatively assigned as the systematic error,  $^{+0.3\%}_{-0.4\%}$  for the electron sample and  $^{+7.4\%}_{-1.0\%}$  for the muon sample.



Parameter	Electron		Muon	
	$-1\sigma$	$+1\sigma$	$-1\sigma$	$+1\sigma$
$f_1$	$19.17^{+6.5}_{-5.9}\%$	$19.15^{+6.5}_{-5.9}\%$	$41.60^{+9.8}_{-8.6}\%$	$34.66^{+9.2}_{-8.2}\%$
$\lambda_1$	$19.16^{+6.5}_{-5.9}\%$	$19.13^{+6.5}_{-5.9}\%$	$41.15^{+9.8}_{-8.6}\%$	$34.25^{+9.2}_{-8.2}\%$
$f_2$	$19.15^{+6.5}_{-5.9}\%$	$19.13^{+6.6}_{-5.9}\%$	$34.08^{+9.2}_{-8.2}\%$	$34.83^{+9.2}_{-8.2}\%$
$\lambda_2$	$19.16^{+6.6}_{-5.9}\%$	$19.16^{+6.6}_{-5.9}\%$	$41.93^{+9.7}_{-8.6}\%$	$33.54^{+9.2}_{-8.2}\%$
$\sigma_d$	$19.20^{+6.5}_{-5.9}\%$	$19.15^{+6.5}_{-5.9}\%$	$34.50^{+9.2}_{-8.2}\%$	$34.52^{+9.2}_{-8.2}\%$

Table 5.20:  $f_{toward}$  fit values varying the  $F_{direct}^{d_0}$  fit values within errors.

	$f^{back} - 1\sigma$	$f^{back} + 1\sigma$
Electron	$19.15^{+6.5}_{-5.9}\%$	$19.18^{+6.5}_{-5.9}\%$
Muon	$34.52^{+9.2}_{-8.2}\%$	$34.54^{+9.2}_{-8.2}\%$

Table 5.21: Fit results of  $f_{toward}$  varying  $f^{back}$  by  $\pm 1\sigma$ .

#### 5.4.7 Direct and bottom $c\tau$ shape

The direct and bottom  $c\tau$  shapes are determined by a fit to the data. In the fit, the fraction of fake  $J/\psi$  events ( $f^{back}$ ) is fixed at the predicted fraction given by  $\frac{R_{side}N_{side}}{N_{signal}}$ . In order to estimate the effect on  $f_{toward}$ , the value of  $f^{back}$  is change by  $\pm 1\sigma$  and the  $J/\psi$  mass signal region  $c\tau$  fit is re-done. The resulting  $F_{direct}^{c\tau}$  and  $F_b^{c\tau}$  shapes are used in a re-fit of  $f_{toward}$ . Table 5.21 shows the results of the fit. The greatest difference from the standard fit is chosen to be a conservative estimate of systematic uncertainty, yielding uncertainty estimates of  $\pm 0.015\%$  and  $\pm 0.01\%$  for the electron and muon channels.

#### 5.4.8 $N_{db}$

In this analysis, the number of events with a directly produced  $J/\psi$  with a lepton from bottom decay ( $n_{db}$ ) is assumed to be zero. In order to measure the effects of this assumption, a fit of  $f_{toward}$  is performed where  $n_{db}$  is a free parameter. The resulting

Source	Electron	Muon
Sequential Rate	$\pm 0.1\%$	$\pm 0.3\%$
B Lifetime	$\pm 0.3\%$	$\pm 2.2\%$
Fragmentation Fractions	$\pm 0.1\%$	$\pm 0.2\%$
$n_{bconv}/n_{dconv}$ ratio	$\pm 0.1\%$	
Residual Conversion Shape	$\pm 0.2\%$	
Direct Impact Parameter Shape	$^{+0.3}_{-0.4}\%$	$^{+7.4}_{-1.0}\%$
$f_{back}$ (for $F_{Direct}^{c\tau}$ and $F_b^{c\tau}$ )	$\pm 0.02\%$	$\pm 0.01\%$
$N_{db}$	$\pm 0.1\%$	$\pm 1.9\%$
Total	$^{+0.5}_{-0.6}\%$	$^{+8.0}_{-3.1}\%$

Table 5.22: *Summary of the estimated values of the systematic uncertainty for  $f_{toward}$ .*

$f_{toward}$  values fit are  $f_{toward}^e = 19.3^{+7.3}_{-6.5}\%$  and  $f_{toward}^\mu = 32.6^{+5.6}_{-4.8}\%$ . The difference in this fit from the standard fit is assigned as the systematic uncertainty due to  $n_{db}$ . We assign a  $\pm 1.9\%$  uncertainty to  $f_{toward}^\mu$  and  $\pm 0.1\%$  to  $f_{toward}^e$ .

#### 5.4.9 Total systematic uncertainty

The individual systematic uncertainties are added in quadrature in order to determine the combined systematic uncertainty. The systematic uncertainties for the electron and muon samples are  $^{+0.5}_{-0.6}\%$  and  $^{+8.0}_{-3.1}\%$ , respectively. Table 5.22 shows the estimates of the systematic uncertainties.

## 5.5 Final Results

The fraction of  $b\bar{b}$  pairs produced in the same azimuthal hemisphere at the Tevatron ( $f_{toward}$ ) has been measured using the event topology  $b \rightarrow J/\psi X; \bar{b} \rightarrow \ell X'$ . The toward fraction in the electron and muon samples is measured to be:

$$f_{toward}^e = 19.2^{+6.5}_{-5.9} \text{ } ^{+0.5}_{-0.6}\% \quad (5.32)$$

$$f_{toward}^{\mu} = 34.5_{-8.2}^{+9.2} \text{ }_{-3.1}^{+8.0} \% \quad (5.33)$$

where the first error is the fit error and the second error is the additional systematic uncertainties due to impact parameter- $c\tau$  shape uncertainties.

## Chapter 6

# Theory Predictions

The following sections compare the measured results to the theory predictions. First, a description of the correction of the measurement to the bottom quark level is given. The 'corrected' measurement is then compared to the next-to-leading order QCD prediction [24] of  $f_{toward}$  for bottom production. A short study of a leading-log Monte Carlo (PYTHIA) demonstrates the necessity to include all bottom Monte Carlo production mechanisms when using leading-log Monte Carlo to describe  $f_{toward}$  measured in experiment.

### 6.1 Correction to Quark Level

At the time of this analysis, no fragmenting, NLO QCD calculation of bottom production at the Tevatron exists. Therefore in order to compare to next-to-leading order calculations, one must 'correct' the experimental measurement to the bottom quark level ( $f_{toward}^{corr}$ ). Due to fragmentation, the conversion from the bottom meson's kinematics (which is measurable) to the bottom quark's kinematics (which is not measurable) does not have a simple relationship. Thus, the correction from bottom hadron to bottom quark kinematics

( $C_{B \rightarrow b}$ ) can have large systematic uncertainties. It is a conjecture of this analysis that most of these uncertainties cancel, as the measurement is a ratio. This assumption is supported later in this section

The correction is:

$$C_{B \rightarrow b} = \frac{f_{toward,mc}^{b\bar{b} \text{ } 90\%}}{f_{toward,mc}^{b \rightarrow J/\psi X; \bar{b} \rightarrow \ell Y}} \quad (6.1)$$

where:  $f_{toward,mc}^{b \rightarrow J/\psi X; \bar{b} \rightarrow \ell Y}$  is the  $f_{toward}$  prediction by PYTHIA with both the  $J/\psi$  and the additional lepton passing the selection criteria, and  $f_{toward,mc}^{b\bar{b} \text{ } 90\%}$  is the fraction of bottom quarks produced in the same hemisphere by PYTHIA which pass the following criteria:

- $p_T^{b_1} > p_T^{J/\psi}$  and  $|y^{b_1}| < y^{J/\psi}$
- $p_T^{b_2} > p_T^\ell$  and  $|y^{b_2}| < y^\ell$

$b_{1,2}$  can be either the bottom quark or antiquark. No requirements are made on the decay products of the bottom quarks.  $p_T^{J/\psi}$  and  $p_T^\ell$  are values of the  $p_T$  of the bottom quark (decaying to the  $J/\psi$  or lepton) in which 90% of the Monte Carlo events passing the selection requirements have a higher  $p_T$ . Similarly,  $y^{J/\psi}$  and  $y^\ell$  are the rapidities of bottom quarks decaying to the  $J/\psi$  or lepton in which 90% of the Monte Carlo events passing the selection requirements have a smaller absolute value of rapidity. The value of 90% is chosen as it has been convention in bottom cross section measurements at hadron colliders since ref. [25].

The prediction is made with the same sample used to estimate the bottom decay impact parameter shape in section 5.1.3. The distributions of the  $p_T$  and rapidity ( $y$ ) of bottom quarks in events that pass  $J/\psi$  and lepton selection are shown in figure 6.1–6.4. Table 6.1 shows the values determined in both the electron and muon samples for three different production mechanisms. The rapidities of all three mechanisms are very similar and are

determined by the detector geometry. The  $p_T$  values are different in the three mechanisms. Flavor creation produces two bottom quarks with similar momenta, while gluon splitting and flavor excitation produce quarks with dissimilar  $p_T$ . The values of  $y^{J/\psi}$ ,  $y^\ell$ ,  $p_T^{J/\psi}$ , and  $p_T^\ell$  used in the correction factor calculation is the average of the three production mechanisms. As an estimate of the systematic uncertainty,  $C_{B \rightarrow b}$  is calculated for each production mechanism separately. The systematical uncertainty is estimated as the largest difference between the individual and combined production mechanisms.

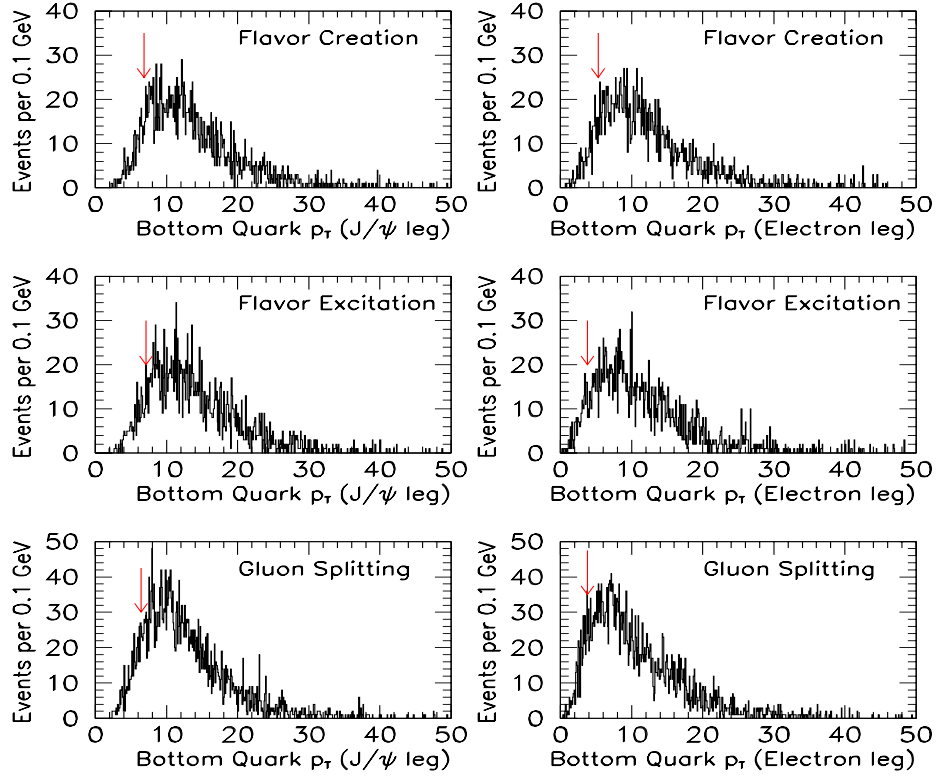


Figure 6.1:  $p_T$  of the bottom quarks in events that pass selection in the electron PYTHIA samples. The arrows indicate the 90% acceptance value.

Table 6.2 shows the  $f_{toward,mc}^{b\bar{b}^{90\%}}$ ,  $f_{toward,mc}^{b \rightarrow J/\psi X; \bar{b} \rightarrow \ell Y}$ , and  $C_{B \rightarrow b}$  for the complete sample and

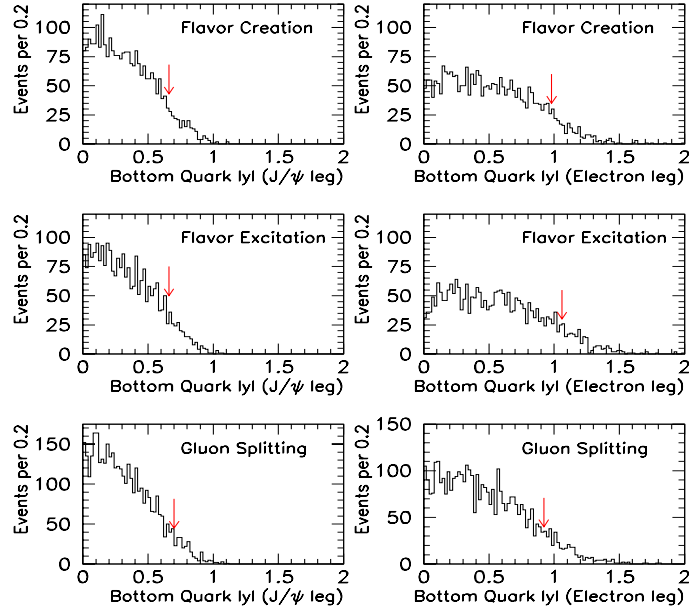


Figure 6.2:  $|y|$  of the bottom quarks in events that pass selection in the electron PYTHIA samples. The arrows indicate the 90% acceptance value.

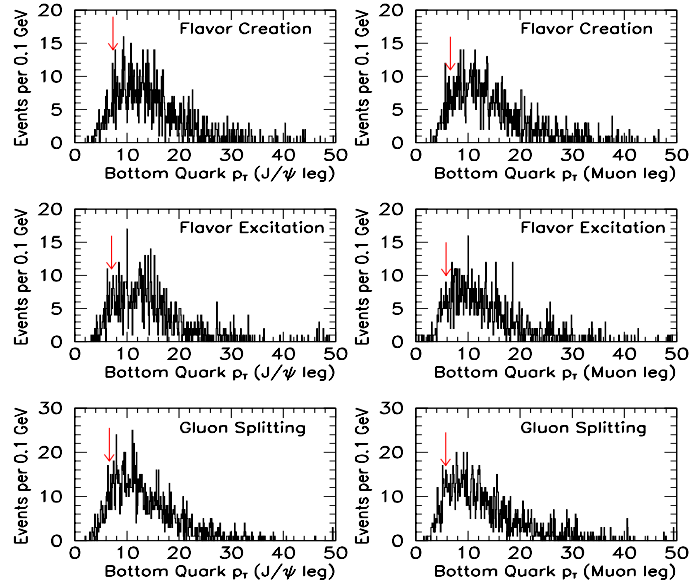


Figure 6.3:  $p_T$  of the bottom quarks in events that pass selection in the muon PYTHIA samples. The arrows indicate the 90% acceptance value.

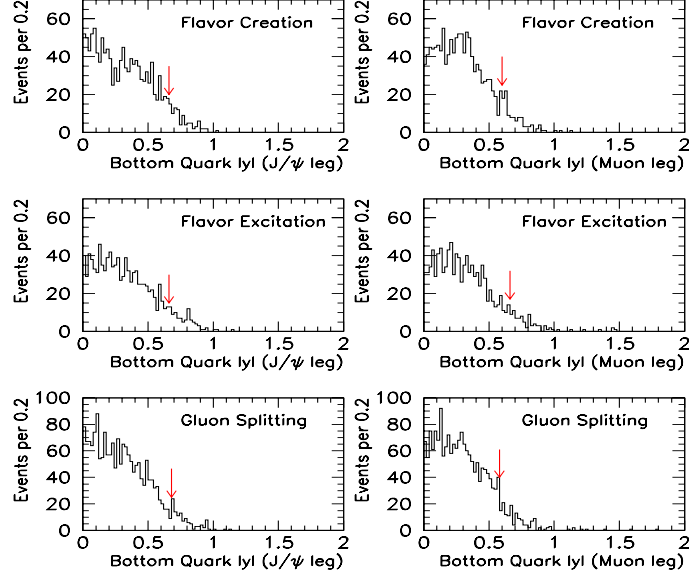


Figure 6.4:  $|y|$  of the bottom quarks in events that pass selection in the muon *PYTHIA* samples. The arrows indicate the 90% acceptance value.

Sample	$p_T^{J/\psi}$	$y^{J/\psi}$	$p_T^e$	$y^e$
FC	6.8 GeV	0.66	5.3 GeV	0.98
FE	7.1 GeV	0.66	3.8 GeV	1.06
GS	6.4 GeV	0.70	3.8 GeV	0.92
Ave	6.8 GeV	0.67	4.3 GeV	0.99

Sample	$p_T^{J/\psi}$	$y^{J/\psi}$	$p_T^\mu$	$y^\mu$
FC	7.3 GeV	0.66	6.6 GeV	0.60
FE	7.0 GeV	0.66	5.8 GeV	0.66
GS	6.6 GeV	0.68	5.7 GeV	0.58
Ave	7.0 GeV	0.67	6.0 GeV	0.61

Table 6.1: 90% acceptance requirements on the bottom quarks decaying to a  $J/\psi$  or a lepton predicting by *PYTHIA* Monte Carlo and a detector simulation. Top: Electron. Bottom: Muon.



	FC	FE	GS	Combined
$f_{toward,mc}^{b\bar{b}^{90\%}}$	$5.1 \pm 0.1\%$	$21.4 \pm 0.5\%$	$46.4 \pm 0.5\%$	$26.4 \pm 0.2\%$
$f_{toward,mc}^{b \rightarrow J/\psi X; \bar{b} \rightarrow \ell Y}$	$5.8 \pm 0.4\%$	$23.4 \pm 0.8\%$	$47.8 \pm 0.8\%$	$27.3 \pm 0.5\%$
$C_{B \rightarrow b}$	$0.879 \pm 0.063$	$0.915 \pm 0.038$	$0.971 \pm 0.020$	$0.967 \pm 0.019$

	FC	FE	GS	Combined
$f_{toward,mc}^{b\bar{b}^{90\%}}$	$3.5 \pm 0.2\%$	$19.5 \pm 0.8\%$	$47.2 \pm 0.8\%$	$25.5 \pm 0.4\%$
$f_{toward,mc}^{b \rightarrow J/\psi X; \bar{b} \rightarrow \ell Y}$	$3.4 \pm 0.5\%$	$20.4 \pm 1.3\%$	$49.3 \pm 1.2\%$	$26.3 \pm 0.7\%$
$C_{B \rightarrow b}$	$1.029 \pm 0.164$	$0.956 \pm 0.072$	$0.957 \pm 0.028$	$0.968 \pm 0.026$

Table 6.2: *Correction factor between the experimental measurement and the bottom quarks. Top: Electron sample. Bottom: Muon sample.*

the three separate production mechanisms. The values estimated are:

$$C_{B \rightarrow b}^e = 0.967 \pm 0.019(\text{stat.}) \pm 0.088(\text{syst.}) \quad (6.2)$$

$$C_{B \rightarrow b}^\mu = 0.968 \pm 0.026(\text{stat.}) \pm 0.061(\text{syst.}) \quad (6.3)$$

The measured toward fraction for the bottom quarks ( $f_{toward}^{corr}$ ) extracted using the correction factor ( $C_{B \rightarrow b}$ ) is:

$$f_{toward}^{corr,e} = 18.6_{-5.7}^{+6.3} {}_{-0.6}^{+0.5} \pm 1.7\% \quad (6.4)$$

$$f_{toward}^{corr,\mu} = 33.4_{-7.9}^{+8.9} {}_{-3.0}^{+7.7} \pm 2.3\% \quad (6.5)$$

where the first error is the fit error, the second error is the additional shape systematic uncertainties on  $f_{toward}$ , and the third error is the uncertainty due to the correction to the bottom quark kinematics.

## 6.2 Comparison to Next-To-Leading Order Theory

The measured forward fraction corrected to the quark level is compared to the NLO QCD predictions [24], using the same requirements as for the correction of the experimental measurements (given in table 6.1). The NLO prediction ( $f_{toward}^{NLO}$ ) is made using  $m_b = 4.75$  GeV, a renormalization/factorization scale  $\mu = \sqrt{m_b^2 + (p_T^b + p_T^{\bar{b}})/2}$  and CTEQ5M [35] and MRST99 [36] PDFs. To estimate the systematic uncertainty in the NLO calculation,  $m_b$  is varied from 4.5–5.0 GeV and  $\mu$  is varied from 0.5–2.0. To study the effects of large initial state parton transverse momenta ( $k_T$ ), the NLO prediction is also made with  $\langle k_T \rangle$  values of 0–4 GeV. The  $k_T$  effects are implemented in the same manner as described in section 2.5 and ref. [49]. In ref. [49], a  $\langle k_T \rangle$  of 3–4 GeV per parton is predicted at the Tevatron. With the lower momenta exchange in the interactions ( $q^2$ ) in this analysis relative the direct photon data used to make the predictions in ref. [49], one may expect a lower  $\langle k_T \rangle$  in this analysis. Tables 6.3 and 6.4 show the predicted  $f_{toward}^{NLO}$  and total cross sections predicted using MRST99 and CTEQ5M PDFs, respectively, for the different input values of  $\langle k_T \rangle$ ,  $m_b$ , and  $\mu$ .

Table 6.5 and figure 6.5 show the summary of the predictions. The NLO predictions do not depend strongly on the PDF selected. The  $f_{forward}^{corr,\mu}$  measured is consistent with the NLO prediction within  $1.6 \sigma$  for all values of  $\langle k_T \rangle$ , with the best agreement with  $\langle k_T \rangle = 3$  GeV. The  $f_{forward}^{corr,e}$  measured differs from the NLO prediction with  $\langle k_T \rangle = 4$  GeV at the  $3.3 \sigma$  level. The measured value is consistent with all  $\langle k_T \rangle \leq 3$  GeV at the  $1.6 \sigma$  level, with the best agreement at  $\langle k_T \rangle = 0$  GeV. Since the NLO prediction for  $\langle k_T \rangle = 0$  GeV and  $\langle k_T \rangle = 3$  GeV differ by only  $\sim 2\sigma$  within renormalization/factorization scale uncertainties, it would not be likely to differentiate between scale and  $k_T$  effects with a more precise

$m_B$	$\mu$	$\langle k_T \rangle$	$\sigma_e$	$f_{toward}^{NLO,e}$	$\sigma_\mu$	$f_{toward}^{NLO,\mu}$
4.75 GeV	1.0	0 GeV	1.63 $\mu\text{b}$	$16.5 \pm 0.2\%$	0.63 $\mu\text{b}$	$16.8 \pm 0.3\%$
4.75 GeV	2.0	0 GeV	1.33 $\mu\text{b}$	$13.2 \pm 0.3\%$	0.52 $\mu\text{b}$	$13.0 \pm 0.2\%$
4.75 GeV	0.5	0 GeV	2.14 $\mu\text{b}$	$20.1 \pm 0.2\%$	0.82 $\mu\text{b}$	$20.8 \pm 0.3\%$
5.0 GeV	1.0	0 GeV	1.50 $\mu\text{b}$	$16.0 \pm 0.2\%$	0.59 $\mu\text{b}$	$16.2 \pm 0.3\%$
4.5 GeV	1.0	0 GeV	1.74 $\mu\text{b}$	$17.2 \pm 0.2\%$	0.65 $\mu\text{b}$	$18.0 \pm 0.4\%$
4.75 GeV	1.0	1 GeV	1.48 $\mu\text{b}$	$19.1 \pm 0.3\%$	0.50 $\mu\text{b}$	$22.1 \pm 0.5\%$
4.75 GeV	2.0	1 GeV	1.21 $\mu\text{b}$	$15.2 \pm 0.2\%$	0.44 $\mu\text{b}$	$16.4 \pm 0.4\%$
4.75 GeV	0.5	1 GeV	1.89 $\mu\text{b}$	$23.9 \pm 0.3\%$	0.65 $\mu\text{b}$	$27.5 \pm 0.5\%$
5.0 GeV	1.0	1 GeV	1.37 $\mu\text{b}$	$18.5 \pm 0.2\%$	0.49 $\mu\text{b}$	$20.5 \pm 0.4\%$
4.5 GeV	1.0	1 GeV	1.59 $\mu\text{b}$	$19.9 \pm 0.3\%$	0.52 $\mu\text{b}$	$23.2 \pm 0.6\%$
4.75 GeV	1.0	2 GeV	1.49 $\mu\text{b}$	$23.1 \pm 0.4\%$	0.55 $\mu\text{b}$	$23.8 \pm 0.9\%$
4.75 GeV	2.0	2 GeV	1.25 $\mu\text{b}$	$18.2 \pm 0.3\%$	0.45 $\mu\text{b}$	$18.8 \pm 0.4\%$
4.75 GeV	0.5	2 GeV	1.93 $\mu\text{b}$	$28.2 \pm 0.4\%$	0.67 $\mu\text{b}$	$30.8 \pm 0.7\%$
5.0 GeV	1.0	2 GeV	1.38 $\mu\text{b}$	$22.3 \pm 0.4\%$	0.50 $\mu\text{b}$	$23.8 \pm 0.6\%$
4.5 GeV	1.0	2 GeV	1.60 $\mu\text{b}$	$24.2 \pm 0.5\%$	0.55 $\mu\text{b}$	$26.4 \pm 0.8\%$
4.75 GeV	1.0	3 GeV	1.68 $\mu\text{b}$	$31.7 \pm 0.6\%$	0.58 $\mu\text{b}$	$31.9 \pm 0.9\%$
4.75 GeV	2.0	3 GeV	1.40 $\mu\text{b}$	$26.4 \pm 0.5\%$	0.49 $\mu\text{b}$	$25.7 \pm 0.7\%$
4.75 GeV	0.5	3 GeV	2.18 $\mu\text{b}$	$37.3 \pm 0.5\%$	0.67 $\mu\text{b}$	$37.4 \pm 0.8\%$
5.0 GeV	1.0	3 GeV	1.53 $\mu\text{b}$	$30.5 \pm 0.5\%$	0.55 $\mu\text{b}$	$29.9 \pm 0.8\%$
4.5 GeV	1.0	3 GeV	1.81 $\mu\text{b}$	$34.0 \pm 0.6\%$	0.62 $\mu\text{b}$	$33.3 \pm 1.0\%$
4.75 GeV	1.0	4 GeV	2.03 $\mu\text{b}$	$45.1 \pm 0.7\%$	0.71 $\mu\text{b}$	$44.4 \pm 1.2\%$
4.75 GeV	2.0	4 GeV	1.70 $\mu\text{b}$	$40.8 \pm 0.6\%$	0.58 $\mu\text{b}$	$39.5 \pm 1.0\%$
4.75 GeV	0.5	4 GeV	2.63 $\mu\text{b}$	$50.2 \pm 0.6\%$	0.91 $\mu\text{b}$	$50.5 \pm 0.9\%$
5.0 GeV	1.0	4 GeV	1.84 $\mu\text{b}$	$43.6 \pm 0.7\%$	0.65 $\mu\text{b}$	$43.4 \pm 1.0\%$
4.5 GeV	1.0	4 GeV	2.22 $\mu\text{b}$	$47.7 \pm 0.8\%$	0.77 $\mu\text{b}$	$48.1 \pm 1.2\%$

Table 6.3: *NLO prediction [24] of total cross section and  $f_{toward}$  using the fiducial requirements from table 6.1 using the CTEQ5M PDF.*

measurement of  $f_{toward}^{corr}$ .

Figures 6.6 and 6.7 illustrate the effects of varying the PDF,  $\langle k_T \rangle$ ,  $m_b$ , and renormalization/factorization scale on the NLO predictions. Varying  $m_b$  mass does not affect the predicted shape, but instead only affects the total cross section predicted. The two different PDFs studied yields very similar shape and total cross section predictions. Only scale and  $\langle k_T \rangle$  variations yield appreciably different shape and total cross section predictions. Varying the renormalization/factorization scale changes the total cross section as expected, lowering the scale increases the total cross section. In addition, the varying

$m_B$	$\mu$	$\langle k_T \rangle$	$\sigma_e$	$f_{toward}^{NLO,e}$	$\sigma_\mu$	$f_{toward}^{NLO,\mu}$
4.75 GeV	1.0	0 GeV	1.59 $\mu\text{b}$	$16.9 \pm 0.2\%$	0.63 $\mu\text{b}$	$16.7 \pm 0.3\%$
4.75 GeV	2.0	0 GeV	1.32 $\mu\text{b}$	$13.1 \pm 0.2\%$	0.52 $\mu\text{b}$	$13.1 \pm 0.2\%$
4.75 GeV	0.5	0 GeV	2.10 $\mu\text{b}$	$20.5 \pm 0.2\%$	0.79 $\mu\text{b}$	$21.8 \pm 0.3\%$
5.0 GeV	1.0	0 GeV	1.48 $\mu\text{b}$	$16.3 \pm 0.2\%$	0.58 $\mu\text{b}$	$16.7 \pm 0.3\%$
4.5 GeV	1.0	0 GeV	1.72 $\mu\text{b}$	$17.3 \pm 0.2\%$	0.65 $\mu\text{b}$	$18.0 \pm 0.4\%$
4.75 GeV	1.0	1 GeV	1.46 $\mu\text{b}$	$19.4 \pm 0.3\%$	0.49 $\mu\text{b}$	$22.7 \pm 0.6\%$
4.75 GeV	2.0	1 GeV	1.21 $\mu\text{b}$	$15.3 \pm 0.2\%$	0.44 $\mu\text{b}$	$16.1 \pm 0.3\%$
4.75 GeV	0.5	1 GeV	1.88 $\mu\text{b}$	$24.1 \pm 0.3\%$	0.62 $\mu\text{b}$	$28.8 \pm 0.5\%$
5.0 GeV	1.0	1 GeV	1.36 $\mu\text{b}$	$18.8 \pm 0.2\%$	0.49 $\mu\text{b}$	$20.5 \pm 0.4\%$
4.5 GeV	1.0	1 GeV	1.55 $\mu\text{b}$	$20.3 \pm 0.3\%$	0.53 $\mu\text{b}$	$23.0 \pm 0.5\%$
4.75 GeV	1.0	2 GeV	1.49 $\mu\text{b}$	$23.2 \pm 0.4\%$	0.53 $\mu\text{b}$	$24.7 \pm 0.6\%$
4.75 GeV	2.0	2 GeV	1.25 $\mu\text{b}$	$18.3 \pm 0.3\%$	0.46 $\mu\text{b}$	$18.4 \pm 0.4\%$
4.75 GeV	0.5	2 GeV	1.89 $\mu\text{b}$	$28.9 \pm 0.4\%$	0.67 $\mu\text{b}$	$31.2 \pm 0.8\%$
5.0 GeV	1.0	2 GeV	1.37 $\mu\text{b}$	$22.4 \pm 0.4\%$	0.50 $\mu\text{b}$	$23.3 \pm 0.5\%$
4.5 GeV	1.0	2 GeV	1.58 $\mu\text{b}$	$24.4 \pm 0.4\%$	0.55 $\mu\text{b}$	$26.2 \pm 0.7\%$
4.75 GeV	1.0	3 GeV	1.65 $\mu\text{b}$	$31.9 \pm 0.6\%$	0.57 $\mu\text{b}$	$32.1 \pm 0.6\%$
4.75 GeV	2.0	3 GeV	1.39 $\mu\text{b}$	$26.3 \pm 0.4\%$	0.49 $\mu\text{b}$	$25.7 \pm 0.7\%$
4.75 GeV	0.5	3 GeV	2.15 $\mu\text{b}$	$36.9 \pm 0.5\%$	0.74 $\mu\text{b}$	$38.4 \pm 0.8\%$
5.0 GeV	1.0	3 GeV	1.52 $\mu\text{b}$	$30.7 \pm 0.5\%$	0.55 $\mu\text{b}$	$29.5 \pm 0.7\%$
4.5 GeV	1.0	3 GeV	1.80 $\mu\text{b}$	$33.6 \pm 0.7\%$	0.62 $\mu\text{b}$	$33.1 \pm 0.9\%$
4.75 GeV	1.0	4 GeV	2.01 $\mu\text{b}$	$44.9 \pm 0.7\%$	0.69 $\mu\text{b}$	$44.9 \pm 0.9\%$
4.75 GeV	2.0	4 GeV	1.67 $\mu\text{b}$	$40.6 \pm 0.3\%$	0.58 $\mu\text{b}$	$38.8 \pm 0.9\%$
4.75 GeV	0.5	4 GeV	2.59 $\mu\text{b}$	$49.7 \pm 0.6\%$	0.90 $\mu\text{b}$	$49.8 \pm 0.9\%$
5.0 GeV	1.0	4 GeV	1.83 $\mu\text{b}$	$42.8 \pm 0.6\%$	0.63 $\mu\text{b}$	$42.4 \pm 1.0\%$
4.5 GeV	1.0	4 GeV	2.23 $\mu\text{b}$	$47.4 \pm 0.7\%$	0.76 $\mu\text{b}$	$46.5 \pm 1.1\%$

Table 6.4: *NLO prediction [24] of total cross section and  $f_{toward}$  using the fiducial requirements from table 6.1 and the MRST99 PDF.*

	$f_{toward}^{e,corr}$
Data	$18.6^{+6.3}_{-5.7} {}^{+0.5}_{-0.6} \pm 1.7\%$
PYTHIA	$26.4\% \pm 0.2\%$ (stat.)
NLO MRST99 $\langle k_T \rangle = 0.0$ GeV	$16.9\% \pm 0.2\%$ (stat.) $^{+3.6\%}_{-3.8\%}$ (sys.)
NLO MRST99 $\langle k_T \rangle = 1.0$ GeV	$19.4\% \pm 0.3\%$ (stat.) $^{+4.8\%}_{-4.1\%}$ (sys.)
NLO MRST99 $\langle k_T \rangle = 2.0$ GeV	$23.2\% \pm 0.4\%$ (stat.) $^{+5.8\%}_{-5.0\%}$ (sys.)
NLO MRST99 $\langle k_T \rangle = 3.0$ GeV	$31.9\% \pm 0.6\%$ (stat.) $^{+5.3\%}_{-5.7\%}$ (sys.)
NLO MRST99 $\langle k_T \rangle = 4.0$ GeV	$44.9\% \pm 0.7\%$ (stat.) $^{+5.4\%}_{-4.8\%}$ (sys.)
NLO CTEQ5M $\langle k_T \rangle = 0.0$ GeV	$16.5\% \pm 0.2\%$ (stat.) $^{+3.7\%}_{-3.3\%}$ (sys.)
NLO CTEQ5M $\langle k_T \rangle = 1.0$ GeV	$19.1\% \pm 0.3\%$ (stat.) $^{+4.9\%}_{-3.9\%}$ (sys.)
NLO CTEQ5M $\langle k_T \rangle = 2.0$ GeV	$23.1\% \pm 0.4\%$ (stat.) $^{+5.2\%}_{-5.0\%}$ (sys.)
NLO CTEQ5M $\langle k_T \rangle = 3.0$ GeV	$31.7\% \pm 0.6\%$ (stat.) $^{+6.0\%}_{-5.4\%}$ (sys.)
NLO CTEQ5M $\langle k_T \rangle = 4.0$ GeV	$45.1\% \pm 0.7\%$ (stat.) $^{+5.5\%}_{-4.6\%}$ (sys.)

	$f_{toward}^{\mu,corr}$
Data	$33.4^{+8.9}_{-7.9} {}^{+7.7}_{-3.0} \pm 2.3\%$
PYTHIA	$25.5\% \pm 0.4\%$ (stat.)
NLO MRST99 $\langle k_T \rangle = 0.0$ GeV	$16.7\% \pm 0.3\%$ (stat.) $^{+5.2\%}_{-3.6\%}$ (sys.)
NLO MRST99 $\langle k_T \rangle = 1.0$ GeV	$22.7\% \pm 0.6\%$ (stat.) $^{+6.1\%}_{-7.0\%}$ (sys.)
NLO MRST99 $\langle k_T \rangle = 2.0$ GeV	$24.7\% \pm 0.6\%$ (stat.) $^{+6.7\%}_{-6.5\%}$ (sys.)
NLO MRST99 $\langle k_T \rangle = 3.0$ GeV	$32.1\% \pm 0.6\%$ (stat.) $^{+6.4\%}_{-6.9\%}$ (sys.)
NLO MRST99 $\langle k_T \rangle = 4.0$ GeV	$44.9\% \pm 0.9\%$ (stat.) $^{+5.1\%}_{-6.6\%}$ (sys.)
NLO CTEQ5M $\langle k_T \rangle = 0.0$ GeV	$16.8\% \pm 0.3\%$ (stat.) $^{+4.1\%}_{-3.8\%}$ (sys.)
NLO CTEQ5M $\langle k_T \rangle = 1.0$ GeV	$22.1\% \pm 0.5\%$ (stat.) $^{+5.6\%}_{-5.9\%}$ (sys.)
NLO CTEQ5M $\langle k_T \rangle = 2.0$ GeV	$23.8\% \pm 0.9\%$ (stat.) $^{+7.4\%}_{-5.0\%}$ (sys.)
NLO CTEQ5M $\langle k_T \rangle = 3.0$ GeV	$31.9\% \pm 0.9\%$ (stat.) $^{+5.7\%}_{-6.5\%}$ (sys.)
NLO CTEQ5M $\langle k_T \rangle = 4.0$ GeV	$44.4\% \pm 1.2\%$ (stat.) $^{+7.1\%}_{-5.0\%}$ (sys.)

Table 6.5: Compilation of the corrected data results, the PYTHIA predictions, and the NLO predictions of  $f_{toward}$  using the fiducial requirements from table 6.1 for the theory and the correction factor  $C_{B \rightarrow b}$  from table 6.2. Top: Electron. Bottom: Muon.

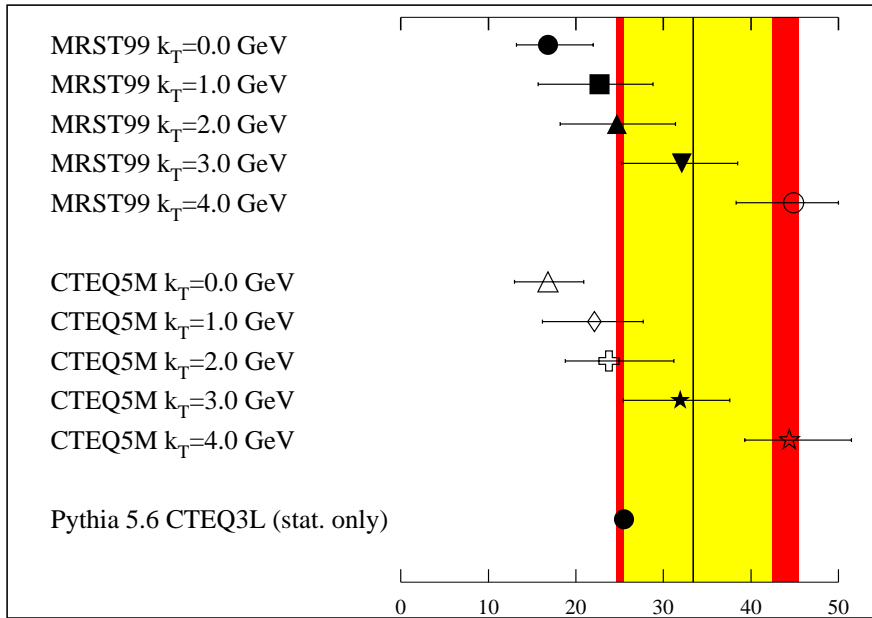
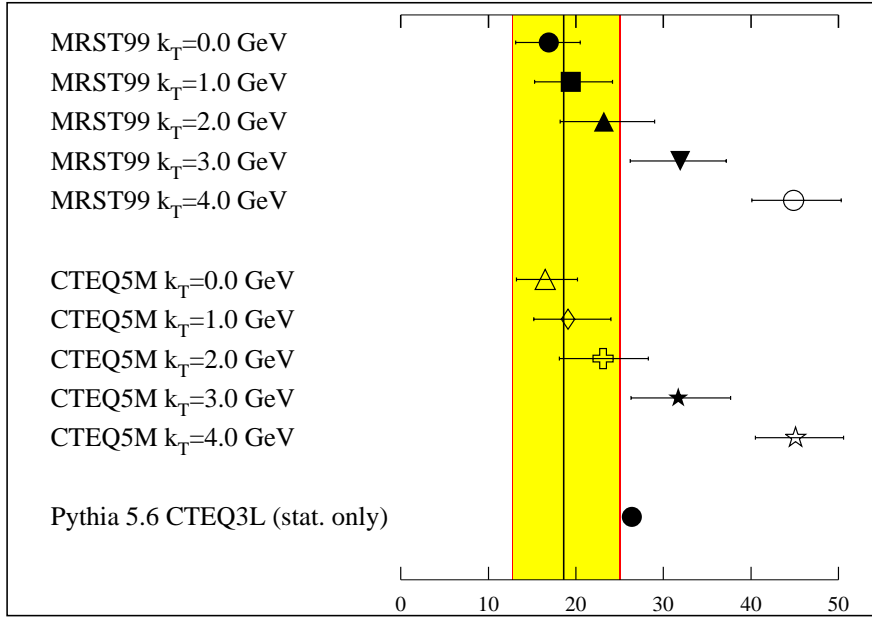


Figure 6.5: NLO prediction [24] of  $f_{toward}$  using various  $k_T$  smearing values. The errors include the statistical and systematic errors on the calculation. The PYTHIA prediction is shown as a reference and only includes statistical errors. The experimental result is shown with the vertical black line. The yellow and red areas indicate the error returned by the fit and the total error including the additional systematics. Top: Electrons. Bottom: Muons

the scale changes the prediction rate at large  $\Delta\phi^{b\bar{b}}$  ( $> 2.9$  radians) relative to the rest of the distribution, while the shape of  $< 2.9$  radian region varies little. Varying the scale changes the relative rates of  $p\bar{p} \rightarrow b\bar{b}$  to  $p\bar{p} \rightarrow b\bar{b}g$  in the NLO prediction. Varying the  $\langle k_T \rangle$  on the other hand, changes the predicted  $\Delta\phi^{b\bar{b}}$  in a more continuous manner. With the increased number of  $J/\psi + \ell$  expected in Run II, a differential azimuthal cross section measurement with 6–12 bins in  $\Delta\phi$  should be able to distinguish between scale uncertainty and  $k_T$  smearing.

### 6.2.1 NLO and PYTHIA $p_T$ and rapidity spectra comparisons

The correction to the quark level and the 90% acceptance regions in  $p_T$  and rapidity are determined by PYTHIA. These quantities are then used to calculate and compare to the NLO QCD prediction. One concern for using this prescription would be a sizable difference in the predicted shapes of the  $p_T$  and rapidity of the bottom quarks in the two models. Figure 6.8 and 6.9 show these distributions for the electron and muon acceptance regions. The NLO predictions and individual PYTHIA contributions are all normalized to the total PYTHIA predicted cross section. The distributions all agree excellently with each other. Thus, the prescription of the calculation of the acceptance regions, correction factors, and NLO predictions is self-consistent.

### 6.2.2 NLO and PYTHIA $\Delta\phi$ , $p_T^{b\bar{b}}$ , and R spectra comparisons

The  $\Delta\phi$ ,  $p_T^{b\bar{b}}$ , and R spectra of PYTHIA and NLO QCD do not effect the acceptance calculation or the fits which gives the experimental  $f_{\text{toward}}$  measurement. It is of general interest to understand when the predictions of PYTHIA and NLO QCD agree in these variables. Figures 6.10 and 6.11 show these distributions. Only the NLO predictions are

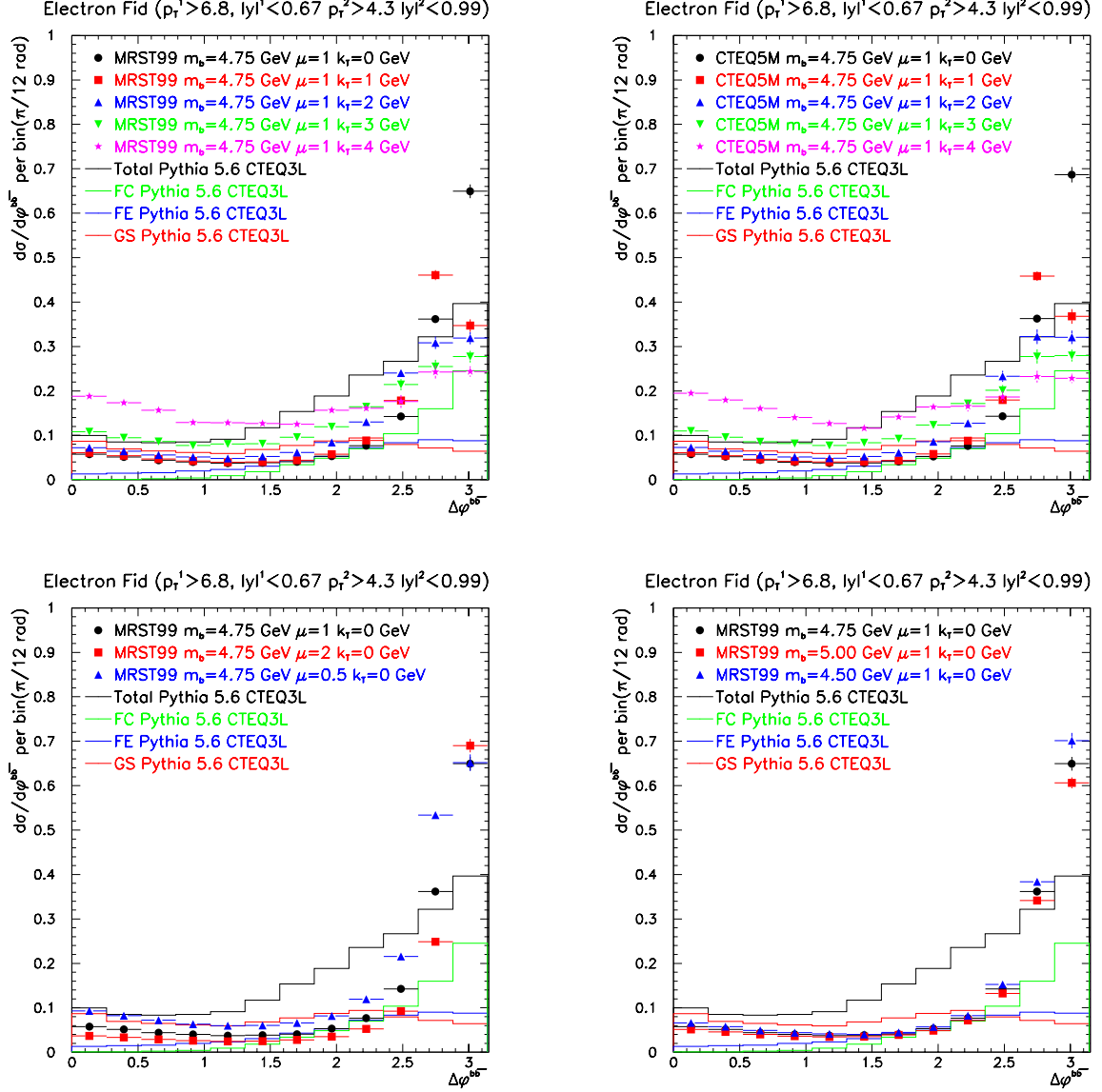


Figure 6.6: NLO prediction [24] of bottom spectra with electron fiducial requirements in table 6.1. The PYTHIA prediction is shown as a reference. Top Left: MRST99 PDF varying the additional  $k_T$  smearing. Top Right: CTEQ5M PDF varying the additional  $k_T$  smearing. Bottom Left: MRST99 PDF varying the renormalization scale  $\mu$ . Bottom Right: MRST99 PDF varying the bottom quark mass  $m_B$ .



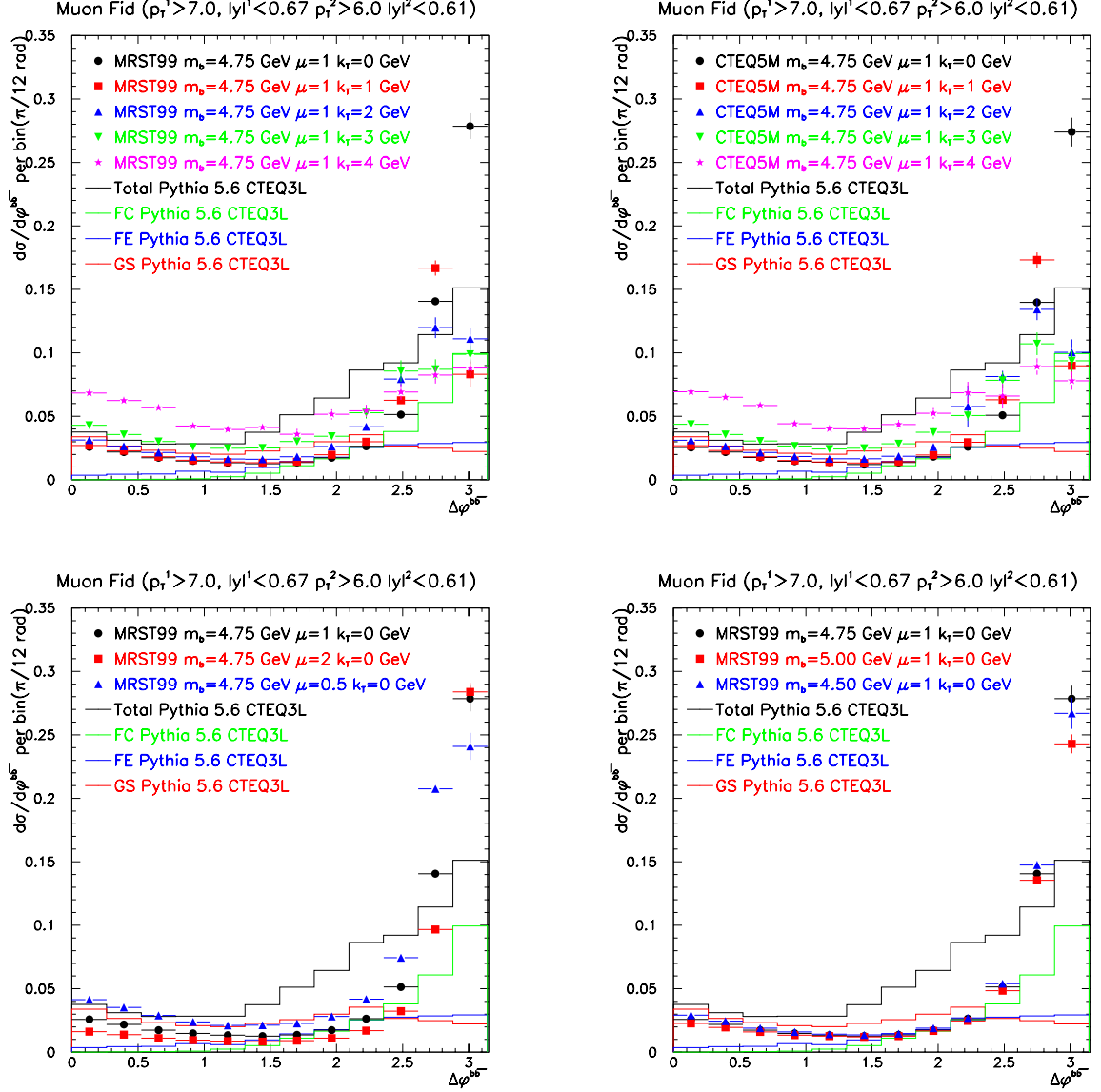


Figure 6.7: NLO prediction [24] of bottom spectra with muon fiducial requirements in table 6.1. The PYTHIA prediction is shown as a reference. Top Left: MRST99 PDF varying the additional  $k_T$  smearing. Top Right: CTEQ5M PDF varying the additional  $k_T$  smearing. Bottom Left: MRST99 PDF varying the renormalization scale  $\mu$ . Bottom Right: MRST99 PDF varying the bottom quark mass  $m_B$ .

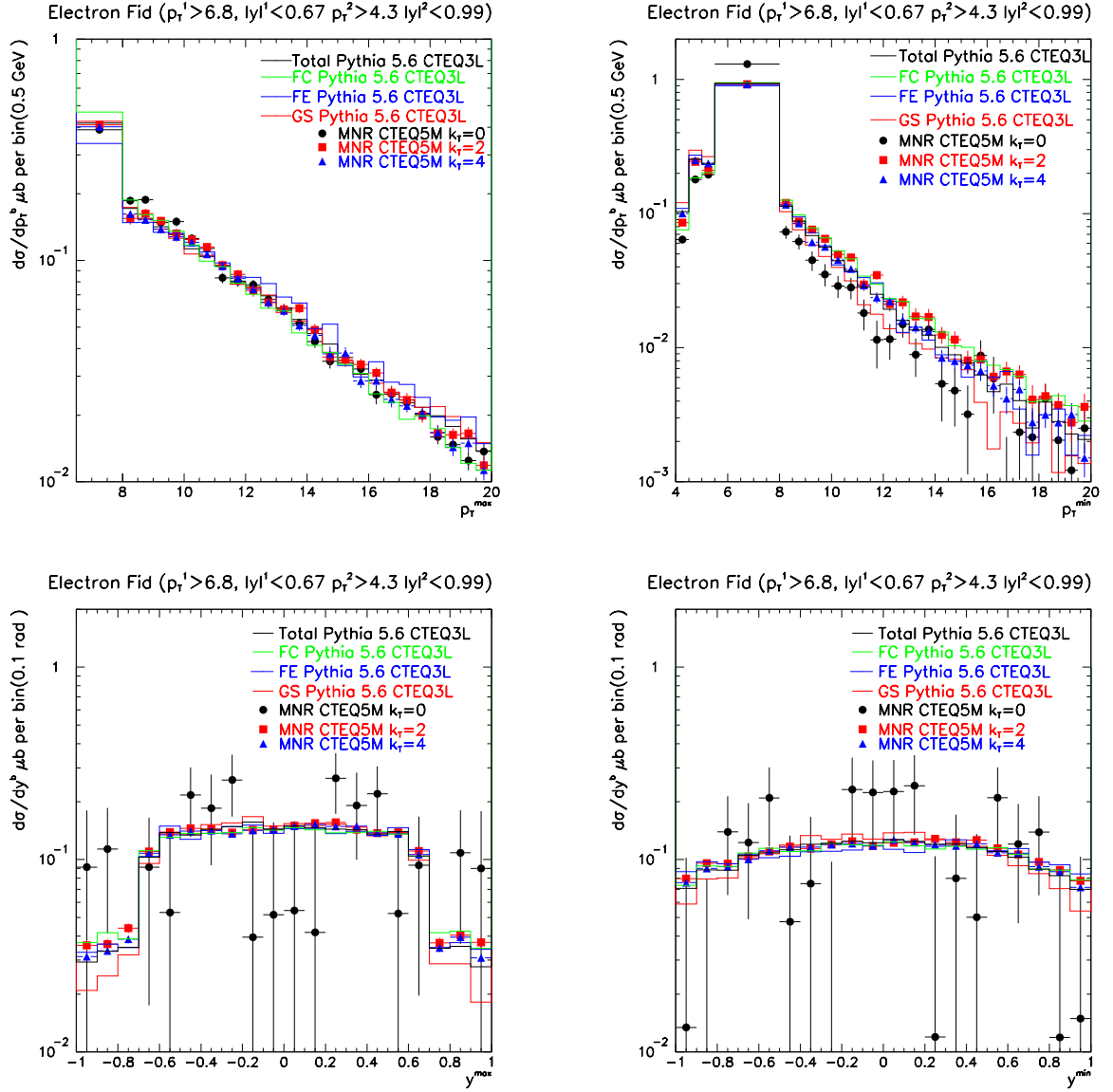


Figure 6.8: Comparison of the NLO prediction [24] of bottom spectra with electron fiducial requirements in table 6.1 to the PYTHIA prediction. The distributions are all normalized to the total PYTHIA prediction. The uneven binning occurs in  $p_T$  regions where the NLO calculation has large negative terms due to virtual diagrams and collinear subtraction. See section 2.3 for a complete explanation. Top Left: Maximum bottom quark  $p_T$ . Top Right: Minimum bottom quark  $p_T$ . Bottom Left: Rapidity of bottom quark with maximum bottom quark  $p_T$ . Bottom Right: Rapidity of bottom quark with minimum bottom quark  $p_T$ .

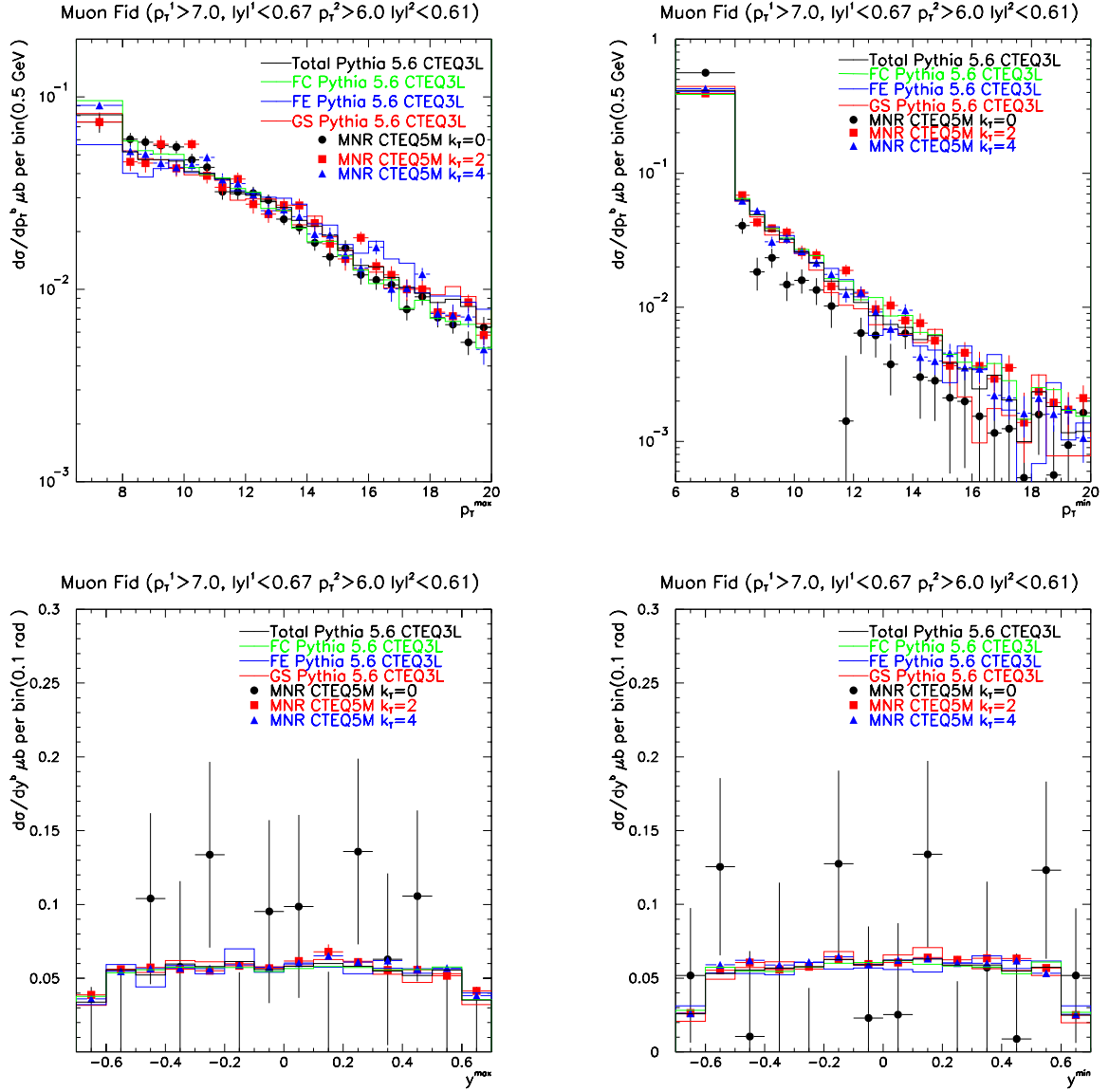


Figure 6.9: Comparison of the NLO prediction [24] of bottom spectra with muon fiducial requirements in table 6.1 to the PYTHIA prediction. The distributions are all normalized to the total PYTHIA prediction. The uneven binning occurs in  $p_T$  regions where the NLO calculation has large negative terms due to virtual diagrams and collinear subtraction. See section 2.3 for a complete explanation. Top Left: Maximum bottom quark  $p_T$ . Top Right: Minimum bottom quark  $p_T$ . Bottom Left: Rapidity of bottom quark with maximum bottom quark  $p_T$ . Bottom Right: Rapidity of bottom quark with minimum bottom quark  $p_T$ .

normalized to the total PYTHIA cross section as the individual PYTHIA contributions are expected to be different.

The first thing to note is that PYTHIA flavor creation only can not be tuned in order to match to the NLO prediction with  $\langle k_T \rangle = 0.0$  GeV. Increasing the initial or final state radiation would yield a  $\Delta\phi$  distributions that is much too wide at large  $\Delta\phi$ . Decreasing the initial state radiation would make the disagreement at low  $\Delta\phi$  to be even larger. The other thing to note is that the NLO QCD and PYTHIA predictions of the shape of  $\Delta\phi$ ,  $p_T^{b\bar{b}}$ , and R spectra agree fairly well with a  $2 \text{ GeV} < \langle k_T \rangle < 3 \text{ GeV}$  in the NLO prediction. Thus, the PYTHIA and NLO QCD have very similar kinematical distributions with the predicted  $\langle k_T \rangle$  at the Tevatron in ref. [49].

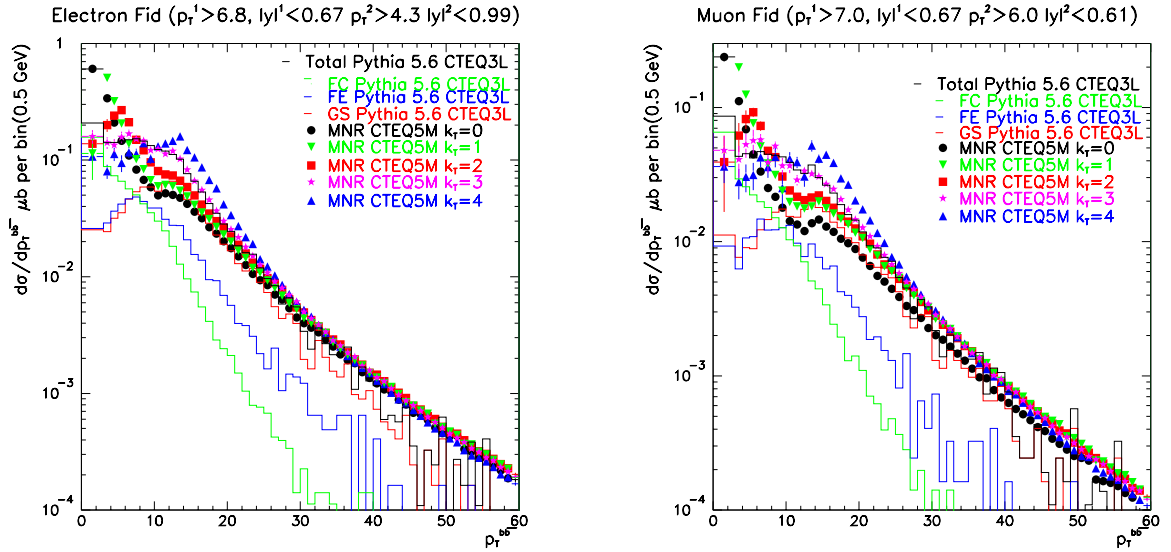


Figure 6.10: Comparison of the NLO prediction [24] of bottom spectra with electron and muon fiducial requirements in table 6.1 to the PYTHIA prediction. Only the NLO predictions are normalized to the total PYTHIA prediction. The uneven binning occurs in  $p_T^{b\bar{b}}$  regions where the NLO calculation has large negative terms due to virtual diagrams and collinear subtraction. See section 2.3 for a complete explanation. Left:  $p_T$  of  $b\bar{b}$  system, electron requirements. Right:  $p_T$  of  $b\bar{b}$  system, muon requirements.

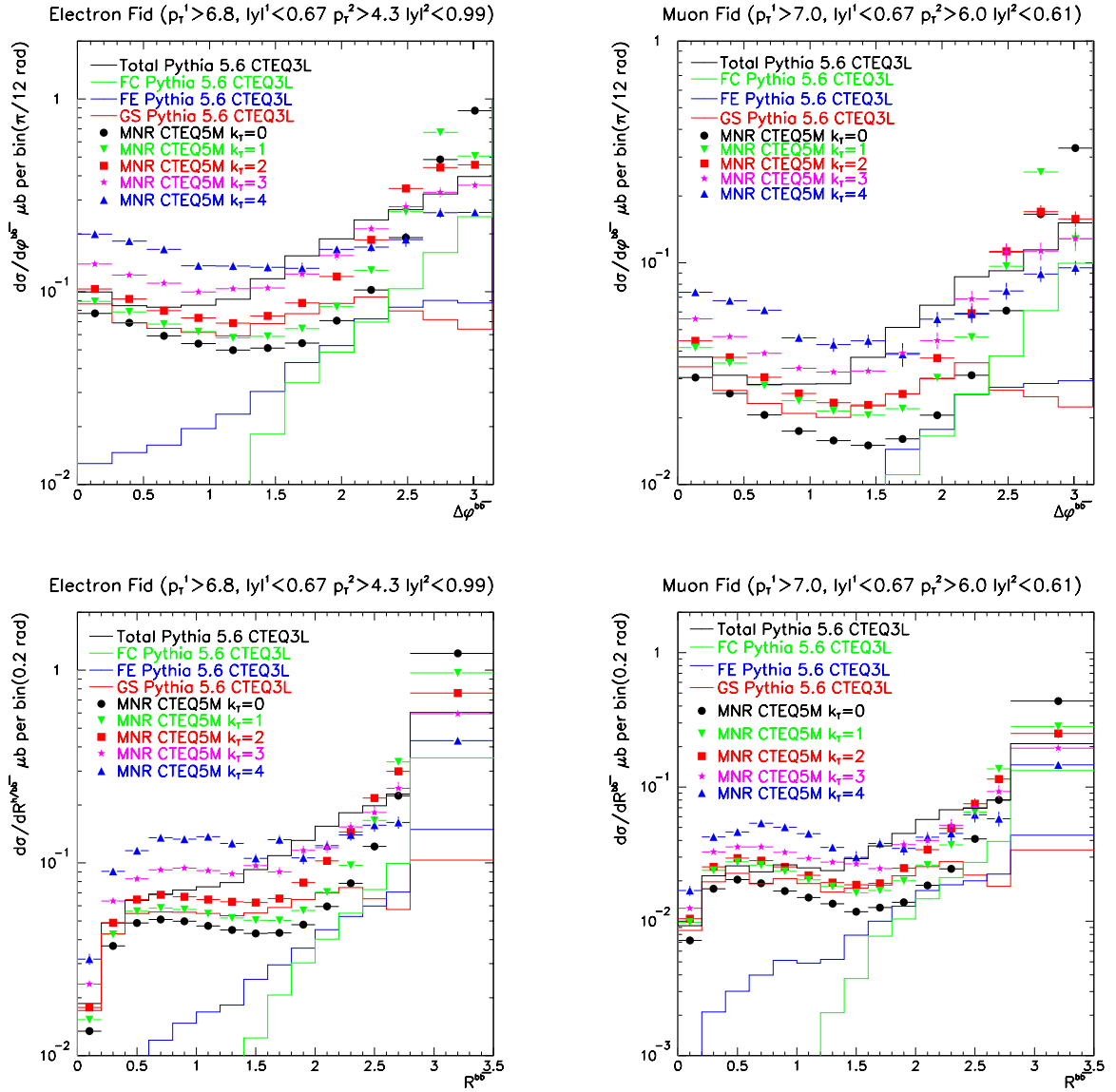


Figure 6.11: Comparison of the NLO prediction [24] of bottom spectra with electron and muon fiducial requirements in table 6.1 to the PYTHIA prediction. Only NLO distributions are normalized to the total PYTHIA prediction. The individual PYTHIA contributions are expected to have different distributions. The uneven binning occurs in  $R$  regions where the NLO calculation has large negative terms due to virtual diagrams and collinear subtraction. See section 2.3 for a complete explanation. Top Left:  $\Delta\phi^{b\bar{b}}$ , electron requirements. Top Right:  $\Delta\phi^{b\bar{b}}$ , muon requirements. Bottom Left: distance  $R$ , electron requirements. Bottom Right: distance  $R$ , muon requirements.

### 6.2.3 NLO and PYTHIA total cross section comparison

In ref. [21], the single bottom cross section measurements are found to agree with leading-log Monte Carlo much better than the full NLO calculations. The ratio between next-to-leading order and leading-log cross section ( $k^{NLO,LL} \equiv \frac{\sigma^{NLO}}{\sigma^{LL}}$ ) for single bottom quarks varies between 0.3–0.5. Small value of  $k^{NLO,LL}$  may indicate a large amount of ‘double counting’ in the the leading-log prediction, due to the lack of interference terms between the three production mechanisms. The ratio between the two predictions while making requirements on both bottom quarks (as is done in this analysis) provides information about the effects of these inference terms. Table 6.6 compiles the PYTHIA and NLO cross section predictions, and the respective ratio for the given PDF and  $\langle k_T \rangle$ . The error on the NLO calculation is from scale and bottom quark mass dependence. The ratio  $k^{NLO,LL}$  varies between 0.7-1.0 depending on the  $\langle k_T \rangle$  used in the NLO calculation. The ratio is closer to 1 once requirements are made on both bottom quarks.

## 6.3 Comparison to Leading-Log Order Theory (PYTHIA)

The next-to-leading order QCD calculations of bottom production for the Tevatron currently available are not practical for many experimental purposes. Typically, the cross section prediction is histogrammed in  $p_T$ ,  $y$ , and  $\phi$  of both bottom quarks. As described previously, the NLO Monte Carlo uses negative counter-terms to control singularities in the  $b\bar{b}$  differential cross-section. In order to ensure that the differential cross section has no negative regions, large number of events have to be calculated and the binning of the histograms must be done extremely carefully. In order to estimate theoretical systematic uncertainties correctly, the calculation would have to be re-done varying the renormalization

	$\sigma_{Total}^e$	$k^e$	$\sigma_{Total}^e$	$k^\mu$
PYTHIA (FC)	0.67 $\mu b$		0.26 $\mu b$	
PYTHIA (FE)	0.55 $\mu b$		0.18 $\mu b$	
PYTHIA (GS)	0.88 $\mu b$		0.31 $\mu b$	
PYTHIA (TOTAL)	2.13 $\mu b$		0.75 $\mu b$	
NLO MRST99 $\langle k_T \rangle = 0.0$ GeV	1.59 $\mu b^{+0.52}_{-0.26} \mu b$	0.75 $^{+0.26}_{-0.12}$	0.63 $\mu b^{+0.16}_{-0.12} \mu b$	0.84 $^{+0.21}_{-0.16}$
NLO MRST99 $\langle k_T \rangle = 1.0$ GeV	1.46 $\mu b^{+0.43}_{-0.27} \mu b$	0.69 $^{+0.20}_{-0.13}$	0.49 $\mu b^{+0.14}_{-0.06} \mu b$	0.65 $^{+0.19}_{-0.08}$
NLO MRST99 $\langle k_T \rangle = 2.0$ GeV	1.49 $\mu b^{+0.32}_{-0.26} \mu b$	0.70 $^{+0.15}_{-0.12}$	0.53 $\mu b^{+0.14}_{-0.08} \mu b$	0.71 $^{+0.19}_{-0.11}$
NLO MRST99 $\langle k_T \rangle = 3.0$ GeV	1.65 $\mu b^{+0.52}_{-0.29} \mu b$	0.78 $^{+0.25}_{-0.14}$	0.57 $\mu b^{+0.18}_{-0.10} \mu b$	0.76 $^{+0.24}_{-0.13}$
NLO MRST99 $\langle k_T \rangle = 4.0$ GeV	2.09 $\mu b^{+0.68}_{-0.49} \mu b$	0.98 $^{+0.32}_{-0.23}$	0.69 $\mu b^{+0.22}_{-0.13} \mu b$	0.92 $^{+0.29}_{-0.17}$
NLO CTEQ5M $\langle k_T \rangle = 0.0$ GeV	1.63 $\mu b^{+0.52}_{-0.32} \mu b$	0.77 $^{+0.25}_{-0.15}$	0.63 $\mu b^{+0.14}_{-0.12} \mu b$	0.84 $^{+0.19}_{-0.16}$
NLO CTEQ5M $\langle k_T \rangle = 1.0$ GeV	1.48 $\mu b^{+0.34}_{-0.29} \mu b$	0.70 $^{+0.16}_{-0.14}$	0.50 $\mu b^{+0.15}_{-0.06} \mu b$	0.67 $^{+0.20}_{-0.09}$
NLO CTEQ5M $\langle k_T \rangle = 2.0$ GeV	1.49 $\mu b^{+0.45}_{-0.17} \mu b$	0.70 $^{+0.21}_{-0.08}$	0.55 $\mu b^{+0.12}_{-0.11} \mu b$	0.73 $^{+0.16}_{-0.15}$
NLO CTEQ5M $\langle k_T \rangle = 3.0$ GeV	1.67 $\mu b^{+0.53}_{-0.30} \mu b$	0.78 $^{+0.25}_{-0.13}$	0.58 $\mu b^{+0.10}_{-0.10} \mu b$	0.77 $^{+0.13}_{-0.13}$
NLO CTEQ5M $\langle k_T \rangle = 4.0$ GeV	2.03 $\mu b^{+0.63}_{-0.49} \mu b$	0.95 $^{+0.29}_{-0.22}$	0.71 $\mu b^{+0.21}_{-0.14} \mu b$	0.95 $^{+0.28}_{-0.19}$

Table 6.6: *PYTHIA* and NLO predictions of the total cross section and their ratio ( $k$ ) using the fiducial requirements from table 6.1.

scale, bottom mass, and parton distribution functions. This program has not been done in previous bottom analyses. Additionally once the bottom quark spectra are determined, the quarks have to be fragmented, which also adds to the uncertainty.

Instead, most analyses use a leading-log Monte Carlo to estimate acceptances, tagging power, etc. The leading-log Monte Carlo produce unweighted bottom hadrons which can be generated relatively quickly and can be input into detector simulations. In addition, the leading-log Monte Carlo includes the effects of color connection in the fragmentation process, as well as underlying event and fragmentation particles. If a comparison to NLO theory is wanted, an acceptance correction of the quark level is made similar to section 6.1.

Unfortunately, the relative cross sections of three production mechanisms have a large uncertainty in leading-log Monte Carlo when varying PDFs or leading-log generators. This uncertainty is as large as a factor of 2 increase or decrease in relative rates [92]. The distributions of  $\Delta\phi$  and  $\Delta y$  are also dependent on the generator used. The fragmentation model in PYTHIA and HERWIG include 'color coherence effects', where ISAJET does not. In addition, the bottom quark mass is included in HERWIG's generation of flavor excitation, where PYTHIA does not. The different leading-log generators include differing amounts of initial state radiation. All these effects lead to variation of the shapes expected for the three mechanisms. Therefore, an experimental measurement of these angular distributions has to be used to tune the leading-log generators, improving their ability to describe bottom production. The large uncertainties in the  $f_{toward}$  measurements does not make an systematic study of the tuning of leading-log Monte Carlo possible, and is therefore beyond the scope of this analysis. In Run II of the Tevatron, the experimental measurement uncertainties should be small enough to constrain the leading-log generators.



	Electron	Muon
Flavor Creation	$5.8 \pm 0.4\%$	$3.4 \pm 0.5\%$
Flavor Excitation	$23.4 \pm 0.8\%$	$20.4 \pm 1.3\%$
Gluon Splitting	$47.8 \pm 0.8\%$	$49.3 \pm 1.2\%$
Combined	$27.3 \pm 0.5\%$	$26.3 \pm 0.7\%$
Experimental Measurement	$18.6^{+6.3}_{-5.7} {}^{+0.5}_{-0.6} \pm 1.7\%$	$33.4^{+8.9}_{-7.9} {}^{+7.7}_{-3.0} \pm 2.3\%$

Table 6.7: *PYTHIA* prediction of  $f_{toward}$  and the experimental measurement.

As an example, the prediction of PYTHIA 5.6 using Bowler fragmentation [43] and CTEQ3L PDF is shown. The sample used for the prediction is the same one used to determine  $F_b^{d_0}$  in section 5.1.3. The detector simulation is applied in the same manner. The toward fraction of the events passing the selection criteria is calculated for the combined samples as well as for each mechanism separately. The Monte Carlo prediction and the measured values of  $f_{toward}^{corr}$  are shown in table 6.7. The Monte Carlo prediction is used for the calculation of  $C_{B \rightarrow b}$  in section 6.1.

The experimental measurements of  $f_{toward}$  are inconsistent with only flavor creation at the  $2.1 \sigma$  and  $3.4 \sigma$  level for the electron and muon samples, respectively. The experimental measurements are more consistent with the combination of all three production mechanisms,  $1.3 \sigma$  and  $0.8 \sigma$  level for the two data samples. The result indicates that all three mechanisms should be included in order to describe the  $\Delta\phi$  shape between bottom hadrons, which is important for the simulation of opposite side flavor taggers. In ref. [21], it is shown that the single bottom differential cross section is also described better using all three mechanisms.

## Chapter 7

# Conclusions

In this thesis, the first measurement of  $b\bar{b}$  azimuthal production correlations at a hadron collider with uniform efficiency over the entire  $\Delta\phi$  range is made. The measurement uses the Run 1B  $J/\psi$  data sample accumulated on the di-muon trigger. An additional lepton is required in the event that passes the soft lepton selection criteria. The  $b\bar{b}$  purity of the samples in different  $\Delta\phi$  regions is determined by a simultaneous unbinned likelihood fit of the pseudo- $c\tau$  of the  $J/\psi$  candidate and the impact parameter of the additional lepton candidate

The measured values of fraction of  $b\bar{b}$  produced in the same azimuthal hemisphere for the electron and muon samples, respectively, are  $f_{toward}^e = 19.2^{+6.5}_{-5.9} \text{ }^{+0.5}_{-0.6}\%$  and  $f_{toward}^\mu = 34.5^{+9.2}_{-8.2} \text{ }^{+8.0}_{-3.1}\%$ , where the first uncertainty is the fit error and the second uncertainty is the additional impact parameter- $c\tau$  shape systematic uncertainty. In order to compare to next-to-leading order theory, the measured value is corrected to the quark level ( $f_{toward}^{corr}$ ). After the correction, the measured values are  $f_{toward}^{corr,e} = 18.6^{+6.3}_{-5.7} \text{ }^{+0.5}_{-0.6} \pm 1.7\%$  and  $f_{toward}^{corr,\mu} = 33.4^{+8.9}_{-7.9} \text{ }^{+7.7}_{-3.0} \pm 2.3\%$  where the first uncertainty is from the fit, the second uncertainty is the

impact parameter- $c\tau$  shape systematic uncertainty, and the third error is the uncertainty on the correction to the quark level. The results are consistent with both leading-log and NLO QCD predictions. The NLO QCD prediction is consistent with the measurements with a parton intrinsic momenta in the prediction as large as  $\langle k_T \rangle = 3 \text{ GeV}$ .  $f_{forward}^{corr,e}$  measured differs from the NLO prediction with  $\langle k_T \rangle = 4 \text{ GeV}$  at the  $3.3 \sigma$  level.

This analysis also has developed and demonstrated techniques that will be very powerful in the current CDF Run II bottom program. The silicon system upgrade has increased the coverage of the interaction region greatly. The muons systems have also undergone a major upgrade which have increased the efficiency of  $J/\psi$  di-muon triggers, while decreasing the triggers' momentum requirements to the level that a bottom meson at rest can produce a  $J/\psi$  which can pass the trigger. With these improvements along with the increase of integrated luminosity projected, a very precise bottom azimuthal differential cross section measurement using this thesis's techniques will be possible, which should have minimal theoretical uncertainties. Such a measurement would be able to simultaneously measure the average initial state momenta of partons ( $\langle k_T \rangle$ ) at the Tevatron as well as provide valuable information on bottom hadroproduction, which has not been theoretically understood since the first measurement of bottom hadroproduction at UA1 [10].

# Bibliography

- [1] H. Fritzsch, M. Gell-Mann and H. Leutwyler, *Advantages of the Color Octet Gluon Picture*. Phys. Lett. **B47** (1973) 365.
- [2] S L. Glashow, *Partial Symmetries of Weak Interactions*. Nucl. Phys. **22** (1961) 579.
- S. Weinberg, *A Model of Leptons*. Phys. Rev. Lett. **19** (1967) 1264.
- A. Salam, *Elementary Particle Theory: Relativistic Groups and Analyticity*, ed. N. Svartholm (1969) 367.
- [3] P. W. Higgs, *Broken Symmetries and the Masses of Gauge Bosons*. Phys. Rev. Lett. **13** (1964) 508.
- [4] Q. R. Ahmad, *Direct Evidence for Neutrino Flavor Transformation from Neutral-Current Interactions in the Sudbury Neutrino Observatory*. Phys. Rev. Lett. **89** (2002) 011301.
- [5] A. G. Holzner, *Search for the Standard Model Higgs Boson at LEP*. arXiv:hep-ex/0208045 (2002).
- [6] M. Kobayashi and T. Maskawa, *CP Violation in the Renormalizable Theory of Weak Interaction*. Prog. Theor. Phys. **49** (1973) 652.
- [7] K. Hagiwara, et al., *Review of Particle Physics. Particle Data Group*. Phys. Rev. D **66** (2000) 010001.
- [8] F. Abe, et. al., *Measurement of  $B^0$  anti- $B^0$  Flavor Oscillations using Jet-Charge and Lepton Flavor Tagging in  $p\bar{p}$  Collisions at  $\sqrt{s} = 1.8$  TeV*. Phys. Rev. **D60** (1999) 072003.
- [9] B. Aubert, et al., *Measurement of CP violating asymmetries in  $B^0$  decays to CP eigenstates*. Phys. Rev. Lett. **86** (2001) 2515.
- [10] C. Albajar, et al., *Beauty Production at the Cern  $p\bar{p}$  Collider*. Phys. Lett. B **256** (1991) 121.
- C. Albajar, et al., *Measurement Of The Bottom Quark Production Cross-section In Proton - Anti-Proton Collisions at  $\sqrt{s} = 0.63$  TeV*. Phys. Lett. B **213** (1988) 405.

- C. Albajar, et al., *Beauty Production at the Cern Proton - Anti-Proton Collider. (Paper 1.)*. Phys. Lett. B **186** (1987) 237.
- [11] S. Abachi, et. al., *Inclusive  $\mu$  and  $b$ -Quark Production Cross Sections in  $p\bar{p}$  Collisions at  $\sqrt{s} = 1.8$  TeV*. Phys. Rev. Lett. **74** (1995) 2632.
- S. Abachi, et al.,  *$J/\psi$  Production in  $p\bar{p}$  Collisions at  $\sqrt{s} = 1.8$  TeV*. Phys. Lett. B **370** (1996) 239.
- B. Abbott, et. al., *Cross Section for  $b$  Jet Production in  $p\bar{p}$  Collisions at  $\sqrt{s} = 1.8$  TeV*. Phys. Rev. Lett. **85** (2000) 5068.
- [12] F. Abe, et al., *Inclusive  $J/\psi$ ,  $\psi(2S)$  and  $b$  Quark Production in  $p\bar{p}$  Collisions at  $\sqrt{s} = 1.8$  TeV*. Phys. Rev. Lett. **69** (1992) 3704.
- F. Abe, et al., *Measurement of the Bottom Quark Production Cross-section using Semi-leptonic Decay Electrons in  $p\bar{p}$  Collisions at  $\sqrt{s} = 1.8$  TeV*. Phys. Rev. Lett. **71** (1993) 500.
- F. Abe, et al., *Measurement of Bottom Quark Production in 1.8 TeV  $p\bar{p}$  Collisions using Semi-leptonic Decay Muons*. Phys. Rev. Lett. **71** (1993) 2396.
- F. Abe, et al., *Inclusive  $\chi(c)$  and  $b$  Quark Production in  $p\bar{p}$  Collisions at  $\sqrt{s} = 1.8$  TeV*. Phys. Rev. Lett. **71** (1993) 2537.
- [13] B. Abbott, et. al., *Small Angle Muon and Bottom Quark Production in  $p\bar{p}$  Collisions at  $\sqrt{s} = 1.8$  TeV*. Phys. Rev. Lett. **84** (2000) 5478.
- [14] D. Acosta, et. al., *Measurement of the  $B^+$  Total Cross-section and  $B^+$  Differential Cross-section  $d\sigma/dp_T$  in  $p\bar{p}$  Collisions at  $\sqrt{s} = 1.8$  TeV*. Phys. Rev. **D65** (2002) 052005.
- F. Abe, et.al., *Measurement of the  $B$  Meson Differential Cross-section,  $d\sigma/dp_T$ , in  $p\bar{p}$  Collisions at  $\sqrt{s} = 1.8$  TeV*. Phys. Rev. Lett. **75** (1995) 1451.
- F. Abe, et al., *Measurement of the  $B$  meson and  $b$  Quark Cross-sections at  $\sqrt{s} = 1.8$  TeV using the Exclusive Decay  $B^0 \rightarrow J/\psi K^{*0}(892)$* . Phys. Rev. D **50** (1994) 4252.
- F. Abe, et al., *A Measurement of the  $B$  meson and  $b$  Quark Cross-sections at  $\sqrt{s} = 1.8$  TeV using the Exclusive Decay  $B^\pm \rightarrow J/\psi K^\pm$* . Phys. Rev. Lett. **68** (1992) 3403.
- [15] T. Affolder, et al., *Measurement of  $b$  Quark Fragmentation Fractions in  $p\bar{p}$  Collisions at  $\sqrt{s} = 1.8$  TeV*. Phys. Rev. Lett. **84** (2000) 1663.

- [16] M. Cacciari and P. Nason, *Is There a Significant Excess in Bottom Hadroproduction at the Tevatron?* Phys. Rev. Lett. **89** (2002) 122003.
- [17] K. Harder, *b Fragmentation and Energy Correlation in  $Z \rightarrow b\bar{b}$  Decays (LEP-1 and SLD Results)*. To be published in the proceedings of 31<sup>st</sup> International Conference on High Energy Physics (ICHEP02) at Amsterdam, Netherlands (2002).
- [18] B. Lampe, *On the Gluon Fragmentation into Heavy Quarks*. INLO-PUB-12-91.
- F. Halzen, W. Y. Keung and D. M. Scott, *Production Of Heavy Quarks: A Nonperturbative Approach*. Phys. Rev. **D27** (1983) 1631.
- [19] P. Abreu, et al., *Measurement of the Rate of  $b\bar{b}b\bar{b}$  Events in Hadronic Z Decays and the Extraction of the Gluon Splitting into  $b\bar{b}$* . Phys. Lett. **B462** (1999) 425.
- R. Barate, et al., *A Measurement of the Gluon Splitting Rate into  $b\bar{b}$  pairs in Hadronic Z decays*. Phys. Lett. **B434** (1998) 437.
- K. Abe, et al., *Improved Measurement of the Probability for Gluon Splitting into  $b\bar{b}$  in  $Z^0$  Decays*. Phys. Lett. B **507** (2001) 61.
- G. Abbiendi, et al., *Production Rates of  $b\bar{b}$  Quark Pairs from Gluons and  $b\bar{b}b\bar{b}$  Events in Hadronic  $Z^0$  Decays*. Eur. Phys. J. **C18** (2001) 447.
- [20] M. H. Seymour, *Heavy Quark Pair Multiplicity in  $e^+e^-$  Events*. Nucl. Phys. **B436** (1995) 163.
- D. J. Miller and M. H. Seymour, *Secondary Heavy Quark Pair Production in  $e^+e^-$  Annihilation*. Phys. Lett. **B435** (1998) 213.
- S. Frixione, M. L. Mangano, P. Nason, and G. Ridolfi, *Heavy-Quark Production*. Adv. Ser. Direct. High Energy Phys. **15** (1998) 609.
- [21] R. D. Field, *The Sources of Q quarks at the Tevatron and Their Correlations*. Phys. Rev. **D65** (2002) 094006.
- [22] E. Norrbin and T. Sjostrand, *Production and Hadronization of Heavy Quarks*. Eur. Phys. J. **C17** (2000) 137.
- [23] P. Nason, et. al., *Bottom Production*. hep-ph/0003142.
- [24] M. Mangano, et. al., *Heavy-Quark Correlations in Hadron Collisions at Next-To-Leading Order*. Nucl. Phys. **B373** (1992) 295.
- [25] C. Albaja, et al., *Measurement of  $b\bar{b}$  Correlations at the CERN  $p\bar{p}$  Collider*. Z. Phys. C **61** (1994) 41.
- [26] B. Abbott, et. al., *The  $b\bar{b}$  Production Cross Section and Angular Correlations in  $p-\bar{p}$  Collisions at  $\sqrt{s} = 1.8$  TeV*. Phys. Lett. **B487** (2000) 264.

- [27] F. Abe et. al., *Measurement of  $b\bar{b}$  Production Correlations,  $B^0$  anti- $B^0$  Mixing and a Limit on  $\epsilon_B$  in  $p\bar{p}$  Collisions at  $\sqrt{s} = 1.8$  TeV*, Phys. Rev. **D55** (1997) 2546.
  - [28] F. Abe, et. al., *Measurement of Correlated  $\mu\text{-}\bar{b}$  Jet Cross Sections in  $p\bar{p}$  Collisions at  $\sqrt{s} = 1.8$  TeV*. Phys. Rev. **D53** (1996) 1051.
  - [29] F. Abe, et.al., *Measurement of  $b\bar{b}$  Rapidity Correlations in  $p\bar{p}$  Collisions at  $\sqrt{s} = 1.8$  TeV*. Phys. Rev. **D61** (2000) 032001.
  - [30] J. Heinrich, et. al., *Soft Lepton Tagging in  $B \rightarrow J/\psi K$  Decays*. CDF internal note CDF/PHYS/BOTTOM/CDF/4745 (1998).
  - [31] F. Abe, et. al., *Observation of  $B_c$  Mesons in  $p\bar{p}$  Collisions at  $\sqrt{s} = 1.8$  TeV*. Phys. Rev. **D58** (1998) 112004.
  - [32] A. Bardi, et al., *The CDF Online Silicon Vertex Tracker*. Nucl. Instrum. Meth. **A485** (2002) 178.
  - [33] J. C. Collins, D. E. Soper, and G. Sterman, *Heavy Particle Production In High-Energy Hadron Collisions*. Nucl. Phys. **B263** (1986) 37.
  - [34] G. Altarelli and G. Parisi, *Asymptotic Freedom In Parton Language*. Nucl. Phys. **B126** (1977) 298.
  - [35] H. L. Lai, et. al., *Global QCD Analysis and the CTEQ Parton Distributions*. Phys. Rev. **D51** (1995) 4763.
  - [36] A. D. Martin, et. al., *Parton Distributions: A New Global Analysis*. Eur. Phys. J. **C4** (1998) 463.
  - [37] P. Nason, et.al., *The One Particle Inclusive Differential Cross-section for Heavy Quark Production in Hadronic Collisions*. Nucl. Phys. **B327** (1989) 49.
  - [38] Y. L. Dokshitzer, D. Diakonov and S. I. Troian, *Hard Semi-inclusive Processes In QCD*. Phys. Lett. **B78** (1978) 290.
- G. Parisi and R. Petronzio, *Small Transverse Momentum Distributions In Hard Processes*. Nucl. Phys. **B154** (1979) 427.
- J. Kodaira and L. Trentadue, *Summing Soft Emission In QCD*. Phys. Lett. **B112** (1982) 66.
- J. C. Collins and D. E. Soper, *Parton Distribution And Decay Functions* Nucl. Phys. **B194** (1982) 445.
- [39] R. D. Field and R. P. Feynman, *A Parameterization Of The Properties Of Quark Jets*. Nucl. Phys. **B136** (1978) 1.

- [40] T. Sjostrand, *The LUND Monte Carlo for Jet Fragmentation and  $e^+e^-$  Physics: Jetset Version 6.2*. Computer Physics Commun. **39** (1986) 347.
  
- T. Sjostrand & M. Bengtson, *The LUND Monte Carlo for Jet Fragmentation and  $e^+e^-$  Physics: Jetset Version 6.3: An Update*. Computer Physics Commun. **43** (1987) 367.
  
- H.-U. Bengtsson and T. Sjostrand, *The LUND Monte Carlo for Hadronic Processes: PYTHIA Version 4.8*. Computer Physics Commun. **46** (1987) 43.
  
- [41] T. Sjostrand, *PYTHIA 5.6 and JETSET 7.3: Physics and Manual* CERN-TH.6488/92 (1992).
  
- [42] C. Peterson, et.al., *Scaling Violations in Inclusive  $e^+e^-$  Annihilation Spectra*. Phys. Rev. **D27** (1983) 105.
  
- [43] M. G. Bowler,  *$e^+e^-$  Production of Heavy Quarks in the String Model*. Z. Phys. **C11** (1981) 169.
  
- B. Anderson, et. al., *Parton Fragmentation and String Dynamics*. Phys. Rep. **97** (1983) 31.
  
- [44] G. Nesom, et. al., *Measurement Of The B Quark Fragmentation Function In  $Z^0$  Decays*. Int. J. Mod. Phys. A **16S1A** (2001) 222.
  
- A. Heister, et al., *Study of the fragmentation of b quarks into B mesons at the Z peak*. Phys. Lett. **B512** (2001) 30.
  
- G. Abbiendi, et. al., *Inclusive Analysis of the Fragmentation Function in Z Decays at LEP*. Submitted to Eur. Phys. J. C. (2002).
  
- G. Barker, et. al., *A Study of b-Quark Fragmentation Function with the DELPHI Detector at LEP I*. Contributed Paper for ICHEP 2002.
  
- [45] J. Chrin, *Upon The Determination Of Heavy Quark Fragmentation Functions In  $e^+e^-$  Annihilation*. Z. Phys. **C36** (1987) 163.
  
- [46] P. Nason and C. Oleari, *A Phenomenological study of Heavy-Quark Fragmentation Functions in  $e^+e^-$  Annihilation*. Nucl. Phys. **B565** (2000) 245.
  
- [47] R. Blair, *Photons and diphotons from the Tevatron*. FERMILAB-CONF-97-294-E (1997).
  
- [48] T. Takano., *Di-photon Production in 1.8 TeV Proton-Antiproton Collisions*. Ph. D. Thesis, University of Tsukuba. (1999)



- [49] L. Apanasevich et.al., *k(T) Effects in Direct Photon Production*. Phys. Rev. D **59** (1999) 074007.
- [50] C. W. Smith & C. D. Curtis, *Operation of the Fermilab  $H^-$  Magnetron Source*. Proc. 4th Int. Symp. on the Production and Neutralization of Negative Ions and Beams, Brookhaven, US, AIP Conf. Proc. No. 158, (1986) 425.
- [51] K. Junck, et. al., *Commissioning and First Operational Experience of the 400-MeV Linac at Fermilab*. FERMILAB-Conf-94-181 (1994).
- [52] H. Edwards, *The Tevatron Energy Doubler: A Superconducting Accelerator*. Ann. Rev. Nucl. Part. Sci. **35** (1985) 605.
- [53] M. D. Church & J. P. Marriner, *The Antiproton Sources: Design and Operation*. Ann. Rev. Nucl. Part. Sci. **43** (1993) 253.
- [54] A. Ruggiero, *The Fermilab Tevatron I Debuncher Ring*. IEEE Trans. Nucl. Sci. **30** (1983) 2478.
- [55] B. Austin, et. al., *Fast Betatron Cooling in the Debuncher Ring for the Fermilab Tevatron I Project*. IEEE Trans. Nucl. Sci. **30** (1983) 2593.
- [56] A. Ando, et. al., *Design of an 8-GeV Accumulator Ring for the Fermilab Tevatron I Project*. IEEE Trans. Nucl. Sci. **30** (1983) 2031.
- [57] Particle Data Group, *High-Energy Collider Parameters*. Phys. Rev. **D 54**, 128 (1996).
- [58] F. Abe, et. al., The CDF Collaboration *The CDF Detector: An Overview*. Nucl. Instrum. Methods Phys. Res. **A 271** (1988) 387.
- [59] P. Azzi, et. al., *SVX': The New CDF Silicon Vertex Detector*. Nucl. Inst. Meth. **A 360** (1995) 137.
- [60] F. Bedeschi, et. al., *Design and Construction of the CDF Central Tracking Chamber*. Nucl. Inst. Meth. **A 271** (1988) 387.
- [61] M. D. Peters, *Run 1B  $dE/dx$  Corrections*. CDF internal note CDF/ANAL/BOTTOM/CDFR/3807 (1996).
- [62] L. Balka, et. al., *The CDF Electromagnetic Calorimeter*. Nucl. Inst. Meth. **A267** (1988) 272.
- [63] S. Bertolucci, et. al., *The CDF Central and Endwall Hadronic Calorimeter*. Nucl. Inst. Meth. **A267** (1988) 301.
- [64] G. Ascoli, et. al., *CDF Central Muon Detector*. Nucl. Inst. Meth. **A268** (1988) 33.
- [65] J. D. Lewis, et. al., *The 1992 CDF Muon System Upgrade*. CDF public note CDF/PUB/MUON/PUBLIC/2858 (1994).
- [66] D. Cronin-Hennessey, A. Beretvas and P. F. Derwent, *Luminosity Monitoring and Measurement at CDF*. Nucl. Instrum. Meth. A **443** (2000) 37.

- [67] D. Amidei, et. al., *A Two Level FASTBUS Based Trigger System for CDF*. Nucl. Instrum. Methods Phys. Res. **A 269** (1988) 68.
- [68] J. Carroll, et. al., *The CDF Level 3 Trigger*. Nucl. Instrum. Methods Phys. Res. **A300** (1991) 552.
- [69] G. Ascoli, et. al., *CDF Central Muon Level-1 Trigger Electronics*. Nucl. Inst. Meth. **A269** (1988) 63.
- [70] G. Foster, et. al., *A Fast Hardware Track-Finder for the CDF Central Tracking Chamber*. Nucl. Instr. Meth. Phys. Res. **A269** (1988) 93.
- [71] S. Pappas & J. Lewis, *Run 1B Low  $p_T$  Central Dimuon Trigger Efficiency*. CDF internal note CDF/ANAL/TRIGGER/CDFR/4076 (1997).
- [72] D. Quarrie & B. Troemel, *YBOS Programmer's Reference Manual*. CDF public note CDF/DOC/CDF/PUBLIC/0156 (1987).
- [73] S. Pappas, *DIMUTG:Dimuon Trigger Simulation for Run 1B*. CDF internal note CDF/ANAL/TRIGGER/CDFR/3537 (1996).
- [74] D. Frei, *Multiple Scattering of Central Muons*. CDF internal note CDF/ANAL/MUON/CDFR/1430 (1991).
- [75] S. Kim and J. Suzuki, *Update on the Search for  $B_c \rightarrow eJ/\psi X$  Using Run 1A and Run 1B data*. CDF internal note CDF/ANAL/BOTTOM/CDFR/3287 (1996).
- [76] J. Marriner, *Secondary Vertex Fit with Mass and Pointing Constraints(CTVMFT)*. CDF public note CDF/DOC/SEC-VTX/public/1996 (1993).
- [77] F. Abe et. al., *Measurement of B Hadron Lifetimes Using  $J/\psi$  Final States at CDF*. Phys. Rev. **D 57** (1998) 538.
- [78] F. Abe, et. al., *Measurement of  $J/\psi$  and  $\psi(2s)$  Polarization in  $p\bar{p}$  Collisions at  $\sqrt{s} = 1.8$  TeV*. Phys. Rev. Lett. **85** (2000) 2886.
- [79] D. E. Groom, et al., *Review of Particle Physics. Particle Data Group*. The European Physical Journal **C15** (2000) 1.
- [80] F. Abe, et. al., *A Measurement of  $\sin(2\beta)$  from  $B \rightarrow J/\psi K_S^0$  with the CDF Detector*. Phys. Rev. **D61** (2000) 072005.
- [81] R. Harris, et. al., *CES Response and  $\chi^2$  for 1990 Test beam Electrons*. CDF internal note CDF/ANAL/ELECTRON/CDFR/1432 (1991).
- [82] P. Avery, et. al., *QQ - The CLEO Event Generator*. Cornell Internal Note CSN-112.
- [83] M. Shapiro, et. al., *A User's Guide to QFL*. CDF public note CDF/ANAL/MONTECARLO/PUBLIC/1810 (1992).
- [84] C. Campagnari and D. Kestenbaum, *Review of SLT algorithm for Run 1B*. CDF internal note CDF/ANAL/TOP/CDFR/3682 (1996).

- [85] O. Long, et. al., *An Update of the Vertex Tagged Inclusive Lepton Data Proper Time Dependent  $B^0$  Mixing Analysis*. CDF internal note CDF/ANAL/BOTTOM/CDFR/4315.
- [86] E. Braaten, et.al., *Perturbative QCD Fragmentation Functions for  $B_c$  and  $B_c^*$  Production*. *Phy. Rev.* **D48** (1993) 5049.
- [87] N. Isgur, et.al., *Semi-leptonic  $B$  and  $D$  decays in the Quark Model*. *Phy. Rev.* **D39** (1998) 2002.
- [88] J. Suzuki, *Observation of the  $B_c$  Meson on 1.8 TeV Proton-Antiproton Collisions*. Ph. D. Thesis, University of Tsukuba (1998).
- [89] F. James & M. Roos, '*MINUIT*': *A System for Function Minimization and Analysis of the Parameter Errors and Correlations*. *Comput. Phys. Commun* **10** (1975) 343.
- [90] H. Mitsushio, *Measurement of Neutral  $B$  Meson Mixing in Electron-Muon Events in 1.8-TeV Proton - Anti-proton Collisions*. Ph. D. Thesis, University of Tsukuba. (1996).
- [91] P. Sphicas, *A  $b\bar{b}$  Monte Carlo Generator*. CDF/DOC/BOTTOM/CDFR/2655 (1994).
- [92] R. D. Field, private communication.

# Appendix A

## $dE/dx$ Fit Description

The  $dE/dx$  fit is used to determine the conversion selection criteria purity and efficiency. In this fit, the particle species ( $e^{+/-}$ ,  $\pi^{+/-}$ ,  $K^{+/-}$ , or  $p^{+/-}$ )<sup>1</sup> of the conversion and pair candidates are fit simultaneously. Events consistent with both the SLT conversion and pair candidates being electrons are assumed to be conversions.

The fit function is an unbinned extended log-likelihood:

$$L = \frac{\mu^N e^{-\mu}}{N!} \prod_i P_i \quad (\text{A.1})$$

where:

$$P_i = \frac{1}{2\pi\sigma_i^{slt}\sigma_i^{pair}\mu} \cdot \sum_{j,k} \left[ N_{j,k} \cdot e^{-\frac{(Q_i^{slt}-Q_{i,j}^{slt})^2}{(\sqrt{2}\sigma_i^{slt})^2}} \cdot e^{-\frac{(Q_i^{pair}-Q_{i,k}^{pair})^2}{(\sqrt{2}\sigma_i^{pair})^2}} \right] \quad (\text{A.2})$$

The parameters are:

N: the number of events in the data

$\mu$ : total number of events fit

$N_{j,k}$ : the number of events with SLT conversion candidates of particle species j and pair

---

<sup>1</sup>The mass difference between charged muons and pions makes it impossible to fit these two components separately. Any muon content of the sample will be fit as pions.

candidates of particle species  $k$

$\sigma_i^{slt}$ : the error on the dE/dx measurement for event  $i$  for SLT conversion candidate

$Q_i^{slt}$ : the corrected dE/dx measured for event  $i$  for SLT conversion candidate

$Q_{i,j}^{slt}$ : predicted dE/dx for particle species  $j$ , event  $i$  for SLT conversion candidate

$\sigma_i^{pair}$ : the error on the dE/dx measurement for event  $i$  for the pair candidate

$Q_i^{pair}$ : the corrected dE/dx measured for event  $i$  for the pair candidate

$Q_{i,k}^{pair}$ : predicted dE/dx for particle species  $k$ , event  $i$  for the pair candidate

## Appendix B

# Conversion Track Quality Study

A large fraction of conversion candidates with SVX hits have a conversion radius outside of the SVX. The track's quality for events with large conversion radius is studied. The conversion sample is divided into events with radius greater or less than 6 cm, where the sample with a radius less than 6 cm is assumed to have 3 real SVX hits and the sample with a radius greater than 6 cm is assumed to have not to have 3 real SVX hits. The number of hits, the number of shared hits, and the  $\chi^2/DOF$  of the SVX fit have been studied to these two samples as well as for the conversion Monte Carlos and SLT electron data.

Figure B.1 shows the number of SVX hits for the candidates. The number of SVX hits in the conversion Monte Carlos agrees well with the conversions in data with radius less than 6 cm. The large radius conversion data has much more 3 SVX hit tracks. Making a 4 SVX track requirement would remove approximately 25% of the data, and therefore the cuts is not applied. Figure B.2 shows the SVX fit  $\chi^2/DOF$ . The conversion data with large conversion radius does have a broader  $\chi^2/DOF$  distribution, but the standard cut of 6 will not do much. Figure B.3 shows the number of shared hits. Again, the number of

conversion with large radius can not be reduced significantly with a cut.

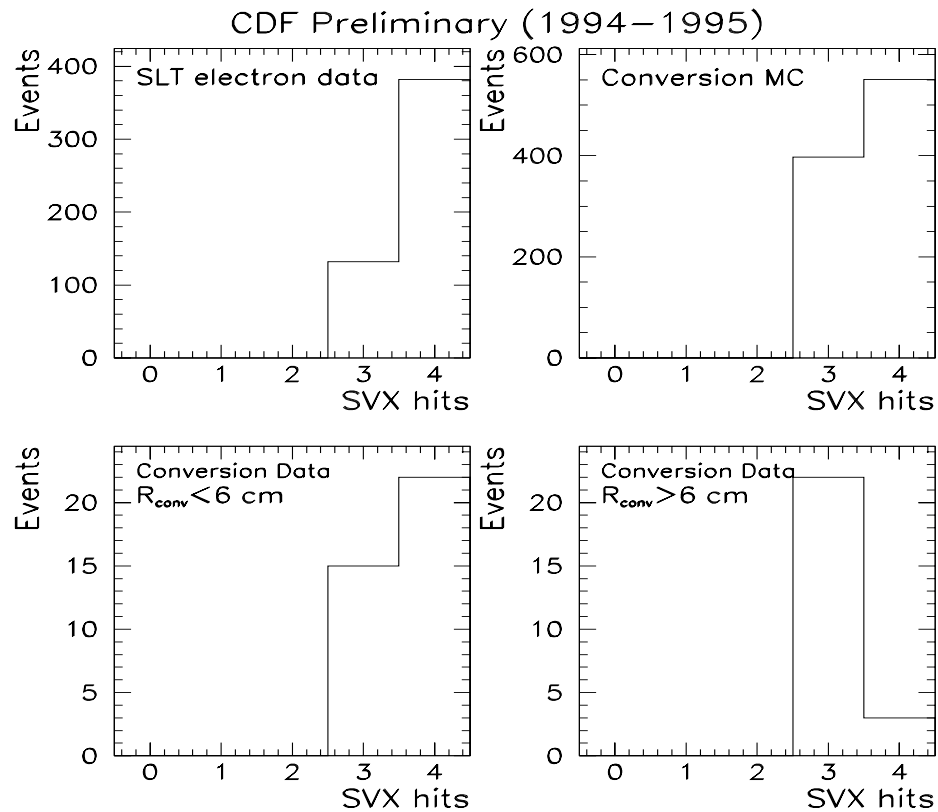


Figure B.1: Number of SVX hits. Top Left: SLT electron data. Top Right: Conversion Monte Carlos. Bottom Left: Conversion data with the conversion radius less than 6 cm. Bottom Right: Conversion data with the conversion radius greater than 6 cm.

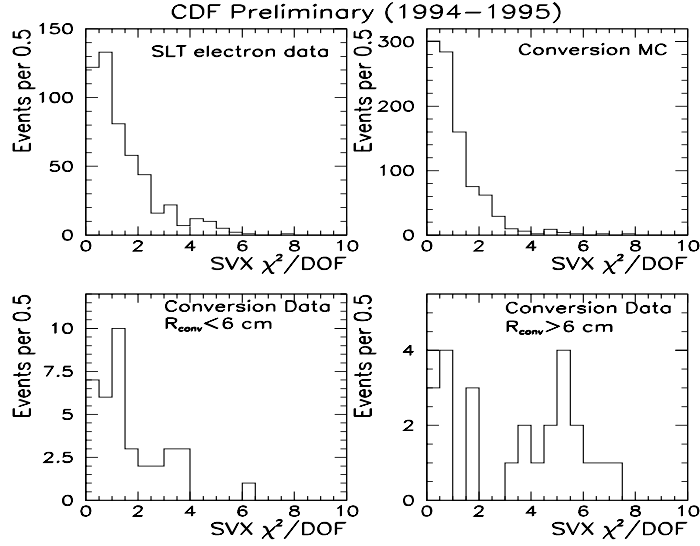


Figure B.2:  $SVX$  fit  $\chi^2/\text{DOF}$ . Top Left:  $SLT$  electron data. Top Right: Conversion Monte Carlos. Bottom Left: Conversion data with the conversion radius less than 6 cm. Bottom Right: Conversion data with the conversion radius greater than 6 cm.

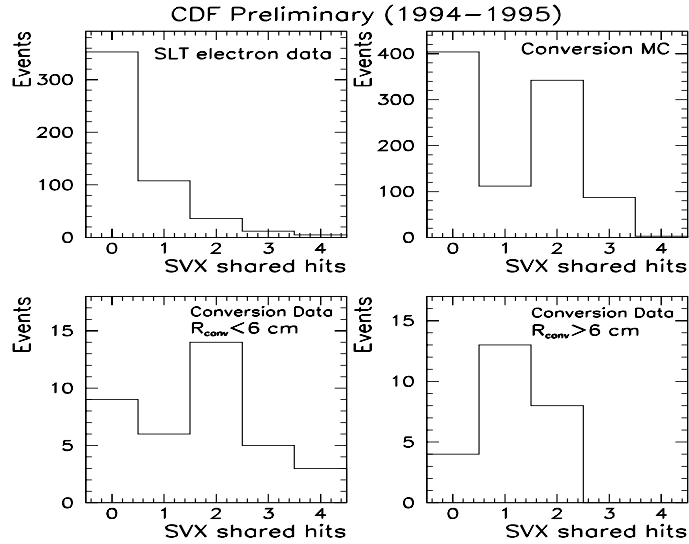


Figure B.3: Number of shared hits. Top Left:  $SLT$  electron data. Top Right: Conversion Monte Carlos. Bottom Left: Conversion data with the conversion radius less than 6 cm. Bottom Right: Conversion data with the conversion radius greater than 6 cm.



## Appendix C

# $B_c \rightarrow J/\psi \ell X$ and $b \rightarrow J/\psi \ell_{\text{fake}} X$ impact parameter- $c\tau$ fit shape

The  $B_c \rightarrow J/\psi \ell X$  and  $b \rightarrow J/\psi \ell_{\text{fake}} X$  impact parameter- $c\tau$  fit shapes attempt to describe the correlations between the impact parameter of the additional lepton candidate and the  $c\tau$  of the  $J/\psi$ . The shape is constructed by first fitting the  $c\tau$ . The impact parameter is then fit at a given  $c\tau$  with the normalization given by the  $c\tau$  fit.

In section 5.1.1, the calculation of the 'pseudo'-decay length ( $c\tau$ ) is described. The factor  $F_{\text{corr}}(p_T^{J/\psi})$  is the correction factor which accounts for the difference of using the  $J/\psi$  kinematic quantities instead of a fully reconstructed bottom hadron. The  $B_c$  meson is much more massive than the other b mesons, and therefore the correction factor  $F_{\text{corr}}(p_T^{J/\psi})$  is different than the other bottom hadrons. In addition, the calculation of  $F_{\text{corr}}(p_T^{J/\psi})$  made no requirements on the other decay products from the bottom hadron. In the  $B_c \rightarrow J/\psi \ell^+ X$  background, the presence of the additional lepton which passes the selection criteria biases the the average  $p_T$  of  $B_c$  to be larger relative to the  $J/\psi$ ; therefore, the pseudo- $c\tau$  measured

using  $F_{corr}(p_T^{J/\psi})$  for the  $B_c$  is not a good approximation of the true proper decay length.

The following functional form is used to describe the  $c\tau$  of the  $B_c$  background

$$F_{B_c}^{ct}(x) = f_1 \cdot F_{b1}^{c\tau}(x) + (1 - f_1) \cdot F_{b2}^{c\tau}(x) \quad (C.1)$$

where  $F_{b1}^{c\tau}$  and  $F_{b2}^{c\tau}$  has the functional form of equation 5.8.

For the  $b \rightarrow J/\psi \ell_{\text{fake}}$  background, the factor  $F_{corr}(p_T^{J/\psi})$  is also incorrect. As in the  $B_c$  background, the additional track from the same vertex biases the ratio between bottom hadron and  $J/\psi$  momentum to be larger relative to events with no requirement of the non- $J/\psi$  decay products. Fortunately, the function used to fit the  $c\tau$  for bottom decay  $J/\psi$  (equation 5.8) can still fit the  $c\tau$  of  $b \rightarrow J/\psi \ell_{\text{fake}}$  events.

$$F_{B_{fake}}^{ct}(x) = F_b^{c\tau}(x) \quad (C.2)$$

The impact parameter distribution widens as a function of the  $c\tau$  of the  $J/\psi$ ; the longer the decay length is, the larger the impact parameter can be. At small  $c\tau$ , the shape of the impact parameter is described by the impact parameter resolution function. At large  $c\tau$ , the displaced vertex effects dominate.

The functional form of the impact parameter shape at a given  $c\tau$  is chosen to take this into account. The function is a gaussian whose width varies with  $c\tau$  convoluted with the impact parameter resolution function. The normalization of the impact parameter at the given  $c\tau$  is determined by the  $c\tau$  only fit. The gaussian width has the following parameterization:

$$\sigma(c\tau) = A \left(1 - e^{-c\tau/B}\right) \quad c\tau > 0 \quad (C.3)$$

$$\sigma(c\tau) = C \quad c\tau \leq 0 \quad (C.4)$$

The impact parameter resolution function is assumed to have the same functional form as  $F_{direct}^{d_0}(x)$  (equation 5.9). The impact parameter shape at a given  $c\tau$  shape for both correlated backgrounds has the form:

$$F_{corr}^{d_0}(x, c\tau) = G(y, \sigma(c\tau)) * F_{direct}^{d_0}(x - y) = \int_{-\infty}^{\infty} F_{direct}^{d_0}(x - y) \cdot G(y, \sigma(c\tau)) dy \quad (C.5)$$

where  $x$  is the impact parameter value.

The combined impact parameter- $c\tau$  shape fit for the  $B_c \rightarrow J/\psi \ell X$  background is:

$$F_{B_c}(x, y) = F_{B_c}^{c\tau}(y) \cdot F_{corr}^{d_0}(x, y) \quad (C.6)$$

with  $x$  and  $y$  being the impact parameter and  $c\tau$ , respectively.

Similarly, the combined impact parameter- $c\tau$  shape fit for the  $b \rightarrow J/\psi \ell_{fake} X$  background is:

$$F_{B_c}(x, y) = F_{B_{fake}}^{c\tau}(y) \cdot F_{corr}^{d_0}(x, y) \quad (C.7)$$

## Appendix D

# Toy Monte Carlos Studies

The impact parameter- $c\tau$  likelihood is tested using a large set of toy Monte Carlo samples. First, input means for the fit various fit components are chosen to be similar to the fit results in data. The constrained terms are chosen to be consistent with the constraint. The input parameters are shown in table D.1.

These inputs are Poisson fluctuated to determine the composition of each sample. Each 'event' is assigned an impact parameter and  $c\tau$  according to the shape function used to describe that type of event .

Next, the fit constraints not yet varied ( $R_{side}$ ,  $R_{conv}$ ,  $N_{B_{fake}}$ ,  $N_{B_c}$ ,  $N_{conv}^t$ ,  $N_{conv}^a$ , and  $N_{convside}$ ) are fluctuated using the appropriate statistic. The fluctuated constraints are then used in the fit of the toy Monte Carlos sample.

A total of 1000 samples are generated and fit for both the electron and muon samples. The fit values are not forced to be non-negative. The pull is calculated for each fit value relative to the non-fluctuated input quantities. The pull is equal to width of the  $\frac{n-\mu}{\sigma_n}$  distribution where  $n$  is the fit value,  $\sigma_n$  is the fit error returned, and  $\mu$  is the average

	Electron		Muon	
	Toward	Away	Toward	Away
$n_{b\bar{b}}$	29.6	124.7	23.0	43.6
$n_{bd}$	1.5	0.1	0.2	8.1
$n_{bconv}$	0.6	1.1	N/A	N/A
$n_{dd}$	37.0	49.5	4.9	17.8
$n_{dconv}$	4.3	7.2	N/A	N/A
$n_{side}^{signal}$	22.5	23.5	17.0	8.5
$n_{side}^{sideband}$	45.0	47.0	34.0	17.0
$n_{B_{fake}}^t$	2.85	0.0	11.7	0.00
$n_{B_c}^t$	10.0	0.0	7.2	0.0

Table D.1: Average inputs into toy Monte Carlo tests of impact parameter- $c\tau$  likelihood.  $n_{side}^{signal}$  is the average number of events generated from the sideband template with a  $J/\psi$  mass in the signal region.  $n_{side}^{sideband}$  is the average number of events generated from the sideband template with a  $J/\psi$  mass in the sideband region.

value of the parameter input. The bias, which is the mean of the  $\frac{n-\mu}{\sigma_n}$  distribution, is also measured. Finally, the average difference between the fitted value and input parameter is calculated,  $\overline{(x - \bar{x})}$ .

Table D.2 shows the pulls, biases and average differences of the fits. The pulls, biases, and average differences for all variables are acceptable for both test samples. All pulls are within  $\pm 6\%$  of 1 and all biases are within  $\pm 0.12\sigma$  of 0. Allowing the likelihood to have negative components yields fit results with meaningful fit values and errors.

Figure D.1 shows the minimum log-likelihood distributions of both samples. 19.6% of the muon toy Monte Carlos samples and 49.8% of the electron toy Monte Carlos samples have a higher minimum log-likelihood than the data. The minimum log-likelihood distributions along with the biases, pulls, and average differences give confidence that the likelihood is working properly and describes the data.

As a further check, figure D.2 shows the distributions of the fit values of  $f_{towards}$  for the

	Electron			Muon		
	Bias	Pull	$\overline{(x - \bar{x})}$	Bias	Pull	$\overline{(x - \bar{x})}$
$r_{side}$	$0.049 \pm 0.032$	$1.005 \pm 0.023$	0.002	$-0.008 \pm 0.032$	$0.999 \pm 0.022$	0.000
$n_{B_{fake}}$	$0.011 \pm 0.033$	$1.028 \pm 0.022$	0.012	$-0.013 \pm 0.03$	$1.010 \pm 0.026$	0.026
$n_{B_c}$	$-0.027 \pm 0.033$	$0.992 \pm 0.022$	-0.030	$-0.044 \pm 0.033$	$0.995 \pm 0.026$	-0.040
$r_{conv}$	$-0.089 \pm 0.035$	$1.081 \pm 0.027$	-0.013			
$n_{bb}^t$	$-0.094 \pm 0.031$	$0.987 \pm 0.021$	-0.59	$-0.003 \pm 0.033$	$1.031 \pm 0.023$	-0.41
$n_{bd}^t$	$0.086 \pm 0.033$	$1.006 \pm 0.026$	0.58	$0.012 \pm 0.034$	$1.050 \pm 0.026$	0.17
$n_{dd}^t$	$-0.075 \pm 0.033$	$1.007 \pm 0.023$	-0.18	$0.091 \pm 0.034$	$0.952 \pm 0.022$	0.46
$n_{dconv}^t$	$-0.011 \pm 0.034$	$1.016 \pm 0.023$	0.171			
$n_{side}^t$	$-0.001 \pm 0.034$	$1.005 \pm 0.025$	0.15	$0.117 \pm 0.036$	$1.018 \pm 0.024$	-0.49
$n_{bb}^a$	$0.032 \pm 0.032$	$0.995 \pm 0.02$	0.30	$-0.046 \pm 0.031$	$0.942 \pm 0.024$	-0.16
$n_{bd}^a$	$0.025 \pm 0.033$	$1.034 \pm 0.025$	-0.17	$-0.046 \pm 0.032$	$0.999 \pm 0.022$	-0.23
$n_{dd}^a$	$0.046 \pm 0.032$	$1.000 \pm 0.024$	-0.022	$0.016 \pm 0.032$	$0.985 \pm 0.025$	0.12
$n_{dconv}^a$	$-0.047 \pm 0.032$	$0.945 \pm 0.024$	0.06			
$n_{side}^a$	$-0.019 \pm 0.032$	$0.998 \pm 0.022$	0.094	$-0.021 \pm 0.035$	$0.999 \pm 0.026$	0.013
$f_1^{d_0}$	$-0.007 \pm 0.031$	$1.003 \pm 0.024$	0.002			
$\lambda_1^{d_0}$	$0.071 \pm 0.031$	$0.985 \pm 0.025$	0.001			
$\sigma^{d_0}$	$-0.036 \pm 0.031$	$0.958 \pm 0.025$	-0.000			
$n_{convside}$	$0.115 \pm 0.034$	$0.997 \pm 0.024$	-0.109			
$f_1^{c\tau}$	$0.010 \pm 0.031$	$0.990 \pm 0.025$	-0.005			
$f_B^{c\tau}$	$-0.054 \pm 0.033$	$1.033 \pm 0.023$	0.004			
$l_1^{c\tau}$	$0.116 \pm 0.032$	$0.982 \pm 0.026$	0.02			
$\lambda_B^{c\tau}$	$-0.098 \pm 0.032$	$0.938 \pm 0.025$	-0.001			
$\sigma^{c\tau}$	$0.071 \pm 0.033$	$1.039 \pm 0.030$	0.000			

Table D.2: Toy Monte Carlo Test Fit Results

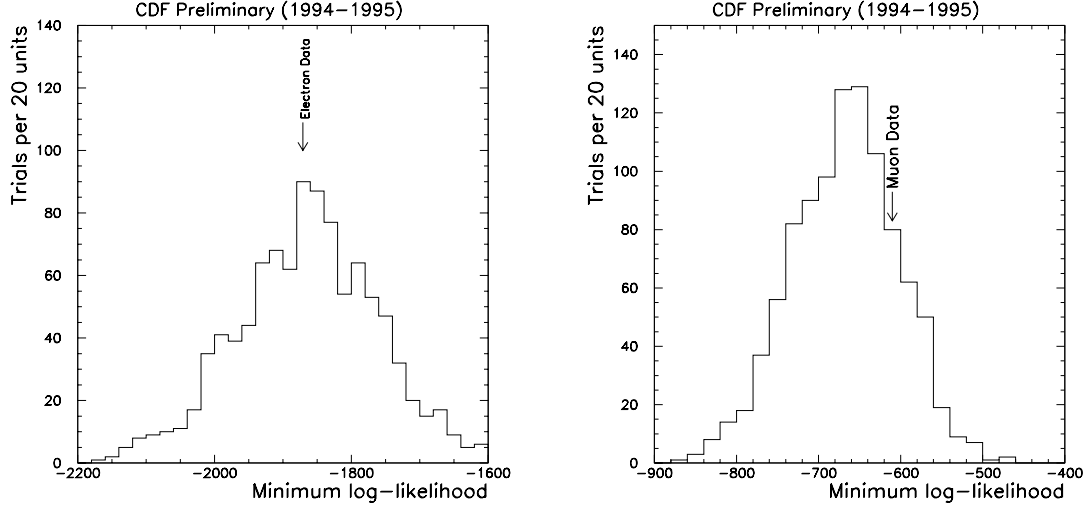


Figure D.1: *The minimum log-likelihood distributions of the toy Monte Carlos Left: Electrons Right: Muons.*

assemblies of toy Monte Carlos. The muon toy Monte Carlos samples has an input mean of  $f_{towards}^{input} = 34.5\%$  and fit a mean of  $f_{towards}^{fit} = 34.5 \pm 0.4\%$ . The width of the fit  $f_{towards}$  distribution is  $10.9 \pm 0.3\%$  which is consistent with the error seen in data of  ${}^{+9.2}_{-8.2}\%$ . The electron toy Monte Carlos have a mean of  $f_{towards}^{fit} = 18.6 \pm 0.2\%$  with a width of  $6.0 \pm 0.1$ . The input value is  $f_{towards}^{input} = 19.2\%$  and the fit error of  ${}^{+6.5}_{-5.8}\%$ , both which are consistent with the fit values.

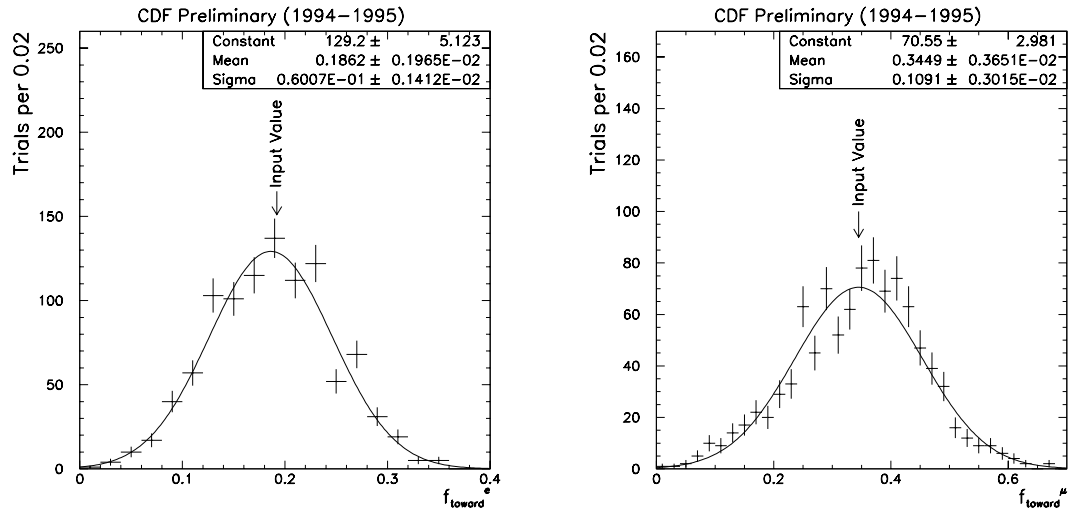


Figure D.2: The fit  $f_{toward}$  distributions of the toy Monte Carlos Left: Electrons Right: Muons.